CIRCUIT-LEVEL MODELING AND SIMULATION OF SEMICONDUCTOR LASERS

BY

PABLO VALENTE MENA

B.S., University of Illinois, 1994
M.S., University of Illinois, 1995

THESIS

Submitted in partial fulfillment of the requirements
for the degree of Doctor of Philosophy in Electrical Engineering
in the Graduate College of the
University of Illinois at Urbana-Champaign, 1998

Urbana, Illinois

CIRCUIT-LEVEL MODELING AND SIMULATION OF SEMICONDUCTOR LASERS

Pablo Valente Mena, Ph.D.
Department of Electrical and Computer Engineering
University of Illinois at Urbana-Champaign, 1998
Sung-Mo Kang, Advisor

The past decade has seen the continued development of a wide array of optoelectronic systems, most notably optoelectronic interconnects for short- and long-distance communications. Consequently, there exists a growing need for suitable computer-aided design tools that would allow the simulation of these applications in advance of their actual fabrication. While such tools are already well-established in conventional electronics, their use in optoelectronics continues to evolve. Of particular importance is the development of optoelectronic device models which can be used in conjunction with electronic components for the circuit-level simulation of optoelectronic circuits.

Motivated by these observations, in this thesis we present circuit-level device models for semiconductor lasers. First, we present the implementation of rate-equation-based quantum-well-laser models in SPICE. Because it is critical that these models determine the correct numerical solution of the rate equations during dc simulation, we demonstrate analytically that the use of variable transformations for the carrier and photon densities limits the models to a single dc-solution regime under nonnegative current injection. We also extract model parameters from measured device characteristics and discuss the reasonable agreement obtained between simulated and experimental data.

We then present circuit-level models for vertical-cavity surface-emitting lasers (VCSELs) and their strong thermally and spatially dependent behavior. The first approach, implemented in both HSPICE and SABER, is a simple thermal model which incorporates a temperature-dependent offset current into the standard laser rate equations in order to describe thermally dependent threshold current and output-power rollover in the LI characteristics. The second model is a comprehensive circuit-level model in SABER which uses analytical temperature dependencies and spatially independent rate equations to describe a VCSEL's thermal *and* spatial behavior. In addition to simulating thermal LI characteristics, this latter model can also be used to simulate multimode competition, temperature-dependent modulation responses, and diffusive transients in the time domain. After presenting the theory and implementation of our VCSEL models, we compare simulated and experimental data for various devices reported in the literature. Despite some important modeling and characterization issues, the data compare favorably.

For you, Mom.

ACKNOWLEDGMENTS

I would first like to thank my advisor, Dr. Sung-Mo Kang, for his guidance and encouragement during my four and a half years of graduate school. The opportunities that he provided me for understanding the intricacies of Ph.D. research have certainly prepared me well for my future endeavors. I am grateful as well to the other faculty members on my committee, Tom DeTemple, George Papen, and James Coleman. Dr. DeTemple’s encouragement and technical insight were invaluable. Furthermore, Dr. Papen helped lend important perspective to much of my work, while Dr. Coleman has provided technical advice which has been greatly appreciated. Also, I would like to acknowledge the many sources of funding for my work, including my National Science Foundation and SURGE Fellowships, the National Science Foundation Engineering Research Center (ECD89-43166), and the DARPA Center for Optoelectronic Science and Technology (MA972-94-1-0004).

I must next thank my colleagues at Motorola’s Applied Simulation and Modeling Research group in Schaumburg, IL, where I have spent the final year of my Ph.D. training. I am indebted to Dr. Jim Morikuni, Dr. Austin Harton, and Dr. Karl Wyatt for providing me the opportunity to simultaneously enjoy the benefits of both the graduate-school and industry experiences. I would especially like to thank Jim, who has been a good friend since I met him during my last year as an undergraduate. He has always been an excellent source of advice, technical or otherwise, and I will not soon forget his efforts to allow me to finish my graduate career at Motorola.

Many thanks go to my friends from the Beckman Institute and CSRL. Matt Bruensteiner, in addition to going to great lengths to supply me with experimental device data, has also provided me with many interesting conversations during these last few years. I would also like to thank everyone who participated in more than a few lunch and basketball outings, particularly Jim Stroming, Ed

Breault, and Ketan Patel. Also, I shouldn’t forget all of my office mates during my stay at the Beckman Institute, including Andrew Xiang, Ashfaq Hossain, John Lockwood, Abhijit Dharchoudhury, Brent Whitlock, Sueng-Yong Park, Woongchul Choi, David Cho, Jenny Yang, Haoran Duan, and Steven Ho. I would also like to thank Yusuf Leblebici, whose advice and perspective have always been appreciated.

Finally, I would like to thank my family. My sisters Else and Yvonne and my aunt Josefa have never had anything but my best interests at heart. I would particularly like to thank my father. More than anyone else since I left home eight years ago, he has become a great friend to me. I could never have endured graduate school without his support, encouragement, and, most importantly, constant willingness to listen. To put it quite simply– thanks, Dad.

TABLE OF CONTENTS

CHAPTER 1

INTRODUCTION

1.1 Optoelectronic System Design and Simulation

Optoelectronics, namely the integration of photonic and electronic components, continues to attract considerable interest as a viable means for alleviating many of the bottlenecks and limitations of purely electronic systems. In general, optoelectronic applications augment traditional electronics, such as transistors, with various photonic components, including optical sources (e.g., lasers), detectors (e.g., photodiodes), and transmission media (e.g., waveguides, lenses, and holograms). A simple example is the optical head of a CD player, in which a semiconductor laser and photodetector, in conjunction with electronic drive circuits and amplifiers, are used to optically probe a compact disc for information.

The most well known examples, however, are *optoelectronic interconnects*. Compared to their electrical counterparts, these interconnects possess a number of advantages, including increased communication bandwidth, reduced interchannel crosstalk, lower levels of power consumption [1.1], and reduced interconnection delays [1.2]. Consequently, they are well-suited to situations where electronic interconnects place unacceptable limits on system performance. For example, optoelectronic interconnects can eliminate bottlenecks in board-level system design [1.1]. Fiber-optic communications is another example in which optical interconnects provide dramatic bandwidth advantages over electrical transmission schemes. Considering these points, it should come as no surprise that the literature is rich with specific design examples, including free-space board-to-board interconnects [1.3], optical clock distribution schemes [1.4], and parallel Gb/s optical links [1.5]-[1.7].

Obviously, the design of these optoelectronic applications would greatly benefit from computer-aided-design (CAD) tools that would allow the optimization and verification of a particular system before its actual fabrication, thereby significantly reducing the design cycle. While such technology is well established for electronics (as evidenced by popular CAD packages such as Mentor Graphics), its optoelectronic counterparts are still maturing. Some industry-standard tools, such as Analogy's SABER [1.8], incorporate optoelectronic device models into a larger design framework, while more dedicated tools have been reported which focus on the design and simulation of optoelectronic systems [1.9]-[1.12]. For example, iFROST [1.12] supports the event-driven simulation of optoelectronic data links, while iSMILE [1.9] incorporates circuit-level photonic device models into a SPICE-like simulation environment. Though these initial efforts have demonstrated the merits of optoelectronic CAD, their continued evolution hinges critically on the corresponding development of suitable models for optoelectronic devices, particularly semiconductor lasers and photodetectors. Ultimately, these models will determine the extent to which optoelectronic CAD tools can be used for the design and simulation of real-world applications. Thus, our specific interest here is the development of circuit-level models for semiconductor lasers.

1.2 Circuit-Level Laser Models

One method for simulating semiconductor lasers is through the use of device-level models, in which a device's internal physical mechanisms are described in great detail. Often, these models incorporate multidimensional analysis of spatial behavior, as well as detailed solutions of the optical characteristics. For example, MINILASE [1.13] is a two-dimensional quantum-well (QW) laser simulator which combines the complex simulation of carrier dynamics, the laser's optical field, and heating effects. Unfortunately, the computationally-intensive nature of device-level programs such as MINILASE makes them less than ideal candidates for optoelectronic system design tools. Typical optoelectronic applications incorporate multiple photonic and electronic components; furthermore, a large number of simulations are typically necessary to optimize the design parameters under a given set of specifications. In this case, we require models with considerably less computational overhead than that provided by device-level models. However, they must still be able to accurately replicate the operating characteristics from actual devices [1.11].

Toward this end, the last twenty years have seen a steadily growing interest in laser models that can be used in conjunction with circuit-level elements such as transistors, resistors, and capacitors. These *circuit-level laser models* facilitate the design of monolithic and hybridly integrated optoelectronic circuits, such as laser transmitters [1.14], by permitting the accurate simulation of a laser's terminal characteristics in a standard circuit-level simulation environment such as SPICE. The majority of these models, the highlights of which are listed in Table 1.1, have been based on rate-equation descriptions of a laser's behavior [1.15]-[1.31]. Katz *et al*. [1.15] introduced one of the first such models, an RLC circuit that implemented small-signal rate equations for carrier and photon densities.

Table 1.1 Highlights of circuit-level semiconductor-laser models.

Researchers	Year	Model Features
Katz *et al.* [1.15]	1981	rate-equation-based, small-signal
Habermayer [1.16]	1981	multimode effects
Tucker [1.17]	1981	large-signal, single-mode
Harder *et al.* [1.18]	1982	noise sources
Kan and Lau [1.21]	1992	small-signal, well-barrier kinetics
Bewtra *et al.* [1.25]	1995	thermal equivalent circuit
Lu *et al.* [1.26]	1995	large-signal, carrier transport
Y. Su *et al.* [1.28]	1996	modeling of VCSEL static LI characteristics
Tsou and Pulfrey [1.30]	1997	inclusion of gateway states

Subsequent large-signal models included Tucker's [1.17], which uses single-mode rate equations, and Habermayer's [1.16], which accounts for longitudinal multimode operation. Recent efforts have incorporated a number of improvements which take into account the detailed behavior of present-day lasers such as QW devices and vertical-cavity surface-emitting lasers (VCSELs). Kan and Lau [1.21] presented one of the first small-signal equivalent circuits of the QW-laser rate equations, which describe the carrier transport between the QWs and surrounding confinement layers, while Lu *et al.* [1.26], as well as Tsou and Pulfrey [1.30], have implemented large-signal QW laser models. Equivalent-circuit models have even been developed which account for the transient thermal response in semiconductor lasers [1.25]. Finally, the increased popularity of vertical-cavity surface-emitting lasers (VCSELs) has resulted in initial investigations into equivalent circuit models of their unique behavior [1.28].

1.3 Research Overview

Motivated by the above research, we present in this thesis the development of rate-equation-based circuit-level models for QW semiconductor lasers and VCSELs. In the course of this work, we had two primary concerns. First, our models should have good solution characteristics. With regards to the QW-laser models, this resulted in implementations with a unique dc solution regime during nonnegative current injection, whereas for the VCSEL models, we identified implementations that could account for the distinct thermal and spatial behavior in these devices without resorting to untenable device-level descriptions. Second, our models should be able to replicate the operating characteristics of actual devices. Through parameter extraction from measured data, we were able to investigate this capability in each of our models.

In the next few chapters, we will present the detailed results of our research. We begin in

Chapter 2 with two rate-equation-based semiconductor QW-laser models for use in SPICE3 [1.32] and related SPICE-like simulators. The first implementation, a one-level model, uses a standard set of rate equations for the active-region carriers and photons, while the two-level model includes an additional equation for describing the interaction of carriers in the laser's quantum wells and confinement layers. A limitation of both sets of equations is the presence of multiple dc solution regimes. In [1.27], Javro and Kang discussed this issue in regards to rate equations with a linear gain-saturation term, and presented variable transformations which in many realistic applications eliminated the spurious regimes. After discussing the limitations of their work, we demonstrate analytically that their transformations, applied to *our* models, do indeed yield a single solution regime during dc analysis. Finally, after presenting our models' equivalent-circuit formulation, including circuit elements that account for parasitic effects, we compare simulated and measured data for two experimental devices.

Next, in Chapter 3, we introduce circuit-level modeling of VCSELs. Because they have become an extremely hot topic in the field of optoelectronics, we first provide a brief overview of their design. As we shall see, thermal and spatial behavior can have a significant impact on VCSEL operation. Because of the particularly severe nature of thermal effects, we present in this chapter a simple circuit-level thermal VCSEL model which can accurately capture the cw thermal operating characteristics, namely thermally dependent threshold current and output-power rollover. Instead of explicitly accounting for the thermal physics in a VCSEL, an offset current is used to account for the temperature effects. After discussing the theory and implementation of this model in HSPICE [1.33] and Analogy's SABER [1.8], we compare simulated and measured data for three VCSELs reported in the literature. Despite various deficiencies in the model, particularly the absence of spatial phenomena, the simulated results compare favorably to the experimental data.

In Chapter 4 we present a more comprehensive circuit-level VCSEL model which accounts for both thermal *and* spatial behavior. Unlike the simple model of Chapter 3, this approach relies on a more detailed description of various thermal and spatial mechanisms at work in VCSELs, including the thermally dependent gain, thermal carrier leakage from the active region, transverse multimode operation, spatial hole burning, and carrier diffusion. Through spatially independent rate equations, assumed shapes for the transverse mode profiles, and analytical expressions for a VCSEL's thermal dependencies, our model is able to replicate much of the characteristic VCSEL behavior, including thermal LI characteristics, multimode competition, temperature-dependent modulation responses, and diffusive effects during transient operation. After discussing the development of the model and its implementation in SABER, we present simulation results demonstrating single- and two-mode operation. Finally, we compare simulated to experimental data for four devices reported in the literature. As we shall see, the results are noticeably improved over those from the simple model; however, they also clarify the need for more detailed research into experimental VCSEL characterization.

Finally, in Chapter 5, we provide a brief overview of our research results, as well as review the areas where future work is necessary. In particular, we identify the need for more sophisticated models and more comprehensive device characterization as two of the most important issues.

1.4 References

[1.1] L. D. Hutcheson, P. Haugen, and A. Husain, “Optical interconnects replace hardwire,” *IEEE Spectrum*, vol. 24, no. 3, pp. 30-35, 1987.

[1.2] J. W. Goodman, F. J. Leonberger, S.-Y. Kung, and R. A. Athale, “Optical interconnections for VLSI systems,” *Proceedings of the IEEE*, vol. 72, no. 7, pp. 850-866, July 1984.

[1.3] D. Z. Tsang, “One-gigabit per second free-space optical interconnection,” *Applied Optics*, vol. 29, no. 14, pp. 2034-2037, 1990.

[1.4] H. Zarschizky, Ch. Gerndt, M. Honsberg, H. W. Schneider, and A. Stemmer, “Optical clock distribution with a compact free space interconnect system,” *Optical and Quantum Electronics*, vol. 26, pp. S471-S481, 1994.

[1.5] J. F. Ewen, K. P. Jackson, R. J. S. Bates, and E. B. Flint, “GaAs fiber-optic modules for optical data processing networks,” *Journal of Lightwave Technology*, vol. 9, no. 12, pp. 1755-1763, 1991.

[1.6] Y.-M. Wong, D. J. Muehlner, C. C. Faudskar, D. B. Buchholz, M. Fishteyn, J. L. Brandner, W. J. Parzygnat, R. A. Morgan, T. Mullally, R. E. Leibenguth, G. D. Guth, M. W. Focht, K. G. Glogovsky, J. L. Zilko, J. V. Gates, P. J. Anthony, B. H. Tyrone, Jr., T. J. Ireland, D. H. Lewis, Jr., D. F. Smith, S. F. Nati, D. K. Lewis, D. L. Rogers, H. A. Aispain, S. M. Gowda, S. G. Walker, Y. H. Kwark, R. J. S. Bates, D. M. Kuchta, and J. D. Crow, “Technology development of a high-density 32-channel 16-Gb/s optical data link for optical interconnection applications for the Optoelectronic Technology Consortium (OETC),” *Journal of Lightwave Technology*, vol. 13, no. 6, pp. 995-1016, 1995.

[1.7] D. B. Schwartz, C. K. Y. Chun, B. M. Foley, D. H. Hartman, M. Lebby, H. C. Lee, C. L. Shieh, S. M. Kuo, S. G. Shook, and B. Webb, “A low-cost high-performance optical interconnect,” *IEEE Transactions on Components, Packaging, and Manufacturing Technology- Part B*, vol. 19, no. 3, pp. 532-539, 1996.

[1.8] *SaberGuide Simulator Reference*, Analogy, Inc., 1996.

[1.9] A. T. Yang and S. M. Kang, “iSMILE: A novel circuit simulation program with emphasis on new device model development,” in *Proceedings of the 26th ACM/IEEE Design Automation Conference*, 1989, pp. 630-633.

[1.10] S. Koh, L. Ye, H. W. Carter, and J. T. Boyd, “Optoelectronic interconnect simulation using a mixed mode simulator,” in *Proceedings of SPIE*, vol. 2400, 1995, pp. 244-251.

[1.11] A. J. Lowery, P. C. R. Gurney, X.-H. Wang, L. V. T. Nguyen, Y.-C. Chan, and M. Premaratne, “Time-domain simulation of photonic devices, circuits and systems,” in *Proceedings of SPIE*, vol. 2693, 1996, pp. 624-635.

[1.12] B. K. Whitlock, “iFROST: A CAD tool for modeling and simulation of optical interconnects,” Ph.D. dissertation, University of Illinois at Urbana-Champaign, 1996.

[1.13] G. H. Song, “Two-dimensional simulation of quantum-well lasers including energy transport,” Ph.D. dissertation, University of Illinois at Urbana-Champaign, 1990.

[1.14] F. Delpiano, R. Paoletti, P. Audagnotto, and M. Puleo, “High frequency modeling and characterization of high performance DFB laser modules,” *IEEE Transactions on Components, Packaging, and Manufacturing Technology- Part B*, vol. 17, no. 3, pp. 412-417, 1994.

[1.15] J. Katz, S. Margalit, C. Harder, D. Wilt, and A. Yariv, “The intrinsic electrical equivalent circuit of a laser diode,” *IEEE Journal of Quantum Electronics*, vol. QE-17, no. 1, pp. 4-7, 1981.

[1.16] I. Habermayer, “Nonlinear circuit model for semiconductor lasers,” *Optical and Quantum Electronics*, vol. 13, pp. 461-468, 1981.

[1.17] R. S. Tucker, “Large-signal circuit model for simulation of injection-laser modulation dynamics,” *IEE Proceedings- Pt. I*, vol. 128, no. 5, pp. 180-184, 1981.

[1.18] C. Harder, J. Katz, S. Margalit, J. Shacham, and A. Yariv, “Noise equivalent circuit of a semiconductor laser diode,” *IEEE Journal of Quantum Electronics*, vol. QE-18, no. 3, pp. 333-337, 1982.

[1.19] R. S. Tucker and D. J. Pope, “Microwave circuit models of semiconductor injection lasers,” *IEEE Transactions on Microwave Theory and Techniques*, vol. MTT-31, no. 3, pp. 289-294, 1983.

[1.20] D. S. Gao, S. M. Kang, R. P. Bryan, and J. J. Coleman, “Modeling of quantum-well lasers for computer-aided analysis of optoelectronic integrated circuits,” *IEEE Journal of Quantum Electronics*, vol. 26, no. 7, pp. 1206-1216, 1990.

[1.21] S. C. Kan and K. Y. Lau, “Intrinsic equivalent circuit of quantum-well lasers,” *IEEE Photonics Technology Letters*, vol. 4, no. 6, pp. 528-530, 1992.

[1.22] S. Sahli, M. Lescure, and J. Boucher, “A nonlinear circuit model for studying the frequency response in buried heterostructure lasers,” *Optical and Quantum Electronics*, vol. 26, pp. 97-107, 1994.

[1.23] M. K. Haldar, J. Wang, and F. V. C. Mendis, “Equivalent circuit of semiconductor lasers with weak coherent optical feedback,” *Electronics Letters*, vol. 31, no. 5, pp. 366-367, 1995.

[1.24] R. Xin-gen, X. Guo-ping, and Z. Zi-sen, “Small-signal circuit model of single-mode laser diode for simulation of nonlinear distortion,” *Journal of Optical Communications*, vol. 16, no. 1, pp. 22-25, 1995.

[1.25] N. Bewtra, D. A. Suda, G. L. Tan, F. Chatenoud, and J. M. Xu, “Modeling of quantum-well lasers with electro-opto-thermal interaction,” *IEEE Journal of Selected Topics in Quantum Electronics*, vol. 1, no. 2, pp. 331-340, 1995.

[1.26] M. F. Lu, J. S. Deng, C. Juang, M. J. Jou, and B. J. Lee, “Equivalent circuit model of quantum-well lasers,” *IEEE Journal of Quantum Electronics*, vol. 31, no. 8, pp. 1418-1422, 1995.

[1.27] S. A. Javro and S. M. Kang, “Transforming Tucker’s linearized laser rate equations to a form that has a single solution regime,” *Journal of Lightwave Technology*, vol. 13, no. 9, pp. 1899-1904, 1995.

[1.28] Y. Su, Y. Chang, and X. Chen, “Circuit model for studying temperature effects on vertical-cavity surface-emitting laser,” in *IEEE LEOS (Lasers and Electro-Optics Society) Annual Meeting*, vol. 1, 1996, pp. 215-216.

[1.29] W. Chen and S. Liu, “Circuit model for multilongitudinal-mode semiconductor lasers,” *IEEE Journal of Quantum Electronics*, vol. 32, no. 12, pp. 2128-2132, 1996.

[1.30] B. P. C. Tsou and D. L. Pulfrey, “A versatile SPICE model for quantum-well lasers,” *IEEE Journal of Quantum Electronics*, vol. 33, no. 2, pp. 246-254, 1997.

[1.31] T. T. Bich-Ha and J.-C. Mollier, “Noise equivalent circuit of a two-mode semiconductor laser with the contribution of both the linear and the nonlinear gain,” *IEEE Journal of Selected Topics in Quantum Electronics*, vol. 3, no. 2, pp. 304-308, 1997.

[1.32] B. Johnson, T. Quarles, A. R. Newton, D. O. Pederson, and A. Sangiovanni-Vincentelli, *SPICE3 Version 3e User’s Manual*, University of California, Berkeley, 1991.

[1.33] *HSPICE User’s Manual*, Meta-Software, Inc., 1996.

CHAPTER 2

QUANTUM-WELL LASER MODELS WITH A SINGLE SOLUTION REGIME

2.1 Motivation

The majority of circuit-level laser models to date have been based on rate-equation descriptions of semiconductor lasers. As discussed in Chapter 1, these models have ranged from RLC-circuit implementations of small-signal rate equations [2.1] to single-mode and multimode large-signal models [2.2], [2.3]. While most models have relied on a pair of equations to describe the active-region carriers and photons, more recent approaches have included additional rate equations to account for the transport of carriers between the active region and surrounding confinement layers [2.4], [2.5]. These improvements have been largely motivated by the fact that the majority of today's semiconductor lasers use quantum wells in their active regions. Thus, in general, we will assume that the rate-equation-based models discussed in this chapter can be used to describe QW semiconductor lasers with varying degrees of accuracy.

An important feature of rate-equation-based QW-laser models lies in their dc characteristics. A model often possesses multiple dc solution regimes, but only one of them is correct. The standard rate equations that use a linear gain-saturation term of the form $(1\text{-}\varepsilon S)$, where S is photon density, possess three dc solution regimes. Javro and Kang [2.6] have reported that in most realistic applications the incorrect solution regimes can be eliminated by applying variable transformations to the rate equations. Specifically, nonphysical negative-power and high-power solutions are avoided when simulating the rate equations with a nonnegative injection current. This approach is particularly useful when dealing with circuit-level models, since without the transformations the user would have to coax the circuit simulation into the correct solution regime by specifying initial conditions and other simulation parameters [2.6].

Unfortunately, as we will show here, the transformations proposed in [2.6] do not always remove the incorrect solution regimes from the standard rate equations. While new variable transformations do work under certain conditions, the equations still present difficulties that cannot be eliminated. In fact, for certain extreme cases, they possess unrealistic solution characteristics. The problem is mostly due to the use of the linear gain-saturation term. As is immediately clear from this expression, when the photon density S exceeds $1/\varepsilon$, this term becomes negative. It is reasonable, then, to assume that rate equations using this term are really only useful for photon densities below this value. On the other hand, the more general expression of $(1+\varepsilon S)^{-1}$, originally suggested by Channin [2.7], is valid for any value of $S \geq 0$. In fact, the linear expression is essentially a first-order Taylor-series expansion of this saturation term when εS is small. In [2.8], Agrawal suggested another expression of the form $(1+\varepsilon S)^{-1/2}$ which is also valid for $S \geq 0$. As we will show, either of these two nonlinear gain-saturation terms is suitable for obtaining models with a unique solution regime.

In this chapter, we identify rate-equation-based QW-laser models that possess a single dc solution regime for any nonnegative injection current [2.9]. After discussing in Section 2.2 the limitations of the model from [2.6], we present our models in Sections 2.3 and 2.4. The first model is based on the standard rate equations that use the gain-saturation term proposed by either Channin or Agrawal. The second one, on the other hand, augments these rate equations with a third equation for carriers in the laser's separate-confinement-heterostructure (SCH) layers. In both cases, we show analytically that the transformations suggested in [2.6] produce models with a unique solution regime. We also describe circuit-level implementations of the models that can be readily implemented in SPICE. Next, in Section 2.5, we discuss the inclusion of parasitics in the model. Then, to validate the model, we present in Section 2.6 the results of parameter extraction for two experimental devices. Final conclusions are made in Section 2.7.

2.2 Limitations of Rate Equations That Use a Linear Gain-Saturation Term

The rate equations discussed in [2.6] can be found in similar forms throughout the literature [2.10]-[2.13]. They are shown below:

$$\frac{dN}{dt} = \frac{I}{qV_{act}} - g_o(N - N_o)(1 - \varepsilon S)S - \frac{N}{\tau_n} + \frac{N_e}{\tau_n} \tag{2.1}$$

$$\frac{dS}{dt} = \Gamma g_o(N - N_o)(1 - \varepsilon S)S + \frac{\Gamma \beta N}{\tau_n} - \frac{S}{\tau_p} \tag{2.2}$$

$$\frac{S}{P_f} = \frac{\Gamma \tau_p \lambda_o}{V_{act} \eta h c} = \vartheta\,. \tag{2.3}$$

In the above equations, N is the active region's carrier density, S is the photon density defined later, P_f is the laser output power, I is the injection current, V_{act} is the active region volume, g_o is the gain coefficient, N_o is the optical transparency density, ε is the phenomenological gain compression factor, τ_n is the carrier lifetime, N_e is the equilibrium carrier density, Γ is the optical confinement factor, β is the spontaneous emission coupling factor, τ_p is the photon lifetime, η is the differential quantum efficiency per facet, λ_o is the emission wavelength, q is the electron charge, h is Planck's constant, and c is the speed of light in a vacuum. The photon density S is defined as $\Gamma S_{tot}/V_{act}$, where S_{tot} is the total number of photons in the active volume and Γ accounts for the fact that only photons in the active region are affected by gain or loss [2.14].

Under dc conditions, Eqs. (2.1)-(2.3) have up to three solution regimes for a single value of injection current I. In addition to the correct nonnegative solution regime, in which the solutions for N and S are nonnegative when $I \geq 0$, there are also a negative-power and a high-power regime. In order to eliminate these nonphysical solutions, the following pair of transformations was introduced in [2.6] for N and P_f:

$$N = N_e \exp\left(\frac{qV}{nkT}\right) \tag{2.4}$$

$$P_f = (m + \delta)^2 \tag{2.5}$$

where V is the voltage across the laser, n is a diode ideality factor (typically set equal to 2), m is a new variable for parameterizing P_f, δ is a small constant, k is Boltzmann's constant, and T is the laser's temperature. Equation (2.4) is a commonly used exponential relationship relating N and V. Both equations force N and P_f to be strictly nonnegative. Thus, by substituting Eqs. (2.4) and (2.5) into Eqs. (2.1)-(2.3), we have a new set of rate equations which have a dc solution for nonnegative injection current only if that solution yields nonnegative carrier and photon densities. Because under most conditions of interest the high-power solution regime corresponds to negative values for the carrier density, it would appear that Eqs. (2.4) and (2.5) ensure that both of the nonphysical solution regimes are avoided. However, under certain conditions even the transformed rate equations cannot eliminate the high-power solution regime.

By rewriting Eqs. (2.1) and (2.2) under dc conditions, we obtain two functions relating carrier density N to photon density S. The intersection points of these two functions are the valid solutions to the dc rate equations. The two functions are

$$N = f_1(S) = \frac{\tau_n I}{qV_{act}(1-\beta)} + \frac{N_e}{(1-\beta)} - \frac{\tau_n S}{\Gamma \tau_p (1-\beta)} \tag{2.6}$$

$$N = f_2(S) = \frac{\tau_n S + \Gamma \tau_n \tau_p g_o N_o (1-\varepsilon S) S}{\Gamma \beta \tau_p + \Gamma \tau_n \tau_p g_o (1-\varepsilon S) S} \tag{2.7}$$

Using the laser parameters found in Table 2.1 [2.6],[2.11], we have graphed equations (2.6) and (2.7) in Fig. 2.1(a) for two different values of the injection current, 0.5 and 2.0 A. As we can see, for low enough injection currents, f_1 and f_2 will intersect at only one point where $N > 0$ and $S > 0$. However, as the current increases, a second nonnegative solution may emerge, corresponding to the high-power solution regime. In Fig. 2.1(b), we plot Eqs. (2.6) and (2.7) after doubling the values of g_o, N_o, and τ_p and setting $V_{act} = 10^{-11}$ cm^3. In this case, we have used currents of 30 and 100 mA. As we can see, the nonphysical high-power solution emerges at even lower values of injection current than before.

Typically, the high-power solution regime should correspond to negative carrier densities. However, analysis of f_1 and f_2 shows that for currents greater than

Table 2.1 Parameters used for plotting the dc solution curves of the standard rate equations from [2.6]. The parameters are from Javro and Kang [2.6] and are taken originally from da Silva *et al.* [2.11].

Parameter	Description	Value
λ_o	Lasing wavelength	1.502×10^{-4} cm
V_{act}	Active region volume	9×10^{-11} cm^3
Γ	Optical confinement factor	0.44
β	Spontaneous emission coupling factor	4×10^{-4}
g_o	Gain coefficient	3×10^{-6} cm^3/s
N_o	Optical transparency density	1.2×10^{18} cm^{-3}
τ_n	Carrier lifetime	3 ns
τ_p	Photon lifetime	1 ps
η	Differential quantum efficiency per facet	0.1
N_e	Equilibrium carrier density	5.41×10^{10} cm^{-3}
ε	Phenomenological gain saturation factor	3.4×10^{-17} cm^3

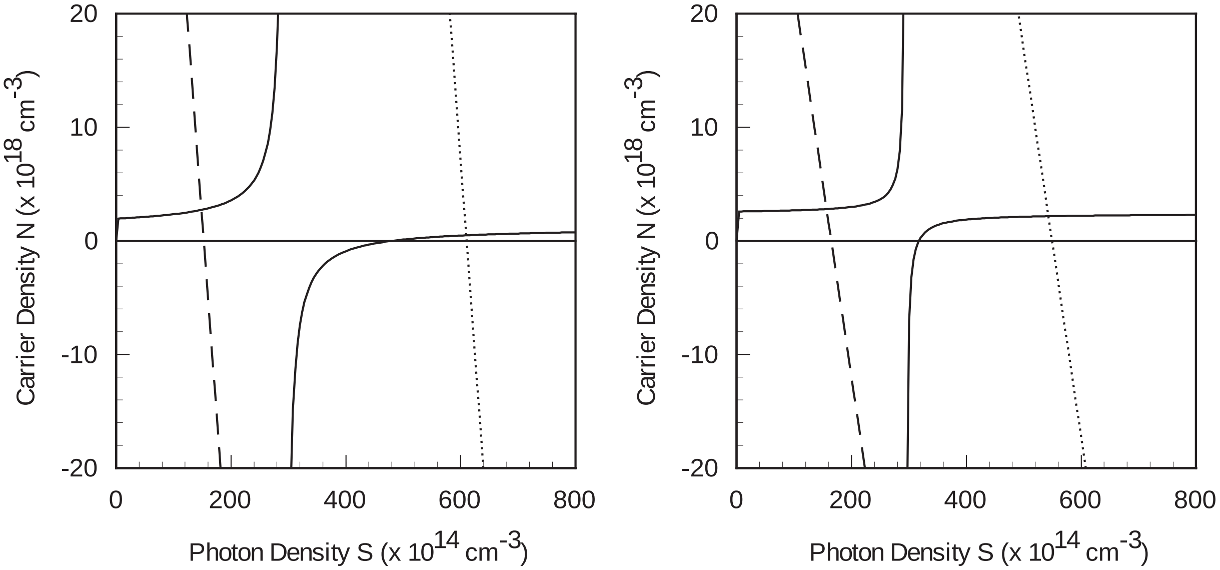

(a) (b)

Figure 2.1 Plots of f_1 and f_2 from Eqs. (2.6)-(2.7) for two different sets of model parameters. (a) Table 2.1 parameters. Dashed line: f_1 for $I = 0.5$ A; dotted line: f_1 for $I = 2.0$ A; solid line: f_2. (b) Modified Table 2.1 parameters. Dashed line: f_1 for $I = 30$ mA; dotted line: f_1 for $I = 100$ mA; solid line: f_2.

$$I_o = V_{act}\left[\frac{q}{\Gamma\tau_p\varepsilon}\left(1 + \frac{1}{\Gamma g_o N_o \tau_p}\right) - \frac{qN_e}{\tau_n}\right] \tag{2.8}$$

the high-power solution regime actually yields positive carrier densities. Thus, a circuit-model implementation of the transformed rate equations proposed in [2.6] can still produce incorrect simulation results for high enough values of injection current. We performed an operating point analysis in SPICE for the circuit implementation of the transformed equations using the adjusted parameters of Fig. 2.1(b). Injection currents of 100 and 200 mA produced output powers of 8.16 and 16.4 mW, respectively, both of which correspond to the high-power solution regime.

Inspection of Fig. 2.1 does suggest an alternative transformation that would completely eliminate the high-power solution regime. The plot of f_2 shows a discontinuity that separates the normal-and high-power solution curves. This discontinuity occurs at a value of $S = 1/\varepsilon_d$, where $1/\varepsilon_d = [1 + \sqrt{1 + 4\beta\varepsilon/g_o\tau_n}]/(2\varepsilon)$. Thus, a transformation which would limit the photon density to values below $1/\varepsilon_d$ would eliminate the high-power regime for *all* values of injection current. One such transformation is

$$P_f = \frac{(m + \delta)^2}{\vartheta\varepsilon_d(m + \delta)^2 + 1} \tag{2.9}$$

Unfortunately, while Eq. (2.9) can produce a set of rate equations with a single solution regime, it does so only for certain sets of model parameters. Comparison of the positive roots of the numerator and denominator of f_2 indicates three possible forms of this function. The typical case corresponds to that shown in Fig. 2.1. This occurs whenever

$$\tau_n > \frac{\varepsilon\beta g_o(\Gamma N_o\tau_p)^2}{1 + g_o(\Gamma N_o\tau_p)} = \tau_{nc} \tag{2.10}$$

However, two alternative forms of f_2 occur when $\tau_n < \tau_{nc}$ and $\tau_n = \tau_{nc}$. Fig. 2.2(a) shows the first case, along with a plot of f_1 when $I = 22.9$ mA. Fig. 2.2(b) shows the second case, along with f_1 when $I = 42$ mA. While these cases are extreme, they do reveal intrinsic problems with Eqs. (2.1) and (2.2), especially when $\tau_n < \tau_{nc}$. As Fig. 2.2(a) demonstrates, not only can multiple nonnegative solutions exist for $S < 1/\varepsilon_d$, but for certain values of injection current such as the one shown in the figure, a valid nonnegative solution does not exist at all.

As the discussion above suggests, the standard rate equations that use a linear gain-saturation term present two difficulties. First, under nonnegative current injection, multiple nonnegative solution regimes can occur even if the transformations suggested in [2.6] are implemented. Second, for certain extreme cases, *no* solution may exist. What is desired are rate equations that will have a single non-

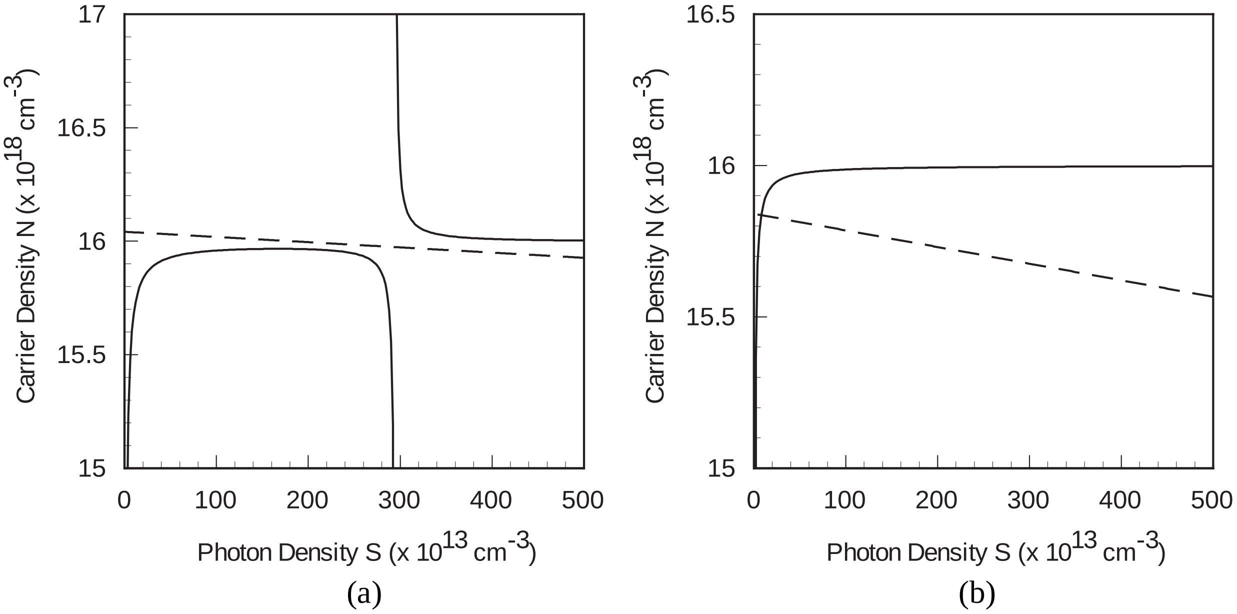

Figure 2.2 Plots of f_1 and f_2 for extreme sets of model parameters. (a) $\tau_n < \tau_{nc}$ using $V_{act} = 9\mathrm{x}10^{-13}$ cm^3, $\Gamma = 0.44$, $\beta = 0.01$, $g_o = 5\mathrm{x}10^{-5}$ cm^3/s, $N_o = 1.6\mathrm{x}10^{19}$ cm^{-3}, $\tau_n = 0.1$ ns, $\tau_p = 10$ ps, $\varepsilon = 3.4\mathrm{x}10^{-16}$ cm^3. Dashed line: f_1 for $I = 22.9$ mA; solid line: f_2. (b) $\tau_n = \tau_{nc}$ using parameters from (a) except for $V_{act} = 4\mathrm{x}10^{-12}$ cm^3 and $\tau_n = 0.239$ ns. Dashed line: f_1 for $I = 42$ mA; solid line: f_2.

negative solution for both carrier and photon densities for *any* nonnegative injection current. Fortunately, rate equations that use the more suitable gain-saturation terms mentioned earlier satisfy this criteria.

2.3 Standard Rate-Equation Model with a Single Solution Regime

2.3.1 Theoretical basis

An alternative version of the standard one-level rate equations ensures that for a nonnegative injection current, exactly one solution exists with nonnegative carrier and photon densities. The equations treated henceforth are more generalized versions of Eqs. (2.1) and (2.2) with the linear gain-saturation term replaced by the term proposed by either Channin or Agrawal. The new equations are shown below:

$$\frac{dN}{dt} = \frac{\eta_i I}{qN_w V_{act}} - R_w(N) - \Gamma_c v_{gr} \frac{\alpha(N)}{\phi(S)} S \tag{2.11}$$

$$\frac{dS}{dt} = -\frac{S}{\tau_p} + N_w R_{w\beta}(N) + N_w \Gamma_c v_{gr} \frac{\alpha(N)}{\phi(S)} S \tag{2.12}$$

$$\frac{S}{P_f} = \frac{\lambda \tau_p}{\eta_c V_{act} hc} = \vartheta \tag{2.13}$$

Equation (2.11) relates the rate of change in carrier concentration N to the injection current I, the carrier recombination rate $R_w(N)$, and the stimulated-emission rate. In order to account for different recombination mechanisms, $R_w(N) = AN+BN^2+CN^3$, where A, B, and C are the unimolecular, radiative, and Auger recombination coefficients, respectively. Equation (2.12) relates the rate of change in photon density S to photon loss, the rate of coupled recombination into the lasing mode, and the stimulated-emission rate. Unlike the photon density defined in Section 2.2, in this case the photon density S is defined as S_{tot}/V_{act} [2.15], where S_{tot} is again the total number of photons in the active volume. Also, the coupling rate is generalized to allow coupling from any of the recombination terms, though in actual practice this coupling will typically only come from the radiative recombination. Thus, $R_{w\beta}(N) = \beta_A AN+\beta_B BN^2+\beta_C CN^3$, where β_A, β_B, and β_C are coupling coefficients. Finally, Eq. (2.13) relates the photon density to the output power P_f. In the above equations, η_i is the current-injection efficiency, N_w is the number of quantum wells, V_{act} is the volume of a single QW, Γ_c is the optical confinement factor of one QW, v_{gr} is the group velocity of the lasing medium, τ_p is the photon lifetime, λ is the lasing wavelength, and η_c is the output-power coupling coefficient. Note that we can convert Eqs. (2.11)-(2.13) into a form analogous to that of Eqs. (2.1)-(2.3), with Γ_c missing from the stimulated emission term of Eq. (2.11) but included in the expression for ϑ, by using the definition for

S from Section 2.2. Thus, both approaches are equivalent as long as the proper definition of S is used.

In the above equations, the stimulated-emission rate includes a carrier-dependent gain term $\alpha(N)$ as well as the gain saturation term $\phi^{-1}(S)$. While the gain term can take on a number of forms, we will consider only two: a linear term such as that used in Eqs. (2.1) and (2.2), and a logarithmic gain term such as that proposed in [2.16] and used previously in other laser models [2.15]. The logarithmic gain has been shown to be an excellent expression for describing the actual relationship between the material gain and the carrier density. The two forms are

$$\alpha(N) = G_o \ln\left(\frac{R_w(N)}{R_w(N_o)}\right) \tag{2.14a}$$

$$\alpha(N) = g_l G_o\left(\frac{N}{N_o} - 1\right) \tag{2.14b}$$

where G_o is the gain coefficient per quantum well, N_o is the optical transparency density, and g_l is a factor obtained when linearizing the logarithmic gain around N_o. Specifically, $g_l = (AN_o+2BN_o^2+3CN_o^3)/(AN_o+BN_o^2+CN_o^3)$.

The gain-saturation function can take on one of the following two forms:

$$\phi^{-1}(S) = \frac{1}{1+\varepsilon\Gamma_c S} \tag{2.15a}$$

$$\phi^{-1}(S) = \frac{1}{\sqrt{1+\varepsilon\Gamma_c S}} \tag{2.15b}$$

These correspond to the expressions proposed by Channin and Agrawal, respectively, with the confinement factor added to account for the revised definition of S. As mentioned before, Eq. (2.15a) is often used instead of the linear gain-saturation term [2.17]-[2.19] and, unlike the latter, is positive for all $S \geq 0$. Eq. (2.15b) is an alternate form of the gain-saturation term for semiconductor lasers and is also applicable for $S \geq 0$. When S is much smaller than $1/\varepsilon\Gamma_c$, Eq. (2.15a) can be approximated by the linear form, as can Eq. (2.15b) with the exception of a factor of 1/2 in the value for $\varepsilon\Gamma_c$. However, because they are suitable for a wider range of photon densities and lead to models with a single solution regime, either of these two expressions is superior to the linear form.

2.3.2 Verification of a single solution regime

Despite the complexity of the above model equations, it is possible to show analytically that for any nonnegative injection current there can exist only one dc solution with nonnegative carrier and photon densities. After some rearrangement of Eqs. (2.11) and (2.12) with $d/dt = 0$, we get two nonlinear dc equations:

$$F_1(S, N) = N_w \phi(S) R_{w\beta}(N) + N_w \Gamma_c v_{gr} S \alpha(N) - \frac{\phi(S)S}{\tau_p} = 0 \tag{2.16}$$

$$F_2(S, N) = \frac{S}{\tau_p} + N_w [R_w(N) - R_{w\beta}(N)] - \frac{\eta_i I}{q V_{act}} = 0 \tag{2.17}$$

Equation (2.16) is obtained via multiplication of both sides of Eq. (2.12) by $\phi(S)$. Equation (2.17) is obtained by combining Eqs. (2.11) and (2.12) in order to eliminate the stimulated-emission term. Both equations implicitly define functions $N = f_1(S)$ and $N = f_2(S)$, respectively, which map out their nonnegative solutions. The intersection points of these two functions are the nonnegative solutions to the dc rate equations. Thus, in order to establish the existence of a unique nonnegative solution regime, we need only show that for each $I \geq 0$ these two functions have exactly one nonnegative intersection point.

First, consider the case $I = 0$. In this case, the only nonnegative solution that satisfies Eq. (2.17) is $S = N = 0$. When the carrier-dependent gain is linear, Eq. (2.16) is also satisfied by this solution. Thus, it is the unique nonnegative intersection point of the functions f_1 and f_2 when $I = 0$. When the gain is logarithmic, $F_1(S,N)$ is undefined at $N = 0$. However, the solution to $F_1(S,N) = 0$ approaches $N = 0$ as $S \to 0$. We could include a small additive constant within the logarithm in order to ensure that the gain is defined at $N = 0$; however, in either case, we can claim that the only possible solution when $I = 0$ is $S = N = 0$.

When $I > 0$, the situation is more complicated. Because analytical expressions for f_1 and f_2 are not available, we need to show indirectly that they have a single intersection point. In the following analysis, we will show that over a range of positive values of S, f_1 and f_2 are strictly-increasing and strictly-decreasing, respectively, with f_1 increasing from zero and f_2 decreasing to zero. Thus, we will establish that f_1 and f_2 have exactly one intersection point, thereby proving that when $I > 0$, (2.16) and (2.17) have a single nonnegative solution.

Let us consider the case $I > 0$, then, and assume that at least one of the products $\beta_A A$, $\beta_B B$, or $\beta_C C$ is positive so that $R_w(N)$, $R_{w\beta}(N)$ and $dR_{w\beta}/dN$ are nonzero when $N > 0$. The function $f_1(S)$ is implicitly defined by Eq. (2.16), $F_1(S,N) = 0$, such that when $S > 0$, $F_1(S,f_1(S)) = 0$ and $f_1(S) > 0$. As we will show shortly, $f_1(S)$ approaches 0 as $S \to 0$, so we may define $f_1(0) = 0$, which is exactly true when the linear gain term of Eq. (2.14b) is used. Because $F_1(S,N)$ has exactly one positive root for N when S takes on any arbitrary positive value, $(S,f_1(S))$ maps out all of the nonnegative solutions to Eq. (2.16).

In order to obtain additional information about $f_1(S)$, we need to establish its continuity and differentiability for all $S > 0$. These features can be demonstrated by considering the partial derivatives of $F_1(S,N)$ and then using the Implicit Function Theorem of calculus [2.20]. $F_1(S,N)$ is defined everywhere within the region $D = \{S > 0, N > 0\}$ and has partial derivatives F_{1N} and F_{1S} that are continuous in this region. These partial derivatives with respect to N and S are

$$F_{1N} = N_w \phi(S) \frac{dR_{w\beta}}{dN} + N_w \Gamma_c v_{gr} S \frac{d\alpha}{dN} \tag{2.18}$$

$$F_{1S} = \left[\frac{-\phi(S)}{\tau_p} + N_w \Gamma_c v_{gr} \alpha(N)\right] + N_w R_{w\beta}(N) \frac{d\phi}{dS} - \frac{S}{\tau_p}\frac{d\phi}{dS} \tag{2.19}$$

Because either form of $\phi(S)$ is positive for $S > 0$ and $dR_{w\beta}/dN > 0$ and $d\alpha/dN > 0$ for $N > 0$, F_{1N} is nonzero everywhere in D. By the Implicit Function Theorem, then, for some point (S_1,N_1) in D such that $F_1(S_1,N_1) = 0$, there exists a continuous and differentiable function $N = f_{1N}(S)$ in some neighborhood of S_1 such that $N_1 = f_{1N}(S_1)$ and $F_1(S,f_{1N}(S)) = 0$ in this neighborhood. However, we already know that $f_1(S)$ is the only such function that exists in D, so $f_1(S) = f_{1N}(S)$. Because the point (S_1,N_1) was arbitrary, $f_1(S)$ must be continuous and differentiable for all $S > 0$.

Because of this differentiability, $f_1'(S) = -F_{1S}/F_{1N}$ for $S > 0$. Our expression for F_{1S} can be greatly simplified at the points satisfying $F_1(S,N) = 0$ by rearranging Eq. (2.16) and plugging the resultant expression $[-\phi(S)/\tau_p + N_w\Gamma_c v_{gr}\alpha(N)] = -N_w\phi(S)R_{w\beta}(N)/S$ into Eq. (2.19). This gives

$$F_{1S} = N_w R_{w\beta}(N)\left[\frac{d\phi}{dS} - \frac{\phi(S)}{S}\right] - \frac{S}{\tau_p}\frac{d\phi}{dS} \tag{2.20}$$

Substituting Eq. (2.15a) for $\phi(S)$ and plugging both F_{1S} and F_{1N} into our expression for $f_1'(S)$ we get

$$f_1'(S) = \frac{\left[\frac{\varepsilon \Gamma_c S^2}{\tau_p} + N_w R_{w\beta}(N)\right]}{N_w \phi(S) S \frac{dR_{w\beta}}{dN} + N_w \Gamma_c v_{gr} S^2 \frac{d\alpha}{dN}} \tag{2.21}$$

Clearly, $f_1'(S) > 0$ at all points in D. If Eq. (2.15b) is used instead, we obtain the same conclusion. Thus, $f_1(S)$ is a strictly-increasing function for $S > 0$. Based on this fact, it is relatively straightforward to show that $\lim_{S \to 0} f_1(S) = 0$. Thus, we have shown that $F_1(S,N) = 0$ defines a unique nonnegative function $N = f_1(S)$ which for $S > 0$ is continuous and strictly-increasing from the point (0,0).

Meanwhile, the function $f_2(S)$ is implicitly defined by Eq. (2.17), $F_2(S,N) = 0$. After some rearrangement, this equation explicitly defines a function $S = g_2(N)$ which is strictly-decreasing and continuous for all $N \geq 0$, with $g_2(0) = \tau_p \eta_i I/qV_{act}$. For some value $N_2 > 0$ such that $F_2(0,N_2) = 0$, $g_2(N_2) = 0$, with $g_2(N) < 0$ for $N > N_2$. Thus, for all S in the interval $[0,\tau_p \eta_i I/qV_{act}]$, g_2^{-1}, the inverse of g_2, maps out *all* of the nonnegative values for S and N that satisfy $F_2(S,N) = 0$. Let $f_2(S) = g_2^{-1}$ over the interval $[0,\tau_p \eta_i I/qV_{act}]$. Over this interval, $f_2(S)$ is a strictly-decreasing continuous function with $f_2(0) = N_2 > 0$ and $f_2(\tau_p \eta_i I/qV_{act}) = 0$.

As the above analysis shows, for either of the two forms of $\phi^{-1}(S)$ from Eq. (2.15), $f_1(S)$ is differentiable and strictly-increasing from the point (0,0) for $S > 0$. Furthermore, $f_2(S)$, which is only defined for values of S in the interval $[0,\tau_p \eta_i I/qV_{act}]$, is strictly-decreasing and continuous with $f_2(0) > 0$ and $f_2(\tau_p \eta_i I/qV_{act}) = 0$. Clearly, f_1 and f_2 will intersect exactly once at a nonnegative point within this interval. Thus, for each $I > 0$ there exists exactly one nonnegative solution (S,N) to the dc rate equations when the gain-saturation terms of Channin or Agrawal are used. As an example of this fact, we have plotted in Fig. 2.3 the graphs of f_1 and f_2 when $I = 10$ mA. We used the new model parameters of Table 2.2, the logarithmic-gain term, and Channin's gain-saturation term. The figure clearly indicates that there is exactly one intersection point.

2.3.3 Model implementation

As we have shown, regardless of whether there are solution regimes with negative values for carrier or photon density, there is *only one* nonnegative solution to Eqs. (2.16) and (2.17) when $I \geq 0$. Thus, it is possible to use the transformations of Eqs. (2.4) and (2.5) in order to ensure that this solution regime is the only one that can be chosen during simulation. Using the approach taken in [2.6], we have implemented an equivalent-circuit model based on Eqs. (2.4)-(2.5) and (2.11)-(2.13) in

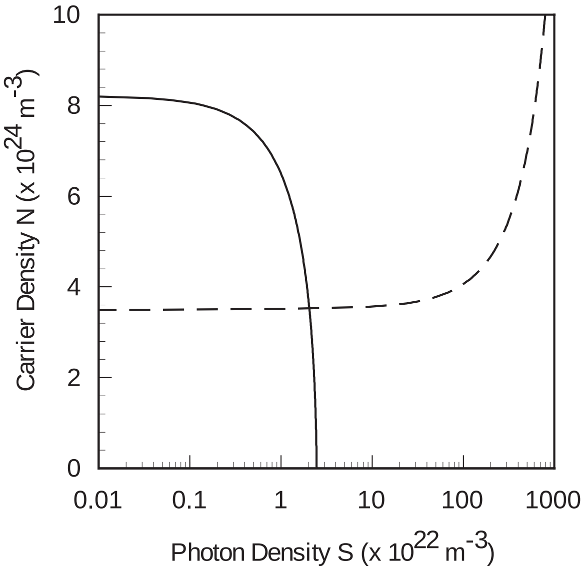

Figure 2.3 Plot of f_1 and f_2 from the alternative one-level model when I = 10 mA. Dashed line: $N = f_1(S)$; solid line: $N = f_2(S)$.

SPICE3 [2.21]. Unlike models based on the rate equations that use a linear gain-saturation term, this circuit model is applicable for all nonnegative values of injection current. It also supports a number of gain terms, including the logarithmic and linear expressions discussed above.

Fig. 2.4 shows the circuit implementation of the model. This equivalent circuit can be obtained through suitable manipulations of the one-level rate equations and the variable transformations. Substituting Eqs. (2.4) and (2.5) into Eqs. (2.11)-(2.13) and rearranging, we obtain

$$\begin{aligned}\frac{qN_e}{nkT}\exp\left(\frac{qV}{nkT}\right)\frac{dV}{dt} &= \frac{\eta_i I}{qN_w V_{act}} - \frac{N_e}{\tau_n}\left[\exp\left(\frac{qV}{nkT}\right) - 1\right] - \frac{N_e}{\tau_n} \\ &\quad - R_{w2}(N) - \vartheta\Gamma_c v_{gr}\frac{\alpha(N)}{\phi(\vartheta(m+\delta)^2)}(m+\delta)^2\end{aligned} \tag{2.22}$$

Table 2.2 Parameters for evaluating both the one- and two-level QW-laser models that have a single solution regime. The parameters are taken from [2.15] and based on data from a number of sources [2.19], [2.23]-[2.28].

Parameter	Description	Value
η_i	current-injection efficiency	0.86
λ	emission wavelength	980 nm
N_w	number of quantum wells	1
V_{act}	volume of one QW	6×10^{-18} m^3
Γ_c	optical confinement factor of one QW	0.019
v_{gr}	lasing medium group velocity	8.571×10^7 m/s
τ_p	photon lifetime	2.759 ps
η_c	output-power coupling coefficient	0.449
N_o	optical transparency density	1.5×10^{18} cm^{-3}
G_o	gain coefficient per QW	1500 cm^{-1}
ε	phenomenological gain-saturation term	1×10^{-17} cm^3
A	QW unimolecular recombination-rate coefficient	1.1×10^8 s^{-1}
B	QW radiative recombination-rate coefficient	0.7×10^{-10} cm^3/s
C	QW Auger recombination-rate coefficient	0.6×10^{-29} cm^6/s
A_b	SCH unimolecular recombination-rate coefficient	1.3×10^8 s^{-1}
B_b	SCH radiative recombination-rate coefficient	1.4×10^{-10} cm^3/s
C_b	SCH Auger recombination-rate coefficient	1.3×10^{-29} cm^6/s
β_A	unimolecular-recombination coupling term	0
β_B	radiative-recombination coupling term	1×10^{-4}
β_C	Auger-recombination coupling term	0
V_{barr}	volume of SCH layer	2.25×10^{-16} m^3
τ_{capt}	QW capture lifetime	45 ps
τ_{em}	QW emission lifetime	400 ps

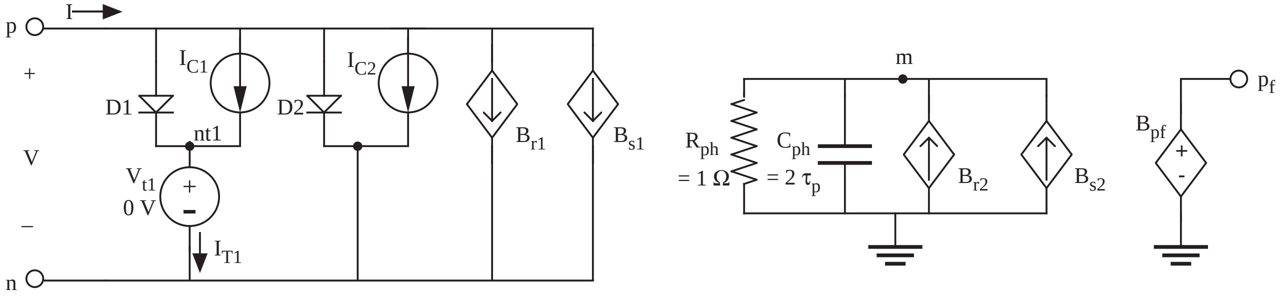

Figure 2.4 Circuit-level implementation of the one-level QW-laser model with a single solution regime.

$$2(m+\delta)\frac{dm}{dt} = \frac{-(m+\delta)^2}{\tau_p} + \frac{N_w}{\vartheta}R_{w\beta}(N) + N_w\Gamma_c v_{gr}\frac{\alpha(N)}{\phi(\vartheta(m+\delta)^2)}(m+\delta)^2 \tag{2.23}$$

where $A = A_2 + 1/\tau_n$ and $R_{w2}(N) = A_2N + BN^2 + CN^3$. After some additional rearrangement of Eqs. (2.22) and (2.23) and the definition of suitable circuit elements, we obtain our final set of equations on which the circuit in Fig. 2.4 is based. Setting $\Theta = 2\eta_i\tau_n/qN_wV_{act}$ and using the fact that $N = \Theta I_{T1}$, the equations are

$$I = I_{T1} + I_{D2} + I_{C2} + B_{r1} + B_{s1} \tag{2.24}$$

$$I_{T1} = I_{D1} + I_{C1} \tag{2.25}$$

$$2\tau_p\frac{dm}{dt} + m = B_{r2} + B_{s2} \tag{2.26}$$

$$B_{pf} = (m+\delta)^2 \tag{2.27}$$

$$I_{D1} = \frac{qN_wV_{act}N_e}{2\eta_i\tau_n}\left[\exp\left(\frac{qV}{nkT}\right) - 1\right] \tag{2.28}$$

$$I_{D2} = \frac{qN_wV_{act}N_e}{2\eta_i\tau_n}\left[\exp\left(\frac{qV}{nkT}\right) - 1 + \frac{2q\tau_n}{nkT}\exp\left(\frac{qV}{nkT}\right)\frac{dV}{dt}\right] \tag{2.29}$$

$$I_{C1} = I_{C2} = \frac{qN_wV_{act}N_e}{2\eta_i\tau_n} \tag{2.30}$$

$$B_{r1} = \frac{qN_wV_{act}}{\eta_i}R_{w2}(\Theta I_{T1}) \tag{2.31}$$

$$B_{s1} = \frac{\lambda\tau_p qN_w\Gamma_c v_{gr}}{\eta_i\eta_c hc}\frac{\alpha(\Theta I_{T1})}{\phi(\vartheta(m+\delta)^2)}(m+\delta)^2 \tag{2.32}$$

$$B_{r2} = \frac{N_w\eta_c V_{act}hc}{\lambda(m+\delta)}R_{w\beta}(\Theta I_{T1}) \tag{2.33}$$

$$B_{s2} = \tau_p N_w\Gamma_c v_{gr}\frac{\alpha(\Theta I_{T1})}{\phi(\vartheta(m+\delta)^2)}(m+\delta) - \delta \tag{2.34}$$

These equations can be mapped directly into the circuit of Fig. 2.4 through a SPICE subcircuit that uses nonlinear dependent sources, with the general forms for the gain and gain-saturation terms replaced in actual practice by expressions from Eqs. (2.14) and (2.15). Diodes $D1$ and $D2$ and current sources I_{C1} and I_{C2} model the linear recombination and charge storage in the device, while B_{r1} and B_{s1} model the effects of additional recombination mechanisms and stimulated emission, respectively, on the carrier density. R_{ph} and C_{ph} help model the time-variation of the photon density under the effects of spontaneous and stimulated emission, which are accounted for by B_{r2} and B_{s2}, respectively. Finally, B_{pf} produces the optical output power of the laser in the form of a voltage. Because the model is implemented as a subcircuit and not embedded within SPICE itself, it lends itself well to implementation by the average user. In Fig. 2.5, we give an example of a SPICE input deck that implements such a subcircuit using the logarithmic gain term and Channin's gain-saturation term. In addition to the parameters of Table 2.2, we set $N_e = 5.9 \times 10^8$ cm^{-3}, $n = 2$, and $\delta = 0$. We also have included a small constant, 10^{-60}, inside the gain's logarithmic term in order to ensure that it is defined when

```
* one-level model using logarithmic gain

ibias 0 p 10m
xlaser p 0 pf ltest1
rout pf 0 1e9

*********************************************************************
.subckt ltest1 p n pf
D1 p nt1 d1mod_ltest1
Ic1 p nt1 3.6641713e-14
Vt1 nt1 n 0
D2 p n d2mod_ltest1
Ic2 p n 3.6641713e-14
Br1 p n i=0*i(Vt1)+20701.692*i(Vt1)*i(Vt1)+28862208*i(Vt1)*i(Vt1)*i(Vt1)
Bs1 p n i=1.3785977*v(m)*v(m)*ln(1e-60+5220.1829*i(Vt1)+
+         54033309*i(Vt1)*i(Vt1)+7.5333001e+10*i(Vt1)*i(Vt1)*i(Vt1))/
+         (1+0.95928574*v(m)*v(m))
Rph m 0 1
Cph m 0 5.518e-12
Br2 0 m i=(0*i(Vt1)+1.0120369*i(Vt1)*i(Vt1)+0*i(Vt1)*i(Vt1)*i(Vt1))/v(m)
Bs2 0 m i=0.67395059*v(m)*ln(1e-60+5220.1829*i(Vt1)+54033309*i(Vt1)*i(Vt1)+
+         7.5333001e+10*i(Vt1)*i(Vt1)*i(Vt1))/(1+0.95928574*v(m)*v(m))
Bpf pf 0 v=v(m)*v(m)
.ends ltest1
.model d1mod_ltest1 D Is=3.6641713e-14 n=2
.model d2mod_ltest1 D Is=3.6641713e-14 n=2 tt=1.8181818e-08
*********************************************************************


.dc ibias 0 50m 0.25m
.end
```

Figure 2.5 Example SPICE deck for the one-level QW-laser model.

$N = 0$. Specifically, we use $\alpha(N) = G_o \ln[10^{-60} + R_w(N)/R_w(N_o)]$. Additional details on the implementation of the single-level model in SPICE3 and other SPICE-like simulators can be found in Appendix A.

2.4 Two-Level Rate-Equation Model

2.4.1 Theoretical basis

In recent years a number of more sophisticated rate-equation-based QW-laser models have been introduced which account for carriers in SCH layers of the laser by introducing additional rate equations [2.4]-[2.5], [2.15], [2.19], [2.22]. These models can therefore account for the transport of carriers across the SCH layer as well as carrier capture and emission by the QWs. In addition to the simple model presented in Section 2.3, we have implemented a more complete QW-laser model which includes a third rate equation that accounts for carriers in the SCH, or barrier, layers. We have analyzed this model and again found that a single nonnegative solution regime exists for nonnegative injection currents. The model equations, based on those found in [2.4]-[2.5], [2.19], and [2.22], are

$$\frac{dN_b}{dt} = \frac{\eta_i I}{qV_{barr}} - R_b(N_b) - \frac{N_b}{\tau_{capt}} + \frac{N_w V_{act}}{V_{barr}} \frac{N}{\tau_{em}} \tag{2.35}$$

$$\frac{dN}{dt} = \frac{V_{barr}}{N_w V_{act}} \frac{N_b}{\tau_{capt}} - \frac{N}{\tau_{em}} - R_w(N) - \Gamma_c v_{gr} \frac{\alpha(N)}{\phi(S)} S \tag{2.36}$$

$$\frac{dS}{dt} = -\frac{S}{\tau_p} + N_w R_{w\beta}(N) + N_w \Gamma_c v_{gr} \frac{\alpha(N)}{\phi(S)} S \tag{2.37}$$

$$\frac{S}{P_f} = \frac{\lambda \tau_p}{\eta_c V_{act} hc} = \vartheta \tag{2.38}$$

Equation (2.35) is the rate equation for carrier density N_b in the SCH layer and relates its rate of change to the injection current I, the SCH recombination rate, and the carrier exchange between the SCH layers and QWs, namely the rate of carrier capture and emission by the QWs. The recombination rate is $R_b(N_b) = A_b N_b + B_b N_b^2 + C_b N_b^3$, where A_b, B_b, and C_b are the unimolecular, radiative, and Auger recombination coefficients, respectively, in the SCH layer. Eq. (2.36) is a modified version of

Eq. (2.11) which now accounts for the carrier exchange between the SCH layers and QWs, with the current-injection term replaced by the capture rate of carriers from the SCH layer and a new term N/τ_{em} for carrier emission from the QWs. Eqs. (2.37) and (2.38) are the same equations for photon density and power as found in the simple one-level model of Section 2.3. Again, the gain and gain-saturation terms of Eqs. (2.14) and (2.15) are used in the model. In addition to the recombination parameters for the SCH layer, the new model parameters include the SCH-layer volume V_{barr}, the QW carrier-capture lifetime τ_{capt}, and the QW emission lifetime τ_{em}.

2.4.2 Verification of a single solution regime

As was the case with the one-level model, we would like to establish analytically that Eqs. (2.35)-(2.38) have a single nonnegative solution for each $I \geq 0$. If $A_b = B_b = C_b = 0$, then under dc conditions Eqs. (2.35)-(2.38) reduce to the one-level model of Eqs. (2.11)-(2.13). From our earlier analysis, we know that in this case a unique nonnegative solution for N and S exists for every $I \geq 0$. Furthermore, from Eq. (2.35) under dc conditions we see that this solution corresponds to a unique nonnegative value for N_b. Thus, in this case the two-level model does indeed have a single nonnegative solution regime.

When any of the SCH recombination coefficients are nonzero, however, then we must examine the solution properties of Eqs. (2.35)-(2.38) in detail. Under dc conditions, Eqs. (2.35)-(2.37) can be rearranged to produce three nonlinear equations in N_b, N, and S. In addition to Eq. (2.16) from the one-level model, we also obtain

$$H_1(S, N, N_b) = R_b(N_b) + \frac{N_b}{\tau_{capt}} - \frac{N_w V_{act} N}{\tau_{em} V_{barr}} - \frac{\eta_i I}{q V_{barr}} = 0 \qquad (2.39)$$

$$H_2(S, N, N_b) = \frac{V_{barr} R_b(N_b)}{V_{act}} + N_w[R_w(N) - R_{w\beta}(N)] + \frac{S}{\tau_p} - \frac{\eta_i I}{q V_{act}} = 0 \tag{2.40}$$

Analogous to the one-level case, these three equations implicitly define nonnegative functions $N = f_1(S)$, $N = f_2(S)$, and $N_b = f_3(S)$ which can be used to identify the nonnegative solutions of the dc rate equations. Thus, we will again show that f_1 and f_2 have a single nonnegative intersection point for $I \geq 0$, thereby establishing the existence of a unique nonnegative solution regime.

When $I = 0$, it can be shown by reasoning similar to that applied to the one-level case that the only possible solution is $S = N = N_b = 0$. When $I > 0$, though, we must again examine the features of the functions f_1 and f_2. Since Eq. (2.16) is repeated in this model, $f_1(S)$ for the two-level model is identical to that from the one-level case. Thus, based on our earlier analysis, we know that for $S > 0$, $f_1(S)$ is a strictly-increasing continuous function which vanishes to zero as $S \rightarrow 0$, regardless of whether Channin's or Agrawal's gain-saturation term is used. Meanwhile, Eqs. (2.39) and (2.40) define a function $f_2(S)$ analogous to that from the one-level model. In the following discussion, we will show that $f_2(S)$, which is only defined over an interval $[0,S_h]$, is strictly-decreasing and continuous over the interval $(0,S_h]$, with $f_2(S) > 0$ for $0 \leq S < S_h$ and $f_2(S_h) = 0$.

Let us consider the solutions to Eqs. (2.39) and (2.40) such that S, N, and $N_b \geq 0$. For $S > \tau_p \eta_i I / q V_{act}$, Eq. (2.40) has no such solution, so we may restrict our attention to values of S in the interval $[0, \tau_p \eta_i I / q V_{act}]$. Consider some value $S = S_i$ in this interval. In this case, for each value of $N \geq 0$ there exists a unique value of $N_b > 0$ such that (S_i,N,N_b) satisfies Eq. (2.39). We can thus define a function $N_b = h_{1Nb}(N)$ which maps these unique values of N_b for each N. As can be easily seen, $h_{1Nb}(N)$ is a strictly-increasing continuous function for $N \geq 0$ with $h_{1Nb}(0) = N_{b1}$ such that $R_b(N_{b1}) + N_{b1}/\tau_{capt} = \eta_i I / q V_{barr}$. Meanwhile, for each value of N in the interval $[0,N_{hi}]$, where $H_2(S_i,N_{hi},0) = 0$, there exists a unique value of $N_b \geq 0$ such that (S_i,N,N_b) satisfies Eq. (2.40). For $N > N_{hi}$ no such solution exists. Let $N_b = h_{2NbSi}(N)$ map out these values for $0 \le N \le N_{hi}$. Over the interval $[0,N_{hi}]$, $h_{2NbSi}(N)$ is a strictly-decreasing function with $h_{2NbSi}(N_{hi}) = 0$ and $h_{2NbSi}(0) = N_{b2Si}$, where $R_b(N_{b2Si}) = \eta_i I/qV_{barr} - V_{act}S_i/\tau_p V_{barr}$. Obviously, h_{1Nb} and h_{2NbSi} will intersect only if $N_{b2Si} \ge N_{b1}$. This intersection point corresponds to a solution to Eqs. (2.39) and (2.40) and will be nonnegative. The condition $N_{b2Si} \ge N_{b1}$ holds up to a value $S_i = S_h = \tau_p V_{barr} N_{b1}/\tau_{capt} V_{act}$. Thus, for each value of S in the interval $[0,S_h]$ there exists a unique pair of nonnegative values for N and N_b that, along with S, satisfies Eqs. (2.39) and (2.40). For all other S, there is no nonnegative solution. Let $f_2(S)$ and $f_3(S)$ map out these values for N and N_b, respectively, in the interval $[0,S_h]$. Thus, every nonnegative solution to Eqs. (2.39) and (2.40) is mapped out by $(S,f_2(S),f_3(S))$ for $0 \le S \le S_h$. Using the parameters of Table 2.2, Fig. 2.6 illustrates the solution curve of these points along with a projection of the curve, corresponding to a plot of $N = f_2(S)$, onto the S-N plane for $I = 10$ mA.

We can show that $f_2(S)$ is strictly-decreasing over the interval $(0,S_h]$ by again employing the

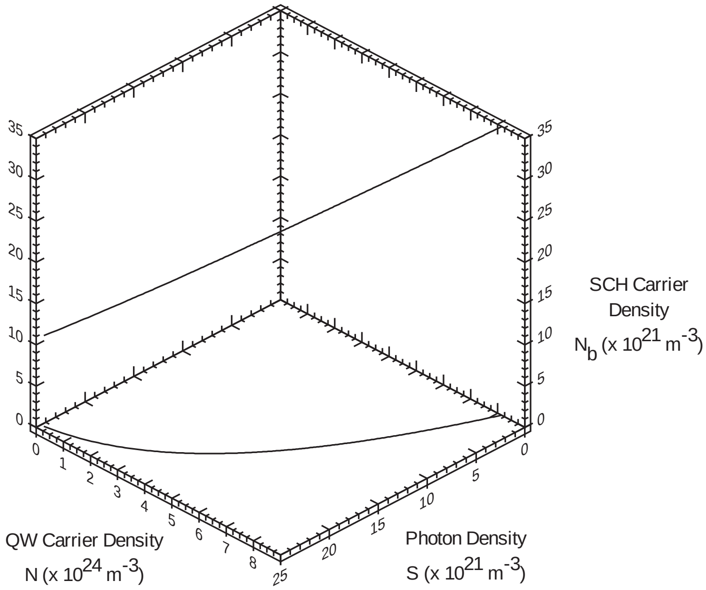

Figure 2.6 Plot of solution curve (S,N,N_b) for Eqs. (2.39)-(2.40) mapped out by $N = f_2(S)$ and $N_b = f_3(S)$ when $I = 10$ mA. Also shown is a projection of this curve onto the S-N plane.

Implicit Function Theorem. Consider the region $D = \{S > 0, N > 0, N_b > 0\}$. In this region, both H_1 and H_2 are defined everywhere. The partial derivatives of these functions with respect to S, N, and N_b are

$$H_{1S} = 0, H_{1N} = -\frac{N_w V_{act}}{\tau_{em} V_{barr}}, H_{1Nb} = \frac{1}{\tau_{capt}} + \frac{dR_b}{dN_b} \tag{2.41}$$

$$H_{2S} = \frac{1}{\tau_p}, H_{2N} = N_w\left[\frac{d(R_w - R_{w\beta})}{dN}\right], H_{2Nb} = \frac{V_{barr}}{V_{act}}\frac{dR_b}{dN_b} \tag{2.42}$$

Each of these partials is continuous in D. Now, consider some solution $P_o = (S_o,N_o,N_{bo})$ in D that solves $H_1 = H_2 = 0$. The Jacobian of H_1 and H_2 relative to N and N_b is

$$\frac{\partial(H_1, H_2)}{\partial(N, N_b)} = \frac{-N_w}{\tau_{em}}\frac{dR_b}{dN_b} - N_w\left[\frac{d(R_w - R_{w\beta})}{dN}\right]\left(\frac{1}{\tau_{capt}} + \frac{dR_b}{dN_b}\right) \tag{2.43}$$

At all points in D this Jacobian is negative and therefore nonzero. By the Implicit Function Theorem, then, around some neighborhood of S_o there exist continuous and differentiable functions $N = f_{2N}(S)$ and $N_b = f_{3Nb}(S)$ which, along with S, solve Eqs. (2.39) and (2.40). However, we already know that f_2 and f_3 are the only such functions in this region when $0 \le S \le S_h$, so $f_2 = f_{2N}$ and $f_3 = f_{3Nb}$ for $0 < S \le S_h$. Since the point P_o was arbitrary, both f_2 and f_3 must be continuous and differentiable over the entire interval $(0,S_h]$.

Because of the differentiability of $f_2(S)$ in the interval $(0,S_h]$, its derivative is

$$f_2'(S) = -\frac{\dfrac{\partial(H_1, H_2)}{\partial(S, N_b)}}{\dfrac{\partial(H_1, H_2)}{\partial(N, N_b)}} = \frac{-\dfrac{1}{\tau_p}\left(\dfrac{1}{\tau_{capt}} + \dfrac{dR_b}{dN_b}\right)}{\dfrac{N_w}{\tau_{em}}\dfrac{dR_b}{dN_b} + N_w\left[\dfrac{d(R_w - R_{w\beta})}{dN}\right]\left(\dfrac{1}{\tau_{capt}} + \dfrac{dR_b}{dN_b}\right)} \tag{2.44}$$

which is negative for all S in $(0,S_h]$. Thus, $f_2(S)$ is a strictly-decreasing continuous function for all S in the interval $(0,S_h]$. Furthermore, when $S = S_h$, $N_{b1} = N_{b2Si}$ and therefore $f_2(S_h) = 0$. Otherwise, for all other S in the interval $[0,S_h]$, $f_2(S) > 0$.

Thus, we have shown that $N = f_2(S)$, which is defined for $0 \le S \le S_h$, is indeed a strictly-decreasing continuous function over the interval $(0,S_h]$ with $f_2(S) > 0$ for $0 \le S < S_h$ and $f_2(S_h) = 0$. Clearly, within the interval $[0,S_h]$, f_1 and f_2 will intersect exactly once, corresponding to a nonnegative solution for N and S. Furthermore, $f_3(S)$ defines the corresponding nonnegative solution for N_b. Thus, for every $I > 0$ there exists exactly one nonnegative solution to the two-level dc rate equations. Consequently, the two-level model of Eqs. (2.35)-(2.38) has a single nonnegative solution for $I \ge 0$ when the gain-saturation terms of Channin or Agrawal are used instead of the linear expression.

Using the model parameters from Table 2.2 (p. 25), the logarithmic-gain term, and the gain-saturation term of Eq. (2.15a), we have plotted in Fig. 2.7 both f_1 and f_2 for I = 10 mA. The parameters, taken from [2.15] and based on data extracted from a number of sources [2.19],[2.23]-[2.28], are for a 300 × 2.5 μm^2 single-QW laser with an 8-nm $\text{In}_{0.2}\text{Ga}_{0.8}\text{As}$ QW and 300-nm $\text{Al}_{0.1}\text{Ga}_{0.9}\text{As}$ SCH

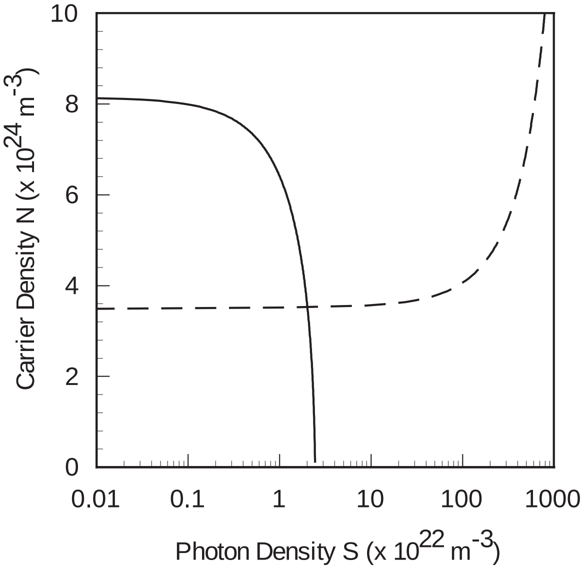

Figure 2.7 Plot of $f_1(S)$ and $f_2(S)$ from the two-level model when I = 10 mA. Dashed line: $N = f_1(S)$; solid line: $N = f_2(S)$.

layers. The QW capture lifetime in this case is actually the transport time across the SCH region. The photon lifetime was calculated using the expression $\tau_p^{-1} = v_{gr}[\alpha_i + \ln(1/R)/L_c]$ from [2.29], where α_i = internal cavity loss = 4.3 cm^{-1}, R = facet reflectivity = 0.32, and L_c = cavity length = 300 μm. The output-power coupling coefficient was determined using $\eta_c = 0.5 \ln(1/R)/[\alpha_i L_c + \ln(1/R)]$ from [2.29]. As expected, the figure shows that there is exactly one intersection point, corroborating the above analysis. Note that Fig. 2.7 is nearly identical to Fig. 2.3 (p. 24) because the additional effect of recombination in the SCH layers has a minimal impact on the dc characteristics for this particular set of model parameters.

2.4.3 Model implementation

As was the case with the one-level equations, the single nonnegative solution regime of Eqs. (2.35)-(2.38) allows us to apply variable transformations to ensure that only this regime is chosen in simulation. We have implemented in SPICE3 equivalent-circuit models of the two-level equations that employ such transformations. Like the one-level model, our two-level implementation is valid for all $I \geq 0$. Equation (2.5) was again used for the output power P_f, while the SCH and QW carrier densities were transformed using

$$N_b = N_e \exp\left(\frac{qV}{nkT}\right) \tag{2.45}$$

$$N = N_{e2} \exp\left(\frac{qV_w}{n_{w2}kT}\right) \tag{2.46}$$

In this case, N_e and N_{e2} are the equilibrium carrier densities in the SCH and QWs, respectively, while n and n_{w2} are the corresponding diode ideality factors. V_w is the voltage across the QWs. In reality, any transformation which would limit N to nonnegative values would have been sufficient, since this variable is implicitly solved within the rate equations and is not directly related to any external currents or voltages. A more realistic relation between N and V_w could have been used, such as that derived by considering the 2-D effects in the QW [2.30]. However, because this does not restrict N to nonnegative values, we chose the simpler expression of Eq. (2.46).

Fig. 2.8 illustrates the two-level circuit implementation, whose equations are obtained via straightforward manipulations of the corresponding rate equations and transformations. Substituting Eqs. (2.5) and (2.45)-(2.46) into Eqs. (2.35)-(2.38) and rearranging we get

$$\frac{qN_e}{nkT}\exp\left(\frac{qV}{nkT}\right)\frac{dV}{dt} = \frac{\eta_i I}{qV_{barr}} - \frac{N_e}{\tau_{capt}}\left[\exp\left(\frac{qV}{nkT}\right) - 1\right] - \frac{N_e}{\tau_{capt}} - R_b(N_b) + \frac{N_w V_{act} N}{\tau_{em} V_{barr}} \tag{2.47}$$

$$\begin{aligned}\frac{qN_{e2}}{n_{w2}kT}\exp\left(\frac{qV_w}{n_{w2}kT}\right)\frac{dV_w}{dt} &= \frac{V_{barr}N_b}{\tau_{capt}N_w V_{act}} - \frac{N_{e2}}{\tau_{em}}\left[\exp\left(\frac{qV_w}{n_{w2}kT}\right) - 1\right] - \frac{N_{e2}}{\tau_{em}} \\ &\quad - R_w(N) - \vartheta\Gamma_c v_{gr}\frac{\alpha(N)}{\phi(\vartheta(m+\delta)^2)}(m+\delta)^2\end{aligned} \tag{2.48}$$

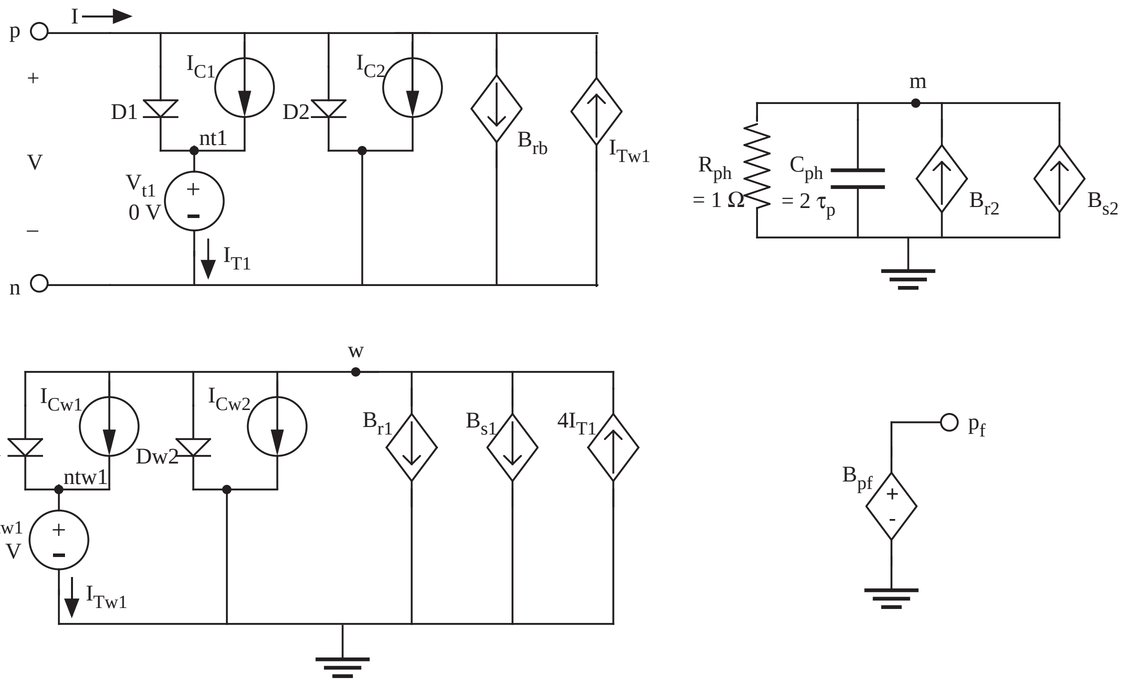

Figure 2.8 Circuit-level implementation of the two-level QW-laser model with a single solution regime.

$$2(m+\delta)\frac{dm}{dt} = \frac{-(m+\delta)^2}{\tau_p} + \frac{N_w}{\vartheta}R_{w\beta}(N) + N_w\mathit{\Gamma}_c v_{gr}\frac{\alpha(N)}{\phi(\vartheta(m+\delta)^2)}(m+\delta)^2 \tag{2.49}$$

Again, after additional rearrangement of the above equations and setting $\mathit{\Theta}_1 = 2\eta_i\tau_{capt}/qV_{barr}$ and $\mathit{\Theta}_2 = \eta_i\tau_{em}/qN_wV_{act}$ the final set of circuit equations are

$$I = I_{T1} + I_{D2} + I_{C2} + B_{rb} - I_{Tw1} \tag{2.50}$$

$$I_{T1} = I_{D1} + I_{C1} \tag{2.51}$$

$$4I_{T1} = I_{Tw1} + I_{Dw2} + I_{Cw2} + B_{r1} + B_{s1} \tag{2.52}$$

$$I_{Tw1} = I_{Dw1} + I_{Cw1} \tag{2.53}$$

$$2\tau_p\frac{dm}{dt} + m = B_{r2} + B_{s2} \tag{2.54}$$

$$B_{pf} = (m+\delta)^2 \tag{2.55}$$

$$I_{D1} = \frac{qV_{barr}N_e}{2\eta_i\tau_{capt}}\left[\exp\left(\frac{qV}{nkT}\right) - 1\right] \tag{2.56}$$

$$I_{D2} = \frac{qV_{barr}N_e}{2\eta_i\tau_{capt}}\left[\exp\left(\frac{qV}{nkT}\right) - 1 + \frac{2q\tau_{capt}}{nkT}\exp\left(\frac{qV}{nkT}\right)\frac{dV}{dt}\right] \tag{2.57}$$

$$I_{C1} = I_{C2} = \frac{qV_{barr}N_e}{2\eta_i\tau_{capt}} \tag{2.58}$$

$$I_{Dw1} = \frac{qN_wV_{act}N_{e2}}{\eta_i\tau_{em}}\left[\exp\left(\frac{qV_w}{n_{w2}kT}\right) - 1\right] \tag{2.59}$$

$$I_{Dw2} = \frac{qN_wV_{act}N_{e2}}{\eta_i\tau_{em}}\left[\exp\left(\frac{qV_w}{n_{w2}kT}\right) - 1 + \frac{2q\tau_{em}}{n_{w2}kT}\exp\left(\frac{qV_w}{n_{w2}kT}\right)\frac{dV_w}{dt}\right] \tag{2.60}$$

$$I_{Cw1} = I_{Cw2} = \frac{qN_wV_{act}N_{e2}}{\eta_i\tau_{em}} \tag{2.61}$$

$$B_{rb} = \frac{qV_{barr}}{\eta_i} R_b(\Theta_1 I_{T1}) \tag{2.62}$$

$$B_{r1} = \frac{2qN_w V_{act}}{\eta_i} R_w(\Theta_2 I_{Tw1}) \tag{2.63}$$

$$B_{s1} = \frac{2\lambda\tau_p q N_w \Gamma_c v_{gr}}{\eta_i \eta_c hc} \frac{\alpha(\Theta_2 I_{Tw1})}{\phi(\vartheta(m+\delta)^2)}(m+\delta)^2 \tag{2.64}$$

$$B_{r2} = \frac{N_w \eta_c V_{act} hc}{\lambda(m+\delta)} R_{w\beta}(\Theta_2 I_{Tw1}) \tag{2.65}$$

$$B_{s2} = \tau_p N_w \Gamma_c v_{gr} \frac{\alpha(\Theta_2 I_{Tw1})}{\phi(\vartheta(m+\delta)^2)}(m+\delta) - \delta \tag{2.66}$$

Here we have used the fact that $N_b = \Theta_1 I_{T1}$ and $N = \Theta_2 I_{Tw1}$. Note that in actual practice the gain and gain-saturation terms should be replaced with expressions from Eqs. (2.14) and (2.15), respectively.

These equations can be mapped directly into the circuit of Fig. 2.8 (p. 36). $D1$, $D2$, I_{C1}, and I_{C2} now describe charge-storage and carrier capture for the SCH carriers, while B_{rb} represents SCH recombination and I_{Tw1} accounts for carrier emission from the QWs. $Dw1$, $Dw2$, I_{Cw1}, and I_{Cw2} represent charge-storage and carrier emission in the QWs, while B_{r1} and B_{s1} account for the effects of recombination and stimulated emission, respectively. $4I_{T1}$ represents carrier capture by the QWs. Finally, the two circuits on the right describe the photon density dynamics and laser output power.

In Fig. 2.9, we give an example of a SPICE input deck that implements the circuit of Fig. 2.8 using the logarithmic gain and Channin's gain-saturation term. Additional details can be found in Appendix A. In addition to the parameters of Table 2.2, we set $N_e = 2.2 \times 10^5$ cm^{-3}, $n = 2$, $N_{e2} = 5.9 \times 10^8$ cm^{-3}, $n_{w2} = 2$, and $\delta = 0$. We again have included 10^{-60} inside the logarithmic term of the gain expression. Examples of dc and transient simulations of the circuit are plotted in Fig. 2.10. The tran-

```
* two-level laser model with logarithmic gain

ibias 0 p 10m ac 1
xlaser p 0 pf ltest1
rout pf 0 1e9

*********************************************************************
.subckt ltest1 p n pf
D1 p nt1 d1mod_ltest1
Ic1 p nt1 1.0246564e-13
Vt1 nt1 n 0
D2 p n d2mod_ltest1
Ic2 p n 1.0246564e-13
Brb p n i=0.0117*i(Vt1)+0.027052971*i(Vt1)*i(Vt1)+
+          0.0053935501*i(Vt1)*i(Vt1)*i(Vt1)
F1 n p Vtw1 1
Dw1  w ntw1 dw1mod_ltest1
Icw1 w ntw1 1.6655324e-12
Vtw1 ntw1 0 0
Dw2  w 0 dw2mod_ltest1
Icw2 w 0 1.6655324e-12
Br1 w 0 i=0.088*i(Vtw1)+20.039238*i(Vtw1)*i(Vtw1)+
+          614.64958*i(Vtw1)*i(Vtw1)*i(Vtw1)
Bs1 w 0 i=2.7571955*v(m)*v(m)*ln(1e-60+114.84402*i(Vtw1)+
+         26152.122*i(Vtw1)*i(Vtw1)+802145.8*i(Vtw1)*i(Vtw1)*i(Vtw1))/
+         (1+0.95928574*v(m)*v(m))
F2 0 w Vt1 4
Rph m 0 1
Cph m 0 5.518e-12
Br2 0 m i=(0*i(Vtw1)+0.00048982585*i(Vtw1)*i(Vtw1)+
+         0*i(Vtw1)*i(Vtw1)*i(Vtw1))/v(m)
Bs2 0 m i=0.67395059*v(m)*ln(1e-60+114.84402*i(Vtw1)+
+         26152.122*i(Vtw1)*i(Vtw1)+802145.8*i(Vtw1)*i(Vtw1)*i(Vtw1))/
+         (1+0.95928574*v(m)*v(m))
Bpf pf 0 v=v(m)*v(m)
.ends ltest1
.model d1mod_ltest1 D Is=1.0246564e-13 n=2
.model d2mod_ltest1 D Is=1.0246564e-13 n=2 tt=9e-11
.model dw1mod_ltest1 D Is=1.6655324e-12 n=2
.model dw2mod_ltest1 D Is=1.6655324e-12 n=2 tt=8e-10
*********************************************************************


.dc ibias 0 50m 0.25m
.end
```

Figure 2.9   Example SPICE deck for the two-level QW-laser model.

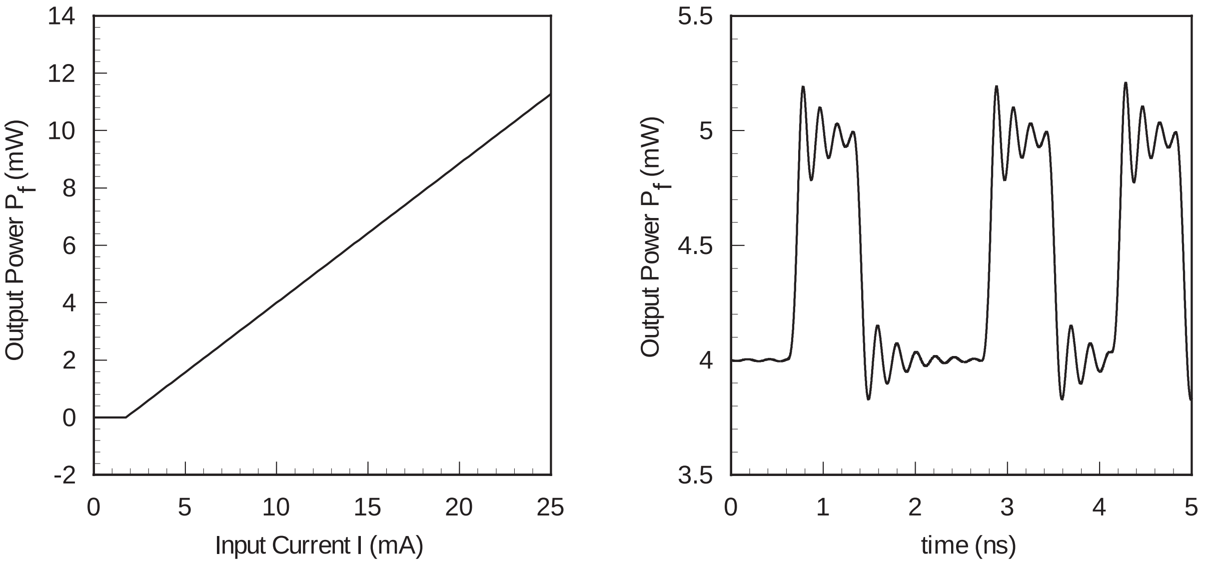

(a)

(b)

Figure 2.10 (a) Plot of LI curve generated from the circuit implementation of Fig. 2.8 using the model parameters of Table 2.2. (b) Transient output power in response to an input current varying between 10 and 12 mA with 100 ps rise and fall times.

sient curve is the output power of the laser in response to an input current varying between 10 and 12 mA with 100-ps rise and fall times.

2.5 Modeling of Junction Capacitance and Parasitic Effects

In order to complete the rate-equation-based models described in Sections 2.3 and 2.4, we have augmented them with additional circuit elements that account for junction capacitance and parasitic effects. The inclusion of parasitics is particularly important, since they often place an ultimate performance limit on many lasers [2.31]-[2.32]. Figure 2.11 illustrates the complete QW-laser equivalent circuit including the cavity model, junction capacitance, and parasitics.

While the junction capacitance should only be important during reverse-bias operation, a rar-

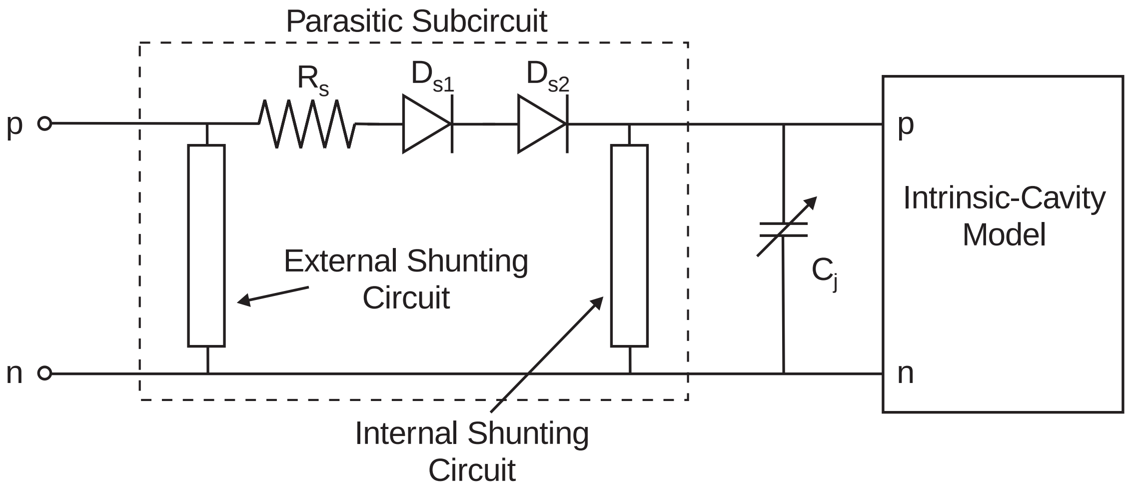

Figure 2.11 Complete QW-laser model including junction capacitance and parasitics.

ity for semiconductor lasers, we have included it in our models for the sake of completeness. We describe this capacitance in exactly the same manner in which it is included in the standard junction diode found in SPICE [2.33]. Essentially, below some critical voltage ($FC \times \phi_o$), the standard junction-capacitance formula can be used, while above this voltage, a linear expression is more appropriate. The resulting equation for the junction capacitance C_j is

$$C_j = \begin{cases} C_{jo}\left(1-\dfrac{V}{\phi_o}\right)^{-m_p} & , \quad \mathrm{V} < FC \times \phi_o \\ \dfrac{C_{jo}}{(1-FC)^{1+m_p}}\left(1-FC(1+m_p)+\dfrac{m_pV}{\phi_o}\right) & , \quad \mathrm{V} \ge FC \times \phi_o \end{cases} \tag{2.67}$$

where C_{jo} is the zero-bias junction capacitance, ϕ_o is the built-in junction potential, m_p is a grading coefficient, and FC is a coefficient for the forward-bias formula. Typically, a value of 0.5 can be used for m_p and FC [2.33].

Parasitics, meanwhile, can take on a variety of forms depending on the particular device in question [2.31], [2.34], and can include both on-chip and packaging elements. Our models account for the on-chip effects via the general parasitic subcircuit shown in Fig. 2.11. In this circuit, R_s models series resistance, while diodes D_{s1} and D_{s2} account for any diode effects at additional heterojunctions in the laser, particularly the cladding layer-contact layer interfaces [2.35]. Meanwhile, the internal shunting circuit can be used to model a constant capacitance C_{ssc} in parallel with the cavity. It could also be used in place of the bias-dependent C_j to model a constant junction capacitance. Finally, the external shunting circuit can be used to account for additional on-chip parasitic resistance and capacitance.

Fig. 2.12 illustrates four possible implementations of the external circuit that use various combinations of resistance $R1$ and capacitance $C1$. Often, the simple shunting capacitance of Fig. 2.12(b) is sufficient to account for on-chip shunting parasitics [2.34], while in other cases the series combination of $R1$-$C1$ in Fig. 2.12(c) is more appropriate [2.31]. The pure resistive parasitic of Fig. 2.12(a) is included for completeness, but will generally not be used.

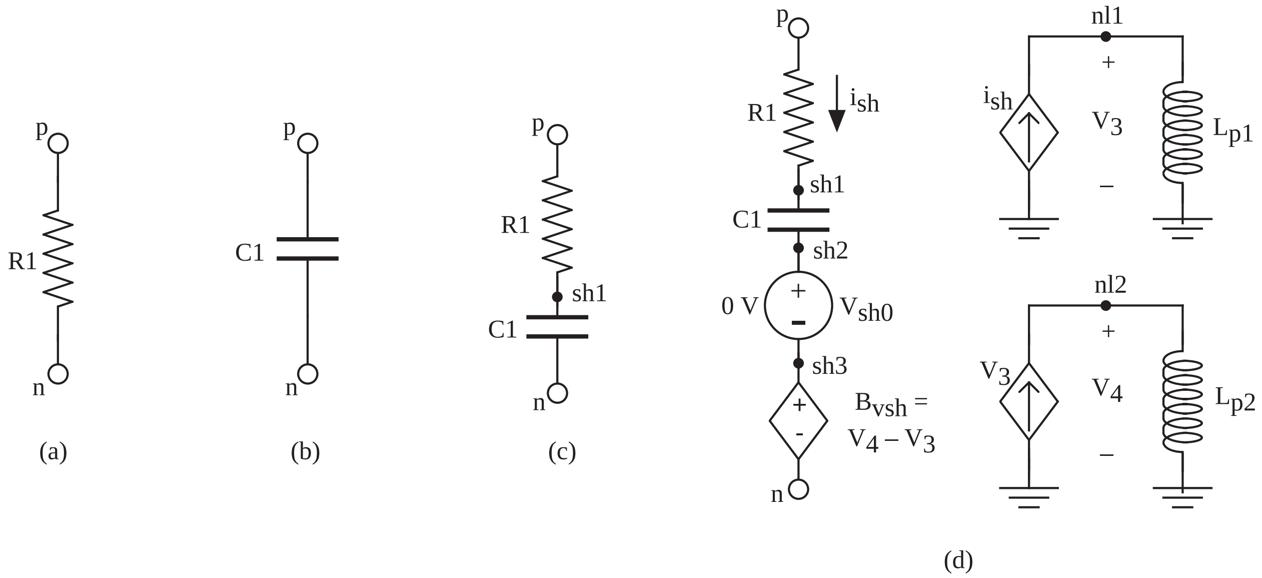

Figure 2.12 Parasitic external shunting circuits: (a) resistance, (b) capacitance, (c) RC circuit, and (d) distributed-RC network.

In some situations, the complex circuit of Fig. 2.12(d) may be necessary in order to properly account for distributed-RC effects in the device, namely frequency-dependent resistance and capacitance. This circuit implements the $R1$-$C1$ combination of Fig. 2.12(c) when $R1$ and $C1$ are described using [2.31]:

$$R1 = \frac{R}{3} - \omega^2 \frac{2R^3C^2}{945} \tag{2.68}$$

$$C1 = \frac{C}{1 + \omega^2 \frac{R^2C^2}{45}} \tag{2.69}$$

where R and C are total resistance and capacitance [2.31], and ω is the modulation frequency in rad/s. Because it is not possible to define frequency-dependent resistance or capacitance in SPICE, we instead translated (2.68) and (2.69) into the circuit of Fig. 2.12(d) using $R1 = R/3$, $C1 = C$, $L_{p1} = R^2C/45$, and $L_{p2} = 2RC/21$.

While the various parasitics described in this section provide a good basis for modeling parasitic effects in a semiconductor laser, the user is free to modify them as necessary on a device-by-device basis. As we shall see in the next section, it is sometimes necessary to use such variations in order to fit our models to experimental data.

2.6 Parameter Extraction from Experimental Data

As the discussion of Sections 2.3 and 2.4 demonstrates, our QW-laser models exhibit improved numerical solution characteristics in the form of a unique solution regime during dc simulation. An equally important issue, however, is their ability to reproduce the operating characteristics of actual devices. Because the models are targeted for the design and simulation of optoelectronic applications, it is critical that they can represent the lasers used in these designs. Thus, in this section, we review the extraction of the two-level QW-laser model parameters from two experimental devices, with the logarithmic gain and Channin's gain-saturation term having been used to model the gain. The first laser is an AlGaAs/GaAs/InGaAs edge-emitting buried heterostructure (BH) laser with cleaved facets. The second is a ridge-waveguide (RW) AlGaAs/GaAs/InGaAs edge-emitter with mirrors formed by a distributed Bragg reflector (DBR) and a cleaved facet [2.36]. These devices were fabricated in J. Coleman's semiconductor laser laboratory at the University of Illinois, and subsequently characterized by G. Papen's research group. Below, after discussing our parameter-extraction methodology, we present a comparison of simulated and experimental results for each device.

2.6.1 Extraction methodology

The fitting of our model to an actual laser first requires the measurement of various device operating characteristics, including a light-current (LI) curve, a current-voltage (IV) curve, and small-signal modulation responses at different biases. We can then extract model parameters from this data via numerical optimization techniques. Starting with an initial set of model parameter values, a simulation is generated corresponding to each measured laser characteristic. A new set of parameters is then determined which reduces the total error between simulation and experiment. This process is repeated until the error is minimized. For the two devices presented here, we performed this numerical optimization via CFSQP (C code for feasible sequential quadratic programming), developed by Lawrence *et al.* at the University of Maryland [2.37].

Because the success of the numerical optimization can depend heavily on the initial parameter values, it is critical that we use a good initial guess. Often, this is not easy due to the absence of detailed device information such as geometry and composition. However, because we had access to such information for the two devices presented here, we were able to make theoretical estimates for most of the model parameters, which we then used as a starting point for numerical optimization. Below, we give a general overview of how the various estimates were made.

First, based on details of the device structure and fabrication, we calculated the geometry-dependent parameters, namely the quantum-well and barrier-layer volumes. Cavity length, SCH width, and QW width were retained for additional calculations of band structure and other parameters. Next, we determined various material parameters, such as carrier effective masses. While most of them are not directly incorporated into our models, they were necessary for determining the remaining model parameters. First, reported values from the literature were used to determine the quantum-well effective masses [2.38], barrier-layer effective masses [2.39], and diffusion coefficients [2.40]. Quantum-well bandgap values were estimated based on simple calculations taking into account strain [2.39], while the barrier-layer values were taken from the literature [2.39]. The conduction and valence band discontinuities between the quantum wells and barrier layers were determined based on a 60%-40% partition of the bandgap discontinuity [2.41], [2.42]. The quantum-well subband locations were then determined using straightforward square-well-potential calculations [2.43]. Reported values were used for the core and cladding refractive indices of the optical cavity [2.39], [2.44]. Finally, the QW and barrier-layer equilibrium carrier densities were calculated numerically [2.45].

Next, we determined values for the gain, loss, and recombination parameters. The values of the gain coefficient G_o [2.16] and gain-saturation factor ε [2.46]-[2.48] were based on reported values in the literature. The transparency density N_o, on the other hand, was calculated analytically based on the Bernard-Duraffourg condition [2.49]. The recombination parameters A, B, C, A_b, B_b, and C_b were estimated from reported values [2.50], [2.51]. After setting the spontaneous emission coupling coefficients β_A and β_C equal to zero, we obtained a crude estimate for β_B based loosely on the theoretical formulation of Petermann [2.52].

We then determined values for the various modal parameters in the model, specifically λ, Γ_c, v_{gr}, τ_p, and η_c. The wavelength λ was determined from the quantum-well bandgap calculations mentioned above. The confinement factor Γ_c and group velocity v_{gr} were obtained via calculations of the laser's optical waveguide using the effective-index method [2.39], while the photon lifetime τ_p and output-power coupling coefficient η_c were calculated [2.29] based on estimates for the laser's internal loss [2.53] and mirror reflectivities. We used Fresnel-reflectivity [2.54] and distributed-mirror calculations [2.29] for the facet and DBRs reflectivities, respectively.

Finally, we determined values for the carrier transport parameters τ_{em} and τ_{capt}, as well as the current injection efficiency η_i. Thermionic emission theory was used to estimate values for τ_{em} [2.19], [2.55]. On the other hand, τ_{capt} was estimated from reported values of QW capture times [2.56] and calculated values for the SCH diffusion time [2.19].

2.6.2 Discrepancy between theoretical and measured modulation responses

Before presenting the results of using the above methodology on our two devices, there is an important issue to consider when dealing with measured small-signal modulation responses. The typical measured modulation response reported in the literature corresponds to a measurement of the microwave modulation response, S_{21} [2.32], [2.34]. The theoretical response, on the other hand, usually is related to a laser's small-signal transfer function T_f, i.e., the ratio of the small-signal output power to the small-signal input current [2.29]. In general, one must properly account for the source impedance [2.31]. Thus, T_f and S_{21} are not equivalent; therefore, care must be taken when fitting a measured modulation response to a simulated one.

The obvious method of accommodating this difference is to compare *simulated* S_{21} curves to the measured data [2.34], [2.57]. However, it is often easier to simulate T_f instead of S_{21}. In this case, as we show in Appendix B, it is possible to relate the two. If we assume a 50-Ω test setup, then S_{21} can be expressed as

$$S_{21} = \frac{2T_f}{Z_{in} + 50} \tag{2.70}$$

where Z_{in} is the laser's input impedance. From (2.70), we see that S_{21} is proportional to the transfer function of the laser as if there were a 50-Ω parasitic resistance in parallel with its electrical terminals. Thus, as an alternative to (2.70), we could simulate the laser with an additional 50-Ω resistance across the input terminals and normalize the calculated transfer function [2.57], thereby providing us with simulated values of normalized S_{21} data. We could then compare this data with measurements, also normalized. In either case, we can properly account for the discrepancy between T_f and S_{21}.

2.6.3 Buried-heterostructure semiconductor laser

Using the approach outlined above, we began our parameter extractions using data from an AlGaAs/GaAs/InGaAs edge-emitting BH laser with cleaved facets. As illustrated in Fig. 2.13, this laser was grown on a GaAs substrate and consists of $Al_{0.60}Ga_{0.40}As$ cladding layers, 1050-Å and 1150-Å GaAs SCH layers, and an 85-Å $In_{0.23}Ga_{0.77}As$ quantum well. The cavity length and width were 560 and 8 μm, respectively. This device was characterized under dc conditions and small-signal modulation, with modulation responses measured at biases of 11-30 mA.

After the determination of an initial set of the cavity model parameters from this data, and subsequent attempts to numerically optimize these values, we realized that in addition to the two-level cavity model, parasitic circuit elements were necessary to fully describe the laser's modulation response. The complete circuit that we adopted is illustrated in Fig. 2.14. As we can see, the parasitic section is a modified version of that presented in Section 2.5; series-diode effects and part of the series resistance are placed externally to a combination of shunting capacitance and series resistance. This variation eliminates the bias-dependent impedances of the diodes from contributing to the small-signal transfer function of the laser.

Using the configuration of Fig. 2.14, we were able to optimize the model parameters and

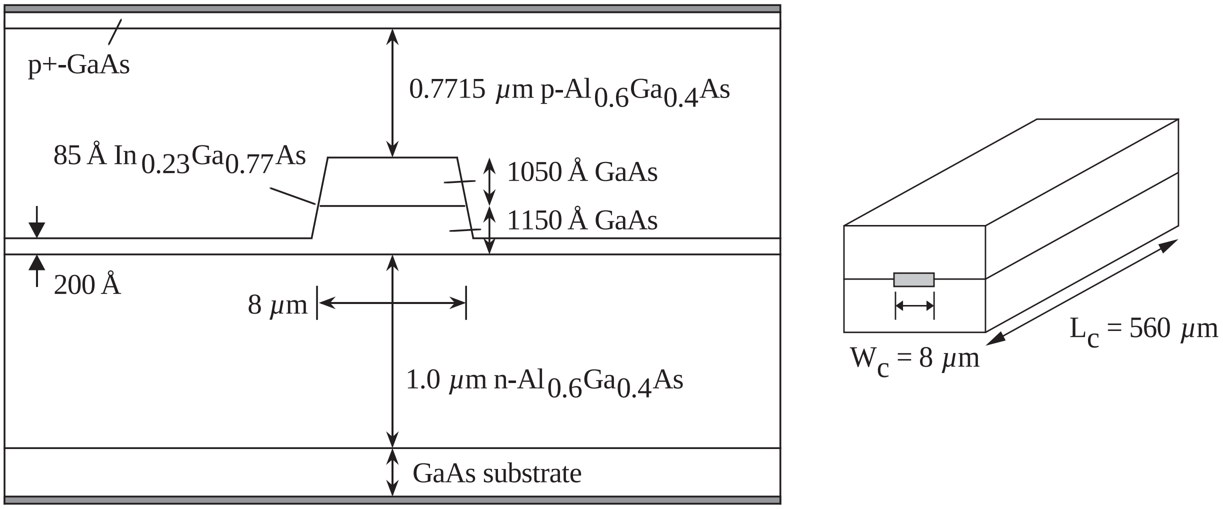

Figure 2.13 Device structure of the AlGaAs/GaAs/InGaAs BH laser.

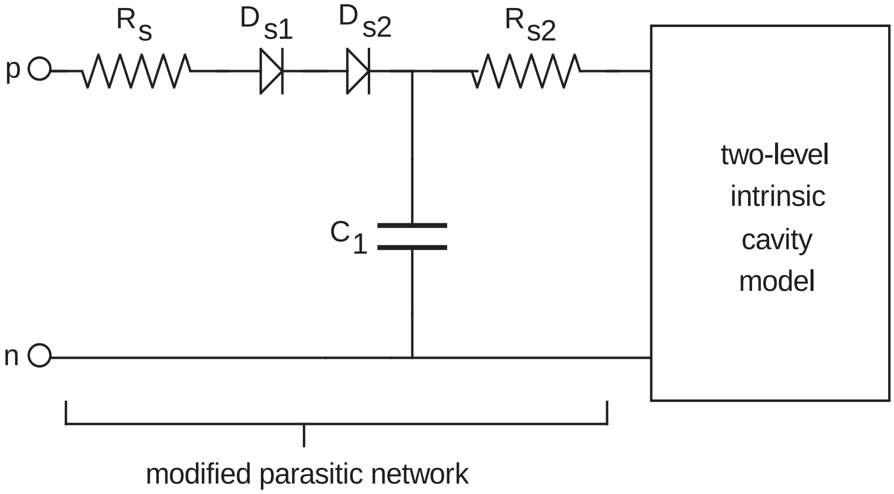

Figure 2.14 Complete QW-laser model used to fit the BH laser.

obtain some reasonable agreement between modeled and experimental LI, IV, and modulation response data. In addition to the final set of intrinsic model parameters given in Table 2.3, we determined the following parameters for the parasitics (where $I_{s1,2}$ and $n_{1,2}$ denote the saturation currents and ideality factors, respectively, of diodes D_{s1} and D_{s2}): R_s = 2.294 Ω, R_{s2} = 6.937 Ω, I_{s1} = 2.967 mA, n_1 = 1.109, I_{s2} = 2.328 mA, n_2 = 1.125, and C_1 = 48 pF. Figure 2.15 shows a comparison of simulated and experimental LIV data, while Fig. 2.16 depicts the magnitudes of the simulated and measured small-signal modulation responses (S_{21}) at bias currents of 11, 12, 14, 15, 16, 17, 19, 21, 25, and 30 mA.

Clearly, the simulated and experimental LIV data compare very well with each other out to

Table 2.3 Extracted intrinsic model parameters for the BH laser.

Parameter	Value
η_i	0.887
λ	1.036 μm
N_w	1
V_{act}	3.859×10^{-17} m^3
Γ_c	0.0325
v_{gr}	8.931×10^{7} m/s
τ_p	4.391 ps
η_c	0.389
N_o	1.222×10^{18} cm^{-3}
G_o	2291 cm^{-1}
ε	1.383×10^{-17} cm^3
A	1.063×10^{8} s^{-1}
B	1.562×10^{-10} cm^3/s
C	1.625×10^{-29} cm^6/s
A_b	1.695×10^{8} s^{-1}
B_b	1.295×10^{-10} cm^3/s
C_b	1.000×10^{-29} cm^6/s
β_A	0
β_B	4.781×10^{-5}
β_C	0
V_{barr}	5.251×10^{-16} m^3
τ_{capt}	18.53 ps
τ_{em}	5.407 ps
N_e	2.642×10^{7} cm^{-3}
n	1.943
N_{e2}	1.29×10^{9} cm^{-3}
n_{w2}	2

~25 mA. However, at higher currents not shown here (near 60 mA), the experimental LI curve begins to roll over, presumably due to thermal effects. Because our model assumes a constant device temperature, it was not able to capture this behavior, but it still works well over the current range shown in Fig. 2.15.

We were not able to obtain a similar level of agreement in the S_{21} data, as can be seen in Fig. 2.16. In particular, at the lower biases of 11 and 12 mA, the curves do not match well at all, with the simulation at 12 mA exhibiting a resonance peak not seen in the experimental data. At higher biases, the correspondence between simulation and measurement begins to improve, with the location of the resonance peaks in the simulated and measured curves showing good agreement at biases above 14 mA. However, the magnitudes of these peaks only exhibit a close match at currents near 21 mA. One of the major sources of discrepancy between the simulated and experimental curves is most likely the kink exhibited in many of the measured S_{21} curves at frequencies below resonance. This discontinuity, conjectured to possibly be due to multimode effects [2.57], significantly impaired the ability of

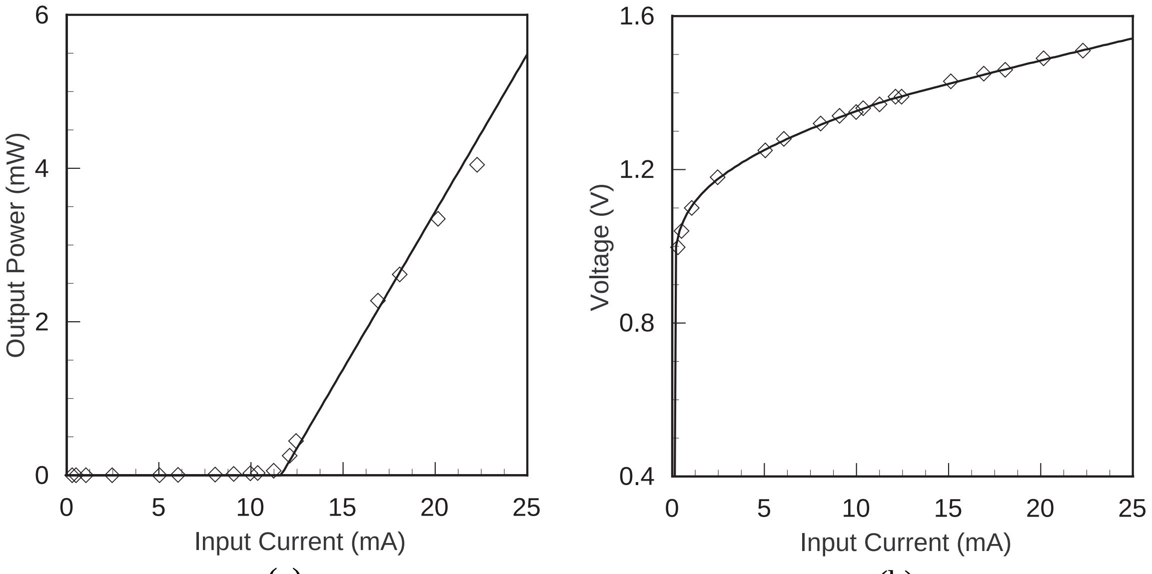

(a) (b)

Figure 2.15 Comparison of simulated (lines) and experimental (points) (a) LI and (b) IV data for the BH semiconductor laser.

our model to accurately match the measurements. However, despite these limitations, the model is still able to capture the general trends in the data, with the worst discrepancy corresponding to the modulation responses at resonance.

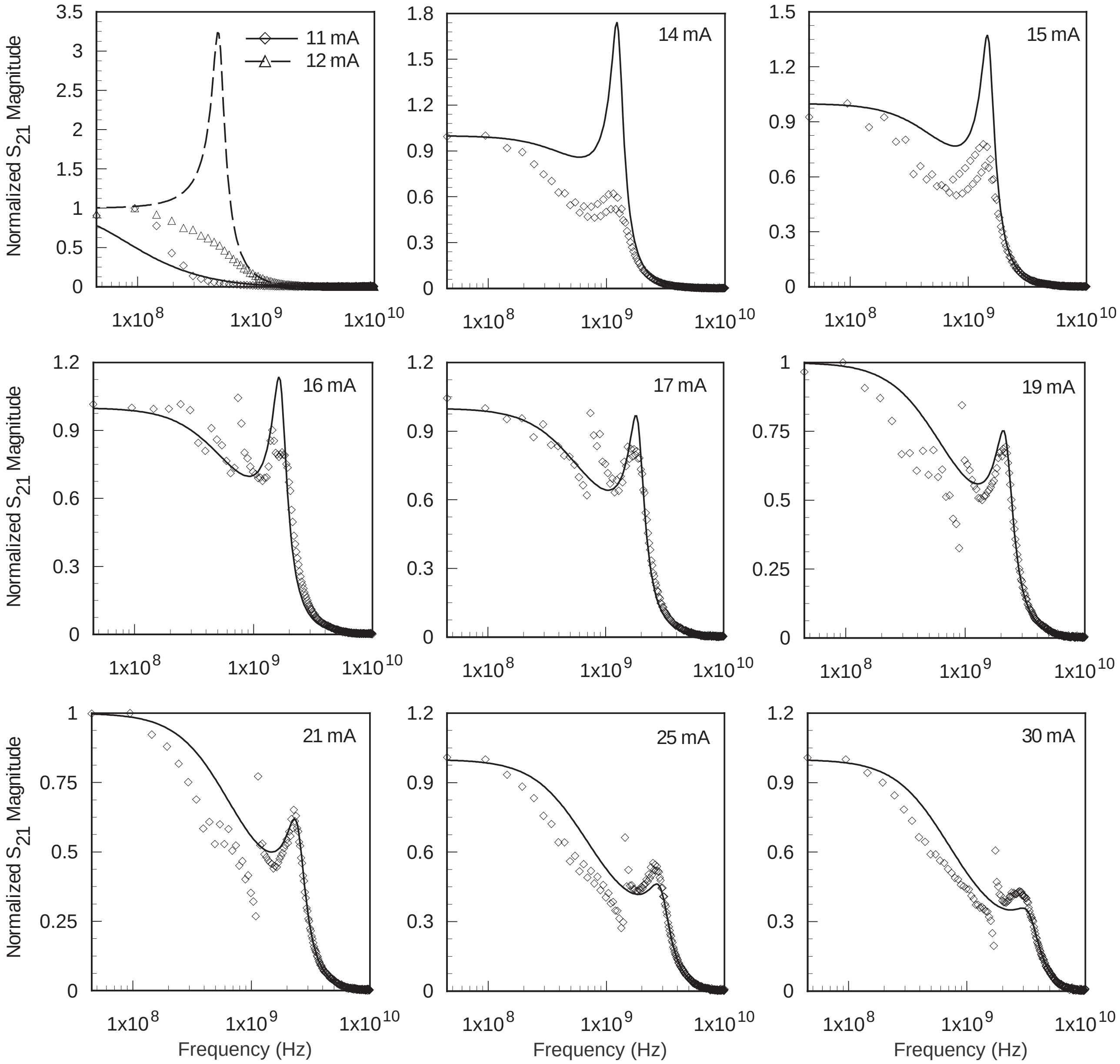

Figure 2.16 Comparison of simulated (lines) and experimental (points) S_{21} data for the BH laser.

2.6.4 DBR semiconductor laser

The second laser from which we extracted model parameters is a ridge-waveguide AlGaAs/GaAs/InGaAs edge-emitting laser with both DBR and cleaved-facet mirrors. As Fig. 2.17 shows, the device consists of $Al_{0.60}Ga_{0.40}As$ cladding layers, 800-Å GaAs SCH layers, and a 75-Å $In_{0.28}Ga_{0.72}As$ quantum well. The cavity length and ridge width were 500 and 4 μm, respectively. Again, we were provided with both dc and small-signal modulation data for this device.

As we did with the BH laser, we again utilized a modified equivalent circuit to account for parasitics. Figure 2.18 depicts the complete model, where we replaced the capacitance C_1 in Fig. 2.14 (p. 48) with a series combination of resistance R_1 and capacitance C_1. The addition of R_1 is required to help improve the fit of the modulation responses at frequencies just below resonance. Using this circuit, we completed the parameter extraction from the provided data and obtained the final set of intrinsic model parameters shown in Table 2.4. In addition, we used the following parameters for the parasitics: R_s = 0.225 Ω, R_{s2} = 26.69 Ω, I_{s1} = 1.518 mA, n_1 = 4.162, I_{s2} = 2.151 mA, n_2 = 3.598, R_1 =

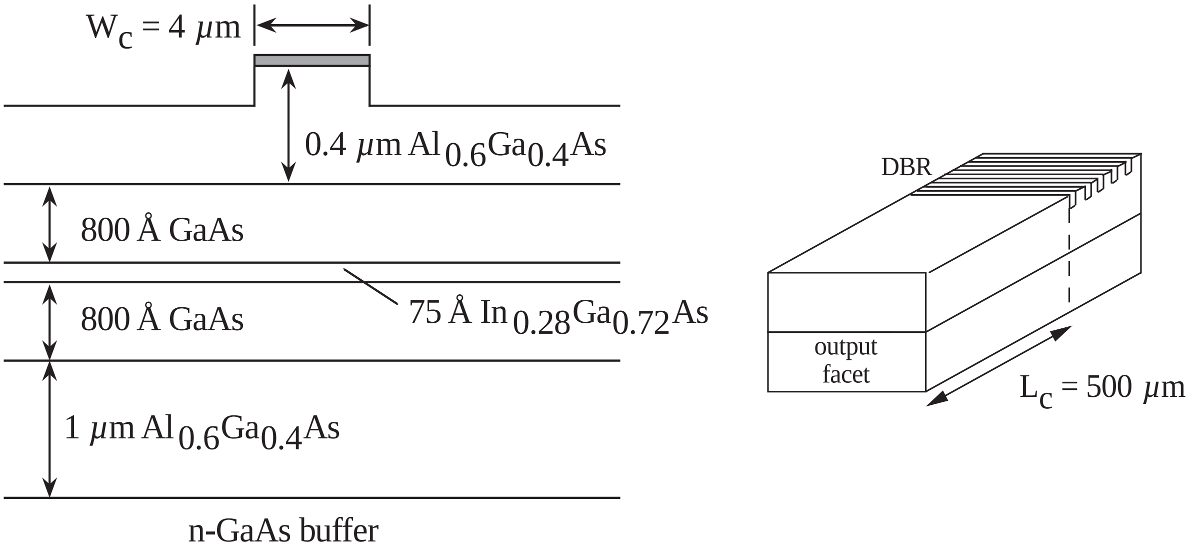

Figure 2.17 Device structure of the AlGaAs/GaAs/InGaAs DBR laser.

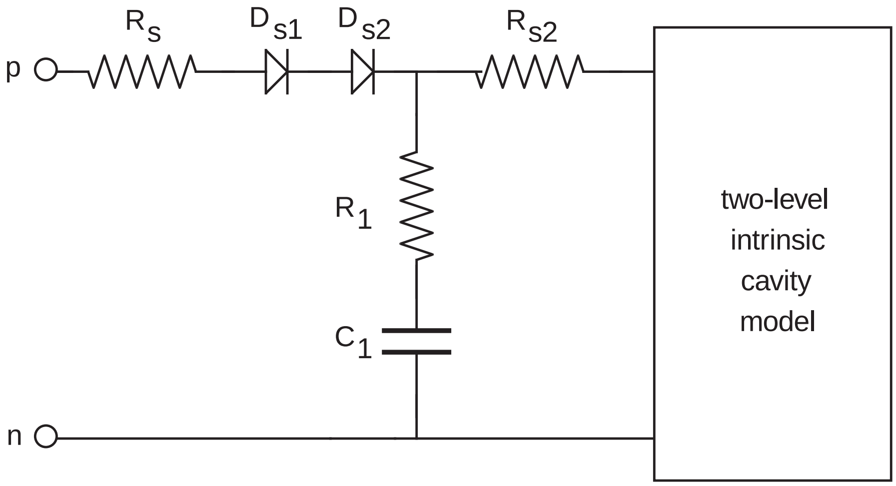

Figure 2.18 Complete QW-laser model used to fit the DBR laser.

Table 2.4 Extracted intrinsic model parameters for the DBR laser.

Parameter	Value
η_i	0.558
λ	1.016 μm
N_w	1
V_{act}	1.445×10^{-17} m^3
Γ_c	0.0301
v_{gr}	7.559×10^{7} m/s
τ_p	1.900 ps
η_c	0.720
N_o	1.12×10^{18} cm^{-3}
G_o	2709 cm^{-1}
ε	1.877×10^{-17} cm^3
A	1.048×10^{8} s^{-1}
B	1.811×10^{-10} cm^3/s
C	1.929×10^{-29} cm^6/s
A_b	4.661×10^{8} s^{-1}
B_b	4.625×10^{-10} cm^3/s
C_b	0.987×10^{-29} cm^6/s
β_A	0
β_B	1.391×10^{-5}
β_C	0
V_{barr}	1.126×10^{-16} m^3
τ_{capt}	13.27 ps
τ_{em}	8.244 ps
N_e	1.984×10^{8} cm^{-3}
n	2.041
N_{e2}	4.47×10^{9} cm^{-3}
n_{w2}	2

3.8 Ω, and C_1 = 20 pF.

Comparison of simulation and experiment reveals that parameter extraction for this device was slightly more successful than for the BH laser. Figures 2.19 compares the simulated and experimental LIV data, while Fig. 2.20 compares the simulated and experimental normalized modulation responses (S_{21}) at biases of 10-21 mA. As we can see, while the IV fit is excellent, the LI characteristic exhibits a noticeable mismatch in the threshold current and slope efficiency, especially near threshold. Furthermore, though not shown here, our model again cannot capture rollover in the LI data at currents above 35 mA. The simulated and measured modulation responses, on the other hand, show fairly good agreement across nearly the full range of bias currents, with the most noticeable discrepancy at 10 and 11 mA. Also, at the higher biases, the magnitude of the simulated resonance peak begins to deviate from the experimental value. In all likelihood, this error would continue to increase

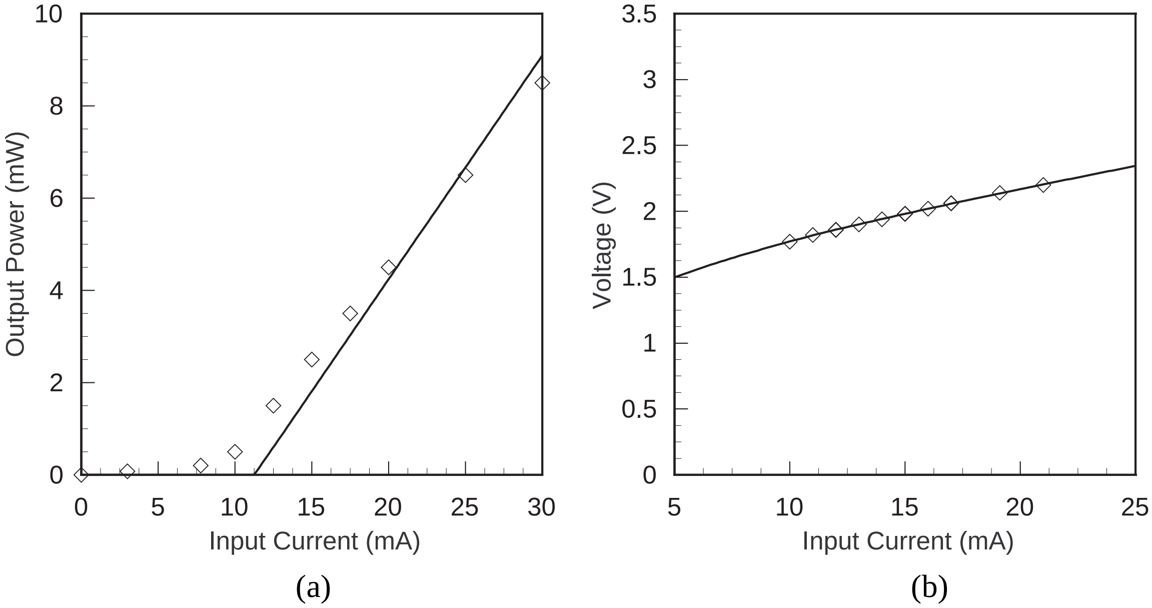

(a) (b)

Figure 2.19 Comparison of simulated (lines) and experimental (points) (a) LI and (b) IV data for the DBR laser.

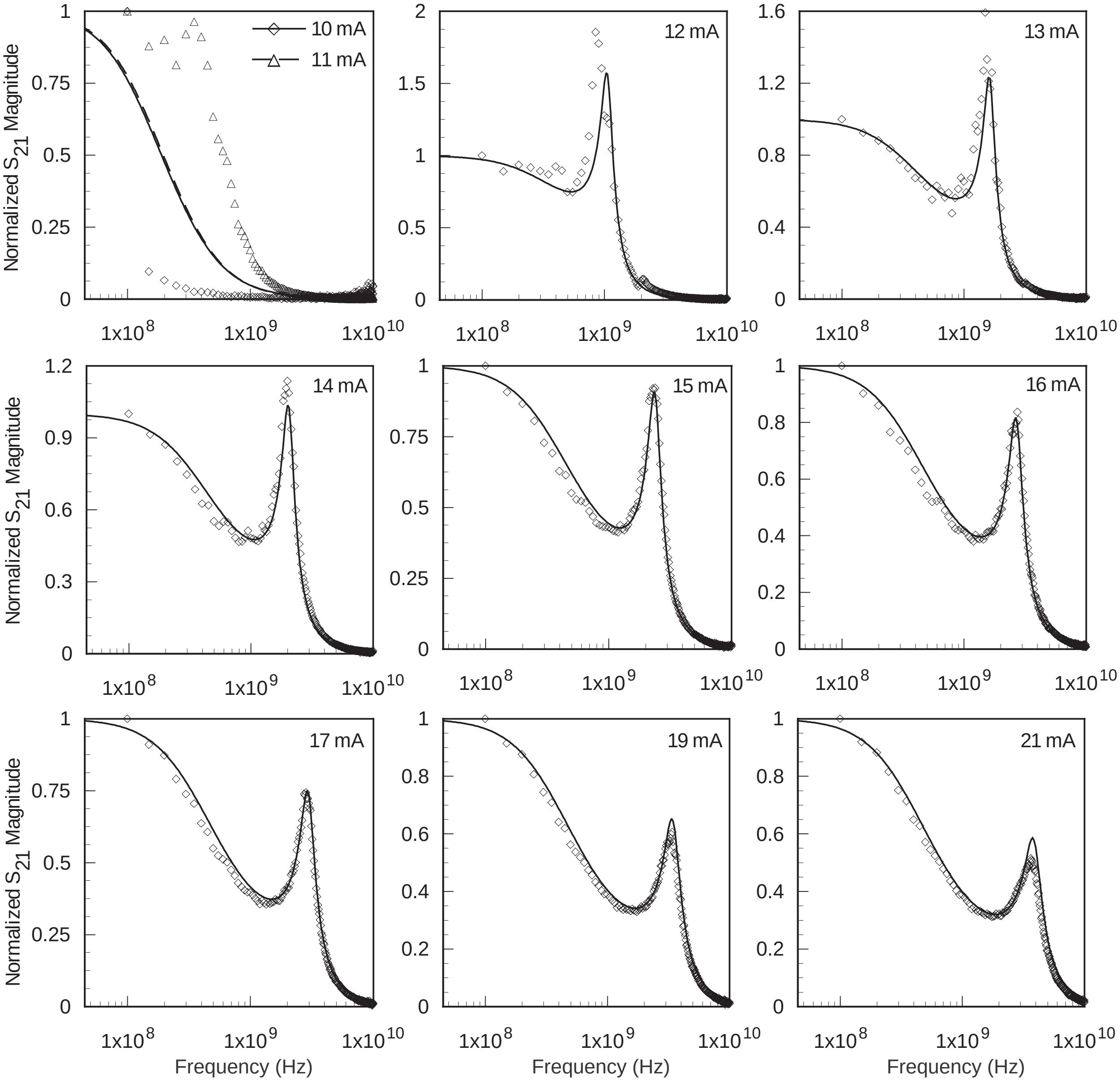

Figure 2.20 Comparison of simulated (lines) and experimental (points) S_{21} data for the DBR laser.

with bias, suggesting that the model parameters are applicable only over the range of operating conditions in the measured data. It should also be noted that while the normalized curves compare very well with each other, the exact curves would exhibit an additional error of roughly 20% due to the mismatch in the LI curves’ slope efficiencies. This highlights the need for an improved fit of the LI data. Another option is to scale η_c at the expense of introducing additional error into the power levels of the simulated LI curve.

2.6.5 Discussion

While we were able to obtain reasonable agreement between experimental and simulated device characteristics, it was not without some difficulty. First, as discussed before, it is critical that the initial estimate of the model parameters provides the numerical optimization process with a good starting point. Even so, we observed that a large number of attempts was necessary to obtain the final set of parameters for both the BH and DBR lasers. Furthermore, much of this process involved trial and error in an effort to coax the optimization routines into improving upon previous solutions.

Part of this problem is due to the difficulty of identifying an appropriate circuit representation of parasitic effects in a given device. Measurement of device impedance via experimental S_{11} characteristics would certainly help alleviate this difficulty, since the optical cavity can typically be approximated as a short circuit in this case [2.31]. Parasitics can then be extracted based on the device impedance values [2.31], allowing the model parameters specific to the rate equations to be extracted from LI and S_{21} data. The resulting reduction of fitting parameters generated during numerical optimization would certainly increase the chances of convergence to a final and accurate solution.

The biggest difficulty that we encountered, however, is the limited range of operating conditions over which the extracted model parameters reproduce experimental device characteristics. Obviously, the inclusion of S_{11} data would help provide additional constraints whereby an improved fit could be obtained during parameter optimization. However, abnormalities in the experimental data, such as the kinks seen in the BH laser's modulation response curves, would continue to hinder the extraction process, since our models are not capable of exhibiting this behavior; the same can be said of the rollover in the measured LI data. Furthermore, as the results for the DBR laser demonstrate, even for “normal” device characteristics, the correspondence between simulation and experiment eventually begins to break down, especially at the boundaries of the experimental data. This limited range of validity for a given set of extracted model parameters could be addressed by additional research into more robust rate-equation-based models which can not only accurately match a given set of experimental data, but also replicate device performance outside of the range of characterized operating conditions. In the absence of such improvements, however, a particular device should be fully characterized at least over its intended range of operation, thereby permitting our model to accurately represent it in simulation.

2.7 Conclusions

In this chapter, we showed that the rate-equation-based laser model with a linear gain-saturation term proposed in [2.6] has limitations in circuit simulation due to the persistence of multiple nonnegative solution regimes during nonnegative current injection. To address this issue, we applied rigorous analysis to demonstrate that one- and two-level rate-equation-based QW-laser models using gain-saturation terms as proposed by Channin and Agrawal do not suffer from this problem and do indeed have a unique nonnegative solution regime. In fact, it is possible to generalize the approach to any gain-saturation term of the form $(1+\varepsilon\Gamma_c S)^{-p}$ where $0 \leq p \leq 1$. After discussing the implementation of the models in SPICE, we then presented an overview of the method for including parasitic effects. Finally, we investigated the extraction of model parameters from experimental data, and presented results for two different edge-emitting semiconductor lasers. While simulation results exhibited reasonable agreement with experiment, they also demonstrated the need for continued investigation into the application of our models to actual devices.

2.8 References

[2.1] J. Katz, S. Margalit, C. Harder, D. Wilt, and A. Yariv, “The intrinsic electrical equivalent circuit of a laser diode,” *IEEE Journal of Quantum Electronics*, vol. QE-17, no. 1, pp. 4-7, 1981.

[2.2] R. S. Tucker, “Large-signal circuit model for simulation of injection-laser modulation dynamics,” *IEE Proceedings, Pt. I.*, vol. 128, no. 5, pp. 180-184, 1981.

[2.3] I. Habermayer, “Nonlinear circuit model for semiconductor lasers,” *Optical and Quantum Electronics*, vol. 13, pp. 461-468, 1981.

[2.4] S. C. Kan and K. Y. Lau, “Intrinsic equivalent circuit of quantum-well lasers,” *IEEE Photonics Technology Letters*, vol. 4, no. 6, pp. 528-530, 1992.

[2.5] M. F. Lu, J. S. Deng, C. Juang, M. J. Jou, and B. J. Lee, “Equivalent circuit model of quantum-well lasers,” *IEEE Journal of Quantum Electronics*, vol. 31, no. 8, pp. 1418-1422, 1995.

[2.6] S. A. Javro and S. M. Kang, “Transforming Tucker’s linearized laser rate equations to a form that has a single solution regime,” *Journal of Lightwave Technology*, vol. 13, no. 9, pp. 1899-1904, 1995.

[2.7] D. J. Channin, “Effect of gain saturation on injection laser switching,” *Journal of Applied Physics*, vol. 50, no. 6, pp. 3858-3860, 1979.

[2.8] G. P. Agrawal, “Effect of gain and index nonlinearities on single-mode dynamics in semiconductor lasers,” *IEEE Journal of Quantum Electronics*, vol. 26, no. 11, pp. 1901-1909, 1990.

[2.9] P. V. Mena, S. M. Kang, and T. A. DeTemple, “Rate-equation-based laser models with a single solution regime,” *Journal of Lightwave Technology*, vol. 15, no. 4, pp. 717-730, 1997.

[2.10] R. S. Tucker and D. J. Pope, “Circuit modeling of the effect of diffusion on damping in a narrow-stripe semiconductor laser,” *IEEE Journal of Quantum Electronics*, vol. 19, no. 7, pp. 1179-1183, 1983.

[2.11] H. J. A. da Silva, R. S. Fyath, and J. J. O’Reilly, “Sensitivity degradation with laser wavelength chirp for direct-detection optical receivers,” *IEE Proceedings, Pt. J*, vol. 136, no. 4, pp. 209-218, 1989.

[2.12] K. Hansen and A. Schlachetzki, “Transferred-electron device as a large-signal laser driver,” *IEEE Journal of Quantum Electronics*, vol. 27, no. 3, pp. 423-427, 1991.

[2.13] D. E. Dodds and M. J. Sieben, “Fabry-Perot laser diode modeling,” *IEEE Photonics Technology Letters*, vol. 7, no. 3, pp. 254-256, 1995.

[2.14] K. Y. Lau and A. Yariv, “High-frequency current modulation of semiconductor injection lasers,” in *Semiconductors and Semimetals*, W. T. Tsang, Ed., Vol. 22, Part B. Orlando: Academic Press, Inc., 1985.

[2.15] L. V. T. Nguyen, A. J. Lowery, P. C. R. Gurney, and D. Novak, “A time-domain model for high-speed quantum-well lasers including carrier transport effects,” *IEEE Journal of Selected Topics in Quantum Electronics*, vol. 1, no. 2, pp. 494-504, 1995.

[2.16] T. A. DeTemple and C. M. Herzinger, “On the semiconductor laser logarithmic gain-current density relation,” *IEEE Journal of Quantum Electronics*, vol. 29, no. 5, pp. 1246-1252, 1993.

[2.17] J. E. Bowers, “High speed semiconductor laser design and performance,” *Solid-State Electronics*, vol. 30, no. 1, pp. 1-11, 1987.

[2.18] D. McDonald and R. F. O’Dowd, “Comparison of two- and three-level rate equations in the modeling of quantum-well lasers,” *IEEE Journal of Quantum Electronics*, vol. 31, no. 11, pp. 1927-1934, 1995.

[2.19] R. Nagarajan, M. Ishikawa, T. Fukushima, R. S. Geels, and J. E. Bowers, “High speed quantum-well lasers and carrier transport effects,” *IEEE Journal of Quantum Electronics,* vol. 28, no. 10, pp. 1990-2008, 1992.

[2.20] W. Kaplan, *Advanced Calculus*, 3rd. edition. Reading, MA: Addison-Wesley Publishing Company, 1984.

[2.21] B. Johnson, T. Quarles, A. R. Newton, D. O. Pederson, and A. Sangiovanni-Vincentelli, *SPICE3 Version 3e User’s Manual*, University of California, Berkeley, 1991.

[2.22] W. Rideout, W. F. Sharfin, E. S. Koteles, M. O. Vassell, and B. Elman, “Well-barrier hole burning in quantum well lasers,” *IEEE Photonics Technology Letters*, vol. 3, no. 9, pp. 784-786, 1991.

[2.23] R. Nagarajan, T. Fukushima, S. W. Corzine, and J. E. Bowers, “Effects of carrier transport on high-speed quantum well lasers,” *Applied Physics Letters*, vol. 59, no. 15, pp. 1835-1837, 1991.

[2.24] J. J. Coleman, K. J. Beernink, and M. E. Givens, “Threshold current density in strained layer $In_xGa_{1-x}As$-GaAs quantum-well heterostructure lasers,” *IEEE Journal of Quantum Electronics*, vol. 28, no. 10, pp. 1983-1989, 1992.

[2.25] R. Nagarajan, T. Fukushima, M. Ishikawa, J. E. Bowers, R. S. Geels, and L. A. Coldren, “Transport limits in high-speed quantum-well lasers: Experiment and theory,” *IEEE Photonics Technology Letters*, vol. 4, no. 2, pp. 121-123, 1992.

[2.26] M. Ohkubo, T. Ijichi, A. Iketani, and T. Kikuta, “980-nm aluminum-free InGaAs/InGaAsP/InGaP GRIN-SCH SL-QW lasers,” *IEEE Journal of Quantum Electronics*, vol. 30, no. 2, pp. 408-414, 1994.

[2.27] S. Tiwari and J. M. Woodall, “Experimental comparison of strained quantum-wire and quantum-well laser characteristics,” *Applied Physics Letters*, vol. 64, no. 17, pp. 2211-2213, 1994.

[2.28] S. W. Corzine, R. H. Yan, and L. A. Coldren, “Theoretical gain in strained InGaAs/AlGaAs quantum wells including valence-band mixing effects,” *Applied Physics Letters*, vol. 57, no. 26, pp. 2835-2837, 1990.

[2.29] G. P. Agrawal and N. K. Dutta, *Semiconductor Lasers*, 2nd. edition. New York: Van Nostrand Reinhold, 1993.

[2.30] Ch. S. Harder, B. J. Van Zeghbroeck, M. P. Kesler, H. P. Meier, P. Vettiger, D. J. Webb, and P. Wolf, “High-speed GaAs/AlGaAs optoelectronic devices for computer applications,” *IBM Journal of Research and Development*, vol. 34, no. 4, pp. 568-584, 1990.

[2.31] K. Y. Lau and A. Yariv, “Ultra-high speed semiconductor lasers,” *IEEE Journal of Quantum Electronics*, vol. QE-21, no. 2, pp. 121-137, 1985.

[2.32] B. J. Thibeault, K. Bertilsson, E. R. Hegblom, E. Strzelecka, P. D. Floyd, R. Naone, and L. A. Coldren, “High-speed characteristics of low-optical loss oxide-apertured vertical-cavity lasers,” *IEEE Photonics Technology Letters,* vol. 9, no. 1, pp. 11-13, 1997.

[2.33] G. Massobrio and P. Antognetti, *Semiconductor Device Modeling with SPICE*, 2nd. ed. New York: McGraw-Hill, Inc., 1993.

[2.34] F. Delpiano, R. Paoletti, P. Audagnotto, and M. Puleo, “High frequency modeling and characterization of high performance DFB laser modules,” *IEEE Transactions on Components, Packaging, and Manufacturing Technology- Part B*, vol. 17, no. 3, pp. 412-417, 1994.

[2.35] S. Javro, Internal Report, University of Illinois at Urbana-Champaign, 1995.

[2.36] R. M. Lammert, J. S. Hughes, S. D. Roh, M. L. Osowski, A. M. Jones, and J. J. Coleman, “Low-threshold narrow-linewidth InGaAs-GaAs ridge-waveguide DBR lasers with first-order surface gratings,” *IEEE Photonics Technology Letters*, vol. 9, no. 2, pp. 149-151, 1997.

[2.37] C. Lawrence, J. L. Zhou, and A. L. Tits, “Users’ guide for CFSQP version 2.5: A C code for solving (large scale) constrained nonlinear (minimax) optimization problems, generating iterates satisfying all inequality constraints,” Institute for Systems Research, University of Maryland, Technical Report TR-94-16r1, 1997.

[2.38] J. Singh, “Electron and hole effective masses in lattice-matched and strained InGaAs”, in *Properties of Lattice-Matched and Strained Indium Gallium Arsenide*, P. B. Bhattacharya, Ed. London: INSPEC, 1993.

[2.39] S. L. Chuang, *Physics of Optoelectronic Devices*. New York: John Wiley & Sons, Inc., 1995.

[2.40] S. M. Sze, *Physics of Semiconductor Devices*, 2nd. ed. New York: John Wiley & Sons, Inc., 1981.

[2.41] B. Jogai, “Valence-band offset in strained GaAs-$In_xGa_{1-x}As$ superlattices,” *Applied Physics Letters*, vol. 59, no. 11, pp. 1329-1331, 1991.

[2.42] S. Adachi, “Heterojunctions of InGaAs and band offsets,” in *Properties of Lattice-Matched and Strained Indium Gallium Arsenide*, P. B. Bhattacharya, Ed. London: INSPEC, 1993.

[2.43] J. T. Verdeyen, *Laser Electronics*, 3rd. ed. Englewood Cliffs, NJ: Prentice Hall, 1995.

[2.44] S. Adachi, “GaAs, AlAs, and $Al_xGa_{1-x}As$: Material parameters for use in research and device applications,” *Journal of Applied Physics*, vol. 58, no. 3, pp. R1-R29, 1985.

[2.45] T. A. DeTemple, *EE388 Applications Software*, University of Illinois, 1994.

[2.46] R. Nagarajan, T. Fukushima, J. E. Bowers, R. S. Geels, and L. A. Coldren, “Single quantum well strained InGaAs/GaAs lasers with large modulation bandwidth and low damping,” *Electronics Letters*, vol. 27, no. 12, pp. 1058-1060, 1991.

[2.47] W. F. Sharfin, J. Schlafer, W. Rideout, B. Elman, R. B. Lauer, J. LaCourse, and F. D. Crawford, “Anomalously high damping in strained InGaAs-GaAs single quantum well lasers,” *IEEE Photonics Technology Letters*, vol. 3, no. 3, pp. 193-195, 1991.

[2.48] R. Nagarajan, T. Fukushima, S. W. Corzine, and J. E. Bowers, “Effects of carrier transport on high-speed quantum well lasers,” *Applied Physics Letters*, vol. 59, no. 15, pp. 1835-1837, 1991.

[2.49] K. Y. Lau, “Ultralow threshold quantum well lasers,” in *Quantum Well Lasers*, P. S. Zory, Jr., Ed. Boston: Academic Press, Inc., 1993.

[2.50] T. A. DeTemple (private communication), 1996.

[2.51] S. Hausser, G. Fuchs, A. Hangleiter, K. Streubel, and W. T. Tsang, “Auger recombination in bulk and quantum well InGaAs,” *Applied Physics Letters*, vol. 56, no. 10, pp. 913-915, 1990.

[2.52] K. Petermann, “Calculated spontaneous emission factor for double-heterostructure injection lasers with gain-induced waveguiding,” *IEEE Journal of Quantum Electronics*, vol. QE-15, no. 7, pp. 566-570, 1979.

[2.53] R. M. Lammert, D. V. Forbes, G. M. Smith, M. L. Osowski, and J. J. Coleman, “InGaAs-GaAs quantum-well lasers with monolithically integrated intracavity electroabsorption modulators by selective-area MOCVD,” *IEEE Photonics Technology Letters*, vol. 8, no. 1, pp. 78-80, 1996.

[2.54] C. A. Balanis, *Advanced Engineering Electromagnetics*. New York: John Wiley & Sons, Inc., 1989.

[2.55] H. Schneider and K. v. Klitzing, “Thermionic emission and Gaussian transport of holes in a GaAs/$Al_xGa_{1-x}As$ multiple-quantum-well structure,” *Physical Review B*, vol. 38, no. 9, pp. 6160-6165, 1988.

[2.56] L. Davis, Y. L. Lam, Y. C. Chen, J. Singh, and P. K. Bhattacharya, “Carrier capture and relaxation in narrow quantum wells,” *IEEE Journal of Quantum Electronics*, vol. 30, no. 11, pp. 2560-2564, 1994.

[2.57] M. Bruensteiner (private communication), 1997.

CHAPTER 3

A SIMPLE THERMAL VCSEL MODEL

3.1 Motivation

3.1.1 Vertical-cavity surface-emitting lasers

Rate-equation-based laser models such as those presented in Chapter 2 have traditionally been geared towards edge-emitting semiconductor lasers. However, in recent years a different type of semiconductor laser has attracted considerable interest, namely, the vertical-cavity surface-emitting laser (VCSEL). This device offers many advantages over edge-emitters, resulting in its growing popularity in the field of optoelectronics, including single-longitudinal-mode operation, circular output beams, suitability for monolithic two-dimensional integration, and compatibility with on-wafer probe testing [3.1].

Today's typical VCSEL has the general device structure illustrated in Fig. 3.1. As we can see, an optical cavity is formed along the device's growth direction, i.e., perpendicular to the plane of the wafer on which the VCSEL is grown. Distributed Bragg reflectors (DBR) form the cavity's mirrors, while the cavity itself is comprised of spacer layers and a QW-based active region. Depending on the specific device structure, the optical output can be taken from the top or bottom of the VCSEL. The many advantages of VCSELs can be related to this simple design. First, because the cavity length is typically very short, the correspondingly large mode spacing limits the optical output to a single longitudinal mode [3.1]. Second, a VCSEL's planarity allows symmetric transverse cross sections, thereby resulting in circular output beams [3.1], [3.2]. This feature, a significant improvement over the elliptical beams exhibited by edge-emitters [3.2], is particularly attractive since it improves cou-

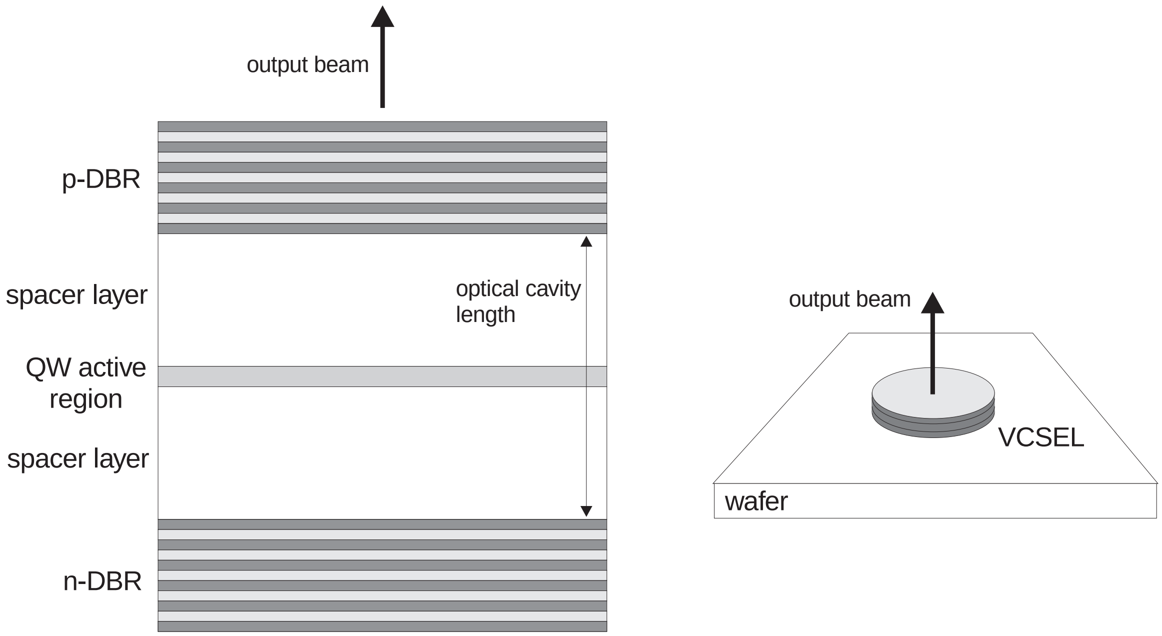

(a) (b)

Figure 3.1 Illustration of a generic VCSEL structure: (a) cross-section, (b) wafer-level view.

pling of the optical output to a fiber [3.3]. Planarity also results in other important advantages, including support for on-wafer probe testing, two-dimensional integration of VCSEL arrays [3.1], and the ability to limit device area to a particular spot size [3.3]. Finally, because of their small volume, VCSELs should ultimately have relatively high modulation bandwidths [3.4].

One of the first VCSELs reported in the literature was a GaInAsP/InP design from Soda *et al.* [3.5], which did not yet include DBR mirrors. Since then, the past two decades have seen a remarkable level of progress in VCSEL designs. Current devices can be broadly classified into four categories [3.2], [3.4]: etched-mesa, buried-heterostructure (BH), proton-implanted, and oxide-confined VCSELs. Figure 3.2 illustrates examples of each of these designs [3.2], [3.4].

In the etched-mesa, or air-post, VCSEL of Fig. 3.2(a), optical confinement is provided via

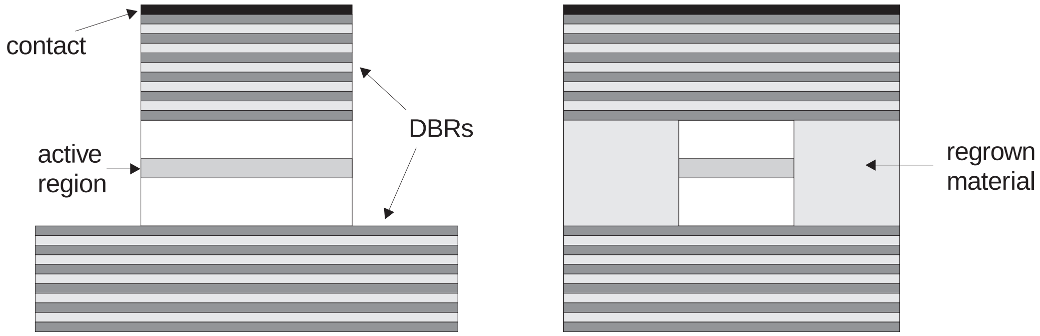

(a) Etched-Mesa VCSEL

(b) Buried-Heterostructure VCSEL

(c) Proton-Implanted VCSEL

(d) Oxide-Confined VCSEL

Figure 3.2 Typical VCSEL structures.

index-guiding from the semiconductor-air interface. The mesa is sometimes surrounded by polyimide [3.6] in order to facilitate electrical contact and testing [3.7]. While etched-mesa VCSELs have been studied extensively in the literature [3.6], [3.8], they possess a number of disadvantages. In particular, side-wall surface recombination and poor heat dissipation [3.2] both place limits on the device performance.

Buried-heterostructure VCSELs, such as the one depicted in Fig. 3.2(b), are alternative index-guided devices which possess a number of attractive features, particularly carrier and optical confinement in the same laser [3.4]. While BH designs have been reported [3.1], [3.9], they continue to enjoy limited success due to various fabrication issues, specifically regarding epitaxial regrowth [3.4].

Another common VCSEL design is the proton-implanted structure of Fig. 3.2(c). Unlike the index-guided etched-mesa and BH lasers, proton-implanted VCSELs' optical waveguiding is due to gain-guiding and thermal lensing [3.2], [3.4], with the implant providing current confinement [3.2] to maximize current flow through the center of the active region. Proton-implanted VCSELs with thresholds on the order of a few mA have been reported [3.10]-[3.11]. Despite their popularity, these devices, as noted above, can exhibit thermal lensing effects [3.2] due to the lack of index-guiding. Consequently, in some cases the threshold current during pulsed operation can actually exceed the cw value [3.12].

Finally, the oxide-confined VCSEL depicted in Fig. 3.2(d) has been the focus of a great deal of research in recent years [3.2]. Selective oxidation of a semiconductor layer near the active region results in a dielectric aperture which yields index guiding and current confinement [3.2]. These devices have exhibited some of the best VCSEL performance to date, including sub-mA threshold currents and modulation rates as high as 20 GHz [3.13]-[3.15].

Various efforts have been made to optimize the basic VCSEL structures described above. For example, placement of the active-layer quantum wells at the peak values of the cavity's standing-wave pattern can result in an increased longitudinal confinement factor, and therefore improved gain [3.16]. This "periodic gain structure" has also been used to improve the generation of femtosecond pulses in mode-locked VCSELs [3.17]. Another improvement has been the introduction of wafer fusion, whereby semiconductor layers from different material systems can be bonded together [3.18]. One obvious advantage of this approach is the ability to use AlGaAs DBRs in conjunction with a long-wavelength InGaAsP active layer [3.18]; corresponding InGaAsP-based mirrors would require a significantly larger number of layers and therefore result in higher device resistance [3.7].

Despite the obvious advantages of VCSELs over edge-emitters, they are not without their drawbacks. In fact, they exhibit a number of undesirable features which, while present in edge-emitters, are considerably more pronounced in VCSELs. The most recognized limitation of a VCSEL's performance is its thermal behavior. Due to their poor heat dissipation and the large resistance introduced by their DBRs [3.19], typical VCSELs undergo relatively severe heating, and consequently can exhibit strong thermally dependent behavior. For example, as noted above, thermal lensing in gain-guided devices can yield considerable differences between cw and pulsed operation, as well as alter the emission profile of the laser's optical modes [3.12]. The most important effect, however, is exhibited in a VCSEL's static LI characteristics. First, analogous to edge-emitters, VCSELs exhibit temperature-dependent threshold current. Second, because device temperature increases with injection current, the output power eventually rolls over and begins to decrease, thereby limiting a device's maximum cw output [3.12].

Another problem with VCSELs is spatial effects, including multitransverse mode operation and transverse variation of the active-layer carrier distribution. For example, multimode operation is possible due to the existence of higher-order transverse modes [3.20]. Carrier diffusion and spatial hole burning can also be a factor, further limiting a VCSEL's performance by contributing to mode competition [3.21] and secondary pulsations in the turn-off transient [3.22].

In an effort to reduce the role of temperature and spatial mechanisms on a VCSEL's operating characteristics, many researchers have proposed novel device designs. Because the temperature dependence of the threshold current is due largely to the thermal shift of the gain peak relative to the emission wavelength, Young *et al.* [3.6], [3.23] proposed a gain-offset VCSEL in which the gain is deliberately blue-shifted relative to the emission wavelength at room temperature. As the temperature increases, the gain peak actually aligns with the emission wavelength, thereby allowing the laser gain to remain relatively constant over a larger range of temperatures. Another solution to the thermal problem involves the use of junction grading in the DBRs [3.2]; the subsequent reduction in series resistance leads to lower heat dissipation. Alternatively, the series resistance, at least in one of the mirrors, can be avoided altogether via the use of intracavity-contacted VCSELs [3.24]. Multimode effects, meanwhile, have been addressed in a variety of ways. For example, spatial filtering [3.25] and inclusion of antiguiding layers [3.26] have both been proposed as methods for extending the range of single-mode operation in VCSELs. Unfortunately, while all of the above efforts have certainly been successful in improving the state-of-the-art in VCSEL design, undesirable thermal and spatial behavior continues to play an important role in VCSEL operation.

3.1.2 The need for a simple thermal VCSEL model

Clearly, in order to effectively design optoelectronic applications incorporating VCSELs, appropriate models are required which account for thermal and spatial effects. While we present a comprehensive model of this behavior in the next chapter, here we will consider VCSEL models which can model the major thermal effects, namely the LI characteristics' temperature-dependent threshold current and output-power rollover identified above. The majority of such models to date have been largely numerical in nature, making use of detailed multidimensional analysis for the description of VCSEL thermal behavior. For example, Nakwaski and Osinski have developed extensive two-dimensional models of thermal heating [3.27], while other researchers have incorporated finite-element analysis of thermal effects into their comprehensive VCSEL simulations [3.28]-[3.30]. While these models are accurate, they are also computationally intensive. As discussed in Chapter 1, this feature makes them unattractive for the computer-aided design of optoelectronic systems, which are typically composed of many photonic and electronic components. For example, multichannel optical links [3.31] and smart pixel systems [3.32] require 1- and 2-D VCSEL arrays. Furthermore, system design often requires a large number of simulations for design optimization and verification. For example, the design of drive circuitry for a VCSEL may require many iterations to determine optimal transistor topology and sizing. These cases clearly require less-complicated VCSEL models.

Models have been developed which can be used to simulate the static LI characteristics without resorting to complicated multidimensional analysis. S. F. Yu *et al.* utilized a thermal rate equation in conjunction with device-parameter temperature dependencies to augment a rate equation description of VCSELs [3.33]. Similarly, Y. Su *et al.* implemented a simplified static model which also makes use of temperature-dependent model parameters [3.34]. However, these models still require a description of the thermally dependent mechanisms in the VCSEL, such as the gain. Even though these models are applicable to circuit-level simulation, we are primarily interested in a simpler approach to modeling the effects of temperature on the dc operating characteristics. Unfortunately, while simpler models of a more empirical nature have been applied to LI characteristics at individual ambient temperatures [3.19],[3.35], they are limited to dc simulation. Thus, to the best of our knowledge, there exists a need for an extremely simple thermal VCSEL model which, in addition to modeling basic laser behavior under dc, small-signal, and transient operation, can inherently describe static LI characteristics over a range of ambient temperatures without resorting to detailed descriptions of the thermal physics. Such models would significantly simplify the optoelectronic system-design process.

In this chapter, we present such a VCSEL model [3.36] based on the standard laser rate equations. By introducing a thermally dependent offset current into these equations, we are able to model in a simple manner the temperature-dependent threshold current and output power roll-over at different ambient temperatures, while retaining the ability to simulate ac and transient behavior as well. After discussing in Section 3.2 the basis for our model and its implementation in conventional SPICE-like simulators, we present in Section 3.3 comparisons of simulation to measured data for three devices reported in the literature. Final conclusions are presented in Section 3.4.

3.2 Model Development

3.2.1 Thermal physics

The strong thermal dependence of VCSELs can be attributed to a number of mechanisms. While Auger recombination [3.37] and optical losses such as intervalence band absorption [3.38] can play a role in the thermal behavior, the majority of effects during static, or cw, operation are due to the temperature-dependent laser gain and carrier leakage out of the active region.

First, as its temperature increases, a VCSEL’s gain spectrum broadens and its peak location shifts to longer wavelengths. The device’s emission wavelength also increases with temperature, though considerably less than the gain peak [3.39]. Consequently, depending on the initial location of the gain peak relative to the wavelength, the laser gain will either decrease or increase with temperature as the gain peak and wavelength become more or less mismatched [3.39]. In fact, an optimal value of temperature should exist in which the mismatch is eliminated to achieve a minimum threshold gain, as has been observed experimentally [3.39].

Second, thermal leakage of carriers out of the active region can lead to a reduction of injection efficiency, which contributes to a VCSEL’s thermal roll-over [3.8]. As the device temperature rises, the position of the active-layer’s Fermi levels increases relative to the bandgap. Consequently, the active-layer becomes increasingly incapable of confining carriers. The resulting leakage can be modeled as a function of carrier density and temperature [3.8]. Because of the carrier-density dependence, spatial hole burning can result in further reduction of the injection efficiency [3.8].

All of these mechanisms affect the static LI characteristics by essentially making a VCSEL's differential efficiency and threshold current functions of temperature and carrier density. Thus, we could model a VCSEL's above-threshold LI curves using $P_o = \eta(T)(I - I_{th}(N,T))$, where P_o is the optical output power, I is the injection current, $\eta(T)$ is the temperature-dependent differential slope efficiency, and $I_{th}(N,T)$ is the threshold current as a function of carrier number N and temperature T [3.8]. To simplify this expression, we first assume that the slope efficiency's temperature dependence has a minimal impact on the output [3.28]. Furthermore, by neglecting the effects of spatial hole burning [3.34], we can assume that the threshold current is solely a function of temperature. Thus, we can describe LI curves over a range of ambient temperatures using a constant slope efficiency and a temperature-dependent threshold current [3.12]. This approach is analogous to the one taken in modeling edge-emitters, where the threshold current is proportional to $\exp(T/T_o)$ and T_o is the characteristic temperature [3.7]. In the case of VCSELs, the temperature dependence not only results in the non-monotonic thermal dependence of the threshold current, but also in the output-power rollover at elevated temperatures.

We could account for this dependence by describing key VCSEL parameters themselves as functions of temperature, in particular the laser gain [3.33],[3.40]. However, this approach requires a description of the thermal physics in the device. Because we want a simple model which avoids such details, we instead opt to partition the thermal threshold current into a constant value of threshold current I_{tho} plus an empirical thermal offset current $I_{off}(T)$ [3.41]. This results in the expression

$$P_o = \eta(I - I_{tho} - I_{off}(T)) \tag{3.1}$$

For simplicity, we choose to model the offset current using a polynomial function of temperature. Initially, a quadratic expression seemed appropriate [3.41], but we soon realized that higher-order terms were necessary. Thus, we use

$$I_{off}(T) = a_0 + a_1 T + a_2 T^2 + a_3 T^3 + a_4 T^4 \tag{3.2}$$

where the coefficients a_0-a_4 can be determined during parameter extraction. All static thermal effects are now accounted for via the offset current, thereby circumventing the need for a more detailed approach. Because (3.2) is not exclusively an increasing function of temperature, it should be able to capture both the general temperature dependence of a VCSEL's threshold current and the rollover in the LI characteristics.

3.2.2 Rate-equation-based model with a thermal offset current

Certainly, (3.1) and (3.2) could be used to directly simulate a VCSEL's LI characteristics, an approach that essentially amounts to a simple curve fit. However, like earlier empirical models [3.19], [3.35] which only focus on dc behavior, this approach would not permit small-signal and transient simulation of VCSELs, critical elements of optoelectronic system design. Fortunately, it is well known that the simple above-threshold LI curve described by $P_o = \eta(I - I_{th})$ can be implemented using the standard laser rate equations [3.7]. Thus, by introducing the offset current into these rate equations through an empirical fit to experimental data, we will be able to model LI curves at different temperatures as well as take advantage of many of the desirable properties of the rate equations, in particular the ability to model non-dc behavior such as small-signal modulation. The modified rate equations are

$$\frac{dN}{dt} = \frac{\eta_i(I - I_{off}(T))}{q} - \frac{N}{\tau_n} - \frac{G_o(N - N_o)S}{1 + \varepsilon S} \tag{3.3}$$

$$\frac{dS}{dt} = -\frac{S}{\tau_p} + \frac{\beta N}{\tau_n} + \frac{G_o(N - N_o)S}{1 + \varepsilon S} \tag{3.4}$$

where S is the photon number, η_i is the injection efficiency, τ_n is the carrier recombination lifetime, G_o is the gain coefficient, N_o is the carrier transparency number, τ_p is the photon lifetime, β is the spontaneous emission coupling coefficient, and ε is the gain-compression factor. The optical output power can be described using $P_o = kS$ [3.41], where k is a scaling factor accounting for the output-power coupling efficiency of the VCSEL. These equations, along with (3.2), comprise the bulk of our model. As we shall see shortly, despite its simplicity, the introduction of the offset current into (3.3) is an extremely effective means for including the thermal dependence of a VCSEL's LI characteristics. However, we still need expressions for the temperature and current-voltage characteristics of the device. Equations (3.5)-(3.6) below accomplish this task.

First, while it is certainly possible to adopt detailed numerical representations of the VCSEL temperature profile as a function of the heat dissipation throughout the device [3.42], a much simpler method is to describe the temperature via a thermal rate equation which accounts for the transient temperature increase as a result of heat dissipation [3.33], [3.37]. Following this approach, we use

$$T = T_o + (IV - P_o)R_{th} - \tau_{th}\frac{dT}{dt} \tag{3.5}$$

where R_{th} is the VCSEL's thermal impedance, τ_{th} is a thermal time constant, T_o is the ambient temperature, and V is the laser voltage. Under dc conditions, the dT/dt term disappears; thus, from the resulting equation it is clear that $(IV - P_o)$ models the power dissipated in the VCSEL, where we assume that any power not carried in the optical output is dissipated as heat in the device. The thermal time constant is necessary to account for the nonzero response time of the device temperature, and has been observed to be on the order of 1 μs [3.12].

The current-voltage (IV) relationship, meanwhile, can be modeled in great detail based on the diode-like character of the VCSEL. However, for simplicity we have elected to represent the voltage across the device as an arbitrary empirical function of current and temperature using

$$V = f(I, T) \tag{3.6}$$

By introducing a capacitor [3.41] or other parasitic components in parallel with this voltage, we can account for the complete electrical characteristics of the VCSEL. The advantage of this approach is that the specific form of (3.6) can be determined on a device-by-device basis. For example, in some cases, a relationship which accounts for a resistance in series with a diode may be most appropriate [3.41], such as

$$V = IR_s + V_T \ln\left(1 + \frac{I}{I_s}\right) \tag{3.7}$$

where R_s is the series resistance, V_T is the diode's thermal voltage, and I_s is the diode's saturation current. In other cases, a polynomial function of current and temperature [3.8] such as

$$V = (b_0 + b_1 T + b_2 T^2 + \ldots) \cdot (c_0 + c_1 I + c_2 I^2 + \ldots) \tag{3.8}$$

may work better, where b_0-b_2 and c_0-c_2 are constants. If we use experimental IV data to help determine all of the other model parameters first, then the exact form of (3.6) can be determined at the very end of parameter extraction for a specific device. Thus, this simplified approach not only allows the voltage's current and temperature dependence to be accurately modeled, but also permits the optical and electrical device characteristics to be largely decoupled from one another, thereby simplifying the extraction of model parameter values from experimental data. Note that in the presence of parasitics, (3.5) should be modified such that it depends on the total device current, not *I*.

3.2.3 Model implementations

Because one of our goals was to be able to use our model in the computer-aided design of optoelectronic systems, we have implemented (3.2)-(3.6) in a number of SPICE-like simulators, including HSPICE [3.43] and Analogy's SABER [3.44]. As desired, this approach permits VCSELs to be simulated in conjunction with electronic components, such as laser drivers, and other optoelectronic devices for which circuit-level models already exist. Below we discuss each implementation.

The HSPICE implementation relies on transformation of the model equations into an equivalent subcircuit representation as described in [3.45] and [3.46]. First, in order to improve the convergence properties of the model during simulation, we transformed P_o into a new variable v_m via $P_o = (v_m + \delta)^2$, and N into v_n via $N = z_n v_n$ [3.41], where δ and z_n are arbitrary constants. Because of the nonlinear character and multiple solution regimes of the rate equations, such transformations help the simulator converge to a correct numerical solution [3.45], as discussed in Chapter 2. After substituting these transformations into (3.2)-(3.6) and applying appropriate manipulations, we obtained the equivalent circuit illustrated in Fig. 3.3, where *pd* and *nd* are the electrical terminals of the VCSEL,

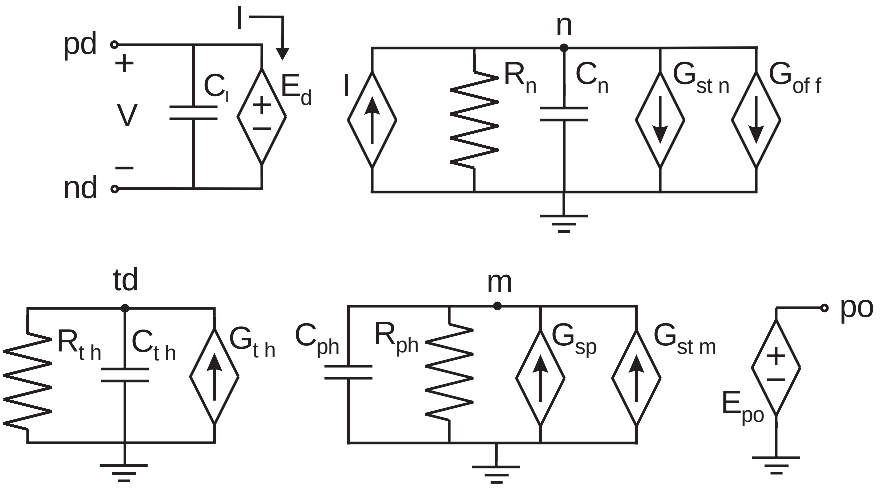

Figure 3.3 Equivalent-circuit representation of the simple thermal VCSEL model.

po is the terminal whose node voltage models the output power P_o, and *td* is the terminal which models the device temperature *T*. Electrical characteristics are modeled via the nonlinear voltage source E_d, which implements (3.6), and the capacitor C_l, which models a simple parasitic shunting capacitance. Other parasitics can be added as necessary. The temperature equation (3.5) is modeled via the resistance R_{th}, the capacitor $C_{th} = \tau_{th}/R_{th}$, and the nonlinear current source G_{th} where [3.37]

$$G_{th} = \frac{T_o}{R_{th}} + [I_{tot}V - P_o] \tag{3.9}$$

and $I_{tot} = I + I_{Cl}$ is the total VCSEL current, with I_{Cl} accounting for current through C_l. The capacitor $C_n = qz_n/\eta_i$, resistor $R_n = \eta_i\tau_n/(qz_n)$, and nonlinear current sources G_{stn} and G_{off} implement the carrier rate equation (3.3), where

$$G_{stn} = \frac{qG_o}{\eta_i k}\frac{(z_n v_n - N_o)(v_m + \delta)^2}{1 + \frac{\varepsilon}{k}(v_m + \delta)^2} \tag{3.10}$$

and G_{off} models the offset current from (3.2). Meanwhile, the capacitor $C_{ph} = 2\tau_p$, resistor $R_{ph} = 1$, and current sources G_{sp} and G_{stm} implement the photon rate equation (3.4), where

$$G_{sp} = \frac{\tau_p \beta k z_n v_n}{\tau_n(v_m + \delta)} \tag{3.11}$$

$$G_{stm} = \frac{G_o \tau_p (z_n v_n - N_o)(v_m + \delta)}{1 + \frac{\varepsilon}{k}(v_m + \delta)^2} - \delta \tag{3.12}$$

Finally, E_{po} transforms v_m into the output power P_o. Figure 3.4 illustrates the HSPICE netlist which implements the equivalent circuit of Fig. 3.3, where we have used a polynomial function of current and temperature for (3.6). Additional details on this implementation can be found in Appendix C.

As noted above, we also implemented our model in Analogy's SABER, a circuit- and system-level simulation tool. Much like HSPICE, SABER supports netlist representations of equivalent circuit models; it uses MAST, a robust behavioral modeling language. We could easily implement the equivalent circuit of Fig. 3.3 into a netlist representation in MAST where, as we just saw, the model equations must be translated into an equivalent circuit notation. A distinct advantage of MAST, however, is that it allows the user to circumvent such a translation. Consequently, the implementation of

```
.SUBCKT las_statictherm  pd nd po td  etai=1 beta=8.98e-4 tn=5e-9
+                                     k=1.165e-8 go=1e4 no=1e7 tp=1e-12
+                                     rth=2000 a0=0 a1=0 a2=0 a3=0 a4=0
+                                    zn=1e8 delta=5e-10 eps=0 tth=1e-6 claser=1e-12
+                                     q=1.60219e-19 kb=1.38062e-23

* electrical representation of laser (V as a fn. of I and T)
ed   pd nd VOL=’(2.298+366.2*i(ed)- 6.097e4*i(ed)*i(ed)+           \\
                 6.76e6*i(ed)*i(ed)*i(ed))*                        \\
                (0.829-1.007e-3*v(td)+6.594e-6*v(td)*v(td)-        \\
                 2.18e-8*v(td)*v(td)*v(td))’
cl   pd nc claser
vcr  nc nd 0

* temperature circuit: v(td) = junction temperature
rth td 0 ’rth’
cth td 0 ’tth/rth’
gth 0 td CUR=’temper/rth + ((i(ed)+i(vcr))*v(pd,nd)-(v(m)+delta)*(v(m)+delta))’

* carrier number circuit (N=zn*v(n)), incl. thermal offset current (goff)
gn   0 n CUR=’i(ed)’
cn   n 0  ’q*zn/etai’
rn   n 0  ’etai*tn/(q*zn)’
gstn n 0  CUR=’(q*go/(etai*k))*(zn*v(n)-no)*(v(m)+delta)*(v(m)+delta)/   \\
                (1+eps*(v(m)+delta)*(v(m)+delta)/k)’
goff n 0  CUR=’a0 + a1*v(td) + a2*v(td)*v(td) +                      \\
                a3*v(td)*v(td)*v(td) + a4*v(td)*v(td)*v(td)*v(td)’

* photon circuit...
cph  m 0 ’2*tp’
rph  m 0 1
gsp  0 m CUR=’tp*beta*k*zn*v(n)/(tn*(v(m)+delta))’
gstm 0 m CUR=’go*tp*(zn*v(n)-no)*(v(m)+delta)/(1+eps*(v(m)+delta)*    \\
              (v(m)+delta)/k)-delta’

* optical output
epo po 0 VOL=’(v(m)+delta)*(v(m)+delta)’

.ENDS las_statictherm
```

Figure 3.4   HSPICE-subcircuit implementation of Fig. 3.3.

circuit-level models in SABER is considerably more straightforward than in HSPICE.

Figure 3.5 illustrates the MAST template that implements our simple thermal VCSEL model. As we can see, the template consists of a header and a body section. In the header, the model parameters and terminals are defined. The body section, on the other hand, is comprised of local variable definitions, intermediate value definitions, and the main model equations. As we can see, we again transformed P_o and N into the variables v_m and v_n using $P_o = (v_m + \delta)^2$ and $N = z_n v_n$. Upon substituting these transformations into (3.3) and (3.4), we obtained the equations for `vn` and `vm` seen in the template. Also, note that the voltage characteristic (3.6) is implemented via `vpn`, where we have again used a polynomial function of current and temperature. Additional details on this SABER implementation can be found in Appendix C.

3.3 Comparison to Experiment

In order to use our model, we must be able to perform parameter extraction from measured data. If we substitute (3.5) into (3.1) under dc conditions, we obtain the expression

$$P_o = \eta[I - I_{tho} - I_{off}(T_o + (IV - P_o)R_{th})] \tag{3.13}$$

Using experimental LI and IV curves, we can use (3.13) to determine good initial values for η, R_{th}, and the coefficients a_0-a_4 that will replicate the experimental LI data at various ambient temperatures T_o. This approach allows the thermal effects to be extracted without any knowledge of the thermal physics at work in the device. The complete set of model parameters can then be determined via additional parameter optimization based on the measured VCSEL operating characteristics, including, if available, experimental small-signal modulation responses. Finally, the empirical expression (3.6) can be determined to describe the experimental IV data. Below we discuss the application of our model to

```
element template las_statictherm  pd nd po = etai, beta, tn, k, go, no, tp, rth,
                                              a0, a1, a2, a3, a4, zn, delta,
                                              eps, tth, claser
electrical pd, nd, po              # pins (electrical- pd,nd; optical- po)
number etai = 1,                   # argument defaults
       beta = 8.98e-4,
       tn = 5e-9,
       k = 1.165e-8,
       go = 1e4,
       no = 1e7,
       tp = 1e-12,
       rth = 2000,
       a0 = 0, a1 = 0, a2 = 0, a3 = 0, a4 = 0,
       zn = 1e8, delta = 5e-10,
       eps = 0,
       tth = 1e-6,
       claser = 1e-12
external number temp             # simulation temperature

{
branch ipn = i(pd->nd), vpn = v(pd,nd)    # cavity branch vars.
branch ipnc = i(pd->nd), vpnc = v(pd,nd)  # capacitor branch vars.
var tc tjct             # junction temperature
var i iinj              # net injection current
val i ioff              # thermal offset current
var v vn                # internal voltage related to carriers
var v vm                # internal voltage related to photons
var i ipo               # current from output node po

# local variables and constants
number kb = 1.38062e-23,
       q  = 1.60219e-19

# define ioff as a function of junction temperature...
ioff  = a0 + a1*tjct + a2*tjct*tjct + a3*tjct*tjct*tjct + a4*tjct*tjct*tjct*tjct

# electrical representation of laser diode (V as a fn. of I and T)
vpn = (2.298 + 366.2*ipn - 6.097e4*ipn**2 + 6.76e6*ipn**3)*           \
      (0.829 - 1.007e-3*tjct + 6.594e-6*tjct**2 - 2.18e-8*tjct**3)
ipnc = d_by_dt(claser*vpnc)

# transformed rate equations (simple n-vn relat’n, quadratic photon transform)
# as well as relations for net injection current and junction temperature
tjct: tjct  = ((ipn+ipnc)*vpn - v(po))*rth + temp - d_by_dt(tth*tjct)
iinj: iinj = ipn - ioff
vn: vn = etai*tn*iinj/(q*zn) - d_by_dt(tn*vn) -                       \
         tn*go*(vn-no/zn)*(vm+delta)*(vm+delta)/k/(1+eps*v(po)/k)
vm: vm = -delta - d_by_dt(2*tp*vm) + tp*k*beta*zn*vn/(tn*(vm+delta)) +   \
         tp*go*(zn*vn-no)*(vm+delta)/(1+eps*v(po)/k)

# optical output
i(po) += ipo
ipo: v(po) = (vm+delta)*(vm+delta)
}
```

Figure 3.5 MAST-template implementation of the simple thermal VCSEL model.

three different devices reported in the literature. As in Chapter 2, parameter optimization was performed using CFSQP [3.47]. As the results will demonstrate, our model is capable of simulating the thermally dependent threshold current and output power rollover of actual VCSELs.

3.3.1 AlGaAs-based VCSEL

The first device is an 863-nm bottom-emitting VCSEL with a 16-μm diameter, as reported by Ohiso *et al.* [3.48]. The device, grown on an $Al_{0.1}Ga_{0.9}As$ substrate, includes a Si-doped $Al_{0.15}Ga_{0.85}As$-AlAs, GaAs-$Al_{0.2}Ga_{0.8}As$ n-type DBR, six quantum wells, and a C-doped $Al_{0.15}Ga_{0.85}As$-$Al_{0.5}Ga_{0.5}As$-AlAs p-type DBR. In addition to presenting a family of LI curves over a 110 °C range of ambient temperatures, the authors also provide a room-temperature IV characteristic. We fit this device data using the following set of model parameters: $\eta_i = 1$, $\beta = 10^{-6}$, $\tau_n = 5$ ns, $k = 2.6 \times 10^{-8}$ W, $G_o = 1.6 \times 10^4$ s^{-1}, $N_o = 1.94 \times 10^7$, $\tau_p = 2.28$ ps, $R_{th} = 2.6$ °C/mW, $a_0 = 1.246 \times 10^{-3}$ A, $a_1 = -2.545 \times 10^{-5}$ A/K, $a_2 = 2.908 \times 10^{-7}$ A/K^2, $a_3 = -2.531 \times 10^{-10}$ A/K^3, and $a_4 = 1.022 \times 10^{-12}$ A/K^4, where we have neglected gain saturation. Furthermore, for simplicity we fit the IV data using a polynomial function of current:

$$\begin{aligned} V = {} & 1.721 + 275I - 2.439 \times 10^4 I^2 + 1.338 \times 10^6 I^3 \\ & - 4.154 \times 10^7 I^4 + 6.683 \times 10^8 I^5 - 4.296 \times 10^9 I^6 \end{aligned} \tag{3.14}$$

As illustrated in Fig. 3.6, the simulation results generated with these parameters are in excellent agreement with experiment across nearly the full range of reported ambient temperatures, 20-130 °C. To the best of our knowledge, this level of agreement is as good as or better than any reported in the literature, including numerical models. One of the only potential drawbacks of our results is the thermal-impedance value that we used, 2.6 °C/mW. Based on the reported temperature increase of 24 °C for an approximate operating point of 6 mA, 2.73 V, and 1.175 mW output power, the actual device thermal impedance is probably closer to 1.6 °C/mW. In all likelihood, the discrepancy arises out of the assumption that carrier-density-dependent effects such as spatial hole burning can be neglected. Nonetheless, despite this assumption, the results are excellent.

3.3.2 Selectively-oxidized VCSEL

The next device is an AlGaInP-based 683-nm selectively-oxidized VCSEL with a 3 μm × 3 μm area, reported in [3.49] and [3.50] by Crawford *et al*. This device consists of compressively-strained InGaP quantum wells, AlGaInP barrier and cladding layers, and AlGaAs graded DBRs. The authors provide both LI and IV curves over a 60 °C range of ambient temperatures.

We fit the model of (3.2)-(3.6) to the experimental device data, this time using the following polynomial function to model the IV data as a function of current *and* temperature [3.8]:

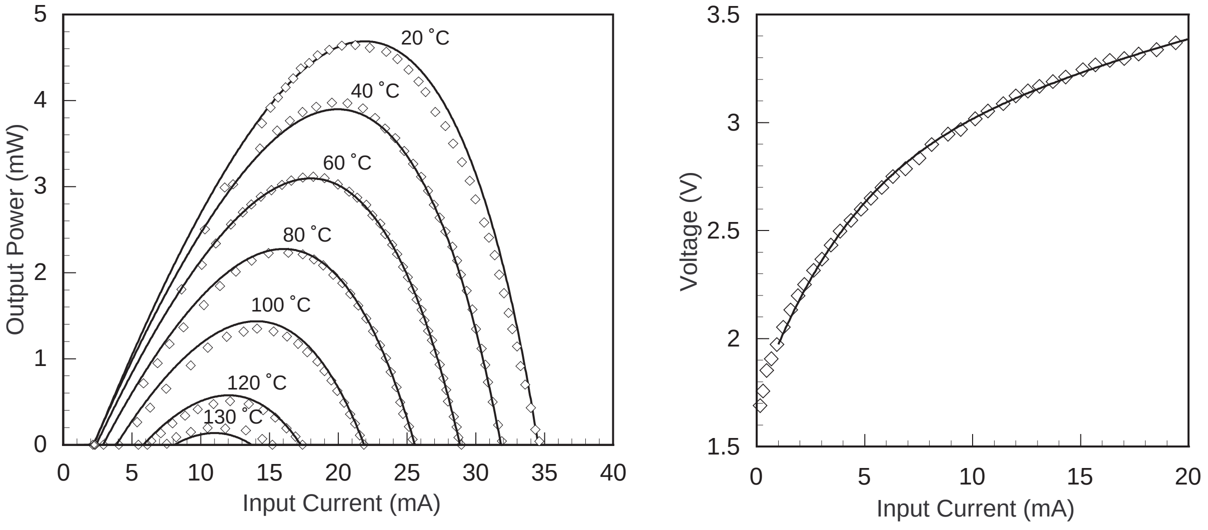

(a) (b)

Figure 3.6 Comparison of measured (data points) and simulated (lines) operating characteristics for the bottom-emitting 863-nm VCSEL [3.48]. (a) LI curves at ambient temperatures of 20-130 ºC. (b) Room-temperature IV curve.

$$V = (0.829 - 1.007 \times 10^{-3} T + 6.594 \times 10^{-6} T^2 - 2.18 \times 10^{-8} T^3) \\ \cdot (2.298 + 366.2 I - 6.097 \times 10^4 I^2 + 6.76 \times 10^6 I^3) \tag{3.15}$$

The remaining model parameters are $\eta_i = 1$, $\beta = 10^{-6}$, $\tau_n = 5$ ns, $k = 2.6 \times 10^{-8}$ W, $G_o = 1.6 \times 10^4$ s^{-1}, $N_o = 1.654 \times 10^7$, $\tau_p = 2.064$ ps, $R_{th} = 9.8$ ºC/mW, $a_0 = -2.734 \times 10^{-4}$ A, $a_1 = -2.125 \times 10^{-5}$ A/K, $a_2 = 1.837 \times 10^{-7}$ A/K^2, $a_3 = 3.183 \times 10^{-10}$ A/K^3, and $a_4 = 0$ A/K^4. We again neglected gain saturation. Note that because the LI data is fit via the parameters I_{tho} and η, there are not enough constraints within the data to uniquely determine all of the model parameters. Consequently, many of the values are the same as those generated for the Ohiso device.

Comparison of the simulated and experimental LI and IV curves is illustrated in Fig. 3.7. Our model shows excellent agreement in the ambient temperature range 25-60 °C. However, at higher ambient temperatures the simulated temperature effects are more pronounced than what the data suggests. In fact, the model was not able to match additional data at 85 °C; experimental measurements showed that the device lased at this temperature, while our model could not. The discrepancy at these

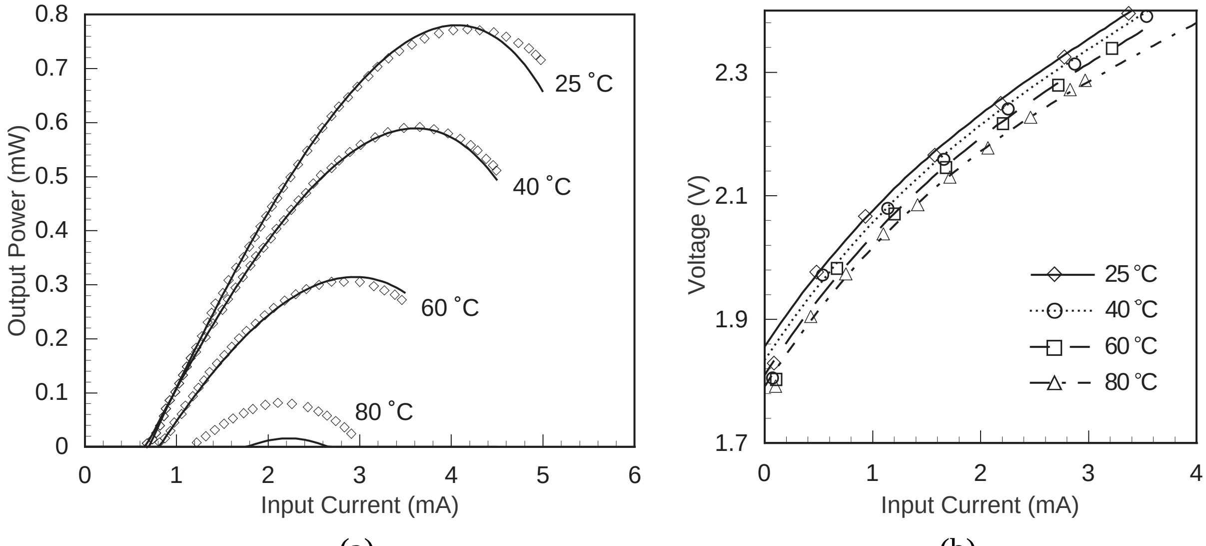

(a) (b)

Figure 3.7 Comparison of measured (data points) and simulated (lines) (a) LI and (b) IV curves for an AlGaInP-based 683-nm VCSEL [3.49] at ambient temperatures of 25-80 °C.

higher ambient temperatures is most likely due to the omission of carrier-density-dependent effects in the model, as was the case with the earlier AlGaAs-based VCSEL. This is further evidenced by the high value of thermal impedance generated during parameter optimization, 9.8 °C/mW. This high value is necessary to compensate for the absence of other physical mechanisms in the model that would augment thermal effects. In fact, we found that for this device, a single expression for the offset current as a function of temperature was not sufficient to model the temperature effects at all of the reported ambient temperatures. Again, this suggests the need for additional mechanisms in the model which contribute to the thermal behavior without being fully temperature-dependent themselves. Despite these limitations, however, we again observe that our model can be used as an accurate representation of the device over a useful range of operation.

3.3.3 Thin-oxide-apertured VCSEL

The last device is a 3.1-μm diameter thin-oxide-apertured VCSEL reported by Thibeault *et al.* [3.13]. The laser is composed of an $Al_{0.9}Ga_{0.1}As$-GaAs p-type DBR, three $In_{0.17}Ga_{0.83}As$-GaAs quantum wells, an $Al_{0.3}Ga_{0.7}As$ cavity, and an AlAs-GaAs n-type DBR. The authors present a single LI curve at a temperature of 23 ºC, as well as a plot of wall-plug efficiency, from which we determined IV data. Although LI data for only one ambient temperature are shown, they clearly exhibit output power rollover at high currents. In addition, modulation responses (S_{21}) at five bias currents and a temperature of 22 ºC are reported. Thus, this device provides us with an opportunity to verify both the dc and small-signal capabilities of our model.

As with the first two devices, we were able to extract the following parameters from the provided data: $\eta_i = 0.821$, $\beta = 2.68 \times 10^{-2}$, $\tau_n = 1.201$ ns, $k = 4.166 \times 10^{-8}$ W, $G_o = 8.486 \times 10^{5}$ s^{-1}, $N_0 = 1.286 \times 10^{6}$, $\tau_p = 2.884$ ps, $\varepsilon = 3.888 \times 10^{-6}$, $R_{th} = 0.896$ ºC/mW, $a_0 = 2.213 \times 10^{-3}$ A, $a_1 = -1.719 \times$

10^{-4} A/K, $a_2 = 3.355 \times 10^{-6}$ A/K^2, $a_3 = 0$ A/K^3, and $a_4 = 0$ A/K^4. Meanwhile, the IV data at 23 ºC was fit using the following simple diode-like relationship:

$$V = 149.8I + 0.9366\ln\left(1 + \frac{I}{7.918 \times 10^{-5}}\right) \tag{3.16}$$

Because parasitic capacitance was considered to be a key limitation to the high-speed performance of this particular device [3.13], we also included a 351-fF capacitor at the input of our model as depicted in Fig. 3.3. Figures 3.8 and 3.9 illustrate the results of fitting our model to the experimental data.

As expected, Fig. 3.8 shows excellent agreement between the simulated and experimental LIV data, with the thermal rollover near 6 mA clearly captured in simulation. Fig. 3.9 presents a comparison between experimental and simulated S_{21} data at bias currents of 0.5, 0.7, 1.0, 1.3, and 2.1 mA and a temperature of 22 °C. The simulation results were normalized at a low-frequency value of 10 MHz. We did not normalize at dc for two reasons. First, in all likelihood, the experimental data was normalized at a low-frequency value not equal to dc. Second, the thermal time constant in (3.5) introduces a

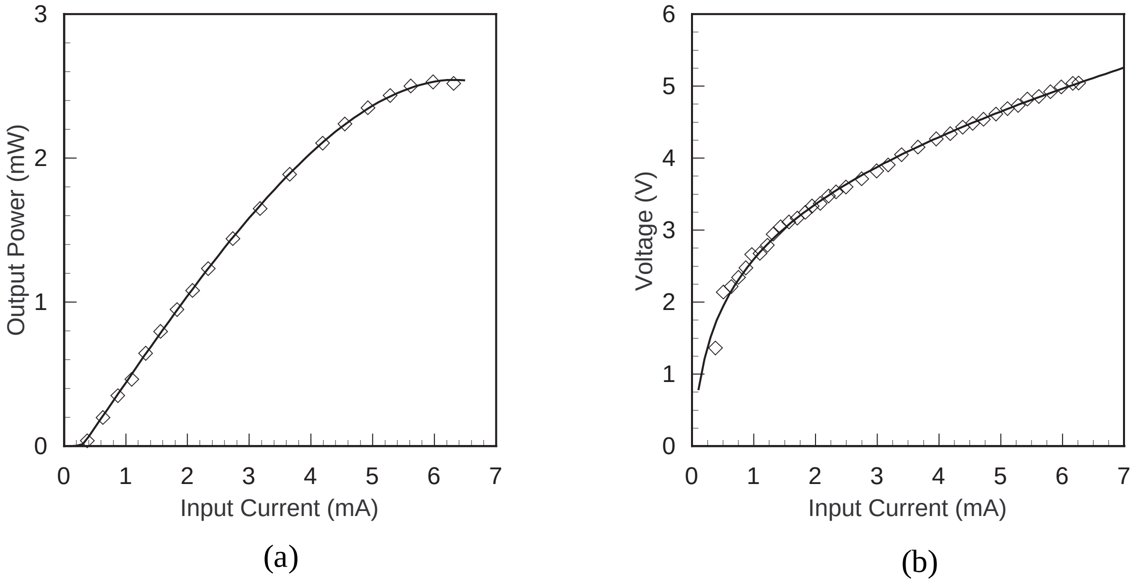

Figure 3.8 Comparison of measured (data points) and simulated (lines) (a) LI and (b) IV curves for an oxide-apertured VCSEL [3.13] at 23 °C.

thermal cutoff at a frequency of roughly $1/(2\pi\tau_{th})$, above which the device temperature no longer responds to the modulation. Consequently, our simulations exhibited a ~5% change in the "dc" modulation response at the thermal cutoff frequency. Since there was no way to identify a similar dip in the measured data, we elected to normalize our simulations at 10 MHz.

As can be seen, there is good agreement between both sets of curves, including the values for the resonance frequencies, with the main discrepancies arising in the magnitude of the resonance peaks themselves. The results would still be reasonable even if we were to account for the ~5% change in the simulated modulation responses at the thermal cutoff frequency. The next chapter will present a more comprehensive model which improves upon the results of Fig. 3.9. Nevertheless, the results are good given the simplicity of the rate equations used. Furthermore, they indicate that our approach allows thermal effects to be included in an extremely simple manner without sacrificing the ability to simulate VCSELs under various regimes of operation, features which, as pointed out before, are very useful in the design and simulation of optoelectronic systems. It should be noted that at cur-

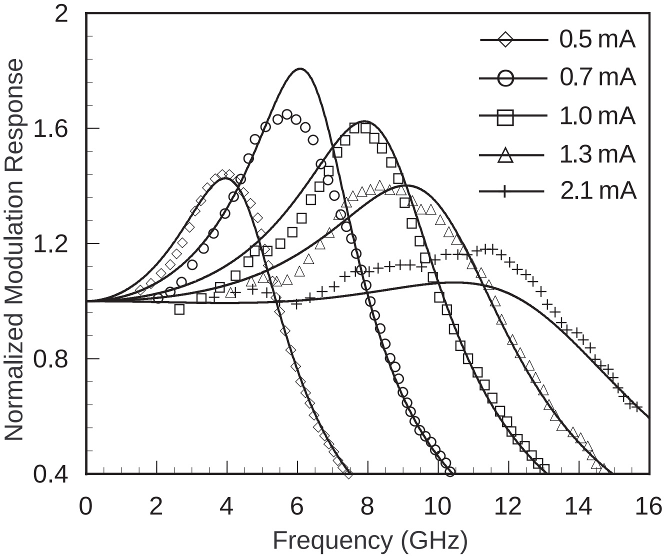

Figure 3.9 Comparison of measured (data points) and simulated (lines) S_{21} curves for the device of Fig. 3.8 at 22 °C.

rents near or beyond rollover, the absence of true thermal-dependent mechanisms such as gain may limit the ability of the model to accurately simulate small-signal and transient behavior. Typically, however, a VCSEL will be operated at currents below the rollover point. In this case, our model can be used to simulate the thermal limits of a device under dc operation, as well as non-dc behavior under more typical operating conditions.

3.4 Conclusions

In this chapter, we have presented a simple rate-equation-based model of VCSEL thermal LI characteristics which utilizes an offset current to account for thermal effects. This model was implemented in two SPICE-like simulators, HSPICE and SABER. As we have seen, the model exhibits good agreement with experiment. Furthermore, we were able to show using a thin-oxide-apertured VCSEL that our model is capable of simulating VCSELs under non-dc operating regimes. Some discrepancies do exist, however, between the simulated and experimental results. In fitting the bottom-emitting device of Fig. 3.6, we obtained a thermal impedance which was larger than the estimated value. Furthermore, for the selectively-oxidized laser of Fig. 3.7, we saw that the model over-predicts thermal effects at higher temperatures. In all likelihood, these errors are due to the assumptions that spatial hole burning can be neglected and that the slope efficiency is constant, the former being the predominant factor. In cases where this issue is critical, the model can be made more comprehensive by including thermally dependent gain [3.40], using a leakage current as a function of carrier number and temperature [3.8], and introducing spatial hole burning effects [3.8]. Such additions should also improve the non-dc capabilities of the model. In the next chapter, we will present a model which incorporates these improvements. However, even without any modifications, we have shown that the introduction of a thermal offset current into the standard rate equations provides an effective means for modeling experimental results without introducing excessive levels of complexity.

3.5 References

[3.1] K. Iga, F. Koyama, and S. Kinoshita, “Surface emitting semiconductor lasers,” *IEEE Journal of Quantum Electronics*, vol. 24, no. 9, pp. 1845-1855, 1988.

[3.2] W. W. Chow, K. D. Choquette, M. H. Crawford, K. L. Lear, and G. R. Hadley, “Design, fabrication, and performance of infrared and visible vertical-cavity surface-emitting lasers,” *IEEE Journal of Quantum Electronics*, vol. 33, no. 10, pp. 1810-1824, 1997.

[3.3] R. S. Geels, S. W. Corzine, and L. A. Coldren, “InGaAs vertical-cavity surface-emitting lasers,” *IEEE Journal of Quantum Electronics*, vol. 27, no. 6, pp. 1359-1367, 1991.

[3.4] L. A. Coldren, E. Hegblom, E. Strzelecka, J. Ko, Y. Akulova, and B. Thibeault, “Recent advances and important issues in vertical-cavity lasers,” in *Proceedings of SPIE*, vol. 3003, 1997, pp. 2-13.

[3.5] H. Soda, K. Iga, C. Kitahara, and Y. Suematsu, “GaInAsP/InP surface emitting injection lasers,” *Japanese Journal of Applied Physics*, vol. 18, no. 12, pp. 2329-2330, 1979.

[3.6] D. B. Young, J. W. Scott, F. H. Peters, M. G. Peters, M. L. Majewski, B. J. Thibeault, S. W. Corzine, and L. A. Coldren, “Enhanced performance of offset-gain high-barrier vertical-cavity surface-emitting lasers,” *IEEE Journal of Quantum Electronics*, vol. 29, no. 6, pp. 2013-2022, 1993.

[3.7] G. P. Agrawal and N. K. Dutta, *Semiconductor Lasers*, 2nd ed. New York: Van Nostrand Reinhold, 1993.

[3.8] J. W. Scott, R. S. Geels, S. W. Corzine, and L. A. Coldren, “Modeling temperature effects and spatial hole burning to optimize vertical-cavity surface-emitting laser performance,” *IEEE Journal of Quantum Electronics*, vol. 29, no. 5, pp. 1295-1308, 1993.

[3.9] A. Ibaraki, K. Furusawa, T. Ishikawa, K. Yodoshi, T. Yamaguchi, and T. Niina, “GaAs buried heterostructure vertical cavity top-surface emitting lasers,” *IEEE Journal of Quantum Electronics*, vol. 27, no. 6, pp. 1386-1390, 1991.

[3.10] R. A. Morgan, M. K. Hibbs-Brenner, T. M. Marta, R. A. Walterson, S. Bounnak, E. L. Kalweit, and J. A. Lehman, “200 ºC, 96-nm wavelength range, continuous-wave lasing from unbonded GaAs MOVPE-grown vertical cavity surface-emitting lasers,” *IEEE Photonics Technology Letters*, vol. 7, no. 5, pp. 441-443, 1995.

[3.11] M. K. Hibbs-Brenner, R. A. Morgan, R. A. Walterson, J. A. Lehman, E. L. Kalweit, S. Bounnak, T. Marta, and R. Gieske, “Performance, uniformity, and yield of 850-nm VCSEL’s deposited by MOVPE,” *IEEE Photonics Technology Letters*, vol. 8, no. 1, pp. 7-9, 1996.

[3.12] G. Hasnain, K. Tai, L. Yang, Y. H. Wang, R. J. Fischer, J. D. Wynn, B. Weir, N. K. Dutta, and A. Y. Cho, “Performance of gain-guided surface emitting lasers with semiconductor distributed Bragg reflectors,” *IEEE Journal of Quantum Electronics*, vol. 27, no. 6, pp. 1377-1385, 1991.

[3.13] B. J. Thibeault, K. Bertilsson, E. R. Hegblom, E. Strzelecka, P. D. Floyd, R. Naone, and L. A. Coldren, “High-speed characteristics of low-optical loss oxide-apertured vertical-cavity lasers,” *IEEE Photonics Technology Letters*, vol. 9, no. 1, pp. 11-13, 1997.

[3.14] D. G. Deppe, D. L. Huffaker, T. Oh, H. Deng, and Q. Deng, “Low-threshold vertical-cavity surface-emitting lasers based on oxide-confinement and high contrast distributed Bragg reflectors,” *IEEE Journal of Selected Topics in Quantum Electronics*, vol. 3, no. 3, pp. 893-904, 1997.

[3.15] K. L. Lear, M. Ochiai, V. M. Hietala, H. Q. Hou, B. E. Hammons, J. J. Banas, and J. A. Nevers, “High-speed vertical cavity surface emitting lasers,” in *1997 Digest of the LEOS Summer Topical Meetings- Vertical-Cavity Lasers*, 1997, pp. 53-54.

[3.16] S. W. Corzine, R. S. Geels, J. W. Scott, R.-H. Yan, and L. A. Coldren, “Design of Fabry-Perot surface-emitting lasers with a periodic gain structure,” *IEEE Journal of Quantum Electronics*, vol. 25, no. 6, pp. 1513-1524, 1989.

[3.17] W. Jiang, M. Shimizu, R. P. Mirin, T. E. Reynolds, and J. E. Bowers, “Femtosecond periodic gain vertical-cavity lasers,” *IEEE Photonics Technology Letters*, vol. 5, no. 1, pp. 23-25, 1993.

[3.18] D. I. Babic, J. Piprek, K. Streubel, R. P. Mirin, N. M. Margalit, D. E. Mars, J. E. Bowers, and E. L. Hu, “Design and analysis of double-fused 1.55-μm vertical-cavity lasers,” *IEEE Journal of Quantum Electronics*, vol. 33, no. 8, pp. 1369-1383, 1997.

[3.19] T. E. Sale, J. S. Roberts, J. P. R. David, R. Grey, J. Woodhead, and P. N. Robson, “Temperature effects in VCSELs,” in *Proceedings of SPIE*, vol. 3003, 1997, pp. 100-110.

[3.20] C. J. Chang-Hasnain, J. P. Harbison, G. Hasnain, A. C. Von Lehmen, L. T. Florez, and N. G. Stoffel, “Dynamic, polarization, and transverse mode characteristics of vertical cavity surface emitting lasers,” *IEEE Journal of Quantum Electronics*, vol. 27, no. 6, pp. 1402- 1409, 1991.

[3.21] A. Valle, J. Sarma, and K. A. Shore, “Spatial holeburning effects on the dynamics of vertical cavity surface-emitting laser diodes,” *IEEE Journal of Quantum Electronics*, vol. 31, no. 8, pp. 1423-1431, 1995.

[3.22] A. Valle, J. Sarma, and K. A. Shore, “Secondary pulsations driven by spatial hole burning in modulated vertical-cavity surface-emitting laser diodes,” *Journal of the Optical Society of America, Pt. B,* vol. 12, no. 9, pp. 1741-1746, 1995.

[3.23] D. B. Young, J. W. Scott, F. H. Peters, B. J. Thibeault, S. W. Corzine, M. G. Peters, S.-L. Lee, and L. A. Coldren, “High-power temperature-insensitive gain-offset InGaAs/GaAs vertical-cavity surface-emitting lasers,” *IEEE Photonics Technology Letters*, vol. 5, no. 2, pp. 129-132, 1993.

[3.24] J. W. Scott, B. J. Thibeault, D. B. Young, L. A. Coldren, and F. H. Peters, “High efficiency submilliamp vertical cavity lasers with intracavity contacts,” *IEEE Photonics Technology Letters*, vol. 6, no. 6, pp. 678-680, 1994.

[3.25] R. A. Morgan, G. D. Guth, M. W. Focht, M. T. Asom, K. Kojima, L. E. Rogers, and S. E. Callis, “Transverse mode control of vertical-cavity top-surface-emitting lasers,” *IEEE Photonics Technology Letters*, vol. 4, no. 4, pp. 374-377, 1993.

[3.26] B.-S. Yoo, H. Y. Chu, H.-H. Park, H. G. Lee, and J. Lee, “Transverse mode characteristics of vertical-cavity surface-emitting lasers buried in amorphous GaAs antiguide layer,” *IEEE Journal of Quantum Electronics*, vol. 33, no. 10, pp. 1794-1800, 1997.

[3.27] W. Nakwaski and M. Osinski, “Self-consistent thermal-electrical modeling of proton-implanted top-surface-emitting semiconductor lasers,” in *Proceedings of SPIE*, vol. 2146, 1994, pp. 365-387.

[3.28] R. Michalzik and K. J. Ebeling, “Modeling and design of proton-implanted ultralow-threshold vertical-cavity laser diodes,” *IEEE Journal of Quantum Electronics*, vol. 29, no. 6, pp. 1963-1974, 1993.

[3.29] G. R. Hadley, K. L. Lear, M. E. Warren, K. D. Choquette, J. W. Scott, and S. W. Corzine, “Comprehensive numerical modeling of vertical-cavity surface-emitting lasers,” *IEEE Journal of Quantum Electronics*, vol. 32, no. 4, pp. 607-616, 1996.

[3.30] J. Piprek, H. Wenzel, and G. Sztefka, “Modeling thermal effects on the light vs. current characteristic of gain-guided vertical-cavity surface-emitting lasers,” *IEEE Photonics Technology Letters*, vol. 6, no. 2, pp. 139-142, 1994.

[3.31] L. J. Norton, F. Carney, N. Choi, C. K. Y. Chun, R. K. Denton, Jr., D. Diaz, J. Knapp, M. Meyering, C. Ngo, S. Planer, G. Raskin, E. Reyes, J. Sauvageau, D. B. Schwartz, S. G. Shook, J. Yoder, and Y. Wen, “OPTOBUS I: A production parallel fiber optical interconnect,” in *IEEE Electronic Components and Technology Conference*, 1997, pp. 204-209.

[3.32] J. A. Neff, “VCSEL-based smart pixels for free-space optical interconnection,” in *IEEE LEOS (Lasers and Electro-Optics Society) Annual Meeting*, 1997, pp. 151-152.

[3.33] S. F. Yu, W. N. Wong, P. Shum, and E. H. Li, “Theoretical analysis of modulation response and second-order harmonic distortion in vertical-cavity surface-emitting lasers,” *IEEE Journal of Quantum Electronics*, vol. 32, no. 12, pp. 2139-2147, 1996.

[3.34] Y. Su, Y. Chang, and X. Chen, “Circuit model for studying temperature effects on vertical-cavity surface-emitting laser,” in *IEEE LEOS (Lasers and Electro-Optics Society) Annual Meeting*, vol. 1, 1996, pp. 215-216.

[3.35] T. Wipiejewski, M. G. Peters, B. J. Thibeault, D. B. Young, and L. A. Coldren, “Size-dependent output power saturation of vertical-cavity surface-emitting laser diodes,” *IEEE Photonics Technology Letters*, vol. 8, no. 1, pp. 10-12, 1996.

[3.36] P. V. Mena, J. J. Morikuni, S. M. Kang, A. V. Harton, and K. W. Wyatt, “A simple rate-equation-based thermal VCSEL model,” submitted for publication in *Journal of Lightwave Technology.*

[3.37] N. Bewtra, D. A. Suda, G. L. Tan, F. Chatenoud, and J. M. Xu, “Modeling of quantum-well lasers with electro-opto-thermal interaction,” *IEEE Journal of Selected Topics in Quantum Electronics*, vol. 1, no. 2, pp. 331-340, 1995.

[3.38] J. Piprek, D. I. Babic, and J. E. Bowers, “Simulation and analysis of 1.55 μm double-fused vertical-cavity lasers,” *Journal of Applied Physics*, vol. 81, no. 8, pp. 3382-3390, 1997.

[3.39] W. Nakwaski, “Thermal aspects of efficient operation of vertical-cavity surface-emitting lasers,” *Optical and Quantum Electronics*, vol. 28, pp. 335-352, 1996.

[3.40] D. M. Byrne and B. A. Keating, “A laser diode model based on temperature dependent rate equations,” *IEEE Photonics Technology Letters*, vol. 1, no. 11, pp. 356-359, 1989.

[3.41] J. J. Morikuni (private communication).

[3.42] M. Osinski and W. Nakwaski, “Thermal effects in vertical-cavity surface-emitting lasers,” *International Journal of High Speed Electronics and Systems*, vol. 5, no. 4, pp. 667-730, 1994.

[3.43] *HSPICE User’s Manual*, Meta-Software, Inc., 1996.

[3.44] *SaberGuide Simulator Reference*, Analogy, Inc., 1996.

[3.45] P. V. Mena, S. M. Kang, and T. A. DeTemple, “Rate-equation-based laser models with a single solution regime,” *Journal of Lightwave Technology*, vol. 15, no. 4, pp. 717-730, 1997.

[3.46] J. J. Morikuni and S. M. Kang, *Computer-Aided Design of Optoelectronic Integrated Circuits and Systems*. Upper Saddle River, NJ: Prentice Hall, 1997.

[3.47] C. Lawrence, J. L. Zhou, and A. L. Tits, "Users' guide for CFSQP version 2.5: A C code for solving (large scale) constrained nonlinear (minimax) optimization problems, generating iterates satisfying all inequality constraints," Institute for Systems Research, University of Maryland, Technical Report TR-94-16r1, 1997.

[3.48] Y. Ohiso, K. Tateno, Y. Kohama, A. Wakatsuki, H. Tsunetsugu, and T. Kurokawa, "Flip-chip bonded 0.85-µm bottom-emitting vertical-cavity laser array on an AlGaAs substrate," *IEEE Photonics Technology Letters*, vol. 8, no. 9, pp. 1115-1117, 1996.

[3.49] M. H. Crawford, K. D. Choquette, H. Q. Hou, R. J. Hickman, K. M. Geib, and B. E. Hammons, "Visible VCSELs: Recent advances and applications," in *1997 Digest of the LEOS Summer Topical Meetings- Vertical-Cavity Lasers*, 1997, pp. 17-18.

[3.50] M. H. Crawford, K. D. Choquette, R. J. Hickman, and K. M. Geib, "InAlGaP vertical cavity surface emitting lasers (VCSELs): Processing and performance," in *International Conference on InP and Related Materials*, 1997, pp. 32-35.

CHAPTER 4

A COMPREHENSIVE VCSEL MODEL

4.1 Motivation

In the previous chapter, we presented a simple circuit-level thermal VCSEL model based on the standard laser rate equations and a thermal offset current. As we showed, the model is able to fit experimental dc and small-signal data from a number of experimental devices reported in the literature. However, there are a number of limitations to the model which suggest the need for a more comprehensive approach.

First of all, as we saw with the AlGaInP-based VCSEL presented by Crawford *et al.* [4.1], the model was not always capable of fitting experimental LI curves over the complete range of reported ambient temperatures. If the device's threshold current and output power rollover were solely functions of temperature, as they are in the model, then this limitation would not exist. Furthermore, as we noted previously, the unusually large value of thermal impedance obtained during parameter extraction suggests that the model's thermal dependence is being used to account for additional effects at work in the device. For example, spatially dependent mechanisms such as spatial hole burning (SHB) can have an important impact on a VCSEL's LI characteristics, effectively reducing the injection efficiency [4.2]. An obvious solution, then, would be the inclusion of such effects in a comprehensive VCSEL model.

Another area where the model is deficient is in the level of agreement obtained between the experimental and simulated small-signal modulation data for the thin-oxide-apertured device of Thibeault *et al.* [4.3] While the results are adequate, there is still noticeable error near resonance for some of the bias points, again suggesting that the simple rate equations used in the model are not accounting for any nonthermal mechanisms in the device that contribute to its modulation response. Furthermore, because all of the model's temperature dependence is modeled through an effective shift in bias point, the modulation response does not account for all of the temperature effects, either. For example, the relaxation oscillation frequency of the modulation response is, among other things, a function of both differential gain and bias power [4.4]. Because our model intentionally ignores the gain's temperature dependence, at elevated temperatures the model should no longer be able to accurately simulate the small-signal modulation response. However, a more comprehensive model which explicitly accounts for a VCSEL's thermal behavior via temperature-dependent mechanisms such as the gain would not suffer this limitation.

Based on the above discussion, it is clear that in order to model a VCSEL's behavior over a wider range of operating conditions, we require a comprehensive model. The advantage of the previous model was its simplicity, which made it ideal for circuit- and system-level design and simulation. However, as we shall show, it *is* possible to develop more extensive models which are still well-suited to these design environments. In order to obtain greater accuracy, though, the simple approach of our earlier efforts must be sacrificed for a more detailed analytical formulation which accounts for a number of important physical mechanisms in a VCSEL, the most important of which we reviewed in the previous chapter. First, the model should explicitly account for any thermally dependent features in a VCSEL, including the variation with temperature of the active region's gain [4.5]. Thermal leakage out of the active region can also play an important role, especially at elevated temperatures and carrier densities [4.2], and should therefore be included as well. Finally, the model should account for the spatial character of a VCSEL's operation. This includes the transverse profiles of its optical modes [4.6], the resulting spatial hole burning of the transverse carrier profile, and lateral diffusion of carriers in the active region [4.2]. These features need to be included, however, without introducing excessive complexity into the model that would render it unsuitable for circuit- and system-level simulation.

Many researchers have addressed these issues to some degree. Numerous approaches have relied on detailed multidimensional analysis to account for the interplay between optical, electrical, and thermal behavior [4.2], [4.7], [4.8]. For example, Scott *et al*. [4.2] modeled the thermal gain, leakage, and spatial-dependence of VCSELs via quantum-well gain calculations and finite-element analysis of the VCSEL active layer. As we have explained, however, while these models are comprehensive, they typically are also computationally-intensive and therefore unattractive for circuit-level simulation. Simpler approaches which could be used, on the other hand, have not accounted for all of the relevant physics. S. F. Yu *et al.* [4.9], for example, presented a rate-equation-based model which accounts for spatial hole burning, as well as the variation of gain with temperature. However, the model is limited to a single mode and neglects thermally dependent carrier leakage out of the active layer. Morozov *et al.* [4.10] implemented a rate-equation-based VCSEL model which does account for multimode behavior. However, thermal effects are neglected. Similarly, J. Dellunde *et al*. [4.11] reported a multimode model which avoids detailed multidimensional analysis via spatially independent rate equations. Like the model of [4.10], however, the gain is considered independent of temperature, and thermal carrier leakage is not included. While the simpler models of [4.9]-[4.11] do lend themselves to implementation in computer-aided design environments, the authors have not chosen to do so, further limiting the usefulness of their models in optoelectronic system design and simulation. Thus, despite these prior efforts, to the best of our knowledge, no one has presented a *comprehensive* VCSEL model which can be used in the design and simulation of optoelectronic applications.

In this chapter, we present a comprehensive VCSEL model, which accounts for thermally dependent gain, thermal leakage of carriers out of the active region, spatial effects, and multimode operation. Furthermore, we implement the model in Analogy's SABER [4.12], an industry-standard circuit- and system-level simulator. Our discussion begins in Sections 4.2-4.3, which present analytical expressions for the thermally dependent gain and carrier leakage, respectively. Section 4.4 then explains the use of spatially independent rate equations for the modeling of a VCSEL's transverse spatial dependence. A simple model based on this approach is presented in this section and used to simulate diffusive turn-off transients in VCSELs. Next, Section 4.5 presents the comprehensive VCSEL model which ties together the various approaches discussed in the earlier sections, while Section 4.6 reviews the various options for modeling the transverse optical mode profiles. Section 4.7 then demonstrates the utility of the model for simulating single- and two-mode VCSELs, and Section 4.8 validates the model against experimental data from four devices presented in the literature. Finally, Section 4.9 presents final conclusions.

4.2 Thermally Dependent Gain

In the previous chapter, all thermal dependencies were lumped into the thermal offset current, effectively introducing a temperature-dependent shift of a VCSEL's injection current. This empirical technique proved to be very useful in simulating a family of cw LI curves, as well as small-signal modulation responses at bias currents below rollover, i.e., in the linear portion of an LI curve. However, as we noted before, in many cases a VCSEL's thermal behavior depends *specifically* on certain temperature-dependent physical mechanisms, most importantly the gain. Consider, for example, the relaxation oscillation frequency under small-signal modulation. From the rate equations, we can approximate this frequency as [4.4]

$$f_R^2 \propto g' P_{bias} \tag{4.1}$$

where f_R is the relaxation oscillation frequency, g' is the differential gain, and P_{bias} is the output-power bias point. In an actual VCSEL, the differential gain is obviously temperature-sensitive; because a thermal offset current cannot capture this dependence, at elevated temperatures our simple model will not accurately calculate the relaxation oscillation frequency. Thus, our new model *must* include analytical expressions that capture the thermal gain variation.

The model in this chapter, like our earlier work, is rate-equation-based. As a result, we again have decided to model the VCSEL gain as a function of carrier number using $G_o(N - N_t)$, where G_o is the gain constant (proportional to the differential gain), N is the carrier number, and N_t is the carrier transparency number. The gain's temperature dependence can be included in a simple manner by making G_o and N_t functions of temperature, an approach that has been used extensively throughout the literature, especially for edge-emitters. In [4.13], a plot of the derivative of the gain as a function of current in a multiple-quantum-well laser is observed to have a $1/T$ dependence, where T is the device temperature. The gain and transparency number have also been modeled as decreasing and increasing linear functions of temperature [4.14], respectively. Another approach, valid in edge emitters, is to model these parameters' temperature dependence via an exponential function of temperature such as $\exp(\pm T/T_X)$, where T_X is a characteristic temperature [4.15]. This approach essentially takes into account the observed exponential temperature dependence of the threshold current in edge-emitters. Byrne and Keating used a similar tactic, augmenting this exponential dependence with a temperature-dependent description of the gain spectrum, where the spectrum's peak location varies linearly with temperature [4.16].

In VCSELs, similar thermal expressions have also been used. Hasnain *et al.* [4.17] modeled the variation of a gain-guided VCSEL's differential gain as a combination of a temperature-dependent gain-spectrum and an inverse function of temperature; the transparency density was essentially described as a linear function of temperature. Other researchers have modeled a VCSEL's gain using a thermally dependent logarithmic expression, with the gain constant and transparency number described as polynomial functions of temperature [4.2], [4.18]. Thus, there exists ample precedent for modeling a VCSEL's gain constant and transparency number as simple analytical functions of temperature. However, some of the proposed expressions assume a monotonic dependence of gain on temperature, which we know is not the case in VCSELs. Furthermore, it is not clear which expressions will work well across a large cross section of device designs and which are specific to a particular VCSEL. In order to gain some insight into what kind of expressions are needed, it is instructive to examine a simplified quantum-mechanical calculation of a VCSEL's gain.

In the previous chapter, we explained that as temperature increases, a VCSEL's gain spectrum broadens and the gain peak moves to longer wavelengths. Because this variation is large relative to the thermal shift of emission wavelength, the gain will have an optimal value for some temperature where the gain peak and wavelength are matched. The gain will be reduced as the temperature increases or decreases from this point [4.5]. As an example, we can perform a relatively simple calculation of this behavior by determining the gain as a function of carrier density and temperature for a single subband transition in a QW.

If we assume a single set of transitions between the electron subband at energy E_{c1} and the heavy-hole subband at energy E_{v1}, then based on Fermi's Golden Rule, we can calculate a laser's material gain using a reduced density of states, Fermi occupation probabilities, a transition matrix element, and a lineshape function which accounts for energy broadening [4.4]. The resulting expression as a function of optical energy is [4.4], [4.19]

$$g(\hbar\omega) = \frac{\pi q^2 \hbar}{n_g c \varepsilon_o m_o^2} \cdot \frac{1}{\hbar\omega} \cdot \int_{E_{c1v1}}^{\infty} |M_T|^2 \rho_r(E_{21})(f_2 - f_1)\mathcal{L}(\hbar\omega - E_{21}) dE_{21} \tag{4.2}$$

where $\hbar\omega$ is the optical energy, q is the electron charge, n_g is the index of refraction, c is the speed of light, ε_o is the free-space permittivity, $E_{c1v1} = E_{c1} - E_{v1}$ is the difference between the first electron and heavy-hole subband energies, $E_{21} = E_2 - E_1$ is the transition energy between a conduction-band electron state at energy E_2 and a heavy-holy state at energy E_1, $|M_T|^2$ is the transition matrix element, $\rho_r(E_{21})$ is the reduced density of states (DOS) for this particular subband transition, f_2 is the electron occupation probability at E_2, f_1 is the electron occupation probability at E_1, and $\mathcal{L}(\hbar\omega - E_{21})$ is the Lorentzian lineshape function. Furthermore, for a single subband, the electron and heavy-hole densities can be calculated using [4.20]

$$n = \frac{m_c k_B T}{\pi \hbar^2 L_z} \ln\left[1 + \exp\left(\frac{E_{fc} - E_{c1}}{k_B T}\right)\right] \tag{4.3}$$

$$p = \frac{m_{hh} k_B T}{\pi \hbar^2 L_z} \ln\left[1 + \exp\left(\frac{E_{v1} - E_{fv}}{k_B T}\right)\right] \tag{4.4}$$

where n and p are the electron and hole densities, respectively, m_c and m_{hh} are the electron and heavy-hole effective masses, respectively, k_B is Boltzmann's constant, E_{fc} is the electron quasi-Fermi level, E_{fv} is the hole quasi-Fermi level, and L_z is the QW width. As we show in Appendix D, if we define the energy E_t [4.20] as $E_t = E_{21} - E_{c1v1}$ and substitute appropriate expressions for $|M_T|^2$, ρ_r, f_2, f_1, and $\mathcal{L}(\hbar\omega - E_{21})$ into (4.2)-(4.4), we obtain the following expression for the gain as a function of temperature T and carrier density n:

$$g(\hbar\omega) = \frac{q^2 m_r |M|^2 \lambda}{4\pi\tau_{in} L_z n_g c^2 \varepsilon_o m_o^2 h} \cdot \int_0^{\infty} \left(1 + \frac{\delta E_{c1}}{\delta E_{c1} + E_t \frac{m_r}{m_c}} \right) \cdot \frac{1}{\left(\frac{\hbar}{\tau_{in}}\right)^2 + (\hbar\omega - E_{c1v1} - E_t)^2} \tag{4.5}$$

$$\cdot \left(\frac{1}{1 + \exp\left(\frac{E_t m_r}{k_b T m_c}\right) \left[\exp\left(\frac{\pi\hbar^2 L_z n}{m_c k_B T}\right) - 1 \right]^{-1}} - \frac{1}{1 + \exp\left(\frac{-E_t m_r}{k_b T m_{hh}}\right) \left[\exp\left(\frac{\pi\hbar^2 L_z n}{m_{hh} k_B T}\right) - 1 \right]} \right) \cdot dE_t$$

where λ is the emission wavelength, m_r is the reduced DOS effective mass $(1/m_c + 1/m_{hh})^{-1}$, $|M|^2$ is the bulk momentum matrix element of the QW material, τ_{in} is the intraband relaxation time, m_o is the free-electron mass, and δE_{c1} is the first electron subband energy relative to the conduction band (i.e., $E_{c1} - E_c$, where E_c is the bulk conduction-band energy).

We have calculated a VCSEL's differential gain and carrier transparency density as functions of temperature using (4.5) and simplifying assumptions for the various parameter values. First, the emission wavelength was described as a linear function of temperature [4.17], $\lambda = \lambda_o + c_\lambda(T - 300)$, where $\lambda_o = 990$ nm and $c_\lambda = 0.084$ nm/K [4.2]. Next, the conduction and valence band subband energies were calculated assuming a 10-nm $In_{0.2}Ga_{0.8}As$ QW surrounded by GaAs barrier layers. The locations of the bulk conduction and valence band edges in these calculations were determined via linear interpolations of the temperature-dependent formulas for GaAs and InAs bulk bandgap energies [4.21], [4.22], where

$$E_{g,\,GaAs} = 1.519 - 5.405 \times 10^{-4} T^2 / (T + 204) \text{ eV} \tag{4.6}$$

$$E_{g,\,InAs} = 0.420 - 2.50 \times 10^{-4} T^2 / (T + 75) \text{ eV} \tag{4.7}$$

Furthermore, the quantum-well effective masses for the electrons and heavy holes were set equal to

$0.06m_o$ and $0.18m_o$, respectively, while the corresponding masses for the barrier layers were set equal to $0.067m_o$ and $0.50m_o$. Finally, the remaining parameter values were set as τ_{in} = 0.1 ps, $|M|^2$ = $27.48(m_o/2)$ [4.4], and n_g = 3.6. We plotted (4.5) as a function of n for various temperatures and determined the transparency density (i.e., the point where the gain is zero); we then calculated the differential gain at this density. Figure 4.1 illustrates the results.

As we can see, the differential gain exhibits a clear peak at approximately 315 K. As the temperature increases beyond this point, the gain slowly diminishes towards zero. As the temperature decreases below 315 K, however, the gain drops off much more rapidly. In fact, for low enough temperatures the emission wavelength is no longer short enough to stimulate transitions between the conduction and valence bands. For the parameters used here, that temperature is approximately 260 K. The transparency density, meanwhile, generally increases with temperature, decreasing slightly with

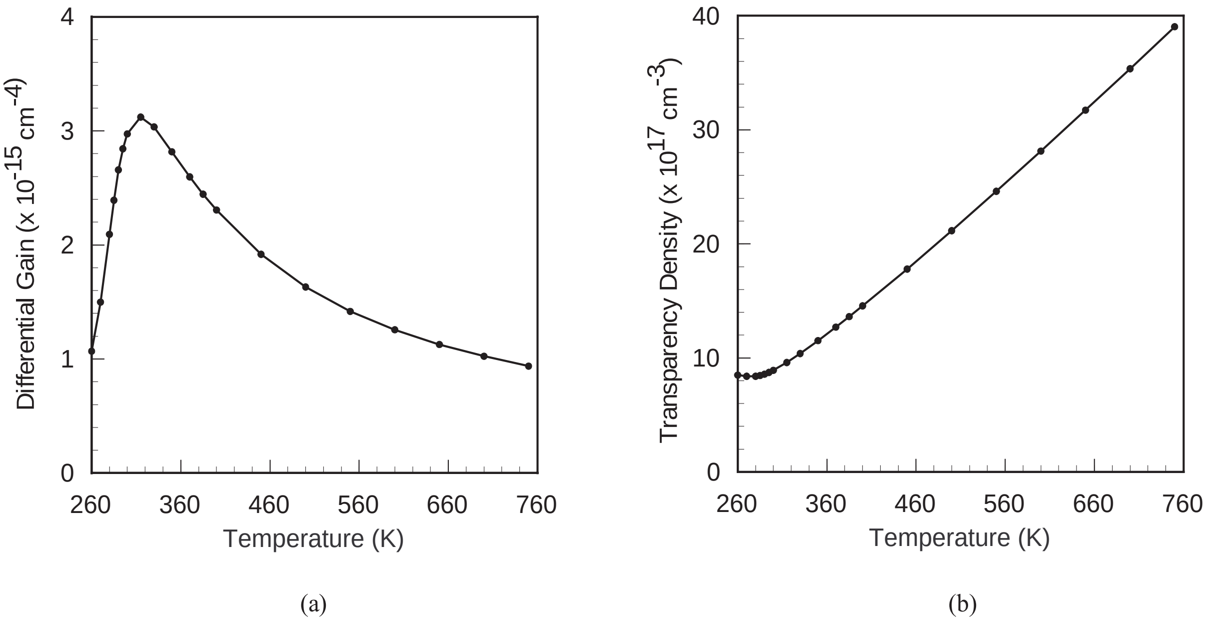

(a) (b)

Figure 4.1 Results of a simple calculation of a VCSEL's (a) differential gain and (b) carrier transparency density.

temperature near 260 K.

The results of Fig. 4.1 suggest that the transparency can most likely be approximated by a polynomial function of temperature, while the differential gain is noticeably more complicated. However, examination of two prior approaches reported in the literature suggests that a simple expression for the latter is still possible. First, as we mentioned before, Hasnain *et al.* [4.17] utilized simple analytical expressions for a gain-guided VCSEL's transparency density and differential gain. They modeled the density as a linear function of temperature, whereas they assumed that the differential gain could be described as the product of an inverse function of temperature and a temperature-dependent gain spectrum, or

$$g' \propto \frac{a}{T} \cdot \left(1 - \frac{2(\lambda(T) - \lambda_p(T))^2}{\Delta\lambda^2(T)} \right) \tag{4.8}$$

where a is a fitting constant, $\lambda_p(T)$ is the temperature-dependent peak-gain wavelength, and $\Delta\lambda(T)$ is the gain spectrum's temperature-dependent full width at half maximum (FWHM). Note that (4.8) eliminates the leading term of $1/\Delta\lambda(T)$ that was spuriously included by the authors, making the spectral term of (4.8) equivalent to that presented in [4.23] and [4.24]. If we assume a square-root dependence on temperature for the FWHM, and a linear dependence on temperature for both λ and λ_p [4.17], then we can reduce (4.8) into the simple form $(a_{g0} + a_{g1}T + a_{g2}T^2)/T^2$, where a_{g0}-a_{g2} are constants.

Similarly, in [4.2], Scott *et al.* model the VCSEL's gain using much more detailed versions of the quantum-mechanical gain calculations discussed above. They then fit plots of the gain versus carrier density to a logarithmic function of the form $A(T)\ln[(n - n_o)/B(T)]$, where n_o is a constant and $A(T)$ and $B(T)$ are polynomial functions of temperature. The authors use two separate polynomials to model $A(T)$ at temperatures both above and below 430 K. By linearizing their gain expression about the transparency density, we can obtain an equivalent linear version of the gain, $g'(n - n_t)$, where $g' = A(T)/B(T)$ and $n_t = n_o + B(T)$. As we expected, we can model the transparency density as a polynomial function of temperature, in this case a quadratic. Meanwhile, as Fig. 4.2(a) shows, g' is very similar in form to the results of Fig. 4.1. Motivated by the fact that Fig. 4.2(a) is generated by the quotient of two polynomials, much like the equation from [4.17], we attempted to fit the curve of Fig. 4.2(a) to the ratio of two quadratics:

$$g' \propto \frac{a_{g0} + a_{g1}T + a_{g2}T^2}{b_{g0} + b_{g1}T + b_{g2}T^2} \tag{4.9}$$

where b_{g0}-b_{g2} are additional constants. The results of this fit can be seen in the dashed curve of Fig. 4.2(a). Clearly, this expression does an excellent job of fitting the data generated by Scott's model.

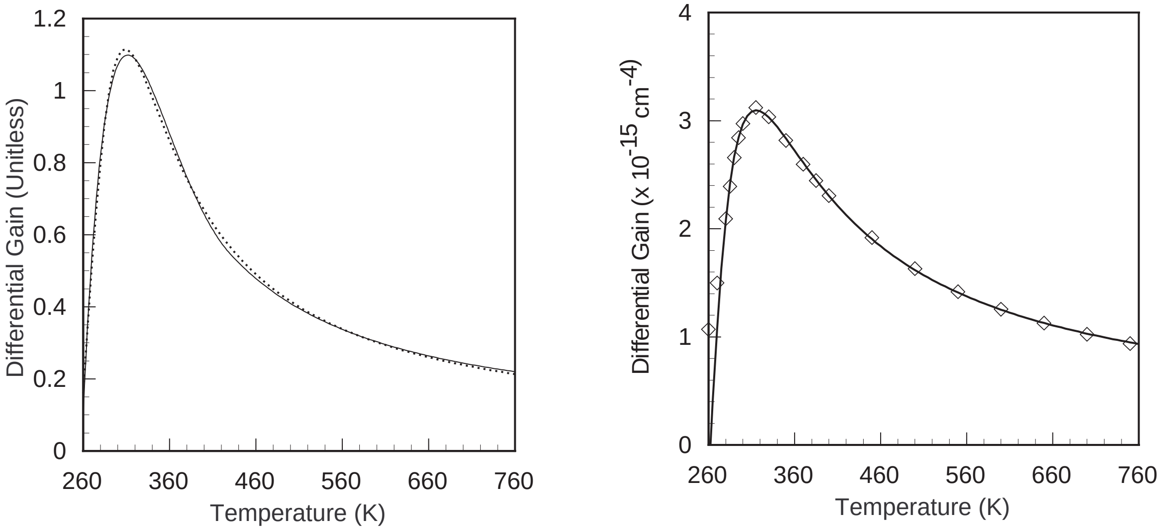

(a) (b)

Figure 4.2 (a) Comparison of differential gain calculations based on the results of [4.2] (solid line) and Eq. (4.9) (dashed line). (b) Comparison of quantum-well gain calculation based on Eq. (4.5) (data points) and the simple expression of (4.9) (line).

Furthermore, this expression can also be used to fit the results of our own quantum-mechanical differential gain calculations. As Fig. 4.2(b) illustrates, the match is excellent. Thus, we have elected to use the general expression of (4.9) to model the thermal dependence of our model's gain constant.

As the above results show, simple expressions based on polynomial functions of temperature can be used to model the thermal dependence of both the gain constant and transparency number in our model. Thus, the complete set of expressions that we have chosen to use in our comprehensive VCSEL model are

$$Gain \equiv G(T)(N - N_t(T)) \tag{4.10}$$

$$G(T) = G_o \cdot \frac{a_{g0} + a_{g1}T + a_{g2}T^2}{b_{g0} + b_{g1}T + b_{g2}T^2} \tag{4.11}$$

$$N_t(T) = N_{to} \cdot (c_{n0} + c_{n1}T + c_{n2}T^2) \tag{4.12}$$

Based on the above discussion, (4.11) should be able to model the nonmonotonic thermal dependence of the gain constant. Also, based on the formulation in [4.2], we have chosen a quadratic function of temperature to model the transparency number. In some cases, such as the gain-guided VCSEL of [4.17], a simple linear relationship will suffice. In these cases, c_{n0} and c_{n2} can be set equal to zero. As we shall see later in this chapter, (4.10)-(4.12) provide a flexible means of accounting for the thermal dependence of the gain in actual VCSELs.

4.3 Thermal Carrier Leakage

While the gain is the most well-recognized thermally dependent mechanism that affects a VCSEL's operation, thermal leakage of carriers out of the active region can also have a severe impact on device performance [4.2]. As we discussed in the previous chapter, as temperature increases, the bandgap of a VCSEL's active region shrinks. Furthermore, the carrier number increases due to a relative increase of the active-region quasi-Fermi levels. Eventually, the large number of carriers and the high temperature no longer allow the active layer to adequately confine carriers, and leakage current becomes a dominant influence on the VCSEL's operation [4.2]. The increase of the carrier number due to spatial hole burning can further accelerate the increase in the leakage [4.2].

Obviously, this leakage must be modeled as a function of both carrier number and temperature, preferably via a simple analytical expression. An obvious choice would be to utilize the well-known formulation of thermionic emission [4.25]. In this case, the leakage current density is proportional to $NT^{1/2}\exp(-T_l/T)$, where T_l is a constant that characterizes the emission's exponential temperature dependence. A similar expression can be derived for heterojunction leakage if we assume that it is proportional to the carrier density immediately outside of the active region [4.26]. The resulting expression does not include a square-root temperature dependence, however. Alternatively, Scott *et al.* assumed that the carrier leakage could be modeled using an approximate homojunction-diode relationship proportional to $\exp[-(E_{gB} - \Delta E_{fcv})/k_BT]$, where E_{gB} is the bandgap of the confinement layers surrounding the active region, and ΔE_{fcv} is the active region's quasi-Fermi-level separation [4.2]. Carrier number can be introduced into this expression if we crudely approximate it using expressions for bulk material [4.27]. In this case, the leakage becomes proportional to $N^2T^{-3}\exp(-T_l/T)$.

Initially, we attempted to model the leakage using a generalized form of the expressions given above. This first expression for the leakage current was

$$I_l = I_{lo}N^iT^m\exp(-T_l/T) \tag{4.13}$$

where I_{lo} is a constant, i = 1 or 2, and m is a fitting constant. While on the surface this expression looks promising, in reality it over-predicts the carrier-number dependence at lower temperatures. As we shall see shortly, spatial effects in VCSELs can result in the increase of the active-layer carrier number even in the absence of thermal effects. Thus, even if the device temperature remains relatively constant, (4.13) can result in an excessive level of leakage via the N^i term. In fact, the main deficiency of (4.13) is that the carrier and temperature dependence are independent of one another, whereas in reality, one would expect the carrier dependence to become more sensitive at higher temperatures.

Due to the limitations of (4.13), we instead took an alternate approach based on the work of Scott *et al.* in [4.2]. As touched on above, they modeled the leakage as a function of the quasi-Fermi-level separation ΔE_{fcv}. Furthermore, to simplify matters, they performed detailed calculations of ΔE_{fcv} as a function of carrier density and then used a curve-fit to model the carrier and temperature dependence of $\Delta E_{fcv} - E_{gB}$ analytically using $\Delta E_{fcv} - E_{gB} = -a_0 + a_1 n + a_2 nT - a_3/(n + a_4)$, where a_0-a_4 are constants. Examination of their results revealed that a_4 could be neglected with little effect on the end result. If we use their expression in terms of carrier number and substitute it into the homojunction diode equation, we obtain the following formula for the thermal leakage current as a function of carrier number and temperature:

$$I_l = I_{lo} \exp\left(\frac{-a_0 + a_1 N + a_2 NT - \frac{a_3}{N}}{T}\right) \tag{4.14}$$

Analogous to Fig. 2(d) from [4.2], Figure 4.3 illustrates plots of (4.14), using values of a_0-a_3 based on data in [4.2], for four different temperatures, 250, 300, 350, and 400 K. As we can see, at 250 K the leakage is negligible for low values of carrier number, and increases dramatically beyond some threshold value. As the temperature increases, the leakage becomes much more sensitive to carrier number. It should be noted that for extremely high values of carrier number, the leakage of (4.14)

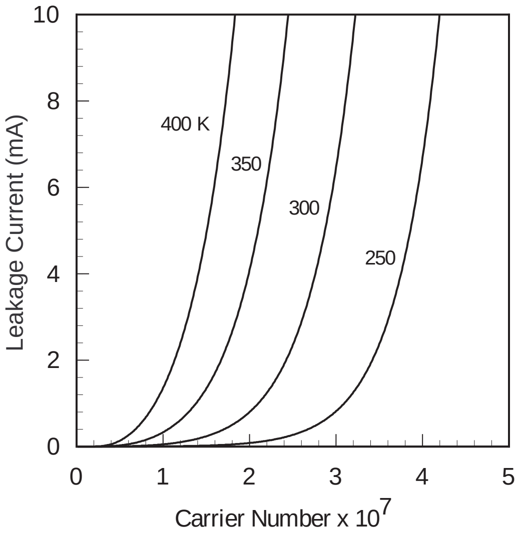

Figure 4.3 Plots of (4.14) at temperatures of 250, 300, 350, and 400 K using a_0 = 3574, a_1 = 2.25x10^{-5}, a_2 = 10^{-7}, and a_3 = 6.13 x 10^9.

actually decreases with temperature. However, as we shall see later in the parameter extraction from experimental device data, this regime of operation is typically not encountered in practice. Consequently, we will use (4.14) to model leakage in our comprehensive VCSEL model.

4.4 Modeling of Spatially Dependent Operation

4.4.1 Spatially dependent VCSEL behavior

While thermal behavior is certainly a major component of VCSEL operation, spatial effects can play an important role as well. The interplay between transverse mode profiles and the transverse carrier distribution in the active region can result in multimode operation, spatial hole burning, and lateral carrier diffusion, all of which can have a significant impact on a VCSEL’s dc and modulation characteristics. Consequently, our comprehensive model must be capable of accounting for them.

As many researchers have observed, while their short cavity length allows VCSELs to have a single longitudinal mode, multi-transverse-mode operation can still occur [4.28]. This multimode behavior has been observed in both index- and gain-guided devices [4.6], [4.28]-[4.32]. Typically, the VCSEL begins to lase in a fundamental single-lobed mode such as the TEM_{00} [4.6] or LP_{01} [4.29] mode. At higher biases, however, other modes begin lasing [4.6]. Consequently, there is a limited region of operation over which a VCSEL will be truly single mode.

The specific forms of the transverse mode profiles are an important component of a VCSEL's spatially dependent behavior. In the simplest case, they can be accounted for via a confinement factor in the expression for the laser gain, as is often done in edge-emitters [4.26]. However, this assumes that the modes do not interact with the transverse carrier profiles. In reality, because the optical modes are not uniform in the transverse direction, they burn holes in the transverse carrier distribution where their intensity is largest. This spatial hole burning (SHB) allows different modes to compete with one another, as described in [4.29]. If the VCSEL begins lasing in its fundamental transverse mode, eventually it will burn a hole in the center of the carrier profile. The corresponding increase in carrier number outside of this hole allows additional modes, whose profiles overlap these carriers, to begin lasing. This interplay between the modes and carriers also can play a role in self-focusing and thermal-lensing effects, which alter the mode profiles and their impact on device performance. For example, the spatial hole burning can cause a transverse variation in the active-region index profile, resulting in self-focusing that can accelerate the onset of multimode effects in weakly-index-guided devices [4.32]. Similarly, thermal lensing can also alter the transverse mode profiles [4.17], and consequently the impact of SHB on device behavior [4.5].

From the above discussion, it is clear that in addition to the transverse mode profiles, we must also properly take into account the transverse spatial dependence of the active region's carriers. This nonuniform carrier profile, induced not only by SHB, but also by nonuniform current injection and poor carrier confinement [4.33], can result in lateral carrier diffusion. This diffusion can be an important mechanism in VCSELs. First of all, as has been well documented in edge-emitters, diffusion can act as a damping mechanism during high-speed modulation [4.34]-[4.36]. In this case, it acts much like other damping mechanisms such as gain saturation [4.36]. Second, diffusion can significantly alter a laser's transient operation. T. Ikegami [4.37] reported the presence of a tail in a DH injection laser's turn-off transient, while Chinone *et al*. [4.38] presented results on the impact of lateral effects on the turn-on behavior of semiconductor lasers. Similar phenomena have been investigated in VCSELs. For example, the study of mode competition during transient operation [4.39] has revealed that in conjunction with SHB, the injection current profile, and the transverse mode shapes, diffusion can be an important contributor to the transient evolution of each mode's output.

A particularly important effect of lateral carrier diffusion that has been observed in VCSELs is the onset of secondary pulsations during the turn-off transient. This phenomenon has already been observed in edge-emitters [4.40]. However, recent work suggests that this behavior should play an important role in VCSELs as well. As discussed in [4.41], if we assume fundamental mode operation, then as the current through the VCSEL is increased, a spatial hole is burned into the carrier profile. When the VCSEL is eventually turned off, carriers begin to diffuse back into the hole. This serves to delay the turn-off, thereby leading to the slow tail mentioned above. However, in certain cases the diffusion results in an increase of the output power [4.42]. If the laser is not completely turned-off at this point, a bump occurs in the falling edge of the output. In the extreme case, the laser will have already stopped lasing and momentarily turn back on again, producing secondary pulsations. As Fig. 4.4 illustrates, optical bumps have been demonstrated in actual VCSELs, with other researchers having reported similar results from other devices [4.43].

Typical attempts to model all of the above behavior have involved detailed multidimensional

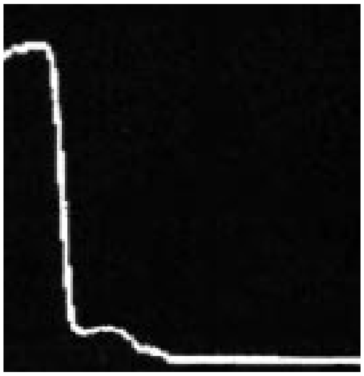

Figure 4.4 A measured VCSEL turn-off transient exhibiting an optical bump.

analysis, approaches which are inadequate for circuit- and system-level simulation. For example, the beam propagation method (BPM) can be used to determine the transverse mode structure [4.44]. Other authors have resorted to finite-element and finite-difference analysis to model the transverse dependence of the active layer carriers [4.2], [4.7], [4.45]. However, transverse spatial effects *can* be modeled without resorting to explicit spatial calculations. The technique involves the use of assumed solutions for the carrier and mode profiles within spatially dependent rate equations.

Furuya *et al*. [4.34] presented one of the original implementations of this approach and applied it to edge emitters. Essentially, one starts out by describing the laser operation via spatially dependent rate equations that include a carrier diffusion term. The functional form of the mode profiles is then assumed in advance, with the actual photon number of each mode left as the only unknowns. An orthogonal-series expansion of the carrier profile whose expansion coefficients are time-dependent is then substituted into the rate equations. Based on the orthogonality condition, a series of integrations can be performed on the spatial rate equations to produce a set of spatially independent differential equations for the photon numbers and expansion coefficients. In the case of [4.34], sinusoidal mode profiles and one-dimensional Fourier-series expansions were used. Tucker and Pope [4.36] used similar equations to model the diffusive damping in a laser's modulation response. Byrne and O’Dowd [4.46], on the other hand, used a comparable set of equations to model a laser in a PCM transmitter. Because of the power of this approach, it has also been used in VCSELs. Moriki *et al*. [4.47] used a Bessel-series expansion in cylindrical coordinates to determine the single transverse mode condition of buried-heterostructure VCSELs, while Dellunde *et al.* [4.11] used the same approach to model the statistics of a VCSEL’s turn-on transient. Similarly, S. F. Yu *et al.* [4.9] used a two-term Bessel-series expansion to model the impact of diffusion and SHB on a single-mode laser. Because of the success of this approach, we shall use it in our own comprehensive model. Before doing so, however, and to better elucidate the merits of this technique, we shall next discuss the use of a simple model based on the equations of [4.36] for modeling the diffusive turn-off transients in VCSELs, including the secondary pulsations described above.

4.4.2 Simple model based on spatially independent rate equations

To demonstrate the ability of spatially independent rate equations to model a VCSEL’s spatially dependent behavior, we, in collaboration with J. Morikuni, used a generalized version of the model presented by Tucker and Pope in [4.36] to model secondary pulsations in a VCSEL’s turn-off transient [4.42]. Assuming single-mode operation and a one-dimensional rectangular coordinate system for the description of the carrier and mode profiles’ transverse dependence, the spatially dependent rate equations upon which this model is based are [4.36]

$$\frac{\partial N(x)}{\partial t} = \frac{\eta_i I(x)}{q} - \frac{N(x)}{\tau_n} - \frac{G_o(N(x) - N_t)S(x)}{1 + \varepsilon S_o} + \frac{L_{eff}^2}{\tau_n} \cdot \frac{\partial^2 N(x)}{\partial x^2} \tag{4.15}$$

$$\frac{\partial S(x)}{\partial t} = -\frac{S(x)}{\tau_p} + \frac{\beta N(x)}{\tau_n} + \frac{G_o(N(x) - N_t)S(x)}{1 + \varepsilon S_o} \tag{4.16}$$

where N is the carrier population, S is the photon population of the fundamental mode, S_o is the average photon number, I is the injection current, η_i is the current-injection efficiency, τ_n is the carrier lifetime, G_o is the gain coefficient, N_t is the carrier transparency number, τ_p is the photon lifetime, and β is the spontaneous emission coupling coefficient. Diffusive effects are incorporated into (4.15) via the last term on the right side, where L_{eff} is the effective carrier diffusion length. Note that, unlike [4.34] and [4.36], we have neglected the dependence of the spontaneous emission on the mode profile [4.46]. Furthermore, we added the injection efficiency η_i, as well as gain-saturation due to the average photon number S_o to account for damping mechanisms unrelated to spatial effects [4.41], [4.48].

In order to eliminate the spatial dependence from (4.15)-(4.16), we first assume forms for the carrier profile $N(x)$ and the mode profile $S(x)$. The latter can be modeled using

$$S(x) = S_o \psi(x) \tag{4.17}$$

where $\psi(x)$ is the normalized mode profile. Note that Tucker and Pope used a sinusoidal function for $\psi(x)$. In order to take into account the dependence of spatial effects on the relative widths of the mode and carrier profiles, we generalized their approach and used the following equation:

$$\psi(x) = \begin{cases} \dfrac{2}{\alpha}\cos^2\left(\dfrac{\pi x}{W_m}\right) & |x| \le \dfrac{W_m}{2} \\ 0 & |x| > \dfrac{W_m}{2} \end{cases} \tag{4.18}$$

In this definition, W_m is used to denote the width of the optical mode and $\alpha \equiv W_m/W$ is the fraction of the active region occupied by the mode, where W models the effective width of the active region. Figure 4.5(a) illustrates (4.18) when $\alpha = 0.75$. Eq. (4.18) reduces to the expression in [4.36] if $\alpha = 1$.

Meanwhile, the carrier profile can be modeled via a Fourier-series expansion [4.34]. In general, if we assume that the carriers are confined to an active region of width W, then

$$N(x) = N_0 - \sum_{i=1}^{\infty} N_i \cos\left(\frac{2\pi i x}{W}\right) \qquad (4.19)$$

where N_0 represents a time-dependent average carrier number, and N_i are the remaining time-dependent expansion coefficients. Following the approach of [4.36], we limit (4.19) to two terms. In this case, N_1 can be interpreted as modeling the extent of the spatial hole created by the fundamental mode. If additional terms were included, this simplistic interpretation would no longer be valid; however, for our purposes here, it is a useful guideline for understanding the interplay between the carrier and mode profiles. Figure 4.5(b) illustrates the shape of the two-term expansion.

After substituting (4.17)-(4.19) into (4.15) and (4.16), we can eliminate the spatial dependence as follows. First, we integrate (4.16) over $(-\infty,+\infty)$. Because the carriers are assumed to be confined to the width W, the last two terms are only integrated over the interval $[-W/2,+W/2]$. In essence, we are integrating out the mode profile's spatial dependence and transforming the spatially dependent gain into an equivalent modal gain. Next, for each term in (4.19), we multiply (4.15) by $\cos(2\pi i x/W)$

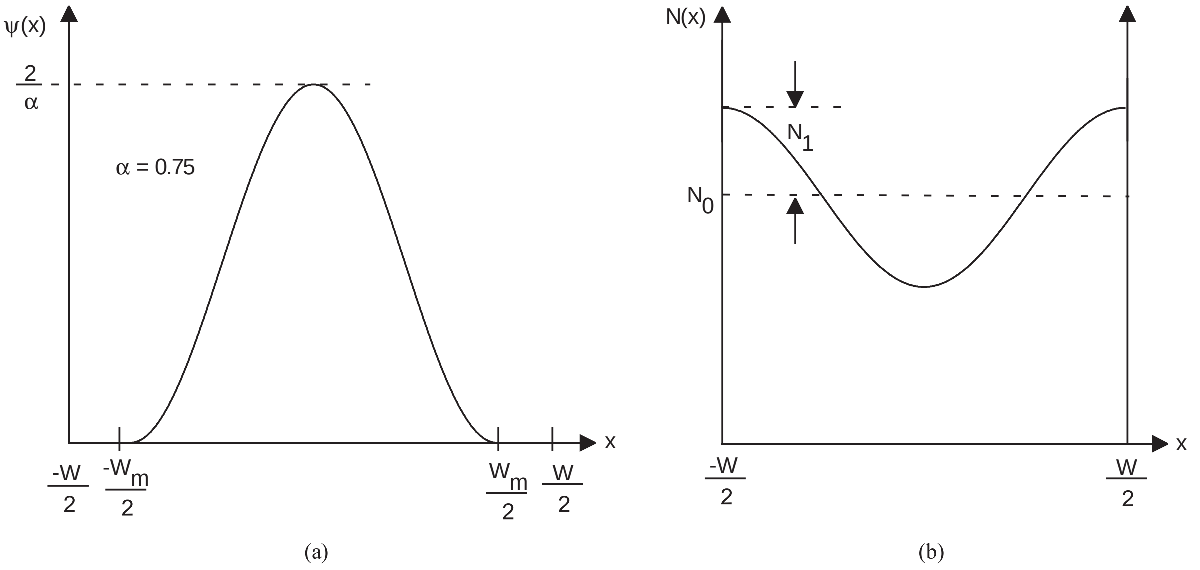

Figure 4.5 Plots of (a) the normalized mode profile $\psi(x)$ for $\alpha = 0.75$, and (b) the two-term Fourier-series expansion of the transverse carrier profile.

and integrate over the interval [–W/2,+W/2], where $i \geq 0$. Because of the orthogonality of the Fourier expansion, this reduces (4.15) to a spatially independent differential equation for N_i. Applying this approach to (4.15) and (4.16), using the two-term Fourier expansion and a uniform injection current profile, we obtain equations very similar to those presented in [4.34], [4.36], and [4.46]:

$$\frac{dS_o}{dt} = -\frac{S_o}{\tau_p} + \frac{\beta N_0}{\tau_n} + \frac{G_o(\gamma_0 N_0 - \gamma_1 N_1 - \gamma_0 N_t)S_o}{1 + \varepsilon S_o} \tag{4.20}$$

$$\frac{dN_0}{dt} = \frac{\eta_i I}{q} - \frac{N_0}{\tau_n} - \frac{G_o(\gamma_0 N_0 - \gamma_1 N_1 - \gamma_0 N_t)S_o}{1 + \varepsilon S_o} \tag{4.21}$$

$$\frac{dN_1}{dt} = -\frac{N_1}{\tau_n}(1 + h_1) + \frac{G_o(\phi_0 N_0 - \phi_1 N_1 - \phi_0 N_t)S_o}{1 + \varepsilon S_o} \tag{4.22}$$

in which S_o can be related to the output power P_o using $P_o = k_{fo}S_o$, where k_{fo} accounts for the output-power coupling efficiency of the VCSEL. In the above equations, $h_1 = (2\pi L_{eff}/W)^2$ [4.36] accounts for the effect of diffusion on the carrier profile, while γ_0, γ_1, ϕ_0, and ϕ_1, overlap-integral values obtained during the integration of (4.15)-(4.16), are

$$\gamma_0 = \frac{1}{W}\int_{-W/2}^{W/2} \psi(x)dx = \begin{cases} 1 & \alpha \leq 1 \\ \dfrac{1}{\alpha} + \dfrac{1}{\pi}\sin\left(\dfrac{\pi}{\alpha}\right) & \alpha > 1 \end{cases} \tag{4.23}$$

$$\gamma_1 = \frac{1}{W}\int_{-W/2}^{W/2} \cos\left(\frac{2\pi x}{W}\right)\psi(x)dx = \begin{cases} \dfrac{\sin(\pi\alpha)}{\pi\alpha(1 - \alpha^2)} & \alpha < 1 \\ 0.5 & \alpha = 1 \\ \dfrac{\sin\left(\dfrac{\pi}{\alpha}\right)}{\pi(\alpha^2 - 1)} & \alpha > 1 \end{cases} \tag{4.24}$$

$$\phi_0 = 2\gamma_1 \tag{4.25}$$

$$\phi_1 = \frac{2}{W}\int_{-W/2}^{W/2}\cos^2\left(\frac{2\pi x}{W}\right)\psi(x)dx = \begin{cases} 1 + \dfrac{\sin(2\pi\alpha)}{2\pi\alpha(1-4\alpha^2)} & \alpha \le 1,\ \alpha \ne 0.5 \\ 1.5 & \alpha = 0.5 \\ \dfrac{1}{\alpha} + \dfrac{2\sin\left(\dfrac{\pi}{\alpha}\right)(2\alpha^2-1)}{\pi(4\alpha^2-1)} & \alpha > 1 \end{cases} \tag{4.26}$$

All of the effects of diffusion, SHB, and cavity dimension are now essentially captured in the parameters h_1 and α. It should be noted that while the overlap integral values of (4.23)-(4.26) seem to add complexity, in fact they do not. Because they are functions of model parameters and not operating conditions, they need only be calculated once. The advantage of the simple mode profile of (4.18) is that these values can be calculated analytically as a function of α. If an exact form of the profile is used, such as a Gaussian, then the overlap integrals would have to be calculated numerically.

As we can see, in converting (4.15)-(4.16) into (4.20)-(4.26), we have completely eliminated any explicit reference to the spatial dependence. Obviously, the solution of the spatially independent model will require considerably fewer computational resources as compared to the spatially dependent version. It is for this reason that we shall use the methodology presented here to incorporate spatial effects into our more comprehensive model. Though the truncation of the Fourier series at a few terms may diminish the relative accuracy of the model, we shall see below that it is fully capable of modeling spatial effects in VCSELs, specifically secondary pulsations in the turn-off transient.

4.4.3 Example simulations

We implemented (4.20)-(4.22) into two circuit-level simulators, HSPICE [4.49] and SABER [4.12]. Implementation details can be found in Appendix E. We then used various sets of parameters to demonstrate the model's ability to simulate a VCSEL's turn-off transient.

We began our simulations with the following set of parameters (using the overlap integrals as defined in (4.23)-(4.26)): $\eta_i = 1$, $\tau_n = 3$ ns, $G_o = 8 \times 10^4$ s^{-1}, $N_t = 15\times 10^6$, $\beta = 2 \times 10^{-7}$, $\tau_p = 5$ ps, $\varepsilon = 0.75 \times 10^{-6}$, $k_{fo} = 0.75 \times 10^{-8}$ W, $h_1 = 5$, and $\alpha = 1$ (i.e., $\gamma_0 = 1$, $\gamma_1 = 0.5$, $\phi_0 = 1$, and $\phi_1 = 1$). These model parameters yield a threshold current of roughly 0.935 mA. We first simulated the response of the model to a square-pulse input current with a low-level bias of 0.93 mA and a high-level of 5 mA. As shown in [4.41], biasing the laser close to threshold and modulating it to a value well above threshold magnifies the presence of secondary pulsations in the turn-off transient. Figure 4.6 illustrates the results. A secondary pulse can clearly be seen immediately after the initial turn-off transient [4.41]. In fact, this demonstrates the extreme case discussed above: when the current is reduced, the laser initially turns off completely and then momentarily begins lasing again due to the filling of a spatial hole by carrier diffusion.

As illustrated in the measured curve of Fig. 4.4, the secondary pulsation can also manifest itself as more of a bump in the falling edge of the laser's output. To simulate this behavior, we used

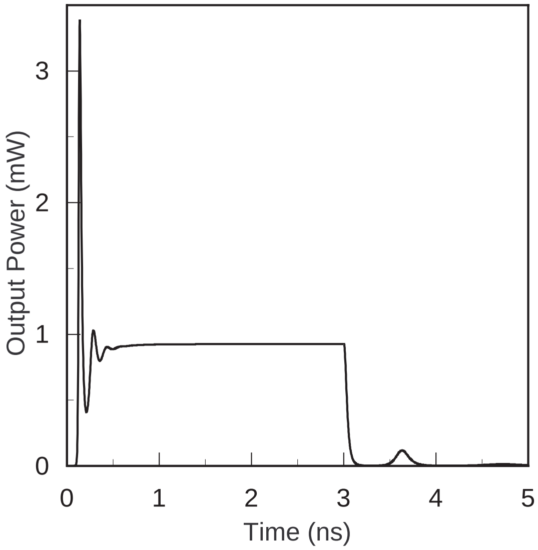

Figure 4.6 Simulation of a secondary pulsation in a VCSEL's turn-off transient.

the following parameters: $\eta_i = 1$, $\tau_n = 5$ ns, $G_o = 4.4 \times 10^4$ s^{-1}, $N_t = 7.5\times 10^6$, $\beta = 4 \times 10^{-2}$, $\tau_p = 3$ ps, $\varepsilon = 1.3 \times 10^{-6}$, $k_{fo} = 1.3 \times 10^{-8}$ W, $h_1 = 10$, and $\alpha = 1$. The corresponding threshold current in this case is 0.483 mA. Consequently, this time we modulated the laser between 0.45 and 5.0 mA, the results of which are illustrated in Fig. 4.7(a). As we can see, the secondary pulsation now occurs before the output power is completely extinguished. This is largely a result of the larger value of β used in this case, which essentially acts as a mechanism for sustaining the lasing action via a higher level of coupled spontaneous emission [4.42]. If we now decrease h_1 to 1, the bump gives way to a slow tail in the turn-off transient, as illustrated in Fig. 4.7(b). Thus, h_1 can have a significant impact on the turn-off transient, as would be expected since it accounts for the role of diffusion in the device. In this case, the smaller value essentially increases the effective lifetime of N_1 in (4.22) [4.42]. As a result, the spatial hole takes longer to fill in [4.42], thereby smoothing out the pulsation in the falling

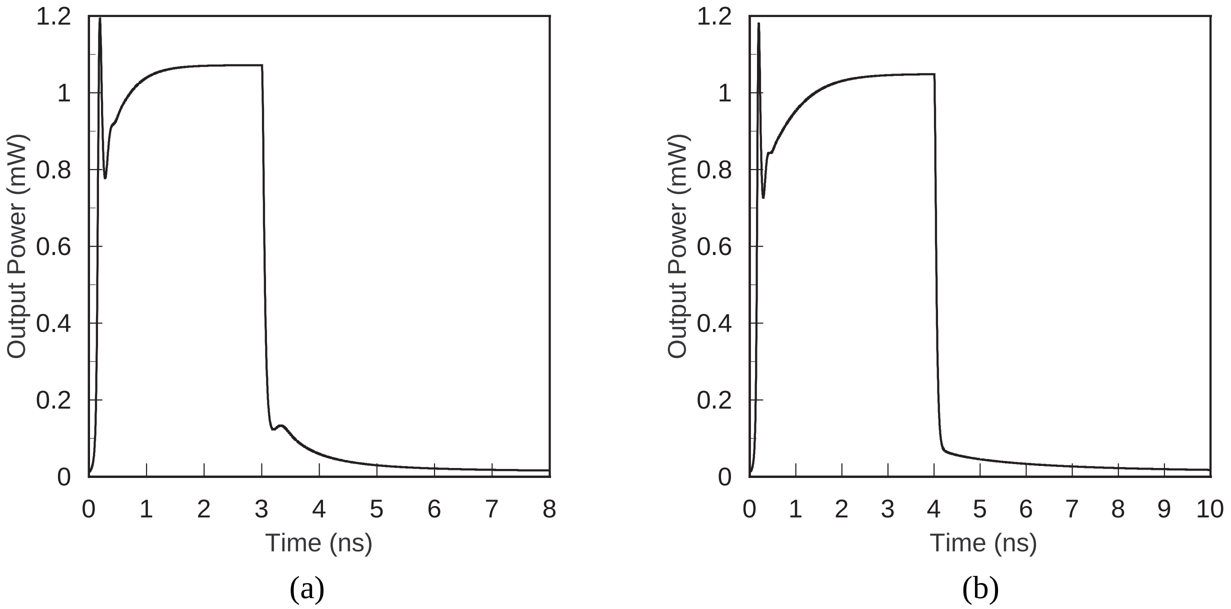

(a) (b)

Figure 4.7 Simulation of (a) an optical bump in the falling edge of a VCSEL's output, and (b) a slow tail during turn-off due to a smaller value of h_1.

edge.

While the above results clearly illustrate the utility of modeling a VCSEL's spatial effects using a simple spatially independent model, it is not clear whether the approach can accurately replicate the results of a true spatially dependent model such as that presented in [4.41]. To demonstrate that it can, we fit our model to the simulated transient response presented in [4.41], which illustrates relaxation oscillations in the turn-on transient and secondary pulsations during turn-off for a laser with a 0.85-mA threshold current and approximately 0.24-mW/mA differential slope efficiency. We used the following set of parameters in our simulation: $\eta_i = 1$, $\tau_n = 2.6$ ns, $G_o = 5.3 \times 10^4$ s^{-1}, $N_t = 7.5\times 10^6$, $\beta = 1.06 \times 10^{-5}$, $\tau_p = 3$ ps, $\varepsilon = 8.385 \times 10^{-7}$, $k_{fo} = 1.29 \times 10^{-8}$ W, $h_1 = 1.8$, and $\alpha = 0.9$. Comparison of our simulated laser transient with the numerical results of [4.41] is depicted in Fig. 4.8. As we can see, our model demonstrates excellent agreement with the more detailed approach, even replicating the shallow tertiary pulsation which immediately succeeds the initial secondary pulse. Even the

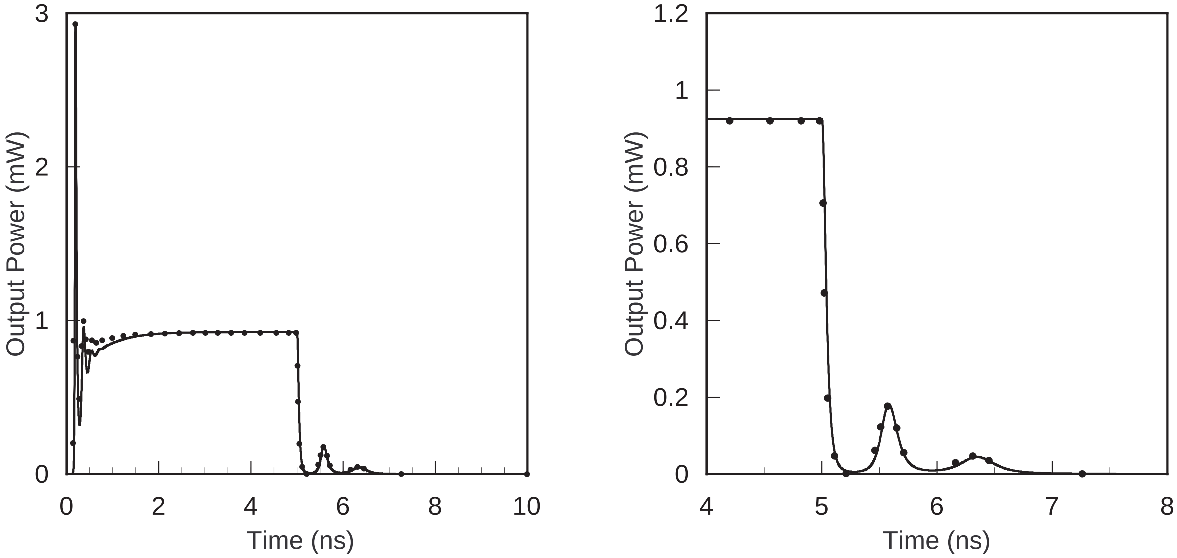

(a) (b)

Figure 4.8 (a) Comparison of simulation results from the spatially independent rate equations (lines) and a more detailed numerical model (points) presented in [4.41]. (b) Detailed comparison of the turn-off transient.

relaxation oscillations in the turn-on transient are captured reasonably well, with the only noticeable discrepancy occurring in the slow rise in the laser turn-on after the initial oscillations.

Based on the above results, it is clear that the use of spatially independent rate equations is an excellent means of accounting for spatial effects without resorting to difficult multidimensional analysis such as finite-element calculations. Thus, in the next section, we finally present our comprehensive VCSEL model which uses an even more generalized version of the approach discussed in this section.

4.5 Comprehensive Models

In this section, we present the implementation of comprehensive multimode VCSEL models in SABER. These models are based on spatially independent rate equations as described in Section 4.4. In addition to including thermal gain and carrier leakage out of a VCSEL's active region, they also account for multimode effects via the inclusion of a photon rate equation for each mode. Furthermore, transverse spatial dependencies are described in the model using either a rectangular or cylindrical coordinate system. While rectangular coordinates provide a simpler representation of the overlap integrals generated during the process of eliminating explicit spatial dependence from the model, in many cases cylindrical coordinates are more appropriate for modeling the geometry of actual VCSELs.

4.5.1 Spatially dependent rate equations

The spatially dependent rate equations upon which our models are based are more robust versions of (4.15)-(4.16). The first equation, based largely on the one presented by Moriki *et al.* in [4.47], describes the carrier number N in the active region (in this case the carrier density scaled by the volume V):

$$\frac{\partial N(\vec{r},t)}{\partial t} = \frac{\eta_i I(\vec{r},t)}{q} - \frac{N(\vec{r},t)}{\tau_n} - \sum_k G_k(\vec{r},t)S_k(t)\psi_k(\vec{r}) + \frac{L_{eff}^2}{\tau_n}\nabla^2 N(\vec{r},t) - \frac{I_l(N,T)}{q} \tag{4.27}$$

where I is the spatially dependent injection current; S_k and ψ_k are the total photon number and normalized transverse mode profile in the k^{th} transverse mode, respectively; G_k is the gain of the k^{th} mode; I_l is the thermal leakage current; τ_n is the carrier lifetime; and L_{eff} is the effective carrier diffusion length. Equation (4.27) is similar to Eq. (7) from [4.47], with the most noticeable differences being the addition of thermal gain and leakage. As we can see, unlike (4.15), (4.27) accounts for multiple transverse modes by including a stimulated emission term for each one. Furthermore, the general spatial vector $\vec{r}$ is used to account for arbitrary coordinate systems; as we shall show later, in rectangular coordinates this vector reduces to the single coordinate x, whereas in cylindrical coordinates it reduces to the radius r. Diffusion is included via the Laplacian of the carrier density. Finally, the leakage current of Section 4.3 is included as an offset to the injection current, similar to the offset current in Chapter 3. However, in this case the current directly models the actual leakage from the VCSEL's active region.

The remaining spatially dependent rate equations describe the total photon number in each mode k, and again are based on those from [4.47]. The equation for mode k is

$$\frac{\partial S_k(t)}{\partial t} = -\frac{S_k(t)}{\tau_{pk}} + \frac{\beta_k}{\tau_n}\cdot\frac{1}{V}\int_{V_T} N(\vec{r},t)dv + \frac{1}{V}\int_{V_T} G_k(\vec{r},t)S_k(t)\psi_k(\vec{r})dv \tag{4.28}$$

where β_k and τ_{pk} are the spontaneous-emission coupling coefficient and photon lifetime, respectively, for the k^{th} mode, and V_T is the total volume of the active region. As we can see, the time rate of change of the total photon number S_k depends on the total photon loss, as well as coupled spontaneous and stimulated emission. The integrations over the active volume V_T account for all of the contributing emission events occurring within the active region. Note that we again neglect the dependence of the spontaneous emission on the mode profiles [4.46], assuming instead that it is accounted for in β_k.

In the above equations, gain and leakage were accounted for via the terms G_k and I_l, respectively. The gain G_k for the k^{th} mode can be described using

$$G_k(\vec{r}, t) = \frac{G(T)(N(\vec{r}, t) - N_t(T))}{1 + \sum_m \varepsilon_{mk} S_m(t)} \tag{4.29}$$

As we can see, this is simply (4.10) with an additional term describing gain saturation. $G(T)$ models the thermally dependent gain constant via (4.11). Because of the small spacing between a VCSEL's transverse modes [4.6],[4.50], we use the same material gain $G(T)[N - N_t(T)]$ for each mode. The gain saturation term, on the other hand, assumes contributions from all of the transverse modes k, where ε_{mk} is the gain saturation factor of mode k due to mode m. A similar approach has been used to model the interaction of longitudinal modes in semiconductor lasers [4.4]. While in principle the gain saturation should also be spatially dependent [4.32], [4.51], for simplicity we choose to neglect this dependence [4.41].

The thermal leakage current, meanwhile, can be described using (4.14). As we did in Section 4.4, we will be using integration to eliminate the spatial dependence of (4.27)-(4.28). Consequently, the use of (4.14) in conjunction with a series expansion for the carrier density would mean that the overlap integrals would no longer be constant, but instead functions of the carrier-profile expansion coefficients, which are themselves functions of the model's operating conditions. In this case, we would have to solve the overlap integrals during simulation, an unacceptable proposition. One solution would be to linearize (4.14). However, because the leakage itself is highly nonlinear, this approach is also untenable. Instead, we opt to replace N in (4.14) with N_0, which, as we saw in the last section, is the constant component of the carrier profile's series expansion and in general accounts for the average carrier number in the active region. Thus,

$$I_l = I_{lo} \exp\left(\frac{-a_0 + a_1 N_0 + a_2 N_0 T - \dfrac{a_3}{N_0}}{T}\right) \tag{4.30}$$

This equation allows us to model the nonlinear leakage without requiring the calculation of the overlap integrals during simulation. Though it appears that any spatial dependence has been eliminated from the leakage, in reality N_0 implicitly accounts for it, since effects such as SHB act to increase the total carrier number in order to compensate for the loss of carriers in the spatial holes.

Equations (4.27)-(4.30) can be converted into spatially independent equations using the methodology of Section 4.4. Below, we perform this conversion for both rectangular and cylindrical device geometries. As we shall see, the resulting equations not only permit the detailed modeling of a VCSEL's thermally and spatially dependent operation, but are simple enough to be implemented in a circuit-level simulator.

4.5.2 Spatially independent model using a rectangular coordinate system

In the simplest case, we can convert (4.27)-(4.30) into spatially independent equations by using the one-dimensional rectangular coordinate system of Section 4.4. This is the same approach taken in [4.34], [4.36], and [4.46]. In this case, we replace $\vec{r}$ with the coordinate x. While this neglects two-dimensional effects, it permits VCSEL operation to be modeled in a simple and intuitive manner. First, we assume that the integrations over V_T can be reduced to one-dimensional integrations over the active-region width W_T, where contributions in the y and z directions are lumped into the gain constant and spontaneous emission coupling coefficient. Next, we assume that the carrier distribution can be modeled using (4.19), where $W \leq W_T$ (and W corresponds to the volume V). From (4.19), we see that this condition assumes that at W, the slope of the carrier profile is zero [4.11]. This assumption can be understood as follows. First, if we choose $W = W_T$, then we are simply forcing the carrier profile to remain flat at the active layer boundaries. When $W < W_T$, however, W corresponds to an effective boundary defined by the current injection profile, where the majority of the current is near the center of the VCSEL [4.11]. In this case, we assume that the carrier distribution peaks near this boundary, and that this peak does not appreciably move with changing operating conditions. Because the carrier-profile expansion is only valid within the width W, the accuracy of the model should begin to decrease as W becomes increasingly smaller than W_T. Typically, though, we can approximate $W = W_T$, even in devices where the carriers can laterally diffuse away from the current confinement region. In this case, the relative widths of the injection-current, carrier, and mode profiles need to be adjusted through parameter extraction to compensate for the absence of more detailed geometrical information.

The normalized photon distribution $\psi_k(x)$, meanwhile, can assume an arbitrary shape depending on the particular device under consideration. Various alternatives are discussed in Section 4.6. In general, however, we define the normalized distribution such that

$$\frac{1}{W} \cdot \int_{-\infty}^{\infty} S_k \psi_k(x) dx = S_k \qquad \Rightarrow \qquad \frac{1}{W} \cdot \int_{-\infty}^{\infty} \psi_k(x) dx = 1 \tag{4.31}$$

Similarly, we define the spatially dependent current using

$$I(x) = I_o f_i(x) \tag{4.32}$$

where I_o is the total current flowing through the device, and $f_i(x)$ is the normalized current distribution defined such that

$$\frac{1}{W}\cdot\int_{-W/2}^{W/2} I_o f_i(x)dx = I_o \qquad \Rightarrow \qquad \frac{1}{W}\cdot\int_{-W/2}^{W/2} f_i(x)dx = 1, \tag{4.33}$$

where we have assumed that the current is confined to the width *W*.

Substituting (4.19) into (4.27)-(4.28), we can now integrate out the spatial dependence from (4.27) and (4.28). In so doing, we make use of the following relations:

$$\int_{-W/2}^{W/2} \cos\left(\frac{2\pi ix}{W}\right)\cos\left(\frac{2\pi jx}{W}\right)dx = \begin{cases} W/2 & i = j \\ 0 & i \neq j \end{cases} \tag{4.34}$$

$$\nabla^2 N(x, t) = \sum_{i=1}^{\infty}\left(\frac{2\pi i}{W}\right)^2 N_i \cos\left(\frac{2\pi ix}{W}\right) \tag{4.35}$$

Equation (4.34) is simply the orthogonality condition of the Fourier series expansion, while (4.35) is the diffusion term from (4.27) in terms of that same expansion. Using these equations, we first scale (4.27) by 1/*W* and integrate over [-*W*/2,+*W*/2], thereby producing the rate equation for N_0. Next, we scale (4.27) by $-(2/W)\cdot\cos(2\pi jx/W)$ and again integrate over [-*W*/2,+*W*/2], this time yielding the rate equations for each term N_j ($j > 0$) in the Fourier expansion of the carrier distribution. Finally, we carry out the integrations in (4.28). The resulting set of spatially independent rate equations is

$$\frac{dN_0}{dt} = \frac{\eta_i I_o}{q} - \frac{N_0}{\tau_n} - \sum_k \frac{G(T)\left[\gamma_{k0}N_0 - \sum_{i=1}^{\infty}\gamma_{ki}N_i - \gamma_{k0}N_t(T)\right]S_k}{1 + \sum_m \varepsilon_{mk}S_m} - \frac{I_l}{q} \tag{4.36}$$

$$\frac{dN_j}{dt} = \frac{-\eta_i I_o}{q}\cdot\zeta_j - \frac{N_j}{\tau_n}(1 + h_j) + \sum_k \frac{G(T)\left[\phi_{jk0}N_0 - \sum_{i=1}^{\infty}\phi_{jki}N_i - \phi_{jk0}N_t(T)\right]S_k}{1 + \sum_m \varepsilon_{mk}S_m} \tag{4.37}$$

$$\frac{dS_k}{dt} = -\frac{S_k}{\tau_{pk}} + \frac{\beta_k}{\tau_n}\left[b_0 N_0 - \sum_{i=1}^{\infty} b_i N_i\right] + \frac{G(T)\left[\lambda_{k0}N_0 - \sum_{i=1}^{\infty}\lambda_{ki}N_i - \lambda_{k0}N_t(T)\right]S_k}{1 + \sum_m \varepsilon_{mk}S_m} \tag{4.38}$$

As was the case with the simple model of Section 4.4, we have managed to replace explicit spatial dependencies with constants. Diffusive effects are accounted for via the parameters h_j, where

$$h_j = \left(\frac{2\pi j L_{eff}}{W}\right)^2 \tag{4.39}$$

The parameters b_i model the integrated spontaneous emission in (4.28), where

$$b_0 = \frac{W_T}{W} \tag{4.40a}$$

$$b_i = \frac{\sin\left(\frac{\pi i W_T}{W}\right)}{\pi i} \tag{4.40b}$$

The current profile is accounted for via

$$\zeta_j = \frac{2}{W}\cdot\int_{-W/2}^{W/2}\cos\left(\frac{2\pi j x}{W}\right)f_i(x)dx \tag{4.41}$$

Finally, overlap of the gain and mode profiles is accounted for by the overlap integral values γ_{ki}, ϕ_{jki}, and λ_{ki}, where

$$\gamma_{ki} = \frac{1}{W}\cdot\int_{-W/2}^{W/2}\cos\left(\frac{2\pi i x}{W}\right)\psi_k(x)dx \tag{4.42}$$

$$\phi_{jki} = \frac{2}{W}\cdot\int_{-W/2}^{W/2}\cos\left(\frac{2\pi i x}{W}\right)\psi_k(x)\cos\left(\frac{2\pi j x}{W}\right)dx \tag{4.43}$$

$$\lambda_{ki} = \frac{1}{W} \cdot \int_{-W_T/2}^{W_T/2} \cos\left(\frac{2\pi i x}{W}\right) \psi_k(x) dx \tag{4.44}$$

For certain mode profiles, such as the sinusoidal distribution from Section 4.4, (4.42)-(4.44) can be calculated analytically. In general, however, numerical integration is necessary. Fortunately, as we noted before, these integrations are required only once for a given set of device parameters.

4.5.3 Spatially independent model using a cylindrical coordinate system

For many VCSELs, a cylindrical coordinate system is a more appropriate choice for modeling the device geometry [4.11], [4.47]. If we neglect azimuthal variations in the carrier and mode profiles [4.11], then we can perform the analysis in terms of the radial coordinate *r*. First, analogous to the approach in rectangular coordinates, we assume that integrations over V_T can be converted into integrations over a *radius* W_T, with azimuthal and longitudinal contributions lumped into the gain constant and spontaneous emission coupling coefficient. Next, we identify a suitable series expansion for the carrier profile. As we mentioned in Section 4.4, in cylindrical coordinates the appropriate choice is a Bessel-series expansion. Let us assume, similar to our approach in rectangular coordinates, that the slope of the carrier profile is zero at some radius $W \le W_T$ [4.11], which corresponds, roughly, to the radius of the current injection. We can then describe the carrier profile using the following Bessel-series expansion [4.11],[4.47]:

$$N(r) = N_0 - \sum_{i=1}^{\infty} N_i J_0\left(\frac{\sigma_i r}{W}\right) \tag{4.45}$$

where σ_i is the i^{th} root of the first-order Bessel function $J_1(x)$, with $\sigma_0 = 0$. As illustrated in Fig. 4.9, the two-term version of (4.45) [4.9] looks very much like that from the Fourier-series expansion, with

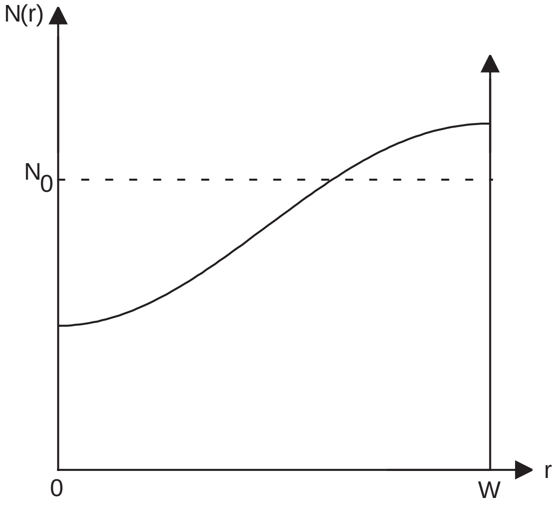

Figure 4.9 Two-term Bessel-series expansion of the radial carrier profile.

the constant term representing an average carrier number, and the second term accounting for a spatial hole produced by the VCSEL’s fundamental transverse mode.

Meanwhile, we can again model the photon distribution $\psi_k(r)$ using an arbitrary mode shape. However, this time we define the normalization condition as

$$\frac{2}{W^2}\cdot\int_0^{\infty} S_k\psi(r)r\,dr = S_k \qquad \Rightarrow \qquad \frac{2}{W^2}\cdot\int_0^{\infty}\psi(r)r\,dr = 1 \tag{4.46}$$

Likewise, the spatially dependent current is

$$I(r) = I_o f_i(r) \tag{4.47}$$

where I_o is the total current flowing through the device, and $f_i(r)$ is the normalized current distribution defined such that

$$\frac{2}{W^2}\cdot\int_0^{W} I_o f_i(r)r\,dr = I_o \qquad \Rightarrow \qquad \frac{2}{W^2}\cdot\int_0^{W} f_i(r)r\,dr = 1\,, \tag{4.48}$$

where we have assumed that the current is confined to the radius W.

Proceeding similarly to the rectangular case, we next substitute (4.45) into (4.27)-(4.28) and integrate out the spatial dependence, making use of the following relations:

$$\int_0^W J_0\left(\frac{\sigma_i r}{W}\right) J_0\left(\frac{\sigma_j r}{W}\right) r dr = \begin{cases} \frac{W^2}{2} \cdot J_0{}^2(\sigma_i) & i = j \\ 0 & i \neq j \end{cases} \tag{4.49}$$

$$\nabla^2 N(r, t) = \sum_{i=1}^{\infty} \left(\frac{\sigma_i}{W}\right)^2 N_i J_0\left(\frac{\sigma_i r}{W}\right) \tag{4.50}$$

where (4.49) is the orthogonality condition of the Bessel-series expansion and (4.50) is the diffusion term from (4.27) in terms of that same expansion. First, we scale (4.27) by $2/W^2$ and integrate over $[0,W]$, thereby producing the rate equation for N_0. Next, we scale (4.27) by $-(2/W^2) \cdot (J_0{}^2(\sigma_j))^{-1}$ and again integrate over $[0,W]$, this time yielding the rate equations for each term N_j ($j > 0$) in the Bessel-series expansion. Finally, we carry out the integrations in (4.28). Note that this approach is equivalent to the one taken in [4.9], [4.11], and [4.47], where the authors also transformed spatially dependent rate equations using a Bessel-series expansion for the carrier profile.

The resulting set of spatially independent rate equations can again be described by (4.36)-(4.38), and are very similar to the equations from [4.47], with the major exception being the inclusion of terms for the thermal gain and carrier leakage. Compared to the rectangular case of Section 4.5.2, the various constant terms described by (4.39)-(4.44) must now be modified to account for the cylindrical coordinate system. Diffusive effects are modeled via the parameters h_j, where

$$h_j = \left(\frac{\sigma_j L_{eff}}{W}\right)^2 \tag{4.51}$$

The integrated spontaneous emission is modeled through the parameters b_i, where

$$b_0 = \left(\frac{W_T}{W}\right)^2 \tag{4.52a}$$

$$b_i = \frac{2W_T}{W\sigma_i} J_1\left(\frac{\sigma_i W_T}{W}\right) \tag{4.52b}$$

Meanwhile, the current distribution is accounted for through

$$\zeta_j = \frac{2}{W^2 {J_0}^2(\sigma_j)} \cdot \int_0^W J_0\left(\frac{\sigma_j r}{W}\right) f_i(r) r dr \tag{4.53}$$

Finally, the overlap integral values γ_{ki}, ϕ_{jki}, and λ_{ki} are

$$\gamma_{ki} = \frac{2}{W^2} \cdot \int_0^W J_0\left(\frac{\sigma_i r}{W}\right) \psi_k(r) r dr \tag{4.54}$$

$$\phi_{jki} = \frac{2}{W^2 {J_0}^2(\sigma_j)} \cdot \int_0^W J_0\left(\frac{\sigma_i r}{W}\right) \psi_k(r) J_0\left(\frac{\sigma_j r}{W}\right) r dr \tag{4.55}$$

$$\lambda_{ki} = \frac{2}{W^2} \cdot \int_0^{W_T} J_0\left(\frac{\sigma_i r}{W}\right) \psi_k(r) r dr \tag{4.56}$$

Because of the use of a Bessel-series expansion, in almost all cases numerical integration is necessary to calculate the above expressions.

4.5.4 Complete model

Summarizing the above results, we see that we can model a VCSEL’s spatial and thermal behavior using the spatially independent rate equations (4.36)-(4.38), expressions (4.11)-(4.12) and (4.30) for the thermal gain and leakage, and the constants h_j, b_i, ζ_j, γ_{ki}, ϕ_{jki}, and λ_{ki}, which are determined according to the choice of coordinate system. To complete the model, we first relate the photon number S_k in each mode to the corresponding output power P_k using

$$P_k = k_{fk} S_k \tag{4.57}$$

where k_{fk} is the output-power coupling coefficient of the k^{th} mode.

Next, as we did in Chapter 3, we model the VCSEL temperature T using a thermal rate equation [4.9], [4.52]:

$$T = T_o + \left(I_{tot} V - \sum_k P_k \right) R_{th} - \tau_{th} \frac{dT}{dt} \tag{4.58}$$

where T_o is the ambient temperature, I_{tot} is the total current flowing through the device, V is the device voltage, and τ_{th} is a thermal time constant. Note that, unlike the equation from Chapter 3, (4.58) accounts for multiple modes.

Finally, we model the electrical characteristics using the same technique we applied to the simple thermal VCSEL model of Chapter 3. We model the device voltage V using an empirical function of temperature and current:

$$V = f(I_o, T) \tag{4.59}$$

where we assume that the current corresponding to this voltage is the cavity injection current I_o. Parasitic effects can be modeled in parallel with this voltage. Figure 4.10 illustrates this arrangement, where the currents I_{tot} and I_o are clearly identified and a parasitic shunting capacitance C_l is used to account for parasitic effects.

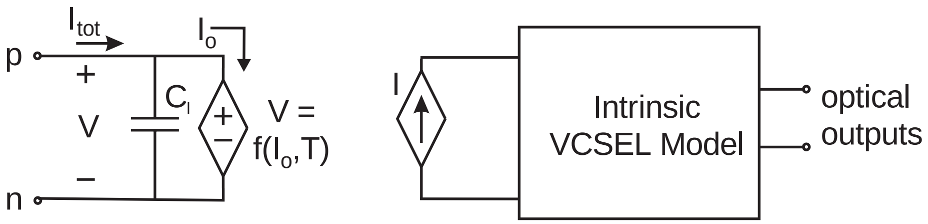

Figure 4.10 Complete VCSEL model, including elements for modeling electrical characteristics.

Examination of our complete model reveals a number of similarities with the efforts of other researchers. As we noted in Section 4.4, many authors have used the Fourier-series expansion to model the transverse carrier profile in semiconductor lasers. However, these efforts were not focused on VCSELs, and therefore neglected thermal behavior. Moriki *et al.* [4.47] suggested the use of a Bessel-series expansion to describe VCSELs, but also neglected thermal effects, as well as parasitics. Dellunde *et al.* [4.11] also used a Bessel-series expansion to generate spatially independent multi-mode rate equations, but again, failed to include thermal behavior or parasitic effects. In [4.9], rate equations similar to the ones presented here are used, with the carrier profile modeled as a two-term Bessel-series expansion. Furthermore, like our approach, device temperature is modeled via a thermal rate equation, and thermal gain is accounted for through polynomial functions of that temperature. In addition, unlike our model, carrier transport is included via an additional rate equation for the confinement-layer carriers, as discussed in Chapter 2. Despite these features, the authors fail to include thermally dependent leakage current, and limit their analysis to a single mode. They also do not model parasitic effects in the device. Clearly then, though our model incorporates various approaches discussed in the literature, to the best of our knowledge this is the first time that they are being used in a comprehensive manner. Furthermore, this is the first time this type of model is being implemented in a circuit-level simulation environment.

4.5.5 Implementation in SABER

We have implemented our model in Analogy’s SABER. As we desired, this allows us to model VCSELs in conjunction with electronics and other optoelectronic devices, thereby facilitating the design and simulation of optoelectronic applications. This would not have been the case if we had implemented a spatially dependent VCSEL model. As we have explained in some detail, the use of less computationally intensive models such as those presented in this chapter is critical for optoelectronic CAD.

As discussed in Chapter 3, a particular advantage of SABER is that, while it supports circuit-level netlisting like SPICE, it also allows device behavior to be described explicitly in terms of differential equations using the behavioral modeling language MAST. This capability dramatically simplifies the implementation of circuit-level models, making our approach particularly attractive for use in optoelectronic system design. Thus, we have implemented two versions of our model as MAST templates, the details of which can be found in Appendix F. The first template models a single-mode VCSEL with a two-term carrier-profile expansion, while the second models a two-mode VCSEL with a three-term carrier-profile expansion. In each case, the constants h_j, b_i, ζ_j, γ_{ki}, ϕ_{jki}, and λ_{ki} are included as model parameters. By not implementing the calculation of these parameters within the templates themselves, we make the model implementations independent of the choice of coordinate-system. Depending on this choice, specific numerical values can be determined independently by the user and passed into the model during simulation.

Another feature of our implementation is the use of variable transformations such as the ones described in Chapters 2 and 3. In this case, we transform P_k, N_0, and N_j into the variables v_{mk}, v_{n0}, and v_{nj}, respectively, using

$$P_k = (v_{mk} + \delta_m)^2 \tag{4.60}$$

$$N_0 = z_n(v_{n0} + \delta_n)^2 \tag{4.61}$$

$$N_j = z_n v_{nj} \tag{4.62}$$

where δ_m, δ_n, and z_n are arbitrary constants. Eqs. (4.60)-(4.61) ensure a nonnegative solution for P_k and N_0 [4.53], while (4.62) scales N_j to improve convergence [4.54].

An example of the single-mode template is illustrated in Fig. 4.11. As we can see, the use of MAST allows the relatively involved differential equations (4.36)-(4.38) to be implemented in a very straightforward manner. By defining the transformations of (4.60)-(4.62) in separate equations, we allow (4.36)-(4.38) to be implemented explicitly in terms of P_k, N_0, and N_j. In later sections, we shall demonstrate that this model, as well as the two-mode version, can be used to simulate the complex behavior of VCSELs. However, we will first discuss various analytical forms for the mode profiles ψ_k.

4.6 Mode Profiles

In order to use the models of Section 4.5, we need expressions for the mode profiles ψ_k. While these expressions will implement fixed mode shapes, in many VCSELs the profiles change as a function of bias. For example, self-focusing in some devices can cause the fundamental mode to shrink with increasing bias [4.32]. Similarly, thermal lensing in gain-guided VCSELs can also result in a shrinking fundamental mode [4.17]. While more exact representations would account for this bias dependence, we have elected to keep our mode profiles fixed, like what would be found in index-guided devices. The discrepancy that may occur in gain-guided or weakly-index-guided devices must then be accounted for during parameter extraction. Below, we review a number of choices for ψ_k in both the rectangular and cylindrical coordinate systems.

4.6.1 Rectangular coordinate system

When using our comprehensive VCSEL model in the rectangular coordinate system, there are two obvious choices for the normalized mode profiles $\psi_k(x)$. The first is based on the simple sinusoid used in Section 4.4. Extending this distribution to higher-order terms, we obtain

```
element template vcsel12 p n pf0 pf1 = etai, tn, go, nto,
                                       tp0, tp1, kf0, kf1, be0, be1,
                                       b, eps00, eps01, eps10, eps11,
                                       lam, gam, phi, zet, h, tth,
                                       rth, ag0, ag1, ag2, bg0, bg1, bg2,
                                       cn0, cn1, cn2, ilo, a0, a1, a2, a3,
                                       claser, zn, dn, dm
electrical p, n, pf0, pf1          # pins (electrical- p,n; optical- pf0,pf1)
number etai = 1, tn = 5e-9, go = 1e4, nto = 1e8,      # argument defaults
       tp0 = 1e-12, tp1 = 1e-12, kf0 = 1e-8, kf1 = 1e-8, be0 = 1e-3, be1 = 1e-3,
       b[0:2] = [1,0,0], eps00 = 0, eps01 = 0, eps10 = 0, eps11 = 0,
       lam[0:1,0:2] = [1,0,0, 1,0,0], gam[0:1,0:2] = [1,0,0, 1,0,0],
       phi[1:2,0:1,0:2] = [1,0,0, 1,0,0, 1,0,0, 1,0,0],
       zet[1:2] = [0,0], h[1:2] = [1,1], tth = 0,
       rth = 1000, ag0 = 1, ag1 = 0, ag2 = 0, bg0=1, bg1 = 0, bg2 = 0,
       cn0 = 1, cn1 = 0, cn2 = 0, ilo = 0, a0 = 0, a1 = 0, a2 = 0, a3 = 0,
       claser = 1e-12, zn = 1e8, dn = 5e-10, dm = 5e-10
external number temp      # simulation temperature

{
branch ipn = i(p->n), vpn = v(p,n)     # cavity branch defns.
branch ipnc = i(p->n), vpnc = v(p,n)   # capacitor branch defns.
val v gth, ntth           # gain/transparency as fns. of temp.
var i fleak               # temp.-dependent leakage-current factor
val v p0                  # output power in modes 0,1,...
val v n0,n1               # carrier number term 0,1,...
var v vn0,vn1             # voltages related to carrier numbers
var v vm0                 # voltage related to modes 0,1,...
var v gm0                 # modal gain values for modes 0,1,...
var i ipf0,ipf1           # current from output node pf0,pf1,...
var tc tjct               # junction temperature

# local variables and constants
number kb = 1.38062e-23, q  = 1.60219e-19

# thermal-gain temperature defines...
gth   = go*(ag0+ag1*(tjct+273.15)+ag2*(tjct+273.15)**2)/                      \
           (bg0+bg1*(tjct+273.15)+bg2*(tjct+273.15)**2)
ntth  = nto*(cn0+cn1*(tjct+273.15)+cn2*(tjct+273.15)**2)
# leakage-current-factor definition
fleak = (ilo/q)*limexp((-a0+a1*zn*(vn0+dn)**2+a2*(tjct+273.15)*zn*(vn0+dn)**2 -   \
                     a3/(zn*(vn0+dn)**2))/(tjct+273.15))

# assign transforms for pk and nj
p0 = (vm0 + dm)**2
n0 = zn*(vn0+dn)**2
n1 = zn*vn1

# electrical representation of laser diode
vpn = 12928.567*ipn/(tjct+273.15-198.73691) +        \
      1.4679311*ln(1+255966.659082*ipn/(tjct+273.15-198.73691))
ipnc = d_by_dt(vpnc*claser)
```

Figure 4.11 MAST-template implementation of the comprehensive VCSEL model for a single mode and a two-term expansion of the carrier profile (*continued on next page*).

```
# determine junction temperature
tjct: tjct = ((ipn+ipnc)*vpn - p0)*rth + temp - d_by_dt(tth*tjct)

# vcsel rate equations for photons
vm0: d_by_dt(p0) = -p0/tp0 + (be0*kf0/tn)*(b[0]*n0 - b[1]*n1)                  \
     + gth*(lam[0,0]*n0 - lam[0,1]*n1 - lam[0,0]*ntth)*p0/(1+eps00*p0/kf0)

# vcsel rate equation for carrier term n0
vn0: d_by_dt(n0) = etai*ipn/q - n0/tn                                            \
     - gth*(gam[0,0]*n0 - gam[0,1]*n1 - gam[0,0]*ntth)*p0/kf0/(1+eps00*p0/kf0)  \
     - fleak

# vcsel rate equation for carrier term n1
vn1: d_by_dt(n1) = -etai*ipn*zet[1]/q - n1*(1+h[1])/tn                           \
     + gth*(phi[1,0,0]*n0 - phi[1,0,1]*n1 -phi[1,0,0]*ntth)*p0/kf0/              \
           (1+eps00*p0/kf0)

# modal gain calculations (neglecting gain compression)
gm0: gm0 = gth*(lam[0,0]*n0 - lam[0,1]*n1 - lam[0,0]*ntth)

# optical output
i(pf0) += ipf0
i(pf1) += ipf1
ipf0: v(pf0) = p0
ipf1: v(pf1) = 0

}
```

Figure 4.11 (*Continued.*)

$$\psi_k(x) = \begin{cases} \dfrac{2W}{W_m}\cos^2\left[\dfrac{\pi(k+1)x}{W_m}\right] & |x| \le \dfrac{W_m}{2},\ k = 0, 2, 4, \ldots \\[2ex] \dfrac{2W}{W_m}\sin^2\left[\dfrac{\pi(k+1)x}{W_m}\right] & |x| \le \dfrac{W_m}{2},\ k = 1, 3, 5, \ldots \\[2ex] 0 & |x| > \dfrac{W_m}{2} \end{cases} \tag{4.63}$$

where W_m defines the mode width. Essentially, (4.63) models the intensity distributions of the harmonics in a 1-D resonator, with the even modes corresponding to cosines and the odd modes corresponding to sines. The leading coefficients were defined according to the normalization condition

(4.31). Figure 4.12 illustrates the first two modes $k = 0$ and 1.

The biggest advantage of (4.63) is that it leads to analytical expressions for the overlap integrals, as we saw in Section 4.4. However, rigorously speaking, it only applies to a cavity with perfect mode confinement. When this is not the case, a more exact representation can be found in the Hermite-Gaussian mode solutions, which have been used to model the mode profiles in actual VCSELs [4.10], [4.32], [4.43]. These solutions can be described using [4.55]:

$$\psi_k(x) = \alpha_k\left[H_k\left(\frac{\sqrt{2}x}{W_m}\right)\right]^2 e^{-2(x/W_m)^2} \tag{4.64}$$

where $H_k(x)$ are the Hermite polynomials, W_m is the characteristic width for this particular set of Hermite-Gaussian solutions, and α_k are normalization constants determined using (4.31). Though in some cases a complex Hermite-Gaussian mode solution may be more appropriate [4.55], the solutions presented here serve as useful representations of a VCSEL's actual mode profiles [4.10]. Figure 4.13 illustrates the first three Hermite-Gaussian modes, where for clarity we have scaled the distributions

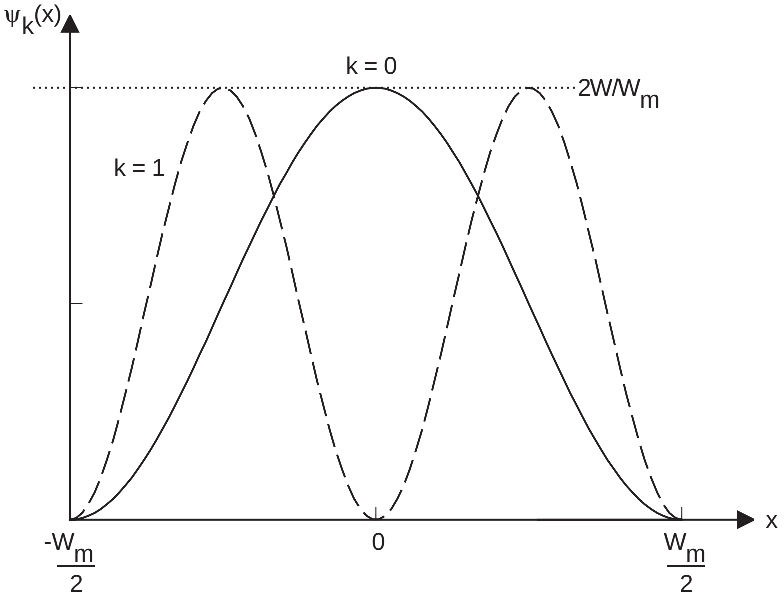

Figure 4.12 First two sinusoidal mode profiles defined by (4.63).

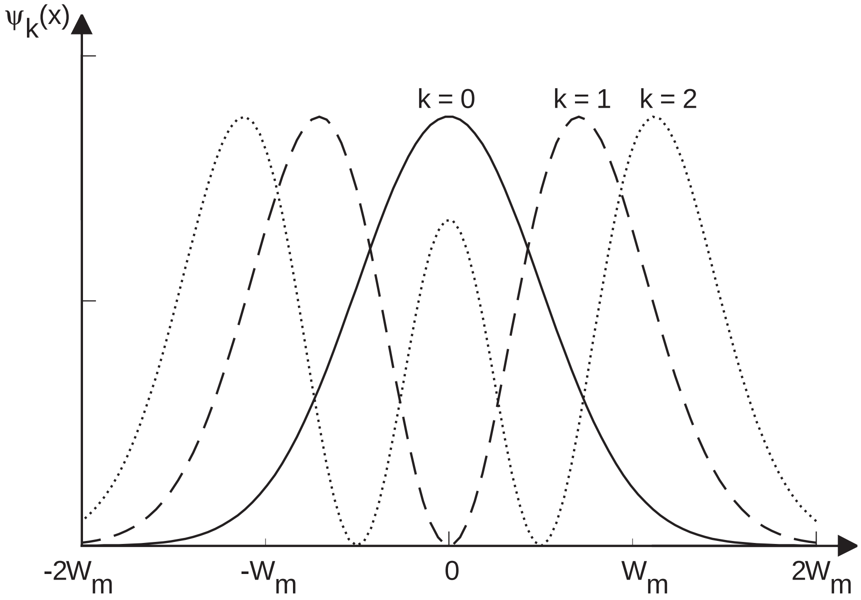

Figure 4.13 First three Hermite-Gaussian modes.

such that their peak values are approximately equal. These solutions correspond to the first three Hermite polynomials:

$$H_0(x) = 1 \tag{4.65a}$$

$$H_1(x) = 2x \tag{4.65b}$$

$$H_2(x) = 4x^2 - 2 \tag{4.65c}$$

As can be seen, the fundamental mode is a Gaussian, while the first higher-order mode has a donut-shape.

4.6.2 Cylindrical coordinate system

In cylindrical coordinates, a simple solution such as the sinusoidal mode profiles described above does not exist. However, mode profiles analogous to the Hermite-Gaussian solutions can be used, namely Laguerre-Gaussian (LG) modes [4.31]. Similar to their Hermite-Gaussian counterparts, these solutions are based on *Laguerre* polynomials, which, in general, have complex arguments [4.31], [4.55]. However, we can still obtain a useful approximation of the transverse mode shapes by neglecting any complex parameters and using the standard Laguerre-Gaussian function [4.55]:

$$\psi_{pl}(r) = \alpha_{pl} \cdot \left(\frac{\sqrt{2}r}{W_m}\right)^{2l} \cdot \left[L_p^l\left(\frac{2r^2}{W_m^2}\right)\right]^2 \cdot e^{-2(r/W_m)^2} \tag{4.66}$$

Note that we have replaced the mode-index *k* with *pl*, where *p* is the radial index and *l* is the azimuthal index. Also, explicit reference to the angular dependence has been ignored. In (4.66), $L_p^l(x)$ are the generalized Laguerre polynomials, α_{pl} is the normalization coefficient defined by (4.46), and W_m is the characteristic width of the family of LG modes. Clearly, (4.66) is very much like (4.64).

Figure 4.14 illustrates three of the lowest-order LG modes, with the normalization constants α_{pl} set to 1. These distributions correspond to the 00, 10, and 11 generalized Laguerre polynomials:

$$L_0^0(x) = 1 \tag{4.67a}$$

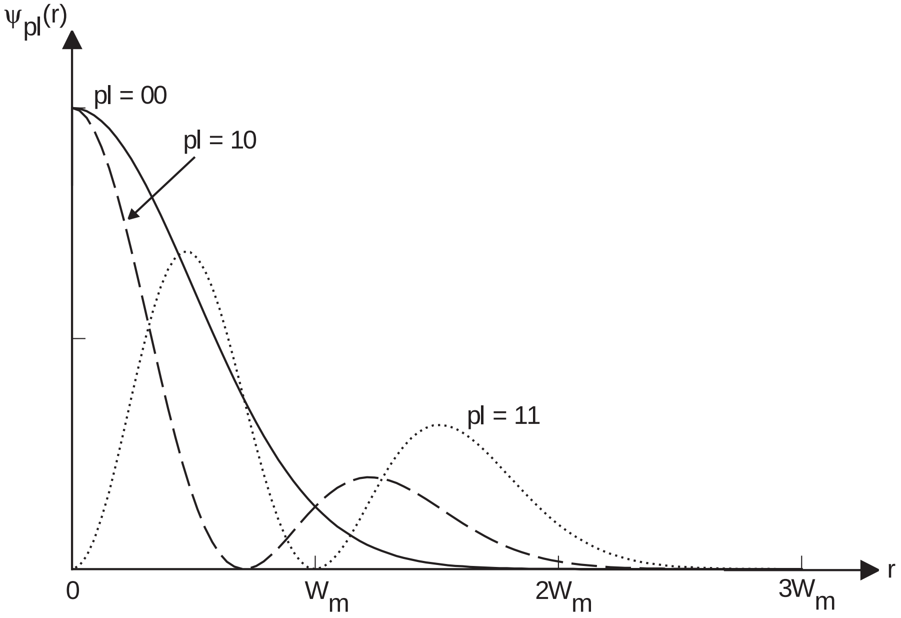

Figure 4.14 The 00, 10, and 11 Laguerre-Gaussian modes.

$$L_1^0(x) = 1 - x \tag{4.67b}$$

$$L_1^1(x) = 2 - x \tag{4.67c}$$

Clearly, the first two higher-order modes do not correspond to donut modes. However, this kind of solution *has* been used to represent the measured mode profiles in actual devices, namely gain-guided VCSELs [4.31], [4.56].

In cases where low-order donut modes are required, a different representation of the mode profiles can be used. The LP_{kl} modes have been used by many researchers to describe VCSEL transverse mode profiles. They have been observed in actual devices [4.29], as well as used extensively to model, among other things, mode competition, mode-partition noise, and gain-switching in VCSELs [4.11], [4.39], [4.41], [4.57]-[4.59]. Neglecting angular dependencies, we can model the LP_{kl} modes using [4.11], [4.39]:

$$\psi_k(r) = \begin{cases} \alpha_k J_k^2(u_k r / W_m) & 0 < r < W_m \\ \alpha_k K_k^2(w_k r / W_m) \cdot \dfrac{J_k^2(u_k)}{K_k^2(w_k)} & r > W_m \end{cases} \tag{4.68}$$

where, because of the absence of angular dependence, we have dropped the mode-index l. In (4.68), α_k is the normalization constant, $J_k(x)$ and $K_k(x)$ are the Bessel functions of the first and second kind, and W_m is a characteristic mode width. The parameters u_k and w_k are eigenvalue solutions of the optical waveguide for which (4.68) is a solution.

To be exact, (4.68) actually represents approximate solutions for a weakly-index-guided cylindrical waveguide [4.11], [4.39]. As discussed in [4.60], for a waveguide with core index n_1, cladding index n_2, core radius W_m, and free-space wave number k_o, the solutions for the transverse mode profiles can be approximately determined in terms of the propagation constant β_k. We can define the eigenvalues u_k and w_k in terms of β_k:

$$u_k = W_m(n_1^2 k_o^2 - \beta_k^2)^{1/2} \tag{4.69}$$

$$w_k = W_m(\beta_k^2 - n_2^2 k_o^2)^{1/2} \tag{4.70}$$

The k^{th} mode solution from (4.68) can then be determined based on the eigenvalue equation

$$u_k \frac{J_{l-1}(u_k)}{J_l(u_k)} = -w_k \frac{K_{l-1}(w_k)}{K_l(w_k)} \tag{4.71}$$

and the normalization constant α_k can be calculated from (4.46).

Figure 4.15 depicts the LP_{01}, LP_{11}, and LP_{21} modes for a cavity with W_m = 3 μm, λ_o = 850 nm (corresponding to $k_o = 7.39 \times 10^6$ m^{-1}), $n_1 = 3.5$, and $n_2 = 3.4$. Similar results are obtained for even smaller index steps such as 0.01. As we can see, the LP_{01} mode is very similar to a Gaussian, while the LP_{11} and LP_{21} modes both correspond to donut-shaped profiles.

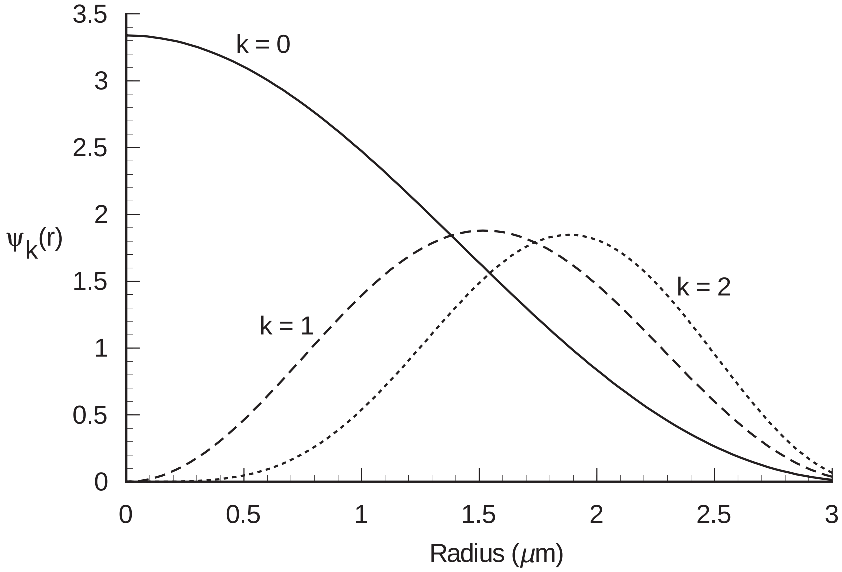

Figure 4.15 Illustration of the radial dependence of the LP_{01}, LP_{11}, and LP_{21} modes.

Now that we have identified various alternatives for the mode profiles ψ_k, we can use our comprehensive VCSEL model to simulate various interesting features of VCSEL operation. In the next section, we will use the LP_{01} and LP_{11} modes to demonstrate the capabilities of our approach; in the following section, we will use a Gaussian mode profile to fit our model to various experimental devices reported in the literature.

4.7 Example Simulations of Single- and Two-Mode Behavior

In order to demonstrate the ability of our comprehensive VCSEL model to replicate actual VCSEL behavior, we have chosen a representative set of model parameters and simulated single- and two-mode devices. While these simulations do not quantitatively validate the model via comparisons with experimental data (as is done in the next section), they do allow us to qualitatively evaluate its merits. As the following results will demonstrate, our model is capable of simulating thermally dependent threshold current, output-power rollover, small-signal behavior as a function of temperature, transient phenomena, and multimode competition.

The model parameters used in our simulations are listed in Table 4.1. A two-term carrier expansion in cylindrical coordinates was used for the single-mode VCSEL, while a three-term expansion was used for the two-mode device. The additional term is included in the latter case to account for the more complicated spatial behavior resulting from multimode operation. In reality, even more terms would improve the accuracy of the results. Also, we elected to use a cylindrical coordinate system in our model, as well as LP_{kl} modes, where LP_{01} models mode 0, and LP_{11} models mode 1 in the two-mode VCSEL. Specifically, we used the modes of Fig. 4.15 as a representative set of distributions. Note that we approximate the modes to be zero for $r > W_m$. We also assumed that the carriers

Table 4.1 Representative set of model parameters used in simulating the single- and two-mode VCSELs.

Parameter	Value
Gain-Constant Parameters	$G_o = 3 \times 10^4$ s^{-1}, $a_{g0} = -0.4$, $a_{g1} = 0.00147$ K^{-1}, $a_{g2} = 7.65 \times 10^{-7}$ K^{-2}, $b_{g0} = 1.3608$, $b_{g1} = -0.00974$ K^{-1}, $b_{g2} = 1.8 \times 10^{-5}$ K^{-2}
Transparency-Number Parameters	$N_{to} = 10^7$, $c_{n0} = -1$, $c_{n1} = 0.008$ K^{-1}, $c_{n2} = 6 \times 10^{-6}$ K^{-2}
Leakage Parameters	$I_{lo} = 9.61$ A, $a_0 = 4588.24$ K, $a_1 = 2.12 \times 10^{-5}$ K, $a_2 = 8 \times 10^{-8}$, $a_3 = 9.01 \times 10^9$ K
Overlap Integral Values γ_{ki}, λ_{ki}	$\gamma_{00} = \lambda_{00} = 1$, $\gamma_{01} = \lambda_{01} = 0.37978$, $\gamma_{02} = \lambda_{02} = -0.0018753$, $\gamma_{10} = \lambda_{10} = 1$, $\gamma_{11} = \lambda_{11} = 0.12344$, $\gamma_{12} = \lambda_{12} = -0.1653$
Overlap Integral Values ϕ_{jki}	$\phi_{100} = 2.3412$, $\phi_{101} = 1.8193$, $\phi_{102} = 0.62489$, $\phi_{110} = 0.76099$, $\phi_{111} = 0.77999$, $\phi_{112} = -0.085866$, $\phi_{200} = -0.020821$, $\phi_{201} = 1.1254$, $\phi_{202} = 1.7041$, $\phi_{210} = -1.8352$, $\phi_{211} = -0.15465$, $\phi_{212} = 0.94864$
h_1, h_2	1-mode: 15,0; 2-mode: 5, 16.76
ζ_0, ζ_1	0, 0
η_i	1.0
τ_n	2.5 ns
τ_{p0}, τ_{p1}	2.5 ps, 1.8 ps
k_{f0}, k_{f1}	1.5×10^{-8} W, 1.5×10^{-8} W
β_0, β_1	0.001, 0.001
b_0, b_1, b_2	1, 0, 0
ε_{00}, ε_{01}, ε_{10}, ε_{11}	5×10^{-7}, 0, 0, 5×10^{-7}
R_{th}	0.9 ºC/mW
τ_{th}	1 μs

are confined to a radius $W = W_m$. Because of this confinement, $W = W_T$ and therefore $\lambda_{ki} = \gamma_{ki}$. The complete set of overlap-integral values is included in Table 4.1. In the case of the single-mode simulations, the parameters corresponding to $k = 1$, $j = 2$, and $i = 2$ can be ignored.

It is worth noting that, in general, there is no need to include an explicit value for the mode width W_m. It is easy to show that for a fixed ratio $\alpha = W_m/W$, the overlap-integral values are independent of the actual device geometry. This fact is simply a generalization of the results of Section 4.4, where the overlap integrals were analytically defined in terms of α. In other words, the overlap integrals capture the shape of the mode relative to the active region dimensions; consequently, the values used here could just as easily be used for devices with different geometries. The only parameters which do explicitly account for the VCSEL geometry are h_j, which are functions of W. However, as Table 4.1 shows, we have elected to use h_j directly as one of the model parameters. Thus, as in Section 4.4, all spatial and diffusive effects can be accounted for via α and h_j.

Also of interest in Table 4.1 are the parameters which model the gain and leakage. Figure 4.16

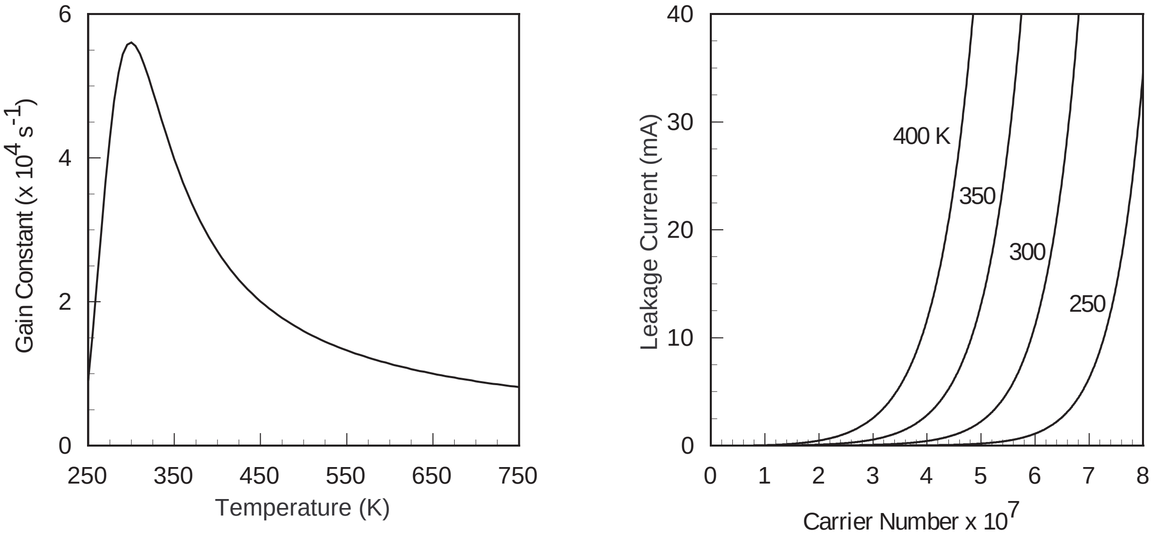

Figure 4.16 Plots of $G(T)$ and $I_l(N_0,T)$ based on the representative model parameters from Table 4.1.

illustrates $G(T)$ and $I_l(N_0,T)$ from (4.11) and (4.30), respectively, using the parameter values of Table 4.1. As we can see, the gain peaks at approximately room temperature, while the leakage current exhibits a form similar to Fig. 4.3. The transparency number $N_t(T)$, not shown here, is an increasing function of temperature.

Not included in the table of model parameters is the functional form for the device voltage V. For simplicity, we have modeled this voltage as the series combination of a 100-Ω resistor R_s and a diode with saturation current $I_s = 10^{-18}$ A and thermal voltage $V_T = 50$ mV. While temperature dependence is not included, this approach still allows us to account for the role of power dissipation in a VCSEL's thermally dependent operation. Note that we have neglected the role of parasitics in our simulations by setting $C_l = 1$ fF.

Using the above parameters, we first simulated a single-mode device at ambient temperatures of 25, 50, and 65 ºC. Figure 4.17 illustrates a family of LI curves at these temperatures. As we can see, just like the simple model of Chapter 3, the new model is able to simulate temperature-dependent threshold current and output-power rollover, with the device performance becoming increasingly

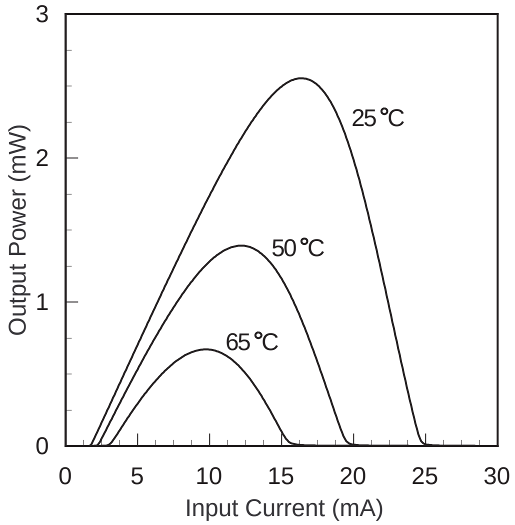

Figure 4.17 Simulated LI curves at ambient temperatures of 25, 50, and 65 ºC for a single-mode VCSEL.

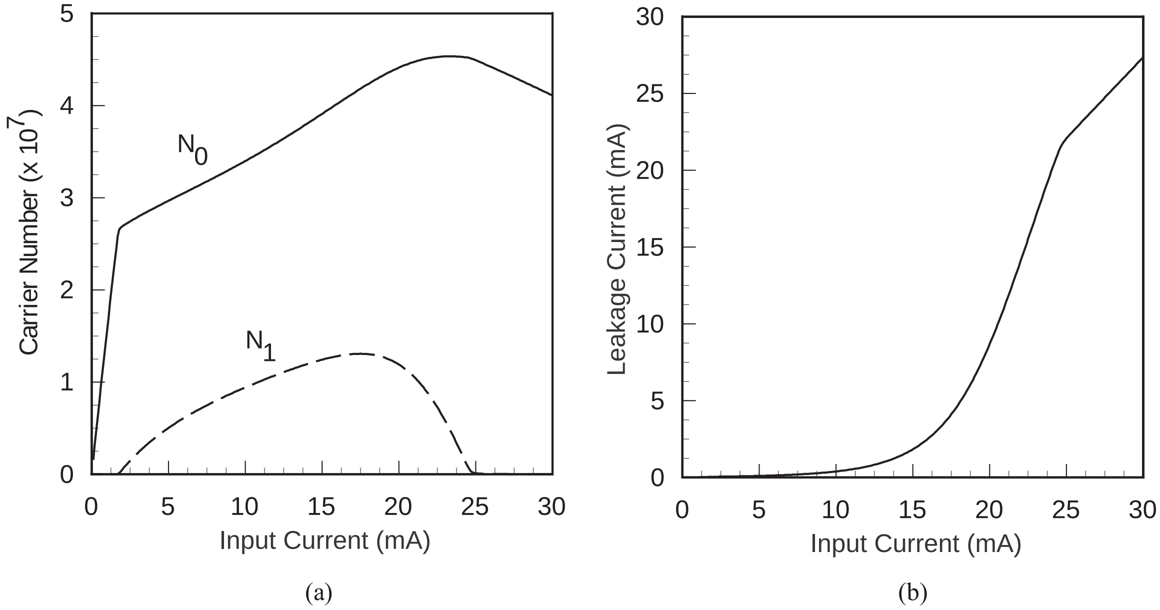

Figure 4.18 Additional dc simulation results at 25 ºC. (a) Carrier numbers N_0 and N_1. (b) Leakage current.

worse as the ambient temperature increases. In the curves of Figure 4.17, while the thermal variation of the gain certainly contributes to the observed behavior, leakage current plays a dominant role in rolling over the output power at elevated currents [4.2]. To demonstrate this fact, Fig. 4.18 illustrates the variation of N_0, N_1, and the leakage current I_l for the 25 ºC LI curve. As we can see, as the current increases and the device begins to lase, a hole is burned into the carrier profile, corresponding to the initial increase of N_1. Consequently, N_0 also begins to increase in order to maintain an above-threshold modal gain. Eventually, the output power rolls over and both N_0 and N_1 begin to decrease again. However, as Fig. 4.18(b) shows, by this time they have contributed to a thermal leakage current which ultimately shuts off the device completely.

In order to better understand the role of carrier leakage in the results of Fig. 4.17, we set the leakage to zero and reran the simulations. The results are shown in Fig. 4.19. As we can see, the elim-

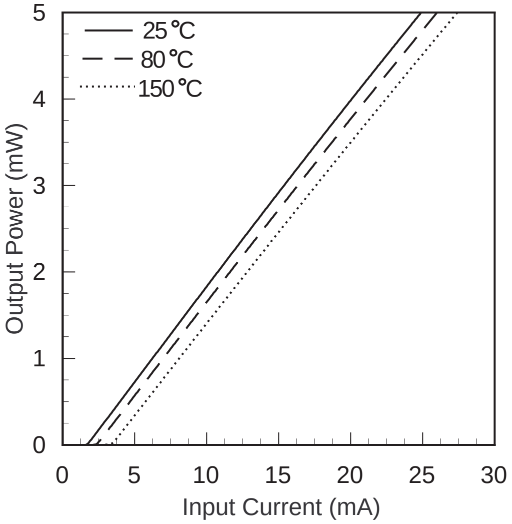

Figure 4.19 LI curves at 25, 80, and 150 ºC for a single-mode VCSEL with the leakage current set equal to zero.

ination of the leakage eliminates the rollover; however, the threshold current still shifts with temperature, obviously due to the thermal dependence of the gain. In the past, researchers have attributed the LI-curve rollover to the gain alone [4.17]. While parameters could be chosen to duplicate this behavior, we feel that in many cases, such as the one shown here, the gain will be largely responsible for shifting the threshold at lower temperatures, while the leakage will be dominant at higher temperatures and currents [4.2]. For example, for the device of [4.2], the threshold current is seen to vary by only a few mA over an approximate 60 ºC increase in ambient temperature, while the device begins to rollover after an approximate current increase of 10 mA or less. For a worst-case turn-on voltage of 5.0 V and a thermal impedance of roughly 1 ºC/mW, this corresponds to a 50 ºC change in temperature. Obviously, as the authors points out, different mechanisms must be affecting the threshold current and rollover in different ways, namely the thermal gain *and* leakage.

We next ran simulations of the single-mode VCSEL under small-signal conditions. Figure 4.20 depicts ac transfer functions at 25 ºC and bias currents of 2, 5, 10, and 20 mA. The curves were

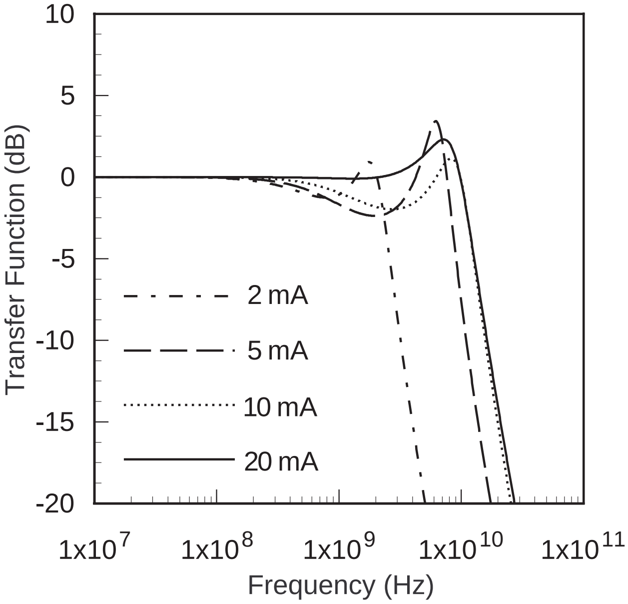

Figure 4.20 Small-signal transfer function of a single-mode VCSEL at 25 ºC and bias currents of 2, 5, 10, and 20 mA.

normalized at a low-frequency value of 10 MHz. For the three biases below the rollover point (2, 5, and 10 mA), the transfer functions' resonance frequencies increase with bias, with the magnitudes of the peaks eventually decreasing. This result is analogous to what one would expect in regular edge-emitting lasers. Note that the dip below the resonance frequency is due to the damping induced by SHB. For currents beyond the rollover point, such as the 20-mA curve of Fig. 4.20, we see that the resonance frequency begins to *decrease*; in other words, it rolls over as well. Similar results have been observed experimentally [4.61].

We can gain further insight into the thermal effects on small-signal modulation by keeping the bias fixed while varying the temperature. Fig. 4.21 illustrates the resulting transfer function for an output-power bias point of 0.5 mW and ambient temperatures of 25 and 50 ºC. As we can see, the res-

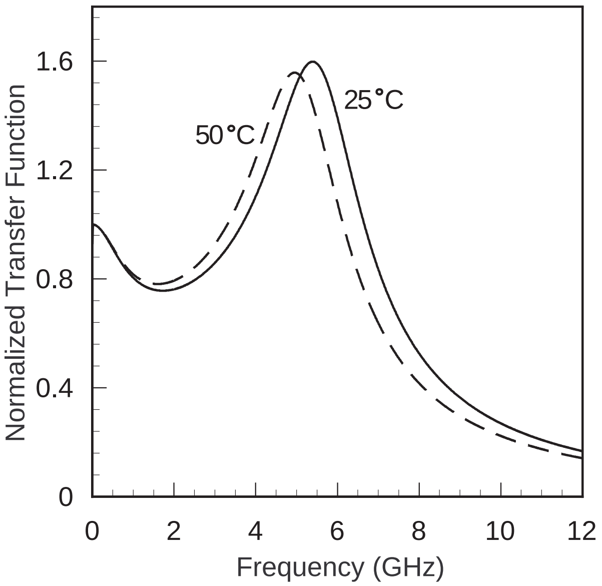

Figure 4.21 Simulated small-signal transfer function at an output-power bias of 0.5 mW and ambient temperatures of 25 and 50 ºC.

onance frequency decreases with temperature. As we touched on in Section 4.2, such a result would be expected, since the gain constant is decreasing over the temperature range 25 to 50 ºC; because the relaxation oscillation frequency is a function of the gain, the associated resonance frequency should decrease for a fixed bias power. Analogous behavior has been experimentally observed in edge-emitters' 3-dB bandwidth [4.62], and most likely would be evident in VCSELs as well.

Thermal effects can also impact the small-signal modulation via the thermal time constant. Typical values of this time constant are on the order of a few μs [4.17]; for frequencies greater than the thermal cutoff $f_{th} = 1/(2\pi\tau_{th})$, the modeled temperature will not be able to change in response to the modulation. The thermal mechanism in the model that is most affected by this result is the leakage, which is a highly sensitive function of temperature. Because the temperature cannot be modulated at frequencies above f_{th}, in many cases the leakage remains constant. Hence, the VCSEL should respond as if there is *no* leakage (or any other thermally varying behavior), resulting in an altered value of the simulated modulation response. Conversely, the response should shift to its dc value at frequencies below f_{th}. Figure 4.22 illustrates this behavior in a simulated ac response at a bias current of 10 mA and a 25 ºC ambient temperature.

Previously, we had normalized the results of Fig. 4.20 at 10 MHz to avoid unnecessary confusion in comparing the results at the different biases. However, it is clear now that the low-frequency effect can be quite important. While this "low-frequency shift" has been observed experimentally [4.63], to the best of our knowledge it has not been addressed in the literature. Thus, additional research is necessary for better understanding whether or not the experimental results correspond to the mechanisms at work in our model, or some other effect.

To complete our single-mode simulations, we modulated the laser with a square-pulse train whose low and high levels were 1.5 and 9.0 mA, respectively. As Fig. 4.23 shows, the behavior

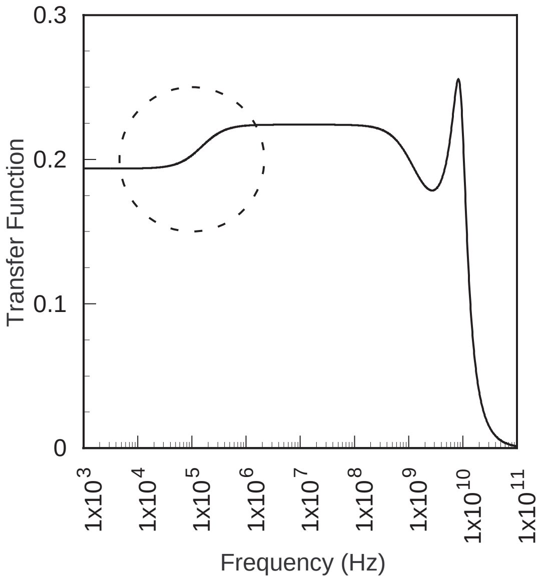

Figure 4.22 Simulated small-signal transfer function exhibiting a "low-frequency-shift" due to thermal effects.

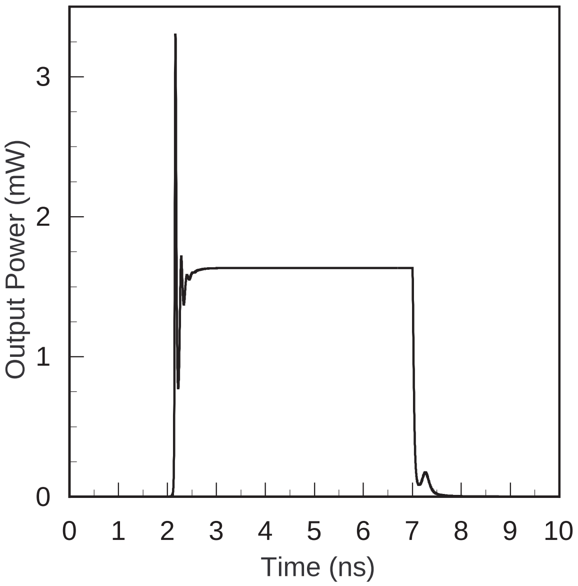

Figure 4.23 Simulated transient response of the single-mode VCSEL, demonstrating an optical bump in the turn-off transient.

described in Section 4.4 is clearly replicated by our model, with an optical bump occurring in the output-power's turn-off transient. While this result amply demonstrates the spatial capabilities of our model, they can be demonstrated with a two-mode VCSEL as well, as we shall see next.

With the single-mode simulations finished, we proceeded to use the parameters of Table 4.1 to simulate a two-mode VCSEL. While much of the behavior shown above should be expected in this laser as well, there are other features worth noting that are specific to a multimode device. First, we considered the device's LI characteristics. Figure 4.24 illustrates LI curves for both modes at temperatures of 25 and 40 ºC. As we can see, the second mode (mode 1, or LP_{11}) has a higher threshold as compared to the fundamental (mode 0, or LP_{01}). This is mostly due to the fact that it achieves threshold after SHB allows its modal gain to reach threshold. Once the LP_{11} mode begins to lase, there is a noticeable kink in the LP_{01} mode's output power, as would be expected since the two modes share the available laser gain. This kink can be seen more clearly by eliminating the leakage current and resimulating the LI curve at 25 ºC. As illustrated in Fig. 4.25, the kink is now much more visible, analogous to nonthermal simulation results presented in the literature [4.39].

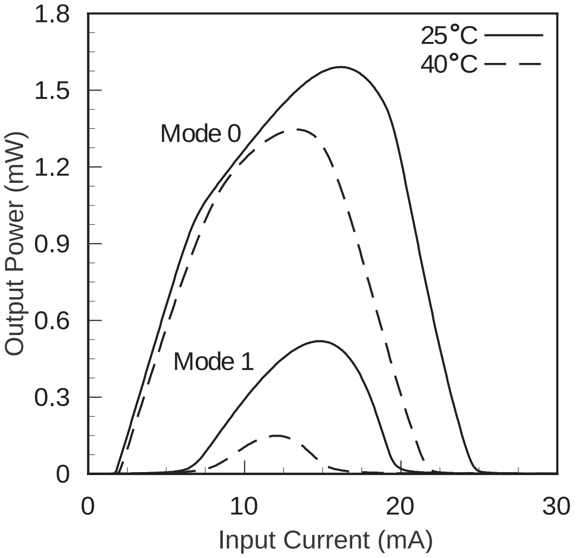

Figure 4.24 Simulated LI characteristics for a two-mode VCSEL at ambient temperatures of 25 and 40 ºC.

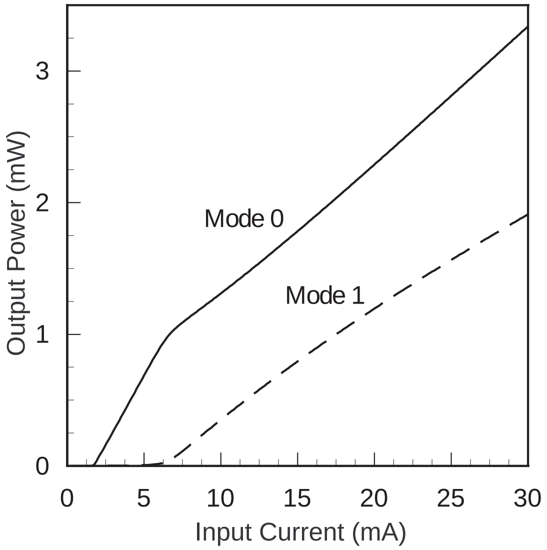

Figure 4.25 Simulated LI characteristics for a two-mode VCSEL at an ambient temperature of 25 ºC, without any carrier leakage.

To better understand the role of spatial effects in arbitrating the competition of the two modes, we ran an additional simulation at 25 ºC without the spatial dependence of the carrier profile. In other words, N_1 and N_2 were fixed at zero. Figure 4.26 shows the simulation results compared to the results of Fig. 4.24. Two observations are immediately obvious. First, the overall output power of the LP_{01} mode is clearly increased when SHB is removed. This corroborates the role SHB plays in reducing the efficiency with which a VCSEL converts current into photons [4.2]. Second, without SHB, the LP_{11} mode never lases, further confirming the importance of spatial effects in a VCSEL's operation.

As a final simulation, we simulated the response of the two-mode VCSEL to a pulse input at 25 ºC, where the low- and high-level currents were 1.5 and 8 mA, respectively; the output power of each mode is illustrated in Fig. 4.27. Again, the importance of SHB can be seen in the additional delay necessary before the LP_{11} mode can lase, as has been shown elsewhere [4.39]. Note that, despite the presence of a second mode, secondary pulsations can still be seen in the turn-off transient of mode 0.

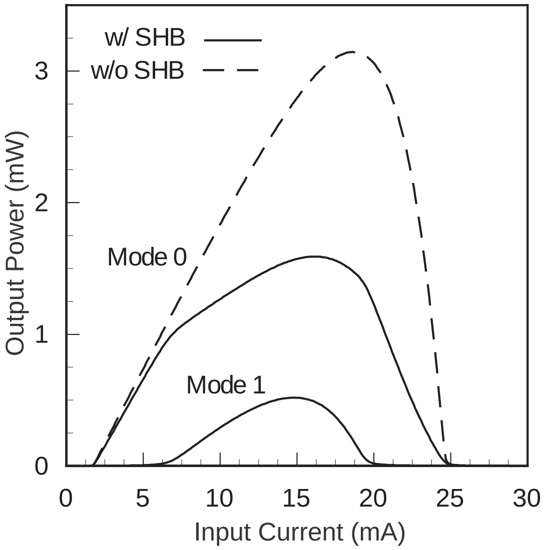

Figure 4.26 Comparison of simulated two-mode LI curves at 25 ºC, both with and without SHB.

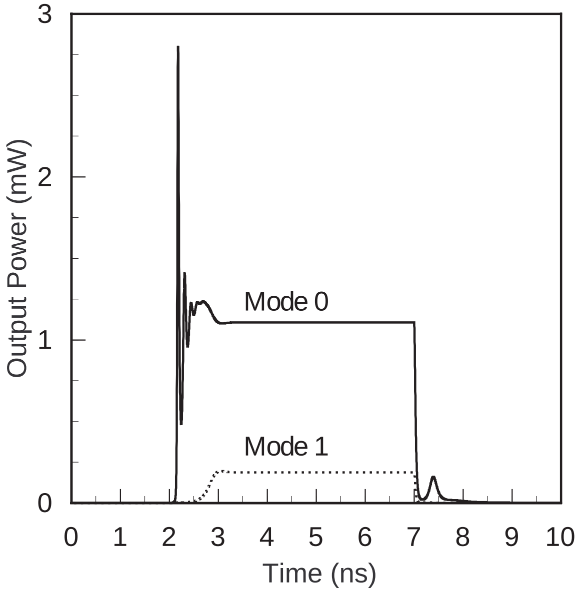

Figure 4.27 Transient simulation of a two-mode VCSEL.

4.8 Comparison to Experiment

While the simulation results presented in the previous section are useful in demonstrating the capabilities of our comprehensive VCSEL model, they do not validate them. To accomplish this task, we identified four experimental devices from the literature and fit our model to measured data. Because the devices do not report any multimode information, we used a single-mode model; furthermore, we based the simulations on a cylindrical coordinate system, using a two-term Bessel-series expansion of the carrier profile. For simplicity, we assumed $W = W_T$. Furthermore, we used the lowest-order Laguerre-Gaussian mode ($\psi_{00}(r)$), i.e., a Gaussian profile, to describe the fundamental lasing mode. As discussed in the previous section, it suffices to consider only the ratio $\alpha = W_m/W$ when calculating the overlap integrals for a given mode profile. Thus, instead of using W_m, W, and L_{eff} as fitting parameters from which the coefficients h_j, b_i, ζ_j, γ_{ki}, ϕ_{jki}, and λ_{ki} can be calculated, we used α

and h_1 directly to account for spatial effects in the model. Model-parameter optimization was carried out using CFSQP [4.64]. As we shall see, our model does a good job of matching the available data. However, the results also point out the need for more comprehensive device characterization than what has already been presented in the literature.

4.8.1 Index-guided InGaAs VCSEL

The first device is an index-guided, vertically-contacted VCSEL from [4.2]. The device has a 100-μm^2 area and is composed of GaAs-AlAs DBR mirrors, three $In_{0.2}Ga_{0.8}As$ quantum wells, and $Al_{0.2}Ga_{0.8}As$ confinement layers. Lateral carrier confinement is provided through an etched-mesa design. The authors only present measured LI characteristics at temperatures of 25, 45, 65, and 85 ºC, without corresponding IV data. However, they do provide an analytical estimate for the thermal impedance and a formula for the device voltage V as a polynomial function of current and temperature. These additional equations and the measured LI curves allowed us to determine the measured IV data at 25, 45, 65, and 85 ºC.

The most attractive feature of this device is that much of the theory used in our comprehensive model to account for thermal effects (i.e., the gain and leakage) is based on work in [4.2]. Thus, we were able to identify useful initial values for the gain and leakage parameters and proceed from there with parameter extraction. Figure 4.28 compares the resulting simulated light-current-voltage (LIV) data with the measured curves, demonstrating a good match between the two. The biggest discrepancy is found in the 25 ºC LI data, where the simulation calculates a lower output power than exhibited in the measured characteristic. However, the error is still less than ~10%. The IV data also exhibits good agreement, with the error increasing below threshold. It is worth noting that the level of agreement shown in the LI data is superior even to the results of the detailed multidimensional analy-

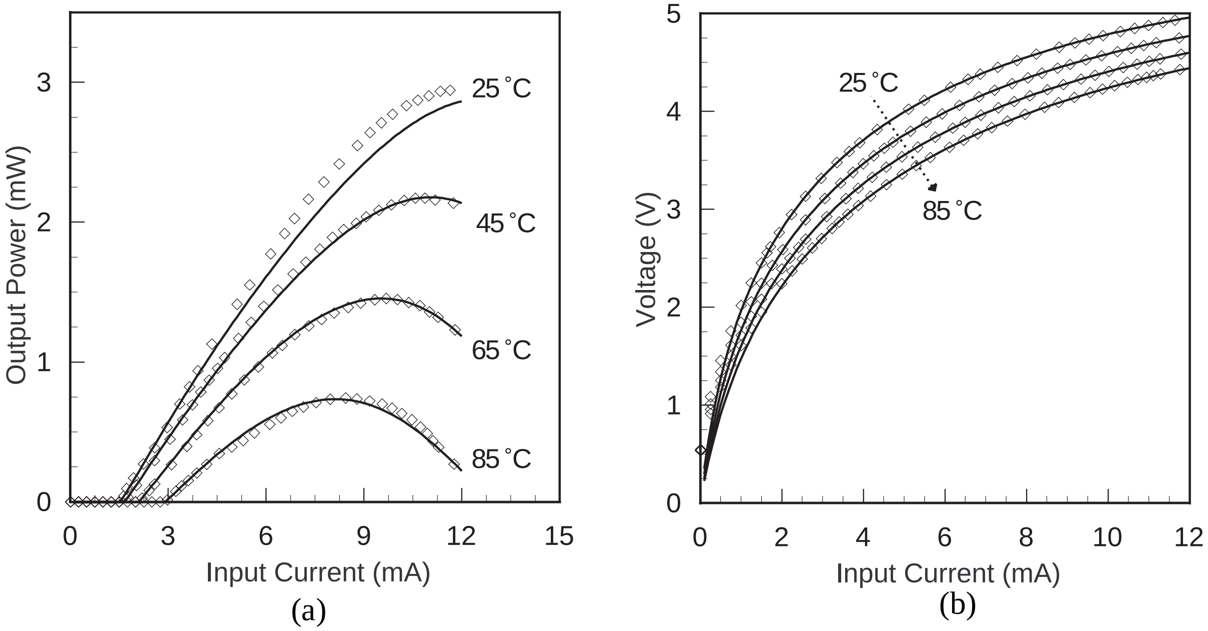

Figure 4.28 Comparison of simulated (lines) and experimental (points) (a) LI and (b) IV data for the index-guided VCSEL of [4.2].

sis used in [4.2]. While the authors of [4.2] focused on predictive modeling capabilities, and therefore were less concerned with an exact match, this result verifies the power of our model for simulating actual devices in an integrated CAD environment.

To obtain these results, we determined the following relevant model parameters, valid over the range of operating conditions in the experimental data: $\eta_i = 0.8$, $\tau_n = 3$ ns, $\tau_{p0} = 2.989$ ps, $k_{f0} = 2.7 \times 10^{-8}$ W, $\beta_0 = 2 \times 10^{-6}$, $h_1 = 3.106$, $\alpha = 0.733$, and $R_{th} = 1.647$ ºC/mW. Gain saturation was ignored. Meanwhile, we fit the IV data using the following empirical expression for V:

$$V = \frac{IR_1}{T - T_1} + n_f \ln\left[1 + \frac{I}{I_1(T - T_1)}\right] \tag{4.72}$$

where $R_1 = 12928.6$, $T_1 = 198.74$, $n_f = 1.468$, and $I_1 = 3.907 \times 10^{-6}$. Suitable parameters were also identified for the thermally dependent gain constant, transparency number, and leakage current. Fig-

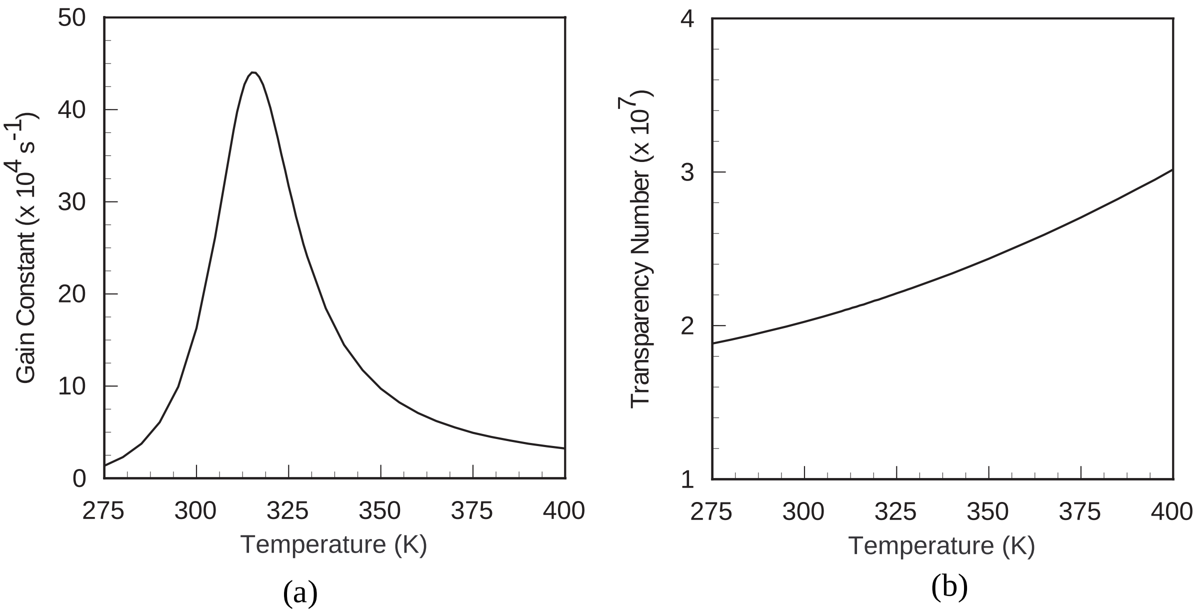

Figure 4.29 Extracted (a) gain constant and (b) carrier transparency number for the device of [4.2].

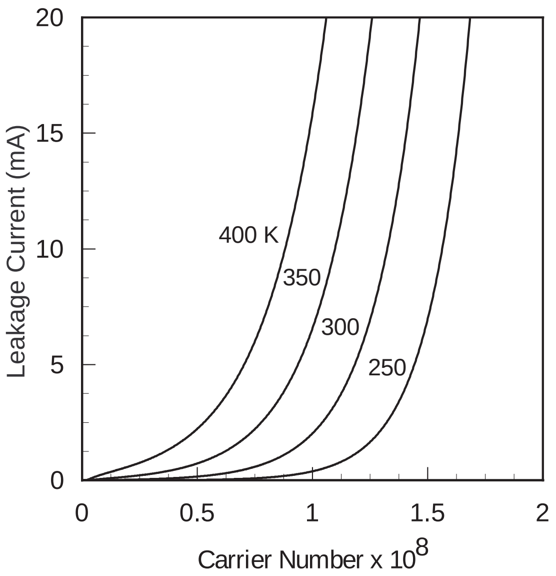

Figure 4.30 Extracted thermal leakage current for the device of [4.2].

ure 4.29 illustrates $G(T)$ and $N_t(T)$, while Fig. 4.30 depicts $I_l(N_0,T)$. As we can see, though the transparency and leakage have reasonable forms, the gain constant is severely peaked near 315 K. This raises an important issue regarding parameter extraction of detailed models such as the one presented here. Because of the relatively large number of parameters used to describe $G(T)$, $N_t(T)$, and $I_l(N_0,T)$, it is difficult to constrain the parameter optimization process to identify the *actual* parameters which would accurately describe these features. Hence, we obtained the gain constant of Fig. 4.29. We will discuss this issue in more detail shortly.

4.8.2 Selectively-oxidized AlGaInP VCSEL

The remaining three devices presented in this section are the same ones used in the previous chapter to validate the simple thermal VCSEL model. We begin by considering the VCSEL reported by Crawford *et al*. in [4.1]. As you may recall, this device was an AlGaInP-based 683-nm selectively-oxidized VCSEL with a 3 μm × 3 μm area. The authors provided both LI and IV curves at ambient temperatures of 25, 40, 60, 80, and 85 ºC.

As before, we used CFSQP to extract the model parameters necessary to fit the given data. As Figure 4.31 shows, we were again able to obtain excellent agreement between the simulated and experimental curves. The largest discrepancies can be seen in the reasonably small error in the 25 ºC LI curve at rollover, as well as the IV data below threshold. Comparison of these results with those of Chapter 3 reveals that our new model provides a much improved level of agreement between simulation and experiment. Not only do the present results match the data at 25, 40, and 60 ºC, but they also show good agreement with the data at 80 and 85 ºC. Consequently, as expected, our more comprehensive models appear to allow VCSEL simulation over a wider range of operating conditions as compared to the simpler model.

The above results were generated via the following model parameters, valid over the range of operating conditions in the experimental data: $\eta_i = 1.0$, $\tau_n = 3$ ns, $\tau_{p0} = 2.455$ ps, $k_{f0} = 2.5 \times 10^{-8}$ W, $\beta_0 = 2 \times 10^{-6}$, $\varepsilon_{00} = 1.79 \times 10^{-6}$, $h_1 = 5.24$, $\alpha = 0.7335$, and $R_{th} = 5.5$ ºC/mW. While the thermal

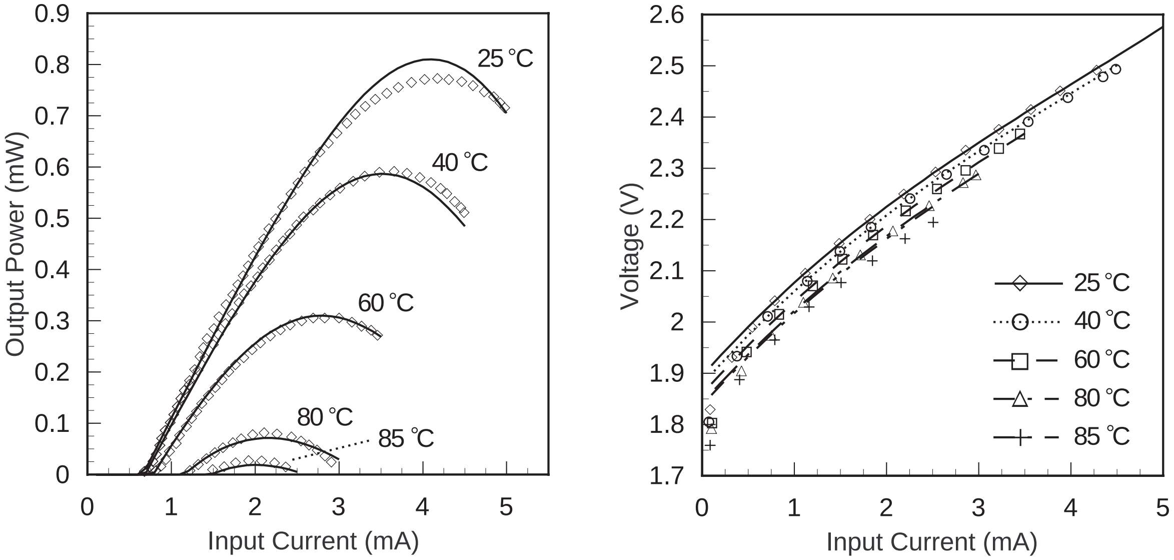

(a) (b)

Figure 4.31 Comparison of simulated (lines) and experimental (points) (a) LI and (b) IV data for the selectively-oxidized VCSEL of [4.1].

impedance is still quite large, its value is certainly more reasonable than the value of 9.8 ºC/mW used in Chapter 3. Most likely, this improvement is due to the inclusion of spatial effects and a more detailed thermal description in the present model. The IV data, meanwhile, was fit using the following empirical expression for *V*:

$$\begin{aligned} V = {} & (1.285 - 0.00442T + 1.13\times10^{-5}T^2 - 1.03\times10^{-8}T^3) \\ & \cdot (2.718 + 308.7I - 3.141\times10^4 I^2 + 2.765\times10^6 I^3) \end{aligned} \tag{4.73}$$

Identification of a more exact functional form would most likely improve the IV fit below threshold. Finally, the fits for the gain constant $G(T)$ and transparency number $N_t(T)$ are shown in Fig. 4.32, while the fit for the leakage current is shown in Fig. 4.33. Again, the plots are all reasonable; however, $G(T)$ has a fairly broad temperature dependence, again suggesting the difficulties with identifying the "most correct" set of parameters during model optimization. It should also be pointed out that the fit

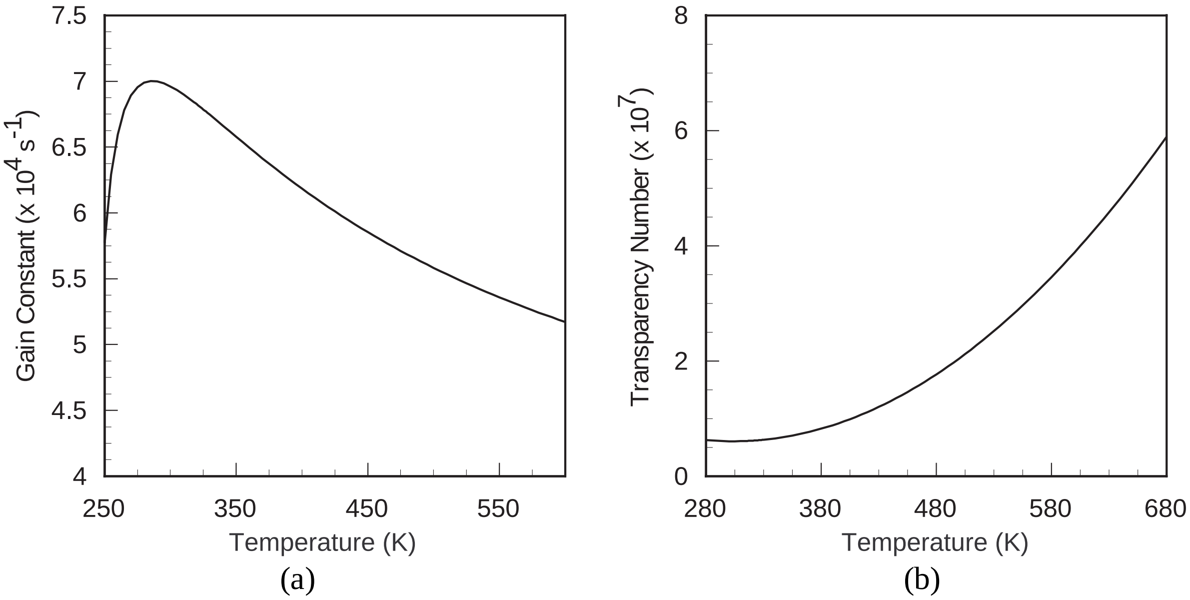

(a) (b)

Figure 4.32 Extracted (a) gain constant and (b) transparency number for the device of [4.1].

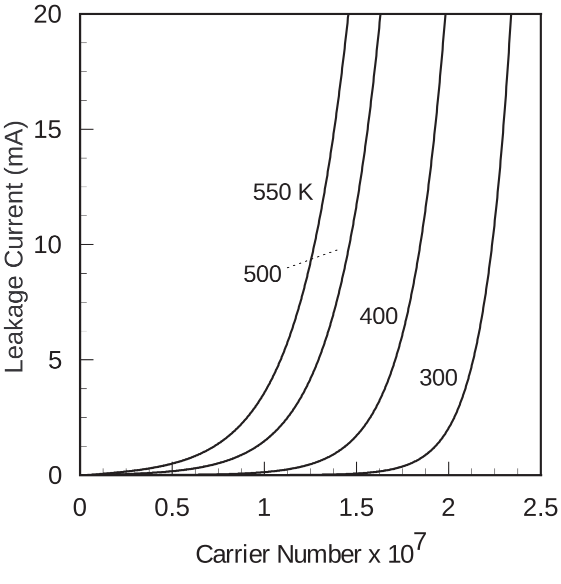

Figure 4.33 Extracted thermal leakage current for the device of [4.1].

for $G(T)$ actually exhibits a discontinuity near 230 K, thereby limiting the range of validity of the fit. As we shall discuss below, additional device characterization is necessary to extend the model's range of operation.

4.8.3 Bottom-emitting AlGaAs VCSEL

The next device is the AlGaAs VCSEL presented by Ohiso *et al.* in [4.65]. This device is an 863-nm bottom-emitting VCSEL with a 16-μm diameter, $Al_{0.1}Ga_{0.9}As$ substrate, Si-doped $Al_{0.15}Ga_{0.85}As$-AlAs, GaAs-$Al_{0.2}Ga_{0.8}As$ n-type DBR, six quantum wells, and a C-doped $Al_{0.15}Ga_{0.85}As$-$Al_{0.5}Ga_{0.5}As$-AlAs p-type DBR. The authors presented a family of LI curves over a 20-130 °C range of ambient temperatures, as well as a room-temperature IV characteristic. Unlike the first two devices presented in this section, the experimental data depict the complete thermal rollover of the LI characteristics, thereby allowing us to validate our model across the full lasing regime of the device for each of the reported ambient temperatures.

Using CFSQP, we obtained the fits shown in Fig. 4.34. Parameter extraction was performed using only the 20, 40, 70, 100, and 130 ºC data. As we can see, the results are comparable to those

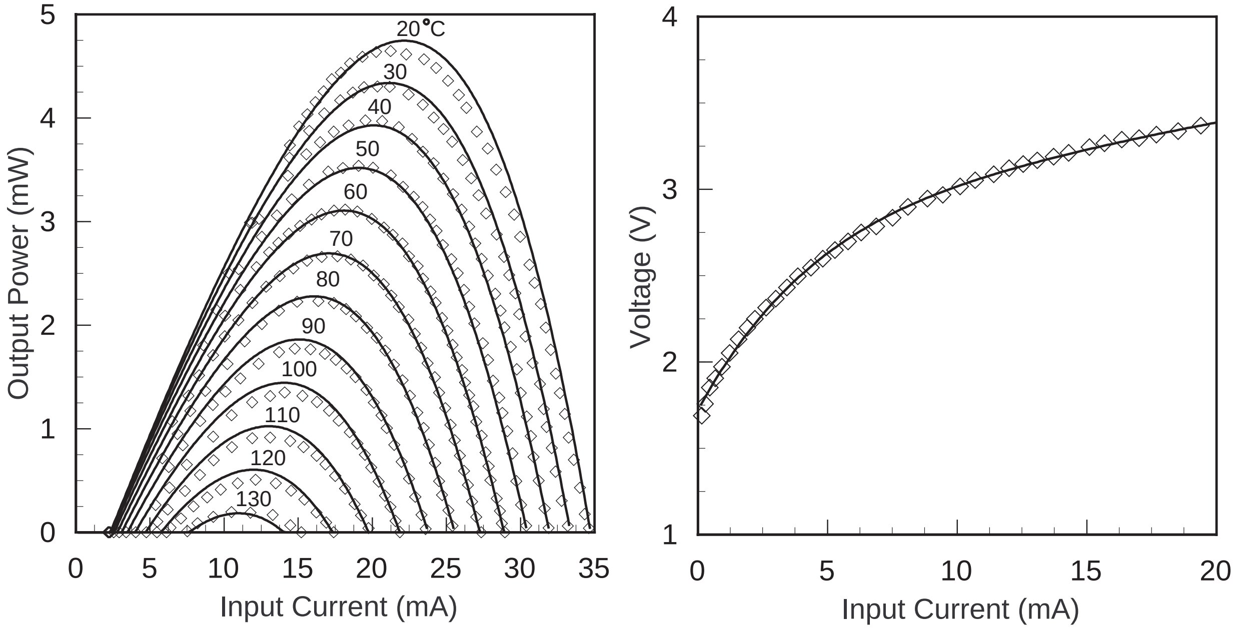

(a) (b)

Figure 4.34 Comparison of simulated (lines) and experimental (points) (a) LI and (b) IV data for the AlGaAs-based VCSEL of [4.65].

presented in Chapter 3 for the simple thermal model. For example, the rollover in the LI data is correctly captured by the model. A potential limitation of the result is the absence of IV data at different ambient temperatures. However, based on the results for the first two devices presented above, we are confident that such data would not significantly change the accuracy of the match between simulation and experiment. These results, in conjunction with those of the first two devices in this section, indicate that our model can be used over a wider cross section of devices than the simpler approach.

The parameter optimization yielding Fig. 4.34 generated the following model parameters (neglecting gain-saturation), valid over the range of operating conditions in the experimental data: $\eta_i = 1.0$, $\tau_n = 1$ ns, $\tau_{p0} = 2.426$ ps, $k_{f0} = 2.5 \times 10^{-8}$ W, $\beta_0 = 2 \times 10^{-6}$, $h_1 = 10.17$, $\alpha = 0.733$, and $R_{th} = 2.4$ °C/mW. Unfortunately, we had to use a value of thermal impedance larger than the estimated value of 1.6 °C/mW. This result suggests that the parameter optimization settled on a solution for which thermal effects are used to account for spatial mechanisms, again pointing out the need for additional investigation into the optimization process. The IV data, meanwhile, was fit using the polynomial function of current from Chapter 3, (3.14). Finally, the fits for the gain constant $G(T)$ and transparency number $N_t(T)$ are shown in Fig. 4.35, and the fit for the leakage is shown in Fig. 4.36. The fits are fairly reasonable; however, one curious feature is the location of the gain peak at 335 K. Because one would expect the peak to be closer to room temperature, this extraction result again indicates the difficulties of the parameter optimization process. Another curiosity is the severe dependence of the leakage on carrier density at 500 K. This latter feature suggests the need for a more exact representation of the leakage. However, as we see, the results are still good enough to match the measured data.

4.8.4 Thin-oxide-apertured VCSEL

The final device of this section is the VCSEL reported by Thibeault *et al.* in [4.3], a 3.1-μm

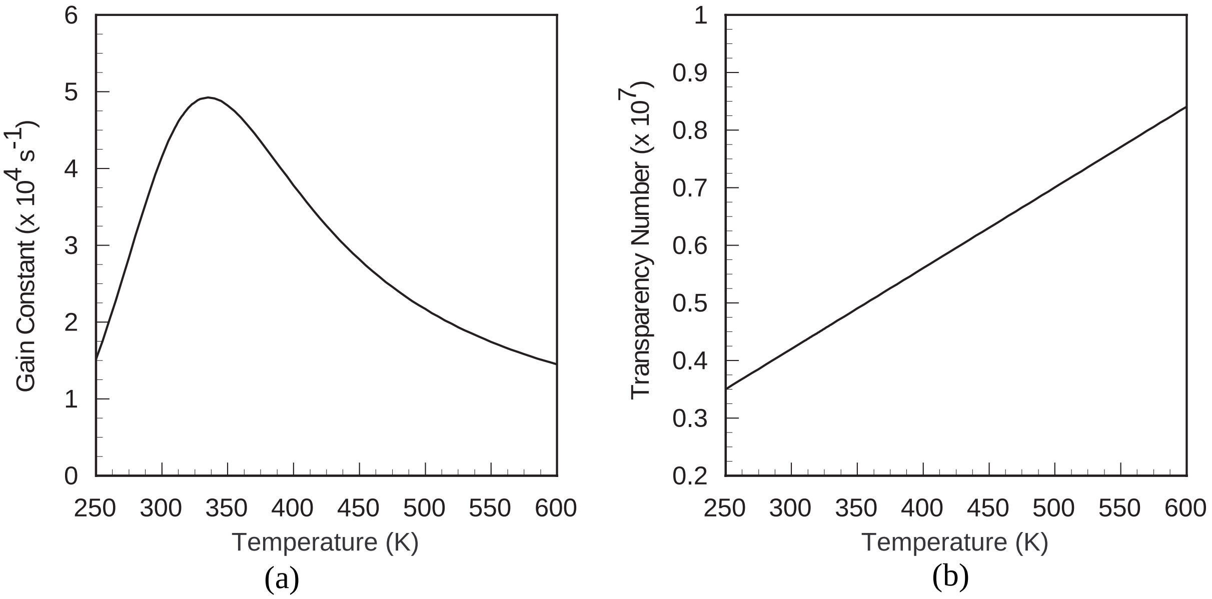

(a) (b)

Figure 4.35 Extracted (a) gain constant and (b) transparency number for the device of [4.65].

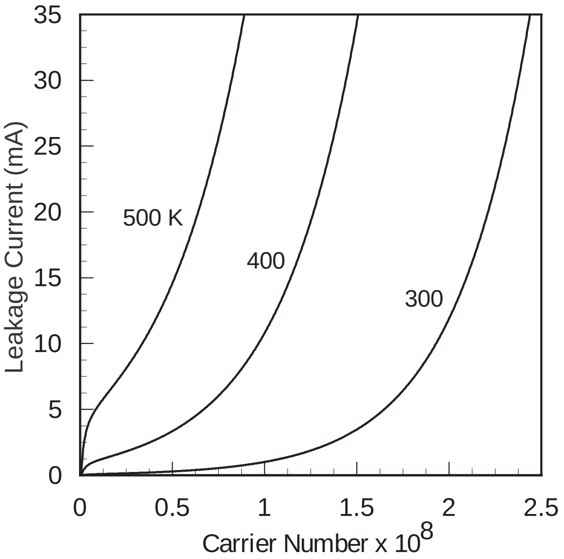

Figure 4.36 Extracted thermal leakage current for the device of [4.65].

diameter, thin-oxide-apertured device composed of an $Al_{0.9}Ga_{0.1}As$-GaAs p-type DBR, three $In_{0.17}Ga_{0.83}As$-GaAs quantum wells, an $Al_{0.3}Ga_{0.7}As$ cavity, and an AlAs-GaAs n-type DBR. The authors reported a single LI curve at a temperature of 23 °C, and the corresponding wall-plug efficiency, from which we were able to determine IV data. They also reported modulation responses

(S_{21}) at an ambient temperature of 22 ºC and bias currents of 0.5, 0.7, 1.0, 1.3, and 2.1 mA. Despite the lack of LIV data at additional ambient temperatures, the 23 ºC curve does exhibit thermal rollover; furthermore, the S_{21} data can be used to analyze the merits of our model under non-dc conditions. As we shall see, compared to the simple approach of Chapter 3, our new model does a superior job of matching all of the reported behavior.

After using CFSQP to optimize the model parameters, we obtained the LIV fit illustrated in Fig. 4.37. As one might expect for such a limited set of dc data, the agreement is very good, with the simulation reasonably matching the thermal rollover at ~6 mA. Figure 4.38 illustrates the results of fitting the S_{21} data. As we touched on in Section 4.7, the simulation results exhibited a low-frequency shift of roughly 5-10% due to the thermal time constant. However, in all likelihood the experimental data was normalized at a low-frequency value not equal to dc. Thus, we normalized our results at a

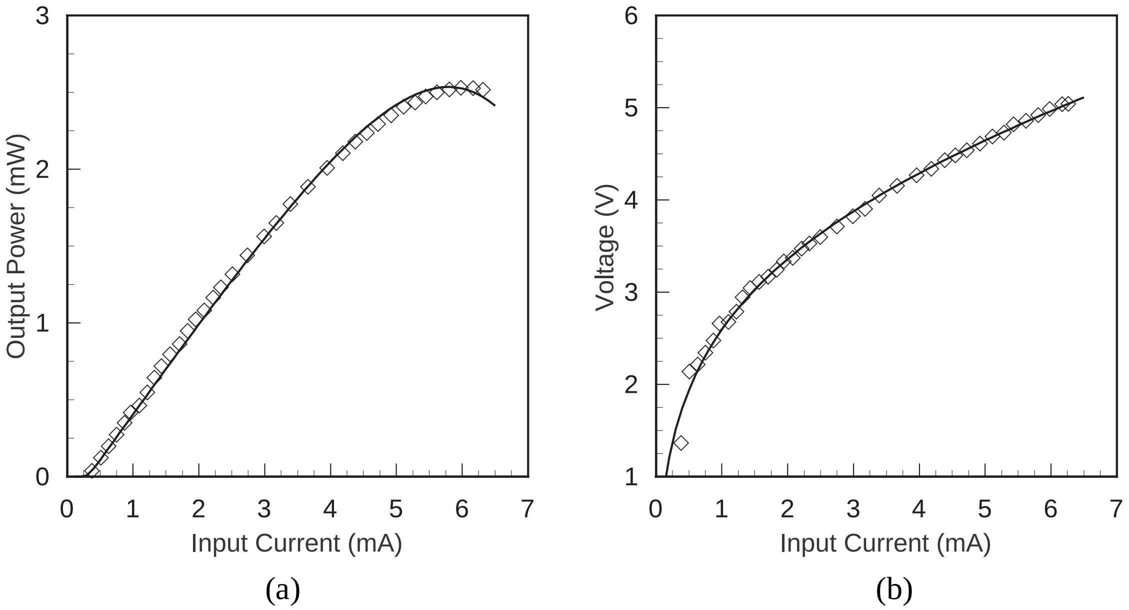

(a) (b)

Figure 4.37 Comparison of simulated (lines) and experimental (points) (a) LI and (b) IV data for the thin-oxide-apertured VCSEL of [4.3] at an ambient temperature of 23 ºC.

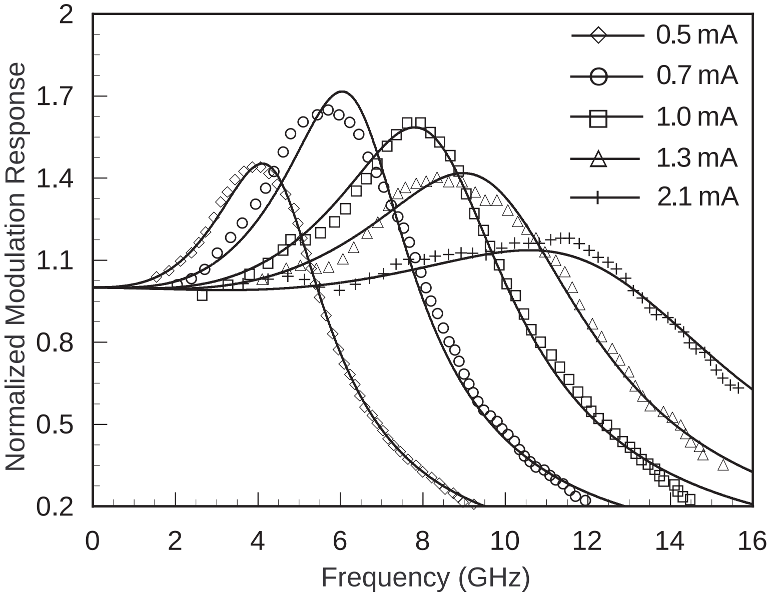

Figure 4.38 Comparison of simulated (lines) and experimental (points) S_{21} data for the device of [4.3].

low non-dc frequency of 10 MHz, effectively removing the "thermal shift" from the simulations. As we can see, the overall agreement between simulation and experiment is noticeably better than the agreement from the simple thermal VCSEL model. It should be noted that the reported data suggested a dip at frequencies just below resonance, such as that depicted in Fig. 4.20. However, because it was difficult to resolve which curve this dip corresponded to, we excluded it from our parameter optimization.

In order to generate the above results, we used the following model parameters, valid over the range of operating conditions present in the experimental data: $\eta_i = 0.805$, $\tau_n = 1.281$ ns, $\tau_{p0} = 2.661$ ps, $k_{f0} = 4.629 \times 10^{-8}$ W, $\beta_0 = 1.251 \times 10^{-2}$, $\varepsilon_{00} = 3.497 \times 10^{-6}$, $h_1 = 19.39$, $\alpha = 1.034$, $R_{th} = 0.9$ ºC/mW, and $\tau_{th} = 1$ μs. The IV data was fit using the empirical function of current from Chapter 3, (3.16). Furthermore, as suggested in [4.3], we included a shunting capacitance of 248.85 fF. Finally, we used the fits of Figs. 4.39, and 4.40 for the thermal gain and leakage current, respectively. As can be seen, these curves look fairly reasonable. However, this is largely due to the limited role that ther-

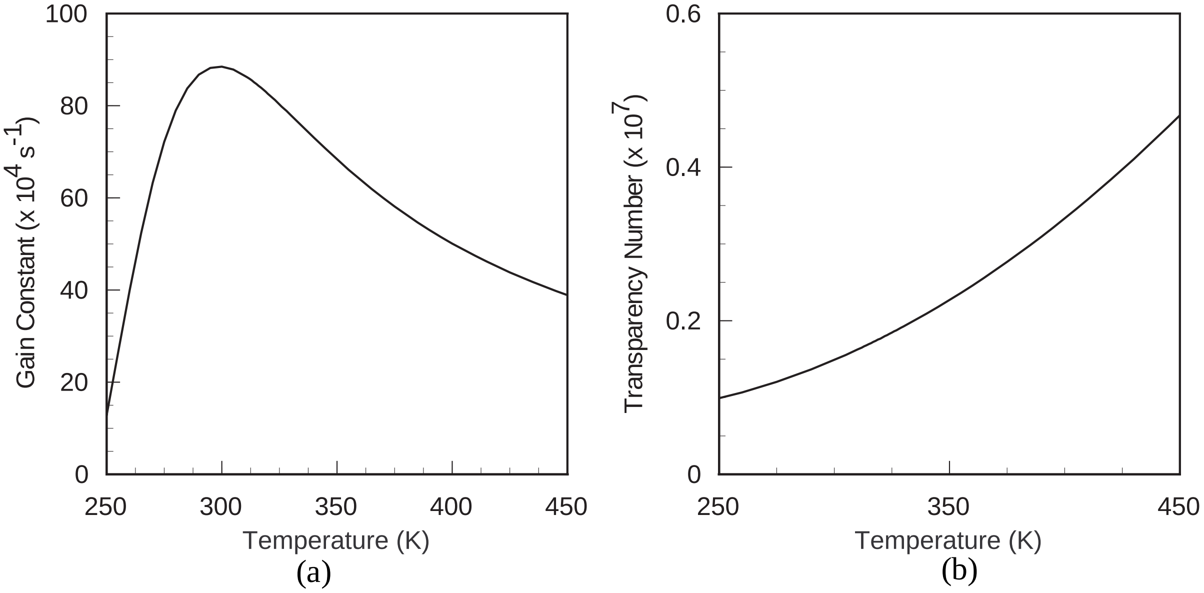

Figure 4.39 Extracted (a) gain constant and (b) transparency number for the device of [4.3].

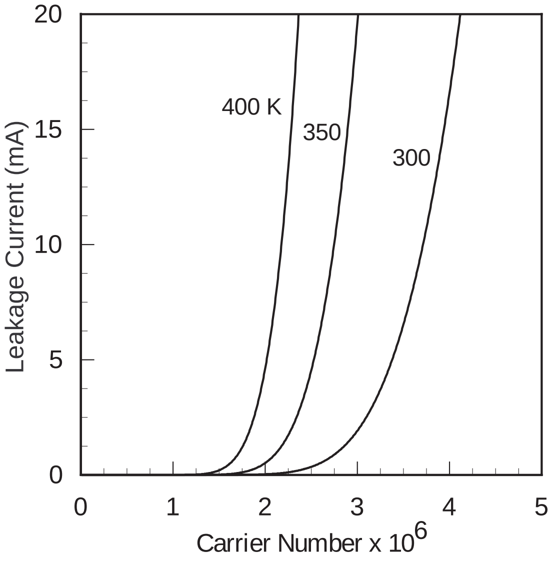

Figure 4.40 Extracted thermal leakage current for the device of [4.3].

mal effects have on the reported data. For example, from Fig. 4.37 we see that for currents up to ~4 mA, the LI curve is quite linear; over this current range, the change in device temperature is not very big. Consequently, we were able to choose *a priori* good functional forms for the gain and leakage.

As we shall discuss shortly, the lack of comprehensive VCSEL characterization in the literature did not allow us to validate our model across a broader range of operating conditions, namely, dc- *and* small-signal modulation at different ambient temperatures. However, even the limited dc and small-signal data presented here provides evidence that our models should be capable of modeling the general operating characteristics of VCSELs.

4.8.5 Discussion

Because our comprehensive VCSEL models are intended for circuit- and system-level CAD environments, they will typically be used to model specific devices. Thus, it is critical that we understand the various issues surrounding the extraction of model parameters from measured data, as well as the device characterization that produces that data. Below, we address some of the issues, including those raised during the validation of our models against the four experimental devices discussed above.

First, in general, the parameter extraction presented above is strictly only valid over the range of *reported* operating conditions. To demonstrate this, we fit the device of Ohiso *et al.* using only the data for the lower half of the reported ambient temperatures. Subsequent simulations revealed that the model could not match the data at the higher temperatures. We observed a similar result when fitting the model to the upper half of the temperatures. This problem can be avoided by ensuring parameter extraction over the complete range of expected operating conditions for a particular device. While this is unacceptable for devices such as transistors, where millions of different components might be used in a single IC design, typical optoelectronic applications do not involve such a large number of lasers, making extended device characterization a viable, if unpleasant, option. Future work should address this issue in an effort to improve the robustness of our models.

Second, it is unclear whether extracted gain and leakage curves accurately model the actual physical mechanisms at work in a particular device. While the results of our model validation demonstrate that the extracted curves are sufficient for replicating measured data, an accurate representation of the gain and leakage may not only improve the results, but also improve the ability of our model to accurately extrapolate device behavior beyond the bounds of the available data. One solution to this problem is to characterize a particular device over a wider range of operating conditions, thereby imposing additional constraints on the parameter optimization process. Alternatively, a more accurate set of analytical expressions could be identified for describing the gain and leakage. However, in the absence of these improvements, it suffices to regard the expressions used in our model as a qualitative representation of the physical mechanisms at work in a VCSEL; parameter optimization simply adjusts this representation to match measured data.

Finally, this discussion raises the most important issue of all, the need for more detailed characterization of VCSELs. To the best of our knowledge, the reported VCSEL characteristics relevant to the work discussed here have largely been limited to LIV data at a few ambient temperatures, small-signal modulation characteristics at a single ambient temperature, and some transient measurements. At the time of this work, we could not obtain small-signal ac data at different temperatures, nor multimode LI curves (with separate data for each mode). As a result, our model validation was limited to the results presented above. In order to more fully characterize the capabilities of our model, future work should investigate comprehensive VCSEL characterization. Of particular interest are the following measurements. First, LIV data at different ambient temperatures should be obtained; if the device is multimode, separate data should be taken for each mode. Second, small-signal ac modulation measurements should be taken at different bias currents *and* ambient temperatures. In this way, the thermal dependence of the modulation, such as the thermal shift in the relaxation oscillation, can be accounted for during parameter extraction. Finally, measurements of a device's emission wavelength as a function of temperature and current should be taken; such measurements would provide an initial estimate of the device's thermal impedance [4.66]. Even this small set of measurements would be useful for the further study of our models.

4.9 Conclusions

In this chapter, we presented a comprehensive VCSEL model based on spatially independent rate equations and analytical expressions for both the laser gain and thermal leakage of carriers out of the active region. Because of the lack of explicit spatial dependence in the models, we were able to implement them in SABER, a circuit- and system-level simulator, thereby facilitating the design and simulation of optoelectronic applications that use VCSELs. After discussing the theoretical basis of the models and their implementation as MAST templates, we presented a variety of simulation results which revealed the models' ability to simulate thermal LI characteristics, small-signal modulation responses, and multimode operation. We also validated the single-mode model against four devices reported in the literature. Finally, we discussed the main issues related to our results, most importantly the need for more detailed VCSEL characterization. Despite various limitations, our results indicate that our models should be a useful tool for the simulation of VCSELs in an integrated CAD environment, as well as provide the basis for future improvements.

4.10 References

[4.1] M. H. Crawford, K. D. Choquette, H. Q. Hou, R. J. Hickman, K. M. Geib, and B. E. Hammons, “Visible VCSELs: Recent advances and applications,” in *1997 Digest of the LEOS Summer Topical Meetings- Vertical-Cavity Lasers*, 1997, pp. 17-18.

[4.2] J. W. Scott, R. S. Geels, S. W. Corzine, and L. A. Coldren, “Modeling temperature effects and spatial hole burning to optimize vertical-cavity surface-emitting laser performance,” *IEEE Journal of Quantum Electronics*, vol. 29, no. 5, pp. 1295-1308, 1993.

[4.3] B. J. Thibeault, K. Bertilsson, E. R. Hegblom, E. Strzelecka, P. D. Floyd, R. Naone, and L. A. Coldren, “High-speed characteristics of low-optical loss oxide-apertured vertical-cavity lasers,” *IEEE Photonics Technology Letters*, vol. 9, no. 1, pp. 11-13, 1997.

[4.4] L. A. Coldren and S. W. Corzine, *Diode Lasers and Photonic Integrated Circuits*. New York: John Wiley & Sons, Inc., 1995.

[4.5] W. Nakwaski, “Thermal aspects of efficient operation of vertical-cavity surface-emitting lasers,” *Optical and Quantum Electronics*, vol. 28, pp. 335-352, 1996.

[4.6] C. J. Chang-Hasnain, J. P. Harbison, G. Hasnain, A. C. Von Lehmen, L. T. Florez, and N. G. Stoffel, “Dynamic, polarization, and transverse mode characteristics of vertical cavity surface emitting lasers,” *IEEE Journal of Quantum Electronics,* vol. 27, no. 6, pp. 1402-1409, 1991.

[4.7] G. R. Hadley, K. L. Lear, M. E. Warren, K. D. Choquette, J. W. Scott, and S. W. Corzine, “Comprehensive numerical modeling of vertical-cavity surface-emitting lasers,” *IEEE Journal of Quantum Electronics*, vol. 32, no. 4, pp. 607-616, 1996.

[4.8] J. Piprek, H. Wenzel, and G. Sztefka, “Modeling thermal effects on the light vs. current characteristic of gain-guided vertical-cavity surface-emitting lasers,” *IEEE Photonics Technology Letters*, vol. 6, no. 2, pp. 139-142, 1994.

[4.9] S. F. Yu, W. N. Wong, P. Shum, and E. H. Li, “Theoretical analysis of modulation response and second-order harmonic distortion in vertical-cavity surface-emitting lasers,” *IEEE Journal of Quantum Electronics*, vol. 32, no. 12, pp. 2139-2147, 1996.

[4.10] V. N. Morozov, J. A. Neff, and H. Zhou, “Analysis of vertical-cavity surface-emitting laser multimode behavior,” *IEEE Journal of Quantum Electronics*, vol. 33, no. 6, pp. 980-988, 1997.

[4.11] J. Dellunde, M. C. Torrent, J. M. Sancho, and K. A. Shore, “Statistics of transverse mode turn-on dynamics in VCSEL’s,” *IEEE Journal of Quantum Electronics*, vol. 33, no. 7, pp. 1197-1204, 1997.

[4.12] *SaberGuide Simulator Reference*, Analogy, Inc., 1996.

[4.13] N. K. Dutta, R. L. Hartman, and W. T. Tsang, "Gain and carrier lifetime measurements in AlGaAs multiquantum well lasers," *IEEE Journal of Quantum Electronics*, vol. QE-19, no. 11, pp. 1613-1616, 1983.

[4.14] R. Huang, J. G. Simmons, P. E. Jessop, and J. Evans, "A relationship for temperature dependence of threshold current for 1.3-μm compressively strained-layer multiple-quantum-well lasers," *IEEE Photonics Technology Letters*, vol. 9, no. 7, pp. 892-894, 1997.

[4.15] J.-W. Pan and J.-I. Chyi, "Theoretical study of the temperature dependence of 1.3-μm AlGaInAs-InP multiple-quantum-well lasers," *IEEE Journal of Quantum Electronics*, vol. 32, no. 12, pp. 2133-2138, 1996.

[4.16] D. M. Byrne and B. A. Keating, "A laser diode model based on temperature dependent rate equations," *IEEE Photonics Technology Letters*, vol. 1, no. 11, pp. 356-359, 1989.

[4.17] G. Hasnain, K. Tai, L. Yang, Y. H. Wang, R. J. Fischer, J. D. Wynn, B. Weir, N. K. Dutta, and A. Y. Cho, "Performance of gain-guided surface emitting lasers with semiconductor distributed Bragg reflectors," *IEEE Journal of Quantum Electronics*, vol. 27, no. 6, pp. 1377-1385, 1991.

[4.18] S. F. Yu, "Dynamic behavior of vertical-cavity surface-emitting lasers," *IEEE Journal of Quantum Electronics*, vol. 32, no. 7, pp. 1168-1179, 1996.

[4.19] R. H. Yan, S. W. Corzine, L. A. Coldren, and I. Suemune, "Corrections to the expression for gain in GaAs," *IEEE Journal of Quantum Electronics*, vol. 26, no. 2, pp. 213-216, 1990.

[4.20] S. L. Chuang, *Physics of Optoelectronic Devices*. New York: John Wiley & Sons, Inc., 1995.

[4.21] Y.-G. Zhao and J. G. McInerney, "Transient temperature response of vertical-cavity surface-emitting semiconductor lasers," *IEEE Journal of Quantum Electronics*, vol. 31, no. 9, pp. 1668-1673, 1995.

[4.22] H. C. Casey, Jr., and M. B. Panish, *Heterostructure Lasers, Part B.* New York: Academic, 1978.

[4.23] W. Chen and S. Liu, "Circuit model for multilongitudinal-mode semiconductor lasers," *IEEE Journal of Quantum Electronics*, vol. 32, no. 12, pp. 2128-2132, 1996.

[4.24] D. M. Byrne, "Accurate simulation of multifrequency semiconductor laser dynamics under gigabits-per-second modulation," *Journal of Lightwave Technology*, vol. 10, no. 8, pp. 1086-1096, 1992.

[4.25] S. M. Sze, *Physics of Semiconductor Devices*, 2nd. ed. New York: John Wiley & Sons, Inc., 1981.

[4.26] G. P. Agrawal and N. K. Dutta, *Semiconductor Lasers*, 2nd ed. New York: Van Nostrand Reinhold, 1993.

[4.27] B. G. Streetman, *Solid State Electronic Devices*, 3rd. ed. Englewood Cliffs, NJ: Prentice Hall, 1990.

[4.28] C. J. Chang-Hasnain, M. Orenstein, A. Von Lehmen, L. T. Florez, J. P. Harbison, and N. G. Stoffel, "Transverse mode characteristics of vertical cavity surface-emitting lasers," *Applied Physics Letters*, vol. 57, no. 3, pp. 218-220, 1990.

[4.29] D. Vakhshoori, J. D. Wynn, G. J. Zydzik, R. E. Leibenguth, M. T. Asom, K. Kojima, and R. A. Morgan, "Top-surface-emittting lasers with 1.9 V threshold voltage and the effect of spatial hole burning on their transverse mode operation and efficiencies," *Applied Physics Letters*, vol. 62, no. 13, pp. 1448-1450, 1993.

[4.30] D. L. Huffaker, D. G. Deppe, and T. J. Rogers, "Transverse mode behavior in native-oxide-defined low threshold vertical-cavity lasers," *Applied Physics Letters*, vol. 65, no. 13, pp. 1611-1613, 1994.

[4.31] E. Zeeb, B. Möller, G. Reiner, M. Ries, T. Hackbarth, and K. J. Ebeling, "Planar proton implanted VCSEL's and fiber-coupled 2-D VCSEL arrays," *IEEE Journal of Selected Topics in Quantum Electronics*, vol. 1, no. 2, pp. 616-623, 1995.

[4.32] G. C. Wilson, D. M. Kuchta, J. D. Walker, and J. S. Smith, "Spatial hole burning and self-focusing in vertical-cavity surface-emitting laser diodes," *Applied Physics Letters*, vol. 64, no. 5, pp. 542-544, 1994.

[4.33] N. K. Dutta, "Analysis of current spreading, carrier diffusion, and transverse mode guiding in surface emitting lasers," *Journal of Applied Physics*, vol. 68, no. 5, pp. 1961-1963, 1990.

[4.34] K. Furuya, Y. Suematsu, and T. Hong, "Reduction of resonancelike peak in direct modulation due to carrier diffusion in injection laser," *Applied Optics*, vol. 17, no. 12, pp. 1949-1952, 1978.

[4.35] D. Wilt, K. Y. Lau, and A. Yariv, "The effect of lateral carrier diffusion on the modulation response of a semiconductor laser," *Journal of Applied Physics*, vol. 52, no. 8, pp. 4970-4974, 1981.

[4.36] R. S. Tucker and D. J. Pope, "Circuit modeling of the effect of diffusion on damping in a narrow-stripe semiconductor laser," *IEEE Journal of Quantum Electronics*, vol. QE-19, no. 7, pp. 1179-1183, 1983.

[4.37] T. Ikegami, “Spectrum broadening and tailing effect in directly modulated injection lasers,” in *European Conference on Optical Fibre Communications*, vol. 132, 1975, pp. 111-113.

[4.38] N. Chinone, K. Aiki, M. Nakamura, and R. Ito, “Effects of lateral mode and carrier density profile on dynamic behaviors of semiconductor lasers,” *IEEE Journal of Quantum Electronics*, vol. QE-14, no. 8, pp. 625-631, 1978.

[4.39] A. Valle, J. Sarma, and K. A. Shore, “Spatial holeburning effects on the dynamics of vertical cavity surface-emitting laser diodes,” *IEEE Journal of Quantum Electronics*, vol. 31, no. 8, pp. 1423-1431, 1995.

[4.40] K. Petermann, *Laser Diode Modulation and Noise*. AH Dordrecht, The Netherlands: Kluwer Academic Publishers, 1991.

[4.41] A. Valle, J. Sarma, and K. A. Shore, “Secondary pulsations driven by spatial hole burning in modulated vertical-cavity surface-emitting laser diodes,” *Journal of the Optical Society of America, Pt. B*, vol. 12, no. 9, pp. 1741-1746, 1995.

[4.42] J. J. Morikuni, P. V. Mena, A. V. Harton, K. W. Wyatt, and S. M. Kang, “Spatially independent VCSEL models for the simulation of diffusive turn-off transients,” submitted for publication in *Journal of Lightwave Technology.*

[4.43] J. Tatum, D. Smith, J. Guenter, and R. Johnson, “High speed characteristics of VCSELs,” in *Proceedings of SPIE*, vol. 3004, 1997, pp. 151-159.

[4.44] M. Shimizu, F. Koyama, K. Iga, “Transverse mode analysis for surface emitting laser using beam propagation method,” *IEICE Transactions*, vol. E 74, no. 10, pp. 3334-3341, 1991.

[4.45] J.-P. Zhang and K. Petermann, “Numerical analysis of transverse mode in gain-guided vertical cavity surface emitting lasers,” *IEE Proceedings- Optoelectronics*, vol. 142, no. 1, pp. 29-35, 1995.

[4.46] D. M. Byrne and R. F. O’Dowd, “Two and three level optical PCM transmitter design for multigigabit systems using a relaxation oscillation technique,” *Journal of Lightwave Technology*, vol. LT-5, no. 10, pp. 1412-1425, 1987.

[4.47] K. Moriki, H. Nakahara, T. Hattori, and K. Iga, “Single transverse mode condition of surface-emitting injection lasers,” *Electronics and Communications in Japan, Part 2*, vol. 71, no. 1, pp. 81-90, 1988.

[4.48] D. J. Channin, “Effect of gain saturation on injection laser switching,” *Journal of Applied Physics*, vol. 50, no. 6, pp. 3858-3860, 1979.

[4.49] *HSPICE User’s Manual*, Meta-Software, Inc., 1996.

[4.50] C. H. Chong and J. Sarma, “Self-consistent calculation of two-dimensional diffusion equation for a modal gain analysis of lasing modes in cylindrical VCSELs,” in *Proceedings of SPIE*, vol. 2146, 1994, pp. 397-408.

[4.51] R. Schatz, “Dynamics of spatial hole burning effects in DFB lasers,” *IEEE Journal of Quantum Electronics*, vol. 31, no. 11, pp. 1981-1993, November 1995.

[4.52] N. Bewtra, D. A. Suda, G. L. Tan, F. Chatenoud, and J. M. Xu, “Modeling of quantum-well lasers with electro-opto-thermal interaction,” *IEEE Journal of Selected Topics in Quantum Electronics*, vol. 1, no. 2, pp. 331-340, 1995.

[4.53] P. V. Mena, S. M. Kang, and T. A. DeTemple, “Rate-equation-based laser models with a single solution regime,” *Journal of Lightwave Technology*, vol. 15, no. 4, pp. 717-730, 1997.

[4.54] J. J. Morikuni (private communication).

[4.55] A. E. Siegmann, *Lasers*. Mill Valley, CA: University Science Books, 1986.

[4.56] O. Buccafusca, J. L. A. Chilla, J. J. Rocca, S. Feld, C. Wilmsen, V. Morozov, and R. Leibenguth, “Transverse mode dynamics in vertical cavity surface emitting lasers excited by fast electrical pulses,” *Applied Physics Letters*, vol. 68, no. 5, pp. 590-592, 1996.

[4.57] R. Michalzik and K. J. Ebeling, “Spatial hole burning effects in gain-guided vertical cavity laser diodes,” in *LEOS (Lasers and Electro-Optics Society) Annual Meeting*, 1993, pp. 550-551.

[4.58] J. Y. Law and G. P. Agrawal, “Effects of spatial hole burning on gain switching in vertical-cavity surface emitting lasers,” *IEEE Journal of Quantum Electronics*, vol. 33, no. 3, pp. 462-468, 1997.

[4.59] J. Y. Law and G. P. Agrawal, “Mode-partition noise in vertical-cavity surface-emitting lasers,” *IEEE Photonics Technology Letters*, vol. 9, no. 4, pp. 437-439, 1997.

[4.60] M. S. Sodha and A. K. Ghatak, *Inhomogeneous Optical Waveguides*. New York: Plenum Press, 1977.

[4.61] J. A. Lehman, R. A. Morgan, D. Carlson, M. H. Crawford, and K. D. Choquette, “High-frequency modulation characteristics of red VCSELs,” *Electronics Letters*, vol. 33, no. 4, pp. 298-300, 1997.

[4.62] D. Novak and M. L. Majewski, “Temperature and optical gain nonlinearity effects on the maximum modulation bandwidth of semiconductor laser diodes,” in *16th Australian Conference on Optical Fibre Technology*, 1991, pp. 354-357.

[4.63] M. Bruensteiner (private communication).

[4.64] C. Lawrence, J. L. Zhou, and A. L. Tits, "Users' guide for CFSQP version 2.5: A C code for solving (large scale) constrained nonlinear (minimax) optimization problems, generating iterates satisfying all inequality constraints," Institute for Systems Research, University of Maryland, Technical Report TR-94-16r1, 1997.

[4.65] Y. Ohiso, K. Tateno, Y. Kohama, A. Wakatsuki, H. Tsunetsugu, and T. Kurokawa, "Flip-chip bonded 0.85-µm bottom-emitting vertical-cavity laser array on an AlGaAs substrate," *IEEE Photonics Technology Letters*, vol. 8, no. 9, pp. 1115-1117, 1996.

[4.66] T. Wipiejewski, M. G. Peters, B. J. Thibeault, D. B. Young, and L. A. Coldren, "Size-dependent output power saturation of vertical-cavity surface-emitting laser diodes," *IEEE Photonics Technology Letters*, vol. 8, no. 1, pp. 10-12, 1996.

CHAPTER 5

CONCLUSIONS AND FUTURE WORK

5.1 Research Summary

As the number of electronic applications that incorporate optoelectronic devices continues to increase, there exists a growing need for simulation tools to facilitate their design. Models for semiconductor lasers and photodetectors, in conjunction with existing models for electronic components, would allow an engineer to verify and optimize a particular design in advance of its actual fabrication, thereby reducing the design cycle considerably. Thus motivated, we presented in this thesis the development and implementation of circuit-level models for QW semiconductor lasers and VCSELs.

First, in Chapter 2 we presented QW-laser models based on two sets of the laser rate equations. The one-level version was based on the standard pair of equations for the active region carrier and photon densities, while the two-level model included a third equation to account for carrier transport between the quantum wells and surrounding confinement layers. As we discussed, a particular problem of the rate equations is the existence of multiple dc-solution regimes. Though Javro and Kang [5.1] presented a model which apparently eliminated the erroneous solutions under nonnegative current injection, we demonstrated that its use of a linear gain-saturation term resulted in the persistence of these solutions. Our models, however, utilized alternative expressions for gain saturation as proposed by Channin [5.2] and Agrawal [5.3]; hence, we were able to show via rigorous analysis that the introduction of transformations for the carrier and photon densities resulted in a single dc-solution. After discussing each model and its implementation in SPICE, we then extracted parameters for the two-level model and compared simulated and experimental data for two devices, a BH and DBR laser. While the results demonstrated the ability of the model to capture the general behavior of semiconductor lasers, their validity was restricted to a limited range of operating conditions. Improved parameter-optimization techniques and additional experimental characterization were suggested as two means to improve these results.

Next, we introduced VCSELs and the need for more-detailed circuit-level models to account for their unique behavior. As we saw, compared to edge-emitting semiconductor lasers, VCSELs exhibit strong thermally and spatially dependent operation. Since the thermal component is the most recognized limitation of a VCSEL’s operation, we presented in Chapter 3 a simple model that accounts for thermal effects via a temperature-dependent offset current. This model was implemented both in HSPICE [5.4] and SABER [5.5], the latter of which was shown to be particularly useful in implementing the model in an extremely straightforward manner. Though the model was successfully used to replicate experimental data from three devices in the literature, it was not without its limitations. In particular, because spatial effects were not explicitly taken into consideration, the model was forced to account for them via its thermal components. This phenomenon was most clearly demonstrated in the large thermal impedance generated for one of the devices, as well as the limited range of operating conditions over which the model matched the experimental data. In spite of these limitations, we noted that the model could still be used to effectively capture a device’s dc behavior as a function of temperature, as well as its modulation response when temperature effects are minimal.

In an effort to address the limitations of this simple model, we discussed in Chapter 4 the development and implementation of a more comprehensive VCSEL model that incorporates both thermal *and* spatial behavior, namely, thermally dependent gain, carrier leakage out of the active layer, transverse multimode operation, spatial hole burning, and transverse carrier diffusion. Instead of incorporating an empirical thermal offset current, we modeled a VCSEL’s thermal dependence via explicit expressions for the gain and carrier leakage as a function of temperature. To account for spatial behavior, we introduced a simple set of spatially independent rate equations, and demonstrated that the use of fixed mode-profile shapes and a truncated series expansion for the active-region carrier profile could be used to model the impact of spatial hole burning and carrier diffusion on a VCSEL's operation. Combining these various components, we then presented our comprehensive VCSEL models, valid for both rectangular and cylindrical coordinate systems. The models were implemented in SABER in order to take advantage of its robust behavioral modeling language, MAST. As we saw through simulation, the model was able to replicate much of a VCSEL's characteristic behavior, including thermally dependent threshold current, rollover of the LI characteristics, thermally dependent small-signal operation, and transverse mode competition. Our models also compared favorably to experimental data from four different devices reported in the literature. Furthermore, the correspondence between simulation and experiment was over a larger range of operating conditions than exhibited by the simple thermal VCSEL model. There were limitations, however. Extracted model parameters were strictly valid only over the range of operating conditions in the experimental data; also, the complexity of the gain and leakage expressions made it difficult for the optimization process to identify their exact form.

5.2 Future Work

While our results demonstrate the ability of circuit-level models to describe the complex behavior of QW lasers and VCSELs, it is obvious that there is still a large number of open areas that should be addressed. Below, we point out some of them.

With regards to the QW laser model, future work should investigate the improvement of parameter extraction from experimental data. As we saw, our results showed a limited range of validity. Improving the robustness and accuracy of the parameter optimization would most likely improve the match between simulation and experiment. Another solution, however, would be to include additional detail in the model, such as the inclusion of addition rate equations that would provide a more detailed account of the carrier transport between the QWs and confinement layers. For example, models have been proposed which include a rate equation for gateway states in between these regions [5.6], [5.7].

Meanwhile, the comprehensive VCSEL model provides many opportunities for additional research. First, thermally dependent mechanisms such as Auger recombination [5.8] and optical losses [5.9] could be added, thereby allowing the model to more accurately account for the actual physics at work in a VCSEL. Second, because our model assumes fixed mode-profile shapes, it is suited primarily for index-guided devices. By allowing the profiles to vary as a function of bias, the model would be more capable of accurately modeling gain-guided lasers. Furthermore, it would also be able to model complex effects such as thermal lensing and self focusing. Future research should investigate simple means for accounting for the mode profiles' dependence on temperature, carrier profile, and current distribution, while retaining the spatially independent nature of the model. Finally, as discussed in Chapter 4, the extraction of model parameters for our model raised a number of important issues. As was the case with the other models in this thesis, we saw that the validity of the extracted parameters was generally limited to the range of operating conditions present in the experimental data. By improving the fit of the thermal gain and carrier leakage, this limitation should be reduced; for example, additional device characterization might better constrain the parameter optimization process, thereby allowing the model to more accurately account for the intrinsic VCSEL behavior and thus predict device characteristics outside of the range of measured data. In general, though, the scarcity of comprehensive device data makes this solution difficult. In fact, this lack of information prevented us from validating all of our models' features, namely, thermally dependent modulation characteristics and multimode behavior. Thus, future work should investigate the more detailed characterization of actual VCSELs, thereby allowing more rigorous validation of the work presented here.

5.3 References

[5.1] S. A. Javro and S. M. Kang, “Transforming Tucker’s linearized laser rate equations to a form that has a single solution regime,” *Journal of Lightwave Technology*, vol. 13, no. 9, pp. 1899-1904, September 1995.

[5.2] D. J. Channin, “Effect of gain saturation on injection laser switching,” *Journal of Applied Physics*, vol. 50, no. 6, pp. 3858-3860, 1979.

[5.3] G. P. Agrawal, “Effect of gain and index nonlinearities on single-mode dynamics in semiconductor lasers,” *IEEE Journal of Quantum Electronics*, vol. 26, no. 11, pp. 1901-1909, 1990.

[5.4] *HSPICE User’s Manual*, Meta-Software, Inc., 1996.

[5.5] *SaberGuide Simulator Reference*, Analogy, Inc., 1996.

[5.6] D. McDonald and R. F. O’Dowd, “Comparison of two- and three-level rate equations in the modeling of quantum-well lasers,” *IEEE Journal of Quantum Electronics*, vol. 31, no. 11, pp. 1927-1934, 1995.

[5.7] B. P. C. Tsou and D. L. Pulfrey, “A versatile SPICE model for quantum-well lasers,” *IEEE Journal of Quantum Electronics*, vol. 33, no. 2, pp. 246-254, 1997.

[5.8] N. Bewtra, D. A. Suda, G. L. Tan, F. Chatenoud, and J. M. Xu, “Modeling of quantum-well lasers with electro-opto-thermal interaction,” *IEEE Journal of Selected Topics in Quantum Electronics*, vol. 1, no. 2, pp. 331-340, 1995.

[5.9] J. Piprek, D. I. Babic, and J. E. Bowers, “Simulation and analysis of 1.55 μm double-fused vertical-cavity lasers,” *Journal of Applied Physics*, vol. 81, no. 8, pp. 3382-3390, 1997.

APPENDIX A

IMPLEMENTATION OF THE QW LASER MODELS IN SPICE

This appendix reviews the implementation of Chapter 2's QW laser models in SPICE3 [A.1], HSPICE [A.2], and Intusoft's ISSPICE [A.3].

A.1 SPICE3/HSPICE Implementation

We have implemented the two QW laser models of Chapter 2 in SPICE3 and HSPICE. While these versions could be implemented directly using subcircuits such as those depicted in Figs. 2.5 and 2.9, we have modified code originally developed by S. Javro to parse a "`.Xmodel`" statement into a subcircuit, thereby allowing the user to handle the models in a manner analogous to other SPICE models.

A laser model declaration in a SPICE3/HSPICE input deck takes the form

```
.Xmodel <model_name> <model> level=<#> <model_parameters>
```

where `<model_name>` names the model declaration; `<model>` identifies the particular laser model being used, with *`laser1`* corresponding to the one-level model of Section 2.3, and *`laser2`* corresponding to the two-level model of Section 2.4; `level` identifies the gain term used in the model and can take on a value of 1-4; and `<model_parameters>` defines the various intrinsic and parasitic parameter values in the model. A specific laser device is entered into a SPICE3/HSPICE input deck as

```
xdevicename <p> <n> <pf> <model_name>
```

where `<p>` and `<n>` designate the laser's p- and n-terminals, `<pf>` designates the output node whose voltage corresponds to the optical output power, and `<model_name>` corresponds to the name of a `.Xmodel` declaration.

In order for SPICE3/HSPICE to understand these statements, the `.Xmodel` statement must be converted into a subcircuit invocation. This translation is carried out via the parsing program *PARSE*, whose source code, written originally by S. Javro, can be found in Section A.3. Specifically, an input netlist `input.ckt` is converted into the more suitable output netlist `output.ckt` using

```
PARSE input.ckt output.ckt [ID]
```

where ID = 0 for SPICE3, 1 for HSPICE. SPICE3 or HSPICE can then simulate `output.ckt`.

A.1.1 *laser1* model

We implemented the one-level rate-equation-based QW laser model of Section 2.3 using Channin's gain saturation term and four possible expressions for the gain. In addition to the linear and logarithmic gain terms of (2.14), we also included a simplified logarithmic gain term, and an expression for the logarithmic gain that was linearized about the threshold carrier density N_{th}. The four gain expressions corresponding to the `level` parameter in the `.Xmodel` statement are

`level 1:`
$$\alpha(N) = G_o \ln\left(\frac{R_w(N)}{R_w(N_o)}\right) \tag{A.1a}$$

`level 2:`
$$\alpha(N) = g_l G_o \ln\left(\frac{N}{N_o}\right) \tag{A.1b}$$

`level 3:`
$$\alpha(N) = g_l G_o \left(\frac{N}{N_o} - 1\right) \tag{A.1c}$$

`level 4:`
$$\alpha(N) = g_l G_o \left(\frac{N}{N_{th}} - 1\right) + G_o \ln\left(\frac{R_w(N_{th})}{R_w(N_o)}\right) \tag{A.1d}$$

Finally, the models also include the junction capacitance and parasitics from Section 2.5, including the four external shunting circuits of Fig. 2.12. The internal shunting circuit uses a capacitance C_{ssc}.

The complete set of `laser1` model parameters is listed in Table A.1, along with default values. If g_l is set equal to zero, then it is internally calculated based on which gain expression is used, where it is assumed that (A.1b)-(A.1d) are generated via first-order expansions of (A.1a). Thus, for (A.1b) and (A.1c),

$$g_l = \frac{AN_o + 2BN_o^2 + 3CN_o^3}{AN_o + BN_o^2 + CN_o^3} \tag{A.2a}$$

whereas for (A.1d),

$$g_l = \frac{AN_{th} + 2BN_{th}^2 + 3CN_{th}^3}{AN_{th} + BN_{th}^2 + CN_{th}^3} \tag{A.2b}$$

Additional implementation details are as follows. First, for modeling purposes, A is split into two parameters, A_2 and τ_n, where $A = A_2 + 1/\tau_n$. If τ_n is set, then $1/\tau_n$ must be less than A, since it is a portion of A's value. Otherwise, τ_n is set equal to $1/A$. Second, the model parameter SHTYPE specifies which external shunting circuit to use, where 0 corresponds to no shunting circuit, and 1-4 corresponds to the various shunting circuits from Figure 2.12(a)-(d), respectively. Third, T_f is used to give information about the operating temperature of the laser, and is set equal to the ratio of this temperature and the overall circuit temperature. Finally, Δ (DELTA) is used as a correction for any logarithmic terms used in the model in the event that their operand becomes equal to zero.

Following is an example of a `laser1` model declaration:

```
.Xmodel ltest1 laser1 level=1
+ Ne=5.96e14 n=2 delta=1e-60
+ etai=0.86 Lambda=980e-9 Nw=1 Vact=6e-18 Gamma=0.019
+ vgr=8.571e7 tp=2.759e-12 etac=0.449 No=1.5e24 Go=1.5e5 eps=1e-23
+ tn=0.5e-8 A=0.6e8 B=0.7e-16 C=0.6e-41 betaA=0 betaB=1e-4 betaC=0
+ cjo=25e-12 vj=2 Cssc=10e-9 Tf=1.5 Rs=5 Is1=1e-3 n1=1 Is2=1e-3 n2=1
```

Table A.1 SPICE3/HSPICE QW-laser-model parameters (*continued on next page*).

Param.	Models	SPICE name	Description, units	Default
level		LEVEL	model level number (1-4)	1
N_e		NE	*laser1:* QW equilibrium carrier density, m^{-3} *laser2:* SCH equilibrium carrier density, m^{-3}	10^{12}
n		N	*laser1:* QW diode ideality factor *laser2:* SCH diode ideality factor	2
N_{e2}	*laser2*	NE2	*laser2:* QW equilibrium carrier density, m^{-3}	10^{12}
n_{w2}	*laser2*	NW2	*laser2:* QW diode ideality factor	1
η_i		ETAI	current injection efficiency	1
λ		LAMBDA	emission wavelength, m	850×10^{-9}
N_w		NW	number of quantum wells	1
V_{act}		VACT	volume of a single QW, m^3	10^{-17}
Γ_c		GAMMA	optical confinement factor for 1 QW	0.1
v_{gr}		VGR	lasing-medium group velocity, m/s	10^8
τ_p		TP	cavity, or photon, lifetime, s	3×10^{-12}
η_c		ETAC	output power coupling coefficient	0.35
N_o		NO	optical transparency density, m^{-3}	10^{24}
N_{th}		NTH	threshold carrier density, m^{-3}	1.25×10^{24}
G_o		GO	gain coefficient per QW, m^{-1}	10^5
g_l		GL	linearized-gain scaling factor	0
ε		EPS	phenomenological gain saturation term, m^3	10^{-23}
τ_n		TN	equivalent linear-recombination time, s	0
A		A	QW unimolecular recombination rate coefficient, s^{-1}	10^8
B		B	QW radiative recombination rate coefficient, m^3/s	10^{-16}
C		C	QW Auger recombination rate coefficient, m^6/s	0
β_A		BETAA	QW unimolecular spontaneous-emission coupling coefficient	0
β_B		BETAB	QW radiative spontaneous-emission coupling coefficient	10^{-6}

Table A.1 (*Continued.*)

Param.	Models	SPICE name	Description, units	Default
β_C		BETAC	QW Auger spontaneous-emission coupling coefficient	0
V_{barr}		VBARR	total volume of barrier layers, m^3	10^{-16}
τ_{capt}	*laser2*	TCAPT	QW carrier capture lifetime, s	10^{-12}
τ_{em}	*laser2*	TEM	QW carrier emission lifetime, s	10^{-9}
A_b	*laser2*	AB	barrier unimolecular recombination rate coefficient, s^{-1}	0
B_b	*laser2*	BB	barrier radiative recombination rate coefficient, m^3/s	0
C_b	*laser2*	CB	barrier Auger recombination rate coefficient, m^6/s	0
C_{jo}		CJO	zero-bias junction capacitance, F	0
m_p		MPOW	diode grading coefficient	0.5
ϕ_o		VJ	built-in junction potential, V	1
FC		FC	coefficient for forward-bias junction capacitance formula	0.5
Δ		DELTA	ln(0) correction parameter	10^{-60}
δ		DEL	correction parameter for output-power quadratic expression	0
R_s		RS	parasitic series resistance, Ω	0
I_{s1}		IS1	p^+-p interface diode (D_{s1}) saturation current, A	0
n_1		N1	p^+-p interface diode (D_{s1}) ideality factor	1
I_{s2}		IS2	n-n^+ interface diode (D_{s2}) saturation current, A	0
n_2		N2	n-n^+ interface diode (D_{s2}) ideality factor	1
C_{ssc}		CSSC	active-layer shunting space-charge capacitance, F	0
shtype		SHTYPE	type of external shunting circuit (0-4)	0
$R1$		R1	shunting resistance, Ω	0
$C1$		C1	shunting capacitance, F	0
L_{p1}		LP1	RC-network modeling inductance #1	0
L_{p2}		LP2	RC-network modeling inductance #2	0
T_f		TF	ratio of diode temperature (K) to circuit temperature (K)	1

A.1.2 *laser2* model

The two-level rate-equation-based QW laser model of Section 2.4 was implemented using Channin's gain saturation term, the four gain expressions of (A.1), and the parasitics of Section 2.5. The complete set of `laser2` model parameters, also listed in Table A.1, are identical to those of `laser1`, with the addition of parameters accounting for the carrier transport between the QWs and SCH layers.

Following is an example of a model declaration for the `laser2` model:

```
.Xmodel ltest1 laser2 level=1
+ Ne=2.2e11 n=2 Ne2=5.96e14 nw2=2
+ etai=0.86 Lambda=980e-9 Nw=1 Vact=6e-18 Gamma=0.019
+ vgr=8.571e7 tp=2.759e-12 etac=0.449 No=1.5e24 Go=1.5e5 eps=1e-23
+ tn=0.5e-8 A=0.6e8 B=0.7e-16 C=0.6e-41 betaA=0 betaB=1e-4 betaC=0
+ Ab=1.3e8 Bb=1.4e-16 Cb=1.3e-41 Vbarr=2.25e-16 tcapt=45e-12
+ tem=400e-12 cjo=25e-12 vj=2 Cssc=10e-9 Tf=1.5
+ Rs=5 Is1=1e-3 n1=1 Is2=1e-3 n2=1
```

A.2 ISSPICE Implementation

We have also implemented our QW laser models in Intusoft's ISSPICE. Unlike the SPICE3 and HSPICE versions, though, this model utilizes ISSPICE's parameter-passing capabilities, wherein model parameters can be passed directly into a subcircuit. Thus, the various laser models are implemented directly as subcircuits in the library file "`qwlaser.lib`," and can be invoked within an ISSPICE netlist using

```
Xlaser <p> <n> <pf> <model> <model_parameters>
*INCLUDE qwlaser.lib
```

where, as before, `<p>` and `<n>` designate the laser's p- and n-terminals, `<pf>` designates the output node whose voltage corresponds to the optical output power, `<model>` is the name of the model used in this invocation, and `<model_parameters>` are the parameter values for this particular invocation. Subcircuits exist for both the one- and two-level models, where the gain is modeled using the four terms of (A.1) along with Channin's gain saturation term. Junction capacitance is also included, while the parasitics of Section 2.5 are not (but can be added as needed by the user). The complete listing of "`qwlaser.lib`" can be found in Section A.2.3.

A.2.1 One-level cavity model

The one-level cavity model of Section 2.3 can be invoked through the four subcircuits `QWLAS11`, `QWLAS12`, `QWLAS13`, and `QWLAS14`, where each one corresponds to one of the gain terms (A.1a)-(A.1d), respectively. The complete set of model parameters used in the one-level model are summarized in Table A.2 along with their default values. There exists a number of slight differences between these parameters and those used in the SPICE3 and HSPICE models. First, g_l is not calculated by the model; a value *must* be provided by the user. Second, we have again partitioned A into A_2 and $1/\tau_n$. In this case however, τ_n *must* have a nonzero value. If $A = 0$, then A_2 must be set equal to $-1/\tau_n$. The user must ensure that all three parameters have assigned values. Following is an example of a model invocation using the full one-level logarithmic gain model `QWLAS11`:

```
Xlaser p n pf QWLAS11 {
+ Ne=1e12 n=2 etai=0.9 Nw=1 Vact=14e-18 A=1e8 B=1e-16 C=1e-40
+ Gamma=0.02 vgr=1e8 betaB=1e-6 eps=1e-23 No=1.2e24
+ Go=53500 Lambda=1.55e-6 tp=3.69186e-12 gl=2 Nth=3.48368e24
+ etac=0.20465 delta=1e-60 betaA=1e-6 betaC=1e-6 Tf=1 A2=0 tn=1e-8 }
*INCLUDE qwlaser.lib
```

A.2.2 Two-level cavity model

The two-level cavity model of Section 2.4 can be invoked through the subcircuits `QWLAS2A1`, `QWLAS2A2`, `QWLAS2A3`, and `QWLAS2A4`, where each one uses one of the gain terms (A.1a)-(A.1d),

Table A.2 ISSPICE one-level intrinsic-cavity model parameters (*continued on next page)*.

Param.	SPICE NAME	Description, units	Default
N_e	NE	QW equilibrium carrier density, m^{-3}	10^{12}
n	N	QW diode ideality factor	2
η_i	ETAI	current-injection efficiency	1
λ	LAMBDA	emission wavelength, m	850×10^{-9}
N_w	NW	number of quantum wells	1
V_{act}	VACT	volume of a single QW, m^3	10^{-17}
Γ_c	GAMMA	optical confinement factor for 1 QW	0.1
v_{gr}	VGR	lasing-medium group velocity, m/s	10^8
τ_p	TP	cavity, or photon, lifetime, s	3×10^{-12}
η_c	ETAC	output power coupling coefficient	0.35
N_o	NO	optical transparency density, m^{-3}	10^{24}
N_{th}	NTH	threshold carrier density, m^{-3}	1.25×10^{24}
G_o	GO	gain coefficient per QW, m^{-1}	10^5
g_l	GL	linearized-gain scaling factor	1
ε	EPS	phenomenological gain-saturation term, m^3	10^{-23}
τ_n	TN	equivalent linear-recombination time, s	10^{-8}
A_2	A2	equal to $(A - 1/\tau_n)$, s^{-1}	0
A	A	QW unimolecular recombination coefficient, s^{-1}	10^8
B	B	QW radiative recombination coefficient, m^3/s	10^{-16}
C	C	QW Auger recombination coefficient, m^6/s	0
β_A	BETAA	QW unimolecular spontaneous-emission coupling coefficient	0
β_B	BETAB	QW radiative spontaneous-emission coupling coefficient	10^{-6}
β_C	BETAC	QW Auger spontaneous-emission coupling coefficient	0
C_{jo}	CJO	zero-bias junction capacitance, F	0
m_p	MPOW	diode grading coefficient	0.5

Table A.2 (*Continued.*)

Param.	SPICE NAME	Description, units	Default
ϕ_o	VJ	built-in junction potential, V	1
FC	FC	coefficient for forward-bias junction capacitance formula	0.5
Δ	DELTA	ln(0) correction parameter	10^{-60}
δ	DEL	correction parameter for output-power quadratic expression	0
T_f	TF	ratio of diode temperature (K) to circuit temperature (K)	1

respectively. In addition, a corresponding set of models exists in which SCH recombination is neglected: `QWLAS2B1`, `QWLAS2B2`, `QWLAS2B3`, and `QWLAS2B4`. The complete set of model parameters used in the two-level model are summarized in Table A.3 along with their default values. Like the one-level versions, g_l is not calculated by the model; thus, a value must be provided by the user. Unlike the one-level models, however, we no longer partition A into A_2 and $1/\tau_n$ (these parameters will be ignored if set by the user). A typical invocation of the two-level model is shown below.

```
Xlaser p n pf QWLAS2a1 {
+ Ne=1e12 n=2 Ne2=1e12 nw2=2 etai=0.9 Nw=1 Vact=14e-18
+ A=1e8 B=1e-16 C=1e-40 Gamma=0.02 vgr=1e8 betaB=1e-6
+ eps=1e-23 No=1.2e24 Go=53500 Lambda=1.55e-6
+ tp=3.69186e-12 gl=2 Nth=3.48368e24 etac=0.20465 delta=1e-60
+ betaA=1e-6 betaC=1e-6 Tf=1
+ Vbarr=1e-16 tcapt=2e-12 tem=2e-9
+ Ab=1e8 Bb=1e-16 Cb=1e-40 }
*INCLUDE qwlaser.lib
```

Table A.3 ISSPICE two-level intrinsic-cavity model parameters.

Param.	SPICE NAME	Description, units	Default
N_e	NE	SCH equilibrium carrier density, m^{-3}	10^{12}
n	N	SCH diode ideality factor	2
N_{e2}	NE2	QW equilibrium carrier density, m^{-3}	10^{12}
n_{w2}	NW2	QW diode ideality factor	1
η_i	ETAI	current-injection efficiency	1
λ	LAMBDA	emission wavelength, m	850×10^{-9}
N_w	NW	number of quantum wells	1
V_{act}	VACT	volume of a single QW, m^3	10^{-17}
Γ_c	GAMMA	optical confinement factor for 1 QW	0.1
v_{gr}	VGR	lasing-medium group velocity, m/s	10^8
τ_p	TP	cavity, or photon, lifetime, s	3×10^{-12}
η_c	ETAC	output power coupling coefficient	0.35
N_o	NO	optical transparency density, m^{-3}	10^{24}
N_{th}	NTH	threshold carrier density, m^{-3}	1.25×10^{24}
G_o	GO	gain coefficient per QW, m^{-1}	10^5
g_l	GL	linearized-gain scaling factor	1
ε	EPS	phenomenological gain-saturation term, m^3	10^{-23}
A	A	QW unimolecular recombination coefficient, s^{-1}	10^8
B	B	QW radiative recombination coefficient, m^3/s	10^{-16}
C	C	QW Auger recombination coefficient, m^6/s	0
β_A	BETAA	QW unimolecular spontaneous-emission coupling coefficient	0
β_B	BETAB	QW radiative spontaneous-emission coupling coefficient	10^{-6}
β_C	BETAC	QW Auger spontaneous-emission coupling coefficient	0
V_{barr}	VBARR	total volume of barrier layers, m^3	10^{-16}
τ_{capt}	TCAPT	QW carrier capture lifetime, s	10^{-12}
τ_{em}	TEM	QW carrier emission lifetime, s	10^{-9}
A_b	AB	SCH unimolecular recombination coefficient, s^{-1}	10^8
B_b	BB	SCH radiative recombination coefficient, m^3/s	10^{-16}
C_b	CB	SCH Auger recombination coefficient, m^6/s	10^{-40}
C_{jo}	CJO	zero-bias junction capacitance, F	0
m_p	MPOW	diode grading coefficient	0.5
ϕ_o	VJ	built-in junction potential, V	1
FC	FC	coefficient for forward-bias junction capacitance formula	0.5
Δ	DELTA	ln(0) correction parameter	10^{-60}
δ	DEL	correction parameter for output-power quadratic expression	0
T_f	TF	ratio of diode temperature (K) to circuit temperature (K)	1

A.2.3 ISSPICE subcircuit library

Below we provide the source for “qwlaser.lib.”

```
***********
* QW-LASER MODEL
* QW-LASER INTRINSIC CAVITY SUBCIRCUITS
* each qw cavity subckt has the name qwlas<a><b>. <a><b> identify the model.
*   - a = model number = 1:  one-level rate-equation model
*                        2a: two-level rate-equation model with SCH recomb.
*                        2b: two-level rate-equation model w/o SCH recomb.
*   - b = level number = 1: full logarithmic gain
*                        2: simplified logarithmic gain
*                        3: gain linearized about optical transparency
*                        4: gain linearized about threshold
* - - - - -
***********
*SYM=QWL1
.SUBCKT QWLAS11 P N PF {
+ NE=1E12 N=2 NE2=1E12 NW2=1 ETAI=1 LAMBDA=850E-9 NW=1 VACT=1E-17
+ GAMMA=0.1 VGR=1E8 TP=3E-12 ETAC=0.35 NO=1E24 NTH=1.25E24 GO=1E5
+ GL=1 EPS=1E-23 TN=1E-8 A2=0 A=1E8 B=1E-16 C=0 AB=1E8 BB=1E-16 CB=1E-40
+ BETAA=0 BETAB=1E-6 BETAC=0 VBARR=1E-16 TCAPT=1e-12 TEM=1e-9
+ CJO=0 MPOW=0.5 VJ=1 FC=0.5 DELTA=1e-60 DEL=0 TF=1 }
D1 P NT1 D1MOD
IC1 P NT1 {1.60219E-19*NW*VACT*NE/(2*ETAI*TN)}
VT1 NT1 N 0
D2 P N D2MOD
IC2 P N {1.60219E-19*NW*VACT*NE/(2*ETAI*TN)}
BR1 P N I={2*A2*TN}*I(VT1)+{4*ETAI*B*TN^2/(1.60219E-19*NW*VACT)}*I(VT1)*I(VT1)+
+   {8*ETAI^2*C*TN^3/(1.60219E-19*NW*VACT)^2}*I(VT1)*I(VT1)*I(VT1)
BS1 P N I={LAMBDA*TP*1.60219E-19*NW*GAMMA*VGR*GO/(ETAI*ETAC*6.6262E-34*3E8)}*
+   (V(M)+{DEL})*(V(M)+{DEL})*LN({DELTA}+
+   {2*A*ETAI*TN/(1.60219E-19*NW*VACT)/(A*NO+B*NO^2+C*NO^3)}*I(VT1)+
+   {4*B*(ETAI*TN/(1.60219E-19*NW*VACT))^2/(A*NO+B*NO^2+C*NO^3)}*I(VT1)*I(VT1)+
+   {8*C*(ETAI*TN/(1.60219E-19*NW*VACT))^3/(A*NO+B*NO^2+C*NO^3)}*I(VT1)*
+   I(VT1)*I(VT1))/(1+{EPS*GAMMA*LAMBDA*TP/(ETAC*VACT*6.6262E–34*3E8)}*(V(M)+{DEL})*
+   (V(M)+{DEL}))
RPH M 0 1
CPH M 0 {2*TP}
BR2 0 M I=({2*ETAI*ETAC*TN*6.6262E-34*3E8*BETAA*A/(1.60219E-19*LAMBDA)}*I(VT1)+
+   {4*ETAI^2*ETAC*TN^2*6.6262E-34*3E8*BETAB*B/((1.60219E-19)^2*LAMBDA*NW*VACT)}*
+   I(VT1)*I(VT1)+
+   {8*ETAI^3*ETAC*TN^3*6.6262E-34*3E8*BETAC*C/((1.60219E-19)^3*LAMBDA*(NW*VACT)^2)}*
+   I(VT1)*I(VT1)*I(VT1))/(V(M)+{DEL})
BS2 0 M I={TP*NW*GAMMA*VGR*GO}*(V(M)+{DEL})*LN({DELTA}+
+   {2*A*ETAI*TN/(1.60219E-19*NW*VACT)/(A*NO+B*NO^2+C*NO^3)}*I(VT1)+
+   {4*B*(ETAI*TN/(1.60219E-19*NW*VACT))^2/(A*NO+B*NO^2+C*NO^3)}*I(VT1)*I(VT1)+
+   {8*C*(ETAI*TN/(1.60219E-19*NW*VACT))^3/(A*NO+B*NO^2+C*NO^3)}*I(VT1)*
+   I(VT1)*I(VT1))/(1+{EPS*GAMMA*LAMBDA*TP/(ETAC*VACT*6.6262E-34*3E8)}*(V(M)+{DEL})*
+   (V(M)+{DEL}))-{DEL}
BPF PF 0 V=(V(M)+{DEL})*(V(M)+{DEL})
.MODEL D1MOD D IS={1.60219E-19*NW*VACT*NE/(2*ETAI*TN)} N={N*TF}
.MODEL D2MOD D IS={1.60219E-19*NW*VACT*NE/(2*ETAI*TN)} N={N*TF} TT={2*TN}
+              CJO={CJO} M={MPOW} VJ={VJ} FC={FC}
```

```
.ENDS
***********
*SYM=QWL1
.SUBCKT QWLAS12 P N PF {
+ NE=1E12 N=2 NE2=1E12 NW2=1 ETAI=1 LAMBDA=850E-9 NW=1 VACT=1E-17
+ GAMMA=0.1 VGR=1E8 TP=3E-12 ETAC=0.35 NO=1E24 NTH=1.25E24 GO=1E5
+ GL=1 EPS=1E-23 TN=1E-8 A2=0 A=1E8 B=1E-16 C=0 AB=1E8 BB=1E-16 CB=1E-40
+ BETAA=0 BETAB=1E-6 BETAC=0 VBARR=1E-16 TCAPT=1e-12 TEM=1e-9
+ CJO=0 MPOW=0.5 VJ=1 FC=0.5 DELTA=1e-60 DEL=0 TF=1 }
D1 P NT1 D1MOD
IC1 P NT1 {1.60219E-19*NW*VACT*NE/(2*ETAI*TN)}
VT1 NT1 N 0
D2 P N D2MOD
IC2 P N {1.60219E-19*NW*VACT*NE/(2*ETAI*TN)}
BR1 P N I={2*A2*TN}*I(VT1)+{4*ETAI*B*TN^2/(1.60219E-19*NW*VACT)}*I(VT1)*I(VT1)+
+   {8*ETAI^2*C*TN^3/(1.60219E-19*NW*VACT)^2}*I(VT1)*I(VT1)*I(VT1)
BS1 P N I={GL*LAMBDA*TP*1.60219E-19*NW*GAMMA*VGR*GO/(ETAI*ETAC*6.6262E-34*3E8)}*
+   (V(M)+{DEL})*(V(M)+{DEL})*LN({DELTA}+{2*ETAI*TN/(1.60219E-19*NW*VACT*NO)}*
+   I(VT1))/(1+{EPS*GAMMA*LAMBDA*TP/(ETAC*VACT*6.6262E-34*3E8)}*(V(M)+{DEL})*
+   (V(M)+{DEL}))
RPH M 0 1
CPH M 0 {2*TP}
BR2 0 M I=({2*ETAI*ETAC*TN*6.6262E-34*3E8*BETAA*A/(1.60219E-19*LAMBDA)}*I(VT1)+
+   {4*ETAI^2*ETAC*TN^2*6.6262E-34*3E8*BETAB*B/((1.60219E-19)^2*LAMBDA*NW*VACT)}*
+   I(VT1)*I(VT1)+
+   {8*ETAI^3*ETAC*TN^3*6.6262E-34*3E8*BETAC*C/((1.60219E-19)^3*LAMBDA*(NW*VACT)^2)}*
+   I(VT1)*I(VT1)*I(VT1))/(V(M)+{DEL})
BS2 0 M I={GL*TP*NW*GAMMA*VGR*GO}*(V(M)+{DEL})*
+   LN({DELTA}+{2*ETAI*TN/(1.60219E-19*NW*VACT*NO)}*I(VT1))/(1+
+   {EPS*GAMMA*LAMBDA*TP/(ETAC*VACT*6.6262E-34*3E8)}*(V(M)+{DEL})*(V(M)+{DEL}))-
+   {DEL}
BPF PF 0 V=(V(M)+{DEL})*(V(M)+{DEL})
.MODEL D1MOD D IS={1.60219E-19*NW*VACT*NE/(2*ETAI*TN)} N={N*TF}
.MODEL D2MOD D IS={1.60219E-19*NW*VACT*NE/(2*ETAI*TN)} N={N*TF} TT={2*TN}
+              CJO={CJO} M={MPOW} VJ={VJ} FC={FC}
.ENDS
***********
*SYM=QWL1
.SUBCKT QWLAS13 P N PF {
+ NE=1E12 N=2 NE2=1E12 NW2=1 ETAI=1 LAMBDA=850E-9 NW=1 VACT=1E-17
+ GAMMA=0.1 VGR=1E8 TP=3E-12 ETAC=0.35 NO=1E24 NTH=1.25E24 GO=1E5
+ GL=1 EPS=1E-23 TN=1E-8 A2=0 A=1E8 B=1E-16 C=0 AB=1E8 BB=1E-16 CB=1E-40
+ BETAA=0 BETAB=1E-6 BETAC=0 VBARR=1E-16 TCAPT=1e-12 TEM=1e-9
+ CJO=0 MPOW=0.5 VJ=1 FC=0.5 DELTA=1e-60 DEL=0 TF=1 }
D1 P NT1 D1MOD
IC1 P NT1 {1.60219E-19*NW*VACT*NE/(2*ETAI*TN)}
VT1 NT1 N 0
D2 P N D2MOD
IC2 P N {1.60219E-19*NW*VACT*NE/(2*ETAI*TN)}
BR1 P N I={2*A2*TN}*I(VT1)+{4*ETAI*B*TN^2/(1.60219E-19*NW*VACT)}*I(VT1)*I(VT1)+
+   {8*ETAI^2*C*TN^3/(1.60219E-19*NW*VACT)^2}*I(VT1)*I(VT1)*I(VT1)
BS1 P N I=(V(M)+{DEL})*(V(M)+{DEL})*
+   ({2*GL*LAMBDA*TP*GAMMA*VGR*GO*TN/(ETAC*VACT*NO*6.6262E-34*3E8)}*I(VT1)-
+   {GL*LAMBDA*TP*1.60219E-19*NW*GAMMA*VGR*GO/(ETAI*ETAC*6.6262E-34*3E8)})/
+   (1+{EPS*GAMMA*LAMBDA*TP/(ETAC*VACT*6.6262E-34*3E8)}*(V(M)+{DEL})*(V(M)+{DEL}))
RPH M 0 1
CPH M 0 {2*TP}
```

```
BR2 0 M I=({2*ETAI*ETAC*TN*6.6262E-34*3E8*BETAA*A/(1.60219E-19*LAMBDA)}*I(VT1)+
+   {4*ETAI^2*ETAC*TN^2*6.6262E-34*3E8*BETAB*B/((1.60219E-19)^2*LAMBDA*NW*VACT)}*
+   I(VT1)*I(VT1)+
+   {8*ETAI^3*ETAC*TN^3*6.6262E-34*3E8*BETAC*C/((1.60219E-19)^3*LAMBDA*(NW*VACT)^2)}*
+   I(VT1)*I(VT1)*I(VT1))/(V(M)+{DEL})
BS2 0 M I=(V(M)+{DEL})*({2*GL*TP*GAMMA*VGR*GO*ETAI*TN/(1.60219E-19*VACT*NO)}*I(VT1)-
+   {GL*TP*NW*GAMMA*VGR*GO})/(1+{EPS*GAMMA*LAMBDA*TP/(ETAC*VACT*6.6262E-34*3E8)}*
+   (V(M)+{DEL})*(V(M)+{DEL}))-{DEL}
BPF PF 0 V=(V(M)+{DEL})*(V(M)+{DEL})
.MODEL D1MOD D IS={1.60219E-19*NW*VACT*NE/(2*ETAI*TN)} N={N*TF}
.MODEL D2MOD D IS={1.60219E-19*NW*VACT*NE/(2*ETAI*TN)} N={N*TF} TT={2*TN}
+              CJO={CJO} M={MPOW} VJ={VJ} FC={FC}
.ENDS
***********
*SYM=QWL1
.SUBCKT QWLAS14 P N PF {
+ NE=1E12 N=2 NE2=1E12 NW2=1 ETAI=1 LAMBDA=850E-9 NW=1 VACT=1E-17
+ GAMMA=0.1 VGR=1E8 TP=3E-12 ETAC=0.35 NO=1E24 NTH=1.25E24 GO=1E5
+ GL=1 EPS=1E-23 TN=1E-8 A2=0 A=1E8 B=1E-16 C=0 AB=1E8 BB=1E-16 CB=1E-40
+ BETAA=0 BETAB=1E-6 BETAC=0 VBARR=1E-16 TCAPT=1e-12 TEM=1e-9
+ CJO=0 MPOW=0.5 VJ=1 FC=0.5 DELTA=1e-60 DEL=0 TF=1 }
D1 P NT1 D1MOD
IC1 P NT1 {1.60219E-19*NW*VACT*NE/(2*ETAI*TN)}
VT1 NT1 N 0
D2 P N D2MOD
IC2 P N {1.60219E-19*NW*VACT*NE/(2*ETAI*TN)}
BR1 P N I={2*A2*TN}*I(VT1)+{4*ETAI*B*TN^2/(1.60219E-19*NW*VACT)}*I(VT1)*I(VT1)+
+   {8*ETAI^2*C*TN^3/(1.60219E-19*NW*VACT)^2}*I(VT1)*I(VT1)*I(VT1)
BS1 P N I=(V(M)+{DEL})*(V(M)+{DEL})*
+   ({2*GL*LAMBDA*TP*GAMMA*VGR*GO*TN/(ETAC*VACT*NTH*6.6262E-34*3E8)}*I(VT1)-
+   {(LAMBDA*TP*1.60219E-19*NW*GAMMA*VGR*GO/(ETAI*ETAC*6.6262E-34*3E8))*
+    (GL-LOG((A*NTH+B*NTH^2+C*NTH^3)/(A*NO+B*NO^2+C*NO^3)))})/
+    (1+{EPS*GAMMA*LAMBDA*TP/(ETAC*VACT*6.6262E-34*3E8)}*(V(M)+{DEL})*(V(M)+{DEL}))
RPH M 0 1
CPH M 0 {2*TP}
BR2 0 M I=({2*ETAI*ETAC*TN*6.6262E-34*3E8*BETAA*A/(1.60219E-19*LAMBDA)}*I(VT1)+
+   {4*ETAI^2*ETAC*TN^2*6.6262E-34*3E8*BETAB*B/((1.60219E-19)^2*LAMBDA*NW*VACT)}*
+   I(VT1)*I(VT1)+
+   {8*ETAI^3*ETAC*TN^3*6.6262E-34*3E8*BETAC*C/((1.60219E-19)^3*LAMBDA*(NW*VACT)^2)}*
+   I(VT1)*I(VT1)*I(VT1))/(V(M)+{DEL})
BS2 0 M I=(V(M)+{DEL})*({2*GL*TP*GAMMA*VGR*GO*ETAI*TN/(1.60219E-19*VACT*NTH)}*I(VT1)-
+   {TP*NW*GAMMA*VGR*GO*
+    (GL-LOG((A*NTH+B*NTH^2+C*NTH^3)/(A*NO+B*NO^2+C*NO^3)))})/
+    (1+{EPS*GAMMA*LAMBDA*TP/(ETAC*VACT*6.6262E-34*3E8)}*(V(M)+{DEL})*(V(M)+{DEL}))-
+   {DEL}
BPF PF 0 V=(V(M)+{DEL})*(V(M)+{DEL})
.MODEL D1MOD D IS={1.60219E-19*NW*VACT*NE/(2*ETAI*TN)} N={N*TF}
.MODEL D2MOD D IS={1.60219E-19*NW*VACT*NE/(2*ETAI*TN)} N={N*TF} TT={2*TN}
+              CJO={CJO} M={MPOW} VJ={VJ} FC={FC}
.ENDS
***********
*SYM=QWL1
.SUBCKT QWLAS2A1 P N PF {
+ NE=1E12 N=2 NE2=1E12 NW2=1 ETAI=1 LAMBDA=850E-9 NW=1 VACT=1E-17
+ GAMMA=0.1 VGR=1E8 TP=3E-12 ETAC=0.35 NO=1E24 NTH=1.25E24 GO=1E5
+ GL=1 EPS=1E-23 TN=1E-8 A2=0 A=1E8 B=1E-16 C=0 AB=1E8 BB=1E-16 CB=1E-40
+ BETAA=0 BETAB=1E-6 BETAC=0 VBARR=1E-16 TCAPT=1e-12 TEM=1e-9
```

```
+ CJO=0 MPOW=0.5 VJ=1 FC=0.5 DELTA=1e-60 DEL=0 TF=1 }
D1 P NT1 D1MOD
IC1 P NT1 {1.60219E-19*VBARR*NE/(2*ETAI*TCAPT)}
VT1 NT1 N 0
D2 P N D2MOD
IC2 P N {1.60219E-19*VBARR*NE/(2*ETAI*TCAPT)}
BRB P N I={2*AB*TCAPT}*I(VT1)+{4*ETAI*BB*TCAPT^2/(1.60219E-19*VBARR)}*I(VT1)*I(VT1)+
+   {8*ETAI^2*CB*TCAPT^3/(1.60219E-19*VBARR)^2}*I(VT1)*I(VT1)*I(VT1)
F1 N P VTW1 1
DW1  W NTW1 DW1MOD
ICW1 W NTW1 {1.60219E-19*NW*VACT*NE2/(ETAI*TEM)}
VTW1 NTW1 0 0
DW2  W 0 DW2MOD
ICW2 W 0 {1.60219E-19*NW*VACT*NE2/(ETAI*TEM)}
BR1 W 0 I={2*A*TEM}*I(VTW1)+{2*ETAI*B*TEM^2/(1.60219E-19*NW*VACT)}*I(VTW1)*I(VTW1)+
+   {2*ETAI^2*C*TEM^3/(1.60219E-19*NW*VACT)^2}*I(VTW1)*I(VTW1)*I(VTW1)
BS1 W 0 I={2*LAMBDA*TP*1.60219E-19*NW*GAMMA*VGR*GO/(ETAI*ETAC*6.6262E-34*3E8)}*
+   (V(M)+{DEL})*(V(M)+{DEL})*LN({DELTA}+
+   {A*ETAI*TEM/(1.60219E-19*NW*VACT)/(A*NO+B*NO^2+C*NO^3)}*I(VTW1)+
+   {B*(ETAI*TEM/(1.60219E-19*NW*VACT))^2/(A*NO+B*NO^2+C*NO^3)}*I(VTW1)*I(VTW1)+
+   {C*(ETAI*TEM/(1.60219E-19*NW*VACT))^3/(A*NO+B*NO^2+C*NO^3)}*I(VTW1)*
+   I(VTW1)*I(VTW1))/(1+{EPS*GAMMA*LAMBDA*TP/(ETAC*VACT*6.6262E-34*3E8)}*(V(M)+{DEL})*
+   (V(M)+{DEL}))
F2 0 W VT1 4
RPH M 0 1
CPH M 0 {2*TP}
BR2 0 M I=({ETAI*ETAC*TEM*6.6262E-34*3E8*BETAA*A/(1.60219E-19*LAMBDA)}*I(VTW1)+
+   {ETAI^2*ETAC*TEM^2*6.6262E-34*3E8*BETAB*B/((1.60219E-19)^2*LAMBDA*NW*VACT)}*I(VTW1)
+   *I(VTW1)+
+   {ETAI^3*ETAC*TEM^3*6.6262E-34*3E8*BETAC*C/((1.60219E-19)^3*LAMBDA*(NW*VACT)^2)}*
+   I(VTW1)*I(VTW1)*I(VTW1))/(V(M)+{DEL})
BS2 0 M I={TP*NW*GAMMA*VGR*GO}*(V(M)+{DEL})*LN({DELTA}+
+   {A*ETAI*TEM/(1.60219E-19*NW*VACT)/(A*NO+B*NO^2+C*NO^3)}*I(VTW1)+
+   {B*(ETAI*TEM/(1.60219E-19*NW*VACT))^2/(A*NO+B*NO^2+C*NO^3)}*I(VTW1)*I(VTW1)+
+   {C*(ETAI*TEM/(1.60219E-19*NW*VACT))^3/(A*NO+B*NO^2+C*NO^3)}*I(VTW1)*
+   I(VTW1)*I(VTW1))/(1+{EPS*GAMMA*LAMBDA*TP/(ETAC*VACT*6.6262E-34*3E8)}*(V(M)+{DEL})*
+   (V(M)+{DEL}))-{DEL}
BPF PF 0 V=(V(M)+{DEL})*(V(M)+{DEL})
.MODEL D1MOD D IS={1.60219E-19*VBARR*NE/(2*ETAI*TCAPT)} N={N*TF}
.MODEL D2MOD D IS={1.60219E-19*VBARR*NE/(2*ETAI*TCAPT)} N={N*TF} TT={2*TCAPT}
+              CJO={CJO} M={MPOW} VJ={VJ} FC={FC}
.MODEL DW1MOD D IS={1.60219E-19*NW*VACT*NE2/(ETAI*TEM)} N={NW2*TF}
.MODEL DW2MOD D IS={1.60219E-19*NW*VACT*NE2/(ETAI*TEM)} N={NW2*TF} TT={2*TEM}
.ENDS
***********
*SYM=QWL1
.SUBCKT QWLAS2A2 P N PF {
+ NE=1E12 N=2 NE2=1E12 NW2=1 ETAI=1 LAMBDA=850E-9 NW=1 VACT=1E-17
+ GAMMA=0.1 VGR=1E8 TP=3E-12 ETAC=0.35 NO=1E24 NTH=1.25E24 GO=1E5
+ GL=1 EPS=1E-23 TN=1E-8 A2=0 A=1E8 B=1E-16 C=0 AB=1E8 BB=1E-16 CB=1E-40
+ BETAA=0 BETAB=1E-6 BETAC=0 VBARR=1E-16 TCAPT=1e-12 TEM=1e-9
+ CJO=0 MPOW=0.5 VJ=1 FC=0.5 DELTA=1e-60 DEL=0 TF=1 }
D1 P NT1 D1MOD
IC1 P NT1 {1.60219E-19*VBARR*NE/(2*ETAI*TCAPT)}
VT1 NT1 N 0
D2 P N D2MOD
IC2 P N {1.60219E-19*VBARR*NE/(2*ETAI*TCAPT)}
```

```
BRB P N I={2*AB*TCAPT}*I(VT1)+{4*ETAI*BB*TCAPT^2/(1.60219E-19*VBARR)}*I(VT1)*I(VT1)+
+   {8*ETAI^2*CB*TCAPT^3/(1.60219E-19*VBARR)^2}*I(VT1)*I(VT1)*I(VT1)
F1 N P VTW1 1
DW1  W NTW1 DW1MOD
ICW1 W NTW1 {1.60219E-19*NW*VACT*NE2/(ETAI*TEM)}
VTW1 NTW1 0 0
DW2  W 0 DW2MOD
ICW2 W 0 {1.60219E-19*NW*VACT*NE2/(ETAI*TEM)}
BR1 W 0 I={2*A*TEM}*I(VTW1)+{2*ETAI*B*TEM^2/(1.60219E-19*NW*VACT)}*I(VTW1)*I(VTW1)+
+   {2*ETAI^2*C*TEM^3/(1.60219E-19*NW*VACT)^2}*I(VTW1)*I(VTW1)*I(VTW1)
BS1 W 0 I={2*GL*LAMBDA*TP*1.60219E-19*NW*GAMMA*VGR*GO/(ETAI*ETAC*6.6262E-34*3E8)}*
+   (V(M)+{DEL})*(V(M)+{DEL})*LN({DELTA}+{ETAI*TEM/(1.60219E-19*NW*VACT*NO)}*
+   I(VTW1))/(1+{EPS*GAMMA*LAMBDA*TP/(ETAC*VACT*6.6262E-34*3E8)}*(V(M)+{DEL})*
+   (V(M)+{DEL}))
F2 0 W VT1 4
RPH M 0 1
CPH M 0 {2*TP}
BR2 0 M I=({ETAI*ETAC*TEM*6.6262E-34*3E8*BETAA*A/(1.60219E-19*LAMBDA)}*I(VTW1)+
+   {ETAI^2*ETAC*TEM^2*6.6262E-34*3E8*BETAB*B/((1.60219E-19)^2*LAMBDA*NW*VACT)}*I(VTW1)
+   *I(VTW1)+
+   {ETAI^3*ETAC*TEM^3*6.6262E-34*3E8*BETAC*C/((1.60219E-19)^3*LAMBDA*(NW*VACT)^2)}*
+   I(VTW1)*I(VTW1)*I(VTW1))/(V(M)+{DEL})
BS2 0 M I={GL*TP*NW*GAMMA*VGR*GO}*(V(M)+{DEL})*
+   LN({DELTA}+{ETAI*TEM/(1.60219E-19*NW*VACT*NO)}*I(VTW1))/(1+
+   {EPS*GAMMA*LAMBDA*TP/(ETAC*VACT*6.6262E-34*3E8)}*(V(M)+{DEL})*(V(M)+{DEL}))-
+   {DEL}
BPF PF 0 V=(V(M)+{DEL})*(V(M)+{DEL})
.MODEL D1MOD D IS={1.60219E-19*VBARR*NE/(2*ETAI*TCAPT)} N={N*TF}
.MODEL D2MOD D IS={1.60219E-19*VBARR*NE/(2*ETAI*TCAPT)} N={N*TF} TT={2*TCAPT}
+              CJO={CJO} M={MPOW} VJ={VJ} FC={FC}
.MODEL DW1MOD D IS={1.60219E-19*NW*VACT*NE2/(ETAI*TEM)} N={NW2*TF}
.MODEL DW2MOD D IS={1.60219E-19*NW*VACT*NE2/(ETAI*TEM)} N={NW2*TF} TT={2*TEM}
.ENDS
***********
*SYM=QWL1
.SUBCKT QWLAS2A3 P N PF {
+ NE=1E12 N=2 NE2=1E12 NW2=1 ETAI=1 LAMBDA=850E-9 NW=1 VACT=1E-17
+ GAMMA=0.1 VGR=1E8 TP=3E-12 ETAC=0.35 NO=1E24 NTH=1.25E24 GO=1E5
+ GL=1 EPS=1E-23 TN=1E-8 A2=0 A=1E8 B=1E-16 C=0 AB=1E8 BB=1E-16 CB=1E-40
+ BETAA=0 BETAB=1E-6 BETAC=0 VBARR=1E-16 TCAPT=1e-12 TEM=1e-9
+ CJO=0 MPOW=0.5 VJ=1 FC=0.5 DELTA=1e-60 DEL=0 TF=1 }
D1 P NT1 D1MOD
IC1 P NT1 {1.60219E-19*VBARR*NE/(2*ETAI*TCAPT)}
VT1 NT1 N 0
D2 P N D2MOD
IC2 P N {1.60219E-19*VBARR*NE/(2*ETAI*TCAPT)}
BRB P N I={2*AB*TCAPT}*I(VT1)+{4*ETAI*BB*TCAPT^2/(1.60219E-19*VBARR)}*I(VT1)*I(VT1)+
+   {8*ETAI^2*CB*TCAPT^3/(1.60219E-19*VBARR)^2}*I(VT1)*I(VT1)*I(VT1)
F1 N P VTW1 1
DW1  W NTW1 DW1MOD
ICW1 W NTW1 {1.60219E-19*NW*VACT*NE2/(ETAI*TEM)}
VTW1 NTW1 0 0
DW2  W 0 DW2MOD
ICW2 W 0 {1.60219E-19*NW*VACT*NE2/(ETAI*TEM)}
BR1 W 0 I={2*A*TEM}*I(VTW1)+{2*ETAI*B*TEM^2/(1.60219E-19*NW*VACT)}*I(VTW1)*I(VTW1)+
+   {2*ETAI^2*C*TEM^3/(1.60219E-19*NW*VACT)^2}*I(VTW1)*I(VTW1)*I(VTW1)
BS1 W 0 I=(V(M)+{DEL})*(V(M)+{DEL})*
```

```
+   ({2*GL*LAMBDA*TP*GAMMA*VGR*GO*TEM/(ETAC*VACT*NO*6.6262E-34*3E8)}*I(VTW1)-
+   {2*GL*LAMBDA*TP*1.60219E-19*NW*GAMMA*VGR*GO/(ETAI*ETAC*6.6262E-34*3E8)})/
+   (1+{EPS*GAMMA*LAMBDA*TP/(ETAC*VACT*6.6262E-34*3E8)}*(V(M)+{DEL})*(V(M)+{DEL}))
F2 0 W VT1 4
RPH M 0 1
CPH M 0 {2*TP}
BR2 0 M I=({ETAI*ETAC*TEM*6.6262E-34*3E8*BETAA*A/(1.60219E-19*LAMBDA)}*I(VTW1)+
+   {ETAI^2*ETAC*TEM^2*6.6262E-34*3E8*BETAB*B/((1.60219E-19)^2*LAMBDA*NW*VACT)}*I(VTW1)
+   *I(VTW1)+
+   {ETAI^3*ETAC*TEM^3*6.6262E-34*3E8*BETAC*C/((1.60219E-19)^3*LAMBDA*(NW*VACT)^2)}*
+   I(VTW1)*I(VTW1)*I(VTW1))/(V(M)+{DEL})
BS2 0 M I=(V(M)+{DEL})*({GL*TP*GAMMA*VGR*GO*ETAI*TEM/(1.60219E-19*VACT*NO)}*I(VTW1)-
+   {GL*TP*NW*GAMMA*VGR*GO})/(1+{EPS*GAMMA*LAMBDA*TP/(ETAC*VACT*6.6262E-34*3E8)}*
+   (V(M)+{DEL})*(V(M)+{DEL}))-{DEL}
BPF PF 0 V=(V(M)+{DEL})*(V(M)+{DEL})
.MODEL D1MOD D IS={1.60219E-19*VBARR*NE/(2*ETAI*TCAPT)} N={N*TF}
.MODEL D2MOD D IS={1.60219E-19*VBARR*NE/(2*ETAI*TCAPT)} N={N*TF} TT={2*TCAPT}
+              CJO={CJO} M={MPOW} VJ={VJ} FC={FC}
.MODEL DW1MOD D IS={1.60219E-19*NW*VACT*NE2/(ETAI*TEM)} N={NW2*TF}
.MODEL DW2MOD D IS={1.60219E-19*NW*VACT*NE2/(ETAI*TEM)} N={NW2*TF} TT={2*TEM}
.ENDS
***********
*SYM=QWL1
.SUBCKT QWLAS2A4 P N PF {
+ NE=1E12 N=2 NE2=1E12 NW2=1 ETAI=1 LAMBDA=850E-9 NW=1 VACT=1E-17
+ GAMMA=0.1 VGR=1E8 TP=3E-12 ETAC=0.35 NO=1E24 NTH=1.25E24 GO=1E5
+ GL=1 EPS=1E-23 TN=1E-8 A2=0 A=1E8 B=1E-16 C=0 AB=1E8 BB=1E-16 CB=1E-40
+ BETAA=0 BETAB=1E-6 BETAC=0 VBARR=1E-16 TCAPT=1e-12 TEM=1e-9
+ CJO=0 MPOW=0.5 VJ=1 FC=0.5 DELTA=1e-60 DEL=0 TF=1 }
D1 P NT1 D1MOD
IC1 P NT1 {1.60219E-19*VBARR*NE/(2*ETAI*TCAPT)}
VT1 NT1 N 0
D2 P N D2MOD
IC2 P N {1.60219E-19*VBARR*NE/(2*ETAI*TCAPT)}
BRB P N I={2*AB*TCAPT}*I(VT1)+{4*ETAI*BB*TCAPT^2/(1.60219E-19*VBARR)}*I(VT1)*I(VT1)+
+   {8*ETAI^2*CB*TCAPT^3/(1.60219E-19*VBARR)^2}*I(VT1)*I(VT1)*I(VT1)
F1 N P VTW1 1
DW1  W NTW1 DW1MOD
ICW1 W NTW1 {1.60219E-19*NW*VACT*NE2/(ETAI*TEM)}
VTW1 NTW1 0 0
DW2  W 0 DW2MOD
ICW2 W 0 {1.60219E-19*NW*VACT*NE2/(ETAI*TEM)}
BR1 W 0 I={2*A*TEM}*I(VTW1)+{2*ETAI*B*TEM^2/(1.60219E-19*NW*VACT)}*I(VTW1)*I(VTW1)+
+   {2*ETAI^2*C*TEM^3/(1.60219E-19*NW*VACT)^2}*I(VTW1)*I(VTW1)*I(VTW1)
BS1 W 0 I=(V(M)+{DEL})*(V(M)+{DEL})*
+   ({2*GL*LAMBDA*TP*GAMMA*VGR*GO*TEM/(ETAC*VACT*NTH*6.6262E-34*3E8)}*I(VTW1)-
+   {(2*LAMBDA*TP*1.60219E-19*NW*GAMMA*VGR*GO/(ETAI*ETAC*6.6262E-34*3E8))*
+    (GL-LOG((A*NTH+B*NTH^2+C*NTH^3)/(A*NO+B*NO^2+C*NO^3)))})/
+   (1+{EPS*GAMMA*LAMBDA*TP/(ETAC*VACT*6.6262E-34*3E8)}*(V(M)+{DEL})*(V(M)+{DEL}))
F2 0 W VT1 4
RPH M 0 1
CPH M 0 {2*TP}
BR2 0 M I=({ETAI*ETAC*TEM*6.6262E-34*3E8*BETAA*A/(1.60219E-19*LAMBDA)}*I(VTW1)+
+   {ETAI^2*ETAC*TEM^2*6.6262E-34*3E8*BETAB*B/((1.60219E-19)^2*LAMBDA*NW*VACT)}*I(VTW1)
+   *I(VTW1)+
+   {ETAI^3*ETAC*TEM^3*6.6262E-34*3E8*BETAC*C/((1.60219E-19)^3*LAMBDA*(NW*VACT)^2)}*
+   I(VTW1)*I(VTW1)*I(VTW1))/(V(M)+{DEL})
```

```
BS2 0 M I=(V(M)+{DEL})*({GL*TP*GAMMA*VGR*GO*ETAI*TEM/(1.60219E-19*VACT*NTH)}*I(VTW1)-
+   {TP*NW*GAMMA*VGR*GO*
+    (GL-LOG((A*NTH+B*NTH^2+C*NTH^3)/(A*NO+B*NO^2+C*NO^3)))})/
+   (1+{EPS*GAMMA*LAMBDA*TP/(ETAC*VACT*6.6262E-34*3E8)}*(V(M)+{DEL})*(V(M)+{DEL}))-
+   {DEL}
BPF PF 0 V=(V(M)+{DEL})*(V(M)+{DEL})
.MODEL D1MOD D IS={1.60219E-19*VBARR*NE/(2*ETAI*TCAPT)} N={N*TF}
.MODEL D2MOD D IS={1.60219E-19*VBARR*NE/(2*ETAI*TCAPT)} N={N*TF} TT={2*TCAPT}
+              CJO={CJO} M={MPOW} VJ={VJ} FC={FC}
.MODEL DW1MOD D IS={1.60219E-19*NW*VACT*NE2/(ETAI*TEM)} N={NW2*TF}
.MODEL DW2MOD D IS={1.60219E-19*NW*VACT*NE2/(ETAI*TEM)} N={NW2*TF} TT={2*TEM}
.ENDS
***********
*SYM=QWL1
.SUBCKT QWLAS2B1 P N PF {
+ NE=1E12 N=2 NE2=1E12 NW2=1 ETAI=1 LAMBDA=850E-9 NW=1 VACT=1E-17
+ GAMMA=0.1 VGR=1E8 TP=3E-12 ETAC=0.35 NO=1E24 NTH=1.25E24 GO=1E5
+ GL=1 EPS=1E-23 TN=1E-8 A2=0 A=1E8 B=1E-16 C=0 AB=1E8 BB=1E-16 CB=1E-40
+ BETAA=0 BETAB=1E-6 BETAC=0 VBARR=1E-16 TCAPT=1e-12 TEM=1e-9
+ CJO=0 MPOW=0.5 VJ=1 FC=0.5 DELTA=1e-60 DEL=0 TF=1 }
D1 P NT1 D1MOD
IC1 P NT1 {1.60219E-19*VBARR*NE/(2*ETAI*TCAPT)}
VT1 NT1 N 0
D2 P N D2MOD
IC2 P N {1.60219E-19*VBARR*NE/(2*ETAI*TCAPT)}
F1 N P VTW1 1
DW1  W NTW1 DW1MOD
ICW1 W NTW1 {1.60219E-19*NW*VACT*NE2/(ETAI*TEM)}
VTW1 NTW1 0 0
DW2  W 0 DW2MOD
ICW2 W 0 {1.60219E-19*NW*VACT*NE2/(ETAI*TEM)}
BR1 W 0 I={2*A*TEM}*I(VTW1)+{2*ETAI*B*TEM^2/(1.60219E-19*NW*VACT)}*I(VTW1)*I(VTW1)+
+   {2*ETAI^2*C*TEM^3/(1.60219E-19*NW*VACT)^2}*I(VTW1)*I(VTW1)*I(VTW1)
BS1 W 0 I={2*LAMBDA*TP*1.60219E-19*NW*GAMMA*VGR*GO/(ETAI*ETAC*6.6262E-34*3E8)}*
+   (V(M)+{DEL})*(V(M)+{DEL})*LN({DELTA}+
+   {A*ETAI*TEM/(1.60219E-19*NW*VACT)/(A*NO+B*NO^2+C*NO^3)}*I(VTW1)+
+   {B*(ETAI*TEM/(1.60219E-19*NW*VACT))^2/(A*NO+B*NO^2+C*NO^3)}*I(VTW1)*I(VTW1)+
+   {C*(ETAI*TEM/(1.60219E-19*NW*VACT))^3/(A*NO+B*NO^2+C*NO^3)}*I(VTW1)*
+   I(VTW1)*I(VTW1))/(1+{EPS*GAMMA*LAMBDA*TP/(ETAC*VACT*6.6262E-34*3E8)}*(V(M)+{DEL})*
+   (V(M)+{DEL}))
F2 0 W VT1 4
RPH M 0 1
CPH M 0 {2*TP}
BR2 0 M I=({ETAI*ETAC*TEM*6.6262E-34*3E8*BETAA*A/(1.60219E-19*LAMBDA)}*I(VTW1)+
+   {ETAI^2*ETAC*TEM^2*6.6262E-34*3E8*BETAB*B/((1.60219E-19)^2*LAMBDA*NW*VACT)}*I(VTW1)
+   *I(VTW1)+
+   {ETAI^3*ETAC*TEM^3*6.6262E-34*3E8*BETAC*C/((1.60219E-19)^3*LAMBDA*(NW*VACT)^2)}*
+   I(VTW1)*I(VTW1)*I(VTW1))/(V(M)+{DEL})
BS2 0 M I={TP*NW*GAMMA*VGR*GO}*(V(M)+{DEL})*LN({DELTA}+
+   {A*ETAI*TEM/(1.60219E-19*NW*VACT)/(A*NO+B*NO^2+C*NO^3)}*I(VTW1)+
+   {B*(ETAI*TEM/(1.60219E-19*NW*VACT))^2/(A*NO+B*NO^2+C*NO^3)}*I(VTW1)*I(VTW1)+
+   {C*(ETAI*TEM/(1.60219E-19*NW*VACT))^3/(A*NO+B*NO^2+C*NO^3)}*I(VTW1)*
+   I(VTW1)*I(VTW1))/(1+{EPS*GAMMA*LAMBDA*TP/(ETAC*VACT*6.6262E-34*3E8)}*(V(M)+{DEL})*
+   (V(M)+{DEL}))-{DEL}
BPF PF 0 V=(V(M)+{DEL})*(V(M)+{DEL})
.MODEL D1MOD D IS={1.60219E-19*VBARR*NE/(2*ETAI*TCAPT)} N={N*TF}
.MODEL D2MOD D IS={1.60219E-19*VBARR*NE/(2*ETAI*TCAPT)} N={N*TF} TT={2*TCAPT}
```

```
+              CJO={CJO} M={MPOW} VJ={VJ} FC={FC}
.MODEL DW1MOD D IS={1.60219E-19*NW*VACT*NE2/(ETAI*TEM)} N={NW2*TF}
.MODEL DW2MOD D IS={1.60219E-19*NW*VACT*NE2/(ETAI*TEM)} N={NW2*TF} TT={2*TEM}
.ENDS
***********
*SYM=QWL1
.SUBCKT QWLAS2B2 P N PF {
+ NE=1E12 N=2 NE2=1E12 NW2=1 ETAI=1 LAMBDA=850E-9 NW=1 VACT=1E-17
+ GAMMA=0.1 VGR=1E8 TP=3E-12 ETAC=0.35 NO=1E24 NTH=1.25E24 GO=1E5
+ GL=1 EPS=1E-23 TN=1E-8 A2=0 A=1E8 B=1E-16 C=0 AB=1E8 BB=1E-16 CB=1E-40
+ BETAA=0 BETAB=1E-6 BETAC=0 VBARR=1E-16 TCAPT=1e-12 TEM=1e-9
+ CJO=0 MPOW=0.5 VJ=1 FC=0.5 DELTA=1e-60 DEL=0 TF=1 }
D1 P NT1 D1MOD
IC1 P NT1 {1.60219E-19*VBARR*NE/(2*ETAI*TCAPT)}
VT1 NT1 N 0
D2 P N D2MOD
IC2 P N {1.60219E-19*VBARR*NE/(2*ETAI*TCAPT)}
F1 N P VTW1 1
DW1  W NTW1 DW1MOD
ICW1 W NTW1 {1.60219E-19*NW*VACT*NE2/(ETAI*TEM)}
VTW1 NTW1 0 0
DW2  W 0 DW2MOD
ICW2 W 0 {1.60219E-19*NW*VACT*NE2/(ETAI*TEM)}
BR1 W 0 I={2*A*TEM}*I(VTW1)+{2*ETAI*B*TEM^2/(1.60219E-19*NW*VACT)}*I(VTW1)*I(VTW1)+
+   {2*ETAI^2*C*TEM^3/(1.60219E-19*NW*VACT)^2}*I(VTW1)*I(VTW1)*I(VTW1)
BS1 W 0 I={2*GL*LAMBDA*TP*1.60219E-19*NW*GAMMA*VGR*GO/(ETAI*ETAC*6.6262E-34*3E8)}*
+   (V(M)+{DEL})*(V(M)+{DEL})*LN({DELTA}+{ETAI*TEM/(1.60219E-19*NW*VACT*NO)}*
+   I(VTW1))/(1+{EPS*GAMMA*LAMBDA*TP/(ETAC*VACT*6.6262E-34*3E8)}*(V(M)+{DEL})*
+   (V(M)+{DEL}))
F2 0 W VT1 4
RPH M 0 1
CPH M 0 {2*TP}
BR2 0 M I=({ETAI*ETAC*TEM*6.6262E-34*3E8*BETAA*A/(1.60219E-19*LAMBDA)}*I(VTW1)+
+   {ETAI^2*ETAC*TEM^2*6.6262E-34*3E8*BETAB*B/((1.60219E-19)^2*LAMBDA*NW*VACT)}*I(VTW1)
+   *I(VTW1)+
+   {ETAI^3*ETAC*TEM^3*6.6262E-34*3E8*BETAC*C/((1.60219E-19)^3*LAMBDA*(NW*VACT)^2)}*
+   I(VTW1)*I(VTW1)*I(VTW1))/(V(M)+{DEL})
BS2 0 M I={GL*TP*NW*GAMMA*VGR*GO}*(V(M)+{DEL})*
+   LN({DELTA}+{ETAI*TEM/(1.60219E-19*NW*VACT*NO)}*I(VTW1))/(1+
+   {EPS*GAMMA*LAMBDA*TP/(ETAC*VACT*6.6262E-34*3E8)}*(V(M)+{DEL})*(V(M)+{DEL}))-
+   {DEL}
BPF PF 0 V=(V(M)+{DEL})*(V(M)+{DEL})
.MODEL D1MOD D IS={1.60219E-19*VBARR*NE/(2*ETAI*TCAPT)} N={N*TF}
.MODEL D2MOD D IS={1.60219E-19*VBARR*NE/(2*ETAI*TCAPT)} N={N*TF} TT={2*TCAPT}
+              CJO={CJO} M={MPOW} VJ={VJ} FC={FC}
.MODEL DW1MOD D IS={1.60219E-19*NW*VACT*NE2/(ETAI*TEM)} N={NW2*TF}
.MODEL DW2MOD D IS={1.60219E-19*NW*VACT*NE2/(ETAI*TEM)} N={NW2*TF} TT={2*TEM}
.ENDS
***********
*SYM=QWL1
.SUBCKT QWLAS2B3 P N PF {
+ NE=1E12 N=2 NE2=1E12 NW2=1 ETAI=1 LAMBDA=850E-9 NW=1 VACT=1E-17
+ GAMMA=0.1 VGR=1E8 TP=3E-12 ETAC=0.35 NO=1E24 NTH=1.25E24 GO=1E5
+ GL=1 EPS=1E-23 TN=1E-8 A2=0 A=1E8 B=1E-16 C=0 AB=1E8 BB=1E-16 CB=1E-40
+ BETAA=0 BETAB=1E-6 BETAC=0 VBARR=1E-16 TCAPT=1e-12 TEM=1e-9
+ CJO=0 MPOW=0.5 VJ=1 FC=0.5 DELTA=1e-60 DEL=0 TF=1 }
D1 P NT1 D1MOD
```

```
IC1 P NT1 {1.60219E-19*VBARR*NE/(2*ETAI*TCAPT)}
VT1 NT1 N 0
D2 P N D2MOD
IC2 P N {1.60219E-19*VBARR*NE/(2*ETAI*TCAPT)}
F1 N P VTW1 1
DW1  W NTW1 DW1MOD
ICW1 W NTW1 {1.60219E-19*NW*VACT*NE2/(ETAI*TEM)}
VTW1 NTW1 0 0
DW2  W 0 DW2MOD
ICW2 W 0 {1.60219E-19*NW*VACT*NE2/(ETAI*TEM)}
BR1 W 0 I={2*A*TEM}*I(VTW1)+{2*ETAI*B*TEM^2/(1.60219E-19*NW*VACT)}*I(VTW1)*I(VTW1)+
+   {2*ETAI^2*C*TEM^3/(1.60219E-19*NW*VACT)^2}*I(VTW1)*I(VTW1)*I(VTW1)
BS1 W 0 I=(V(M)+{DEL})*(V(M)+{DEL})*
+   ({2*GL*LAMBDA*TP*GAMMA*VGR*GO*TEM/(ETAC*VACT*NO*6.6262E-34*3E8)}*I(VTW1)-
+   {2*GL*LAMBDA*TP*1.60219E-19*NW*GAMMA*VGR*GO/(ETAI*ETAC*6.6262E-34*3E8)})/
+   (1+{EPS*GAMMA*LAMBDA*TP/(ETAC*VACT*6.6262E-34*3E8)}*(V(M)+{DEL})*(V(M)+{DEL}))
F2 0 W VT1 4
RPH M 0 1
CPH M 0 {2*TP}
BR2 0 M I=({ETAI*ETAC*TEM*6.6262E-34*3E8*BETAA*A/(1.60219E-19*LAMBDA)}*I(VTW1)+
+   {ETAI^2*ETAC*TEM^2*6.6262E-34*3E8*BETAB*B/((1.60219E-19)^2*LAMBDA*NW*VACT)}*I(VTW1)
+   *I(VTW1)+
+   {ETAI^3*ETAC*TEM^3*6.6262E-34*3E8*BETAC*C/((1.60219E-19)^3*LAMBDA*(NW*VACT)^2)}*
+   I(VTW1)*I(VTW1)*I(VTW1))/(V(M)+{DEL})
BS2 0 M I=(V(M)+{DEL})*({GL*TP*GAMMA*VGR*GO*ETAI*TEM/(1.60219E-19*VACT*NO)}*I(VTW1)-
+   {GL*TP*NW*GAMMA*VGR*GO})/(1+{EPS*GAMMA*LAMBDA*TP/(ETAC*VACT*6.6262E-34*3E8)}*
+   (V(M)+{DEL})*(V(M)+{DEL}))-{DEL}
BPF PF 0 V=(V(M)+{DEL})*(V(M)+{DEL})
.MODEL D1MOD D IS={1.60219E-19*VBARR*NE/(2*ETAI*TCAPT)} N={N*TF}
.MODEL D2MOD D IS={1.60219E-19*VBARR*NE/(2*ETAI*TCAPT)} N={N*TF} TT={2*TCAPT}
+              CJO={CJO} M={MPOW} VJ={VJ} FC={FC}
.MODEL DW1MOD D IS={1.60219E-19*NW*VACT*NE2/(ETAI*TEM)} N={NW2*TF}
.MODEL DW2MOD D IS={1.60219E-19*NW*VACT*NE2/(ETAI*TEM)} N={NW2*TF} TT={2*TEM}
.ENDS
***********
*SYM=QWL1
.SUBCKT QWLAS2B4 P N PF {
+ NE=1E12 N=2 NE2=1E12 NW2=1 ETAI=1 LAMBDA=850E-9 NW=1 VACT=1E-17
+ GAMMA=0.1 VGR=1E8 TP=3E-12 ETAC=0.35 NO=1E24 NTH=1.25E24 GO=1E5
+ GL=1 EPS=1E-23 TN=1E-8 A2=0 A=1E8 B=1E-16 C=0 AB=1E8 BB=1E-16 CB=1E-40
+ BETAA=0 BETAB=1E-6 BETAC=0 VBARR=1E-16 TCAPT=1e-12 TEM=1e-9
+ CJO=0 MPOW=0.5 VJ=1 FC=0.5 DELTA=1e-60 DEL=0 TF=1 }
D1 P NT1 D1MOD
IC1 P NT1 {1.60219E-19*VBARR*NE/(2*ETAI*TCAPT)}
VT1 NT1 N 0
D2 P N D2MOD
IC2 P N {1.60219E-19*VBARR*NE/(2*ETAI*TCAPT)}
F1 N P VTW1 1
DW1  W NTW1 DW1MOD
ICW1 W NTW1 {1.60219E-19*NW*VACT*NE2/(ETAI*TEM)}
VTW1 NTW1 0 0
DW2  W 0 DW2MOD
ICW2 W 0 {1.60219E-19*NW*VACT*NE2/(ETAI*TEM)}
BR1 W 0 I={2*A*TEM}*I(VTW1)+{2*ETAI*B*TEM^2/(1.60219E-19*NW*VACT)}*I(VTW1)*I(VTW1)+
+   {2*ETAI^2*C*TEM^3/(1.60219E-19*NW*VACT)^2}*I(VTW1)*I(VTW1)*I(VTW1)
BS1 W 0 I=(V(M)+{DEL})*(V(M)+{DEL})*
+   ({2*GL*LAMBDA*TP*GAMMA*VGR*GO*TEM/(ETAC*VACT*NTH*6.6262E-34*3E8)}*I(VTW1)-
```

```
+   {(2*LAMBDA*TP*1.60219E-19*NW*GAMMA*VGR*GO/(ETAI*ETAC*6.6262E-34*3E8))*
+    (GL-LOG((A*NTH+B*NTH^2+C*NTH^3)/(A*NO+B*NO^2+C*NO^3)))})/
+   (1+{EPS*GAMMA*LAMBDA*TP/(ETAC*VACT*6.6262E-34*3E8)}*(V(M)+{DEL})*(V(M)+{DEL}))
F2 0 W VT1 4
RPH M 0 1
CPH M 0 {2*TP}
BR2 0 M I=({ETAI*ETAC*TEM*6.6262E-34*3E8*BETAA*A/(1.60219E-19*LAMBDA)}*I(VTW1)+
+   {ETAI^2*ETAC*TEM^2*6.6262E-34*3E8*BETAB*B/((1.60219E-19)^2*LAMBDA*NW*VACT)}*I(VTW1)
+   *I(VTW1)+
+   {ETAI^3*ETAC*TEM^3*6.6262E-34*3E8*BETAC*C/((1.60219E-19)^3*LAMBDA*(NW*VACT)^2)}*
+   I(VTW1)*I(VTW1)*I(VTW1))/(V(M)+{DEL})
BS2 0 M I=(V(M)+{DEL})*({GL*TP*GAMMA*VGR*GO*ETAI*TEM/(1.60219E-19*VACT*NTH)}*I(VTW1)-
+   {TP*NW*GAMMA*VGR*GO*
+    (GL-LOG((A*NTH+B*NTH^2+C*NTH^3)/(A*NO+B*NO^2+C*NO^3)))})/
+   (1+{EPS*GAMMA*LAMBDA*TP/(ETAC*VACT*6.6262E-34*3E8)}*(V(M)+{DEL})*(V(M)+{DEL}))-
+   {DEL}
BPF PF 0 V=(V(M)+{DEL})*(V(M)+{DEL})
.MODEL D1MOD D IS={1.60219E-19*VBARR*NE/(2*ETAI*TCAPT)} N={N*TF}
.MODEL D2MOD D IS={1.60219E-19*VBARR*NE/(2*ETAI*TCAPT)} N={N*TF} TT={2*TCAPT}
+              CJO={CJO} M={MPOW} VJ={VJ} FC={FC}
.MODEL DW1MOD D IS={1.60219E-19*NW*VACT*NE2/(ETAI*TEM)} N={NW2*TF}
.MODEL DW2MOD D IS={1.60219E-19*NW*VACT*NE2/(ETAI*TEM)} N={NW2*TF} TT={2*TEM}
.ENDS
***********
```

A.3 SPICE3/HSPICE Parsing Code

Below we provide the source code that implements the netlist-parsing program *PARSE*, which was originally written by S. Javro to support models similar to those presented in [A.4]. We modified the code to support the models from Chapter 2.

```
/*****************************************************************************************
  parse.c
  - - -
  SPICE3/HSPICE parsing routines with laser
  model implementation for SPICE/HSPICE
  - - -
  Original: S. Javro, 1994
  Revisions: P. Mena, 1995, 1996 (modified Javro code to support models from Chapter 2)
   - - -
  Usage:
         PARSE [input_file] [output_file] [0-SPICE3, 1- HSPICE]
 ****************************************************************************************/

#include <ctype.h>
#include <stdio.h>
```

```
#include <stdlib.h>
#include <math.h>

/* physical constants */
#define q 1.60219e-19
#define h 6.6262e-34
#define kb 1.38062e-23
#define c 3e8

void print_err(int i);
void readln();
void read_str(int *ptr, char in_str[], int err_no, int size);
void parse_system();
void init_params();
void laser1();
void laser2();

FILE    *input_ptr;
FILE    *output_ptr;
char    in_buff[255];
char    command[50];
char    name[30];
char    model[30];
char    com_buf[750];
char    var_name[75][20];    /* 75 variable names of length 20 */
double  var_val[75];         /* and the corresponding values   */
int     No_of_vars;

intouttype;
charistr[2][7]  = { “i=”, “cur=’” };
charvstr[2][7]  = { “v=”, “vol=’” };
charlnstr[2][5] = { “ln”, “log” };
charCSstr[2][3] = { “B”,  “G”   };
char    VSstr[2][3] = { “B”,  “E”   };
chartlstr[2][3] = { ““,   “‘”   };

/***************************************************************************/
/* Model parameters                                                        */
/***************************************************************************/
int    level;             /* model level number                          */
double Ne;                /* N-V relation equilibrium density, m^-3      */
double n;                 /* diode ideality factor (~2)                  */
double Ne2;               /* QW N-V relation equilibrium density, m^-3   */
double nw2;               /* QW N-V diode ideality factor                */
double etai;              /* current injection efficiency                */
double Lambda;            /* central emission wavelength, m              */
double Nw;                /* number of quantum wells                     */
double Vact;              /* volume of a single quantum well, m^3        */
double Gamma;             /* optical confinement factor for 1 q.w.       */
double vgr;               /* lasing medium group velocity, m/s           */
double tp;                /* cavity lifetime, s                          */
double etac;              /* output power coupling coeff.                */
double No;                /* optical transparency density, m^-3          */
double Nth;               /* threshold carrier density, m^-3             */
double Go;                /* gain coeff. per QW, m^-1                    */
double gl;                 /* linearized gain scaling factor              */
double eps;               /* nonlinear gain parameter, m^3               */
```

```
double tn;                /* equivalent linear recomb. lifetime, s       */
double A2;                /* adjusted unimolec. rec. rate coeff., s^-1   */
double A;                 /* QW unimolecular recomb. rate coeff., s^-1   */
double B;                 /* QW radiative recomb. rate coeff., m^3/s     */
double C;                 /* QW Auger recombination rate coeff., m^6/s   */
double Ab;                /* barrier unimolec. rec. rate coeff, s^-1     */
double Bb;                /* barrier radiative rec. rate coeff, m^3/s    */
double Cb;                /* barrier Auger recomb. rate coeff., m^6/s    */
double betaA;             /* QW unimolecular spont. em. coupling coeff.  */
double betaB;             /* QW radiative spont. em. coupling coeff.     */
double betaC;             /* QW Auger spont. emission coupling coeff.    */
double Vbarr;             /* total volume of barrier layers, m^3         */
double tcapt;             /* quantum well carrier capture lifetime, s    */
double tem;               /* quantum well carrier emission lifetime, s   */
double cjo;               /* zero-bias space-charge capacitance, F       */
double mpow;              /* grading coefficient (space-charge cap.)     */
double vj;                /* junction potential (s-c cap.), V            */
double fc;                /* coeff. for forw.-bias s-c. cap. formula     */
double delta;             /* log(0) correction parameter                 */
double del;               /* correction parameter for m^2 at m=0         */
int    del_flag;          /* flag indicating del is set                */
char   delstr[20];        /* default del string if del == 0           */
char   delsubstr[5];      /* default tail-string if del == 0           */
double Rs;                /* parasitic series resistance, ohms           */
double Is1;               /* p+-p interface diode sat. current, A        */
double n1;                /* p+-p interface diode ideality factor        */
double Is2;               /* n+-n interface diode sat. current, A        */
double n2;                /* n+-n interface diode ideality factor        */
double Cssc;              /* active layer shunting space-charge cap., F  */
int    shtype;            /* type of shunting circuit (0-4)              */
double R1;                /* shunting resistance, ohms                   */
double C1;                /* shunting capacitance, F                     */
double Lp1;               /* RC-network modeling inductance 1            */
double Lp2;               /* RC-network modeling inductance 2            */
double Tf;                /* (diode temp. (K))/(circuit temp. (K))       */

/***************************************************************************/
/* Error handler.   (Originally by S. Javro, 1994)                         */
/***************************************************************************/
char    *err_msg[]={
                    “Unexpected string termination”,
                    “Unable to read device name”,
                    “Unable to read model name”,
                    “Incomplete variable assignment”,
                    “Invalid number format”,
                    “Input and Output files must be different”,
                    “Cannot open the input file”,
                    “Cannot open the output file”,
                    “Input file is empty”,
                    “Unknown model definition”,
                    “Invalid output-type (0 or 1)”
                   };

void print_err(int i)
{
 printf(“ERROR (%d): %s.\n”,i,err_msg[i]);
 exit(1);
```

```
}

/***************************************************************************/
/* readln()   (originally by S. Javro, 1994)                               */
/* PURPOSE  : read 1 complete line from the input file into the in_buff    */
/*            string.   */
/* CALLED BY: parse_system(), main(argc,argv)   */
/***************************************************************************/
void readln()
{
 char cc;
 int  i;

 for (i=0;i<254;i++)
    {
     cc = tolower(fgetc(input_ptr));    /* convert all upper to lower case */
     if (feof(input_ptr)) break;
     if (cc == ‘\n’) break;
     in_buff[i] = cc;
    }
 in_buff[i] = ‘\0’;
}

/***************************************************************************/
/* read_str(ptr,in_str,err_no)   (originally by S. Javro, 1994)            */
/* PURPOSE : places one word from com_buf into in_str and updates ptr to   */
/*           point to the next word in com_buf. If a string terminator (\0)*/
/*           occurs the error routine is called to indicate an illegal     */
/*           situation (i.e. there is no remaining data when we expect     */
/*           some).                                                        */
/* NOTE     : The routine will only place size characters into in_str, the */
/*            remaining letters in the word are ignored.                   */
/* CALLED BY: parse_system()   */
/***************************************************************************/
void read_str(int *ptr, char in_str[], int err_no, int size)
{
 int st,j;

 for (j=0,st=0;;*ptr +=1)
    {
     if (com_buf[*ptr] == ‘\0’) print_err(err_no);

     if ((!isspace(com_buf[*ptr])) && (j < size))
       {
        st =-1;
        in_str[j++] = com_buf[*ptr];
       }
      else
       if (st == -1) break;
    }
 in_str[j] = ‘\0’;
}

/***************************************************************************/
/* parse_system() (originally by S. Javro, 1994)                           */
/* PURPOSE    : read in the spice3 type specifications of .Xmodel. It      */
/*              put the data into name, model, var_name[] and var_val[],   */
```

```
/*              so that the modeller routines can process the data.        */
/* CALLED BY  : main (argc,argv)   */
/***************************************************************************/
void parse_system()
{
 int i,j,k;
 int st;                /* started reading a string */
 double  val;
 char    var[30];

 /*------------------------------------------------------------------------*/
 /* read in the whole definition and get the next input line for the next    */
 /* iteration of main().                                                      */
 /*------------------------------------------------------------------------*/
 for (j=0,i=0;;)
    {
     for (st=0;(in_buff[i] != ‘\0’);i++)
        {
         if ((!isspace(in_buff[i])) &&       /* remove un-needed spaces,  */
             (in_buff[i] != ‘(‘) &&          /* brackets, equal signs and */
             (in_buff[i] != ‘)’) &&          /* commas                    */
             (in_buff[i] != ‘=’) &&
             (in_buff[i] != ‘,’))
           {
            st = -1;
            com_buf[j++] = in_buff[i];
           }
         else
          if (st == -1)            /* allow only one space between key words */
            {
             com_buf[j++] = ‘ ‘;
             st = 0;
            }
        }

     if (com_buf[j-1] != ‘ ‘)          /* ensure there is a space between   */
       com_buf[j++] = ‘ ‘;             /* all entries in the com_buf string */

     readln();
     for (i=0;in_buff[i]==’ ‘;i++);    /* Move to first non space character */
     if (in_buff[i] != ‘+’) break;
     i++;                              /* Move beyond the ‘+’ character     */
    }

 com_buf[j] = ‘\0’;

 /*------------------------------------------------------------------------*/
 /* Now to perform the parsing upon com_buf                                   */
 /*------------------------------------------------------------------------*/
 i = 0;
 read_str(&i,name,0,28);     /* move to the end of the .Xmodel command       */

 read_str(&i,name,1,28);     /* read component name                          */

 read_str(&i,model,2,28);    /* read the model’s name                        */

 /*-----------------------------------------------------------------------*/
```

```
 /* Read in all the variable names and their values.                        */
 /*-------------------------------------------------------------------------*/
 No_of_vars = 0;
 for (;;)
    {
     if (com_buf[++i] == ‘\0’ )
       break;                   /* finished reading all the variables       */

     read_str(&i,var_name[No_of_vars],0,18);

     read_str(&i,var,3,28);      /* get the ASCII number from com_buf       */

     if (sscanf(var,”%lf”,&val) !=  1)  /* use scanf to read the number     */
        print_err(4);                   /* from the var string              */

     /*-----------------------------------------------------------------*/
     /* Find the parameter’s suffix and correct val accordingly         */
     /*-----------------------------------------------------------------*/
     for (k=strlen(var)-1;(!isdigit(var[k]));k--);
                                          /* find where the suffix starts */

     switch (toupper(var[k+1]))
       {
        case ‘T’ : val *= 1e12;   break;
        case ‘G’ : val *= 1e9;    break;
        case ‘M’ : if (toupper(var[k+2]) == ‘E’)
                     val *= 1e6;
                    else
                     val *= 1e-3;
                   break;
        case ‘K’ : val *= 1e3;    break;
        case ‘U’ : val *= 1e-6;   break;
        case ‘N’ : val *= 1e-9;   break;
        case ‘P’ : val *= 1e-12;  break;
        case ‘F’ : val *= 1e-15;  break;
       }
     var_val[No_of_vars++] = val;
    }
}

/**************************************************************************/
/* init_params()                                                          */
/* PURPOSE  : initialize model parameters to default values               */
/* CALLED BY: main(argc,argv)                                             */
/**************************************************************************/
void init_params()
{
level=1;           /* model level number                           */
Ne=1e12;           /* N-V relation equilibrium density, m^-3       */
n=2;               /* diode ideality factor (~2)                   */
Ne2=1e12;          /* QW N-V relation equilibrium density, m^-3    */
nw2=1;             /* QW N-V diode ideality factor                 */
etai=1;            /* current injection efficiency                 */
Lambda=850e-9;     /* central emission wavelength, m               */
Nw=1;              /* number of quantum wells                      */
Vact=1e-17;        /* volume of a single quantum well, m^3         */
Gamma=0.1;         /* optical confinement factor for 1 q.w.        */
```

```
vgr=1e8;           /* lasing medium group velocity, m/s           */
tp=3e-12;          /* cavity lifetime, s                          */
etac=0.35;         /* output power coupling coeff.                */
No=1e24;           /* optical transparency density, m^-3          */
Nth=1.25e24;       /* threshold carrier density, m^-3             */
Go=1e5;            /* gain coeff. per QW, m^-1                    */
gl=0;               /* linearized gain scaling factor              */
eps=1e-23;         /* nonlinear gain parameter, m^3               */
tn=0;              /* equivalent linear recomb. lifetime, s       */
A2=1e8;            /* adjusted unimolec. rec. rate coeff., s^-1   */
A=1e8;             /* QW unimolecular recomb. rate coeff., s^-1   */
B=1e-16;           /* QW radiative recomb. rate coeff., m^3/s     */
C=0;               /* QW Auger recombination rate coeff., m^6/s   */
Ab=0;              /* barrier unimolec. rec. rate coeff, s^-1     */
Bb=0;              /* barrier radiative rec. rate coeff, m^3/s    */
Cb=0;              /* barrier Auger recomb. rate coeff., m^6/s    */
betaA=0;           /* QW unimolecular spont. em. coupling coeff.  */
betaB=1e-6;        /* QW radiative spont. em. coupling coeff.     */
betaC=0;           /* QW Auger spont. emission coupling coeff.    */
Vbarr=1e-16;       /* total volume of barrier layers, m^3         */
tcapt=1e-12;       /* quantum well carrier capture lifetime, s    */
tem=1e-9;          /* quantum well carrier emission lifetime, s   */
cjo=0;             /* zero-bias space-charge capacitance, F       */
mpow=0.5;          /* grading coefficient (space-charge cap.)     */
vj=1;              /* junction potential (s-c cap.), V            */
fc=0.5;            /* coeff. for forw.-bias s-c. cap. formula     */
delta=1e-60;       /* log(0) correction parameter                 */
del=0;            /* correction parameter for m^2 at m=0         */
del_flag = 0;            /* flag indicating del is set          */
strcpy(delstr,”v(m)”);   /* default del string if del == 0     */
strcpy(delsubstr,””);    /* default tail-string if del == 0     */
Rs=0;              /* parasitic series resistance, ohms           */
Is1=0;             /* p+-p interface diode sat. current, A        */
n1=1;              /* p+-p interface diode ideality factor        */
Is2=0;             /* n+-n interface diode sat. current, A        */
n2=1;              /* n+-n interface diode ideality factor        */
Cssc=0;            /* active layer shunting space-charge cap., F  */
shtype=0;          /* type of shunting circuit (0-4)              */
R1=0;              /* shunting resistance, ohms                   */
C1=0;              /* shunting capacitance, F                     */
Lp1=0;             /* RC-network modeling inductance 1            */
Lp2=0;             /* RC-network modeling inductance 2            */
Tf=1;              /* (diode temp. (K))/(circuit temp. (K))       */
}

/***************************************************************************************/
/* Large-signal 2-rate equation model subcircuit text. (Based on S. Javro code, 1994)  */
/***************************************************************************************/
char *las_mod1[] = {
“*********************************************************************\n”,
“.subckt %s %s n pf\n”,
“Rs p %s %.8g\n”,
“Ds1 %s %s ds1mod_%s\n”,
“Ds2 %s pi ds2mod_%s\n”,
“Cssc pi n %.8g\n”,
“R1 %s n %.8g\n”,
“C1 %s n %.8g\n”,
```

```
“R1 %s sh1 %.8g\n”,
“C1 sh1 n %.8g\n”,
“C1 sh1 sh2 %.8g\n”,
“Vsh0 sh2 sh3 0\n”,
“%svsh sh3 n %sv(nl2)-v(nl1)%s\n”,
“Fl1 0 nl1 Vsh0 1\n”,
“Lp1 nl1 0 %.8g\n”,
“Gl2 0 nl2 nl1 0 1\n”,
“Lp2 nl2 0 %.8g\n”,
“D1 pi nt1 d1mod_%s\n”,
“Vt1 nt1 n 0\n”,
“D2 pi n d2mod_%s\n”,
“%sr1 pi n %s%s%s\n”,
“%ss1 pi n %s%s%s\n”,
“Rph m 0 1\n”,
“Cph m 0 %.8g\n”,
“%sr2 0 m %s%s%s\n”,
“%ss2 0 m %s%s%s\n”,
“%spf pf 0 %s%s*%s%s\n”,
“.ends %s\n”,
“.model d1mod_%s D Is=%.8g n=%.8g\n”,
“.model d2mod_%s D Is=%.8g n=%.8g tt=%.8g cjo=%.8g m=%.8g vj=%.8g fc=%.8g\n”,
“.model ds1mod_%s D Is=%.8g n=%.8g\n”,
“.model ds2mod_%s D Is=%.8g n=%.8g\n”,
“Ic1 pi nt1 %.8g\n”,
“Ic2 pi n %.8g\n”
};

char *l1expr[] = {
“%.8g*i(Vt1)+%.8g*i(Vt1)*i(Vt1)+%.8g*i(Vt1)*i(Vt1)*i(Vt1)”,
“%.8g*%s*%s*%s(%.8g+%.8g*i(Vt1)+%.8g*i(Vt1)*i(Vt1)+%.8g*i(Vt1)*i(Vt1)*i(Vt1))/
(1+%.8g*%s*%s)”,
“%.8g*%s*%s*%s(%.8g+%.8g*i(Vt1))/(1+%.8g*%s*%s)”,
“%s*%s*(%.8g*i(Vt1)-%.8g)/(1+%.8g*%s*%s)”,
“(%.8g*i(Vt1)+%.8g*i(Vt1)*i(Vt1)+%.8g*i(Vt1)*i(Vt1)*i(Vt1))/%s”,
“%.8g*%s*%s(%.8g+%.8g*i(Vt1)+%.8g*i(Vt1)*i(Vt1)+%.8g*i(Vt1)*i(Vt1)*i(Vt1))/
(1+%.8g*%s*%s)%s”,
“%.8g*%s*%s(%.8g+%.8g*i(Vt1))/(1+%.8g*%s*%s)%s”,
“%s*(%.8g*i(Vt1)-%.8g)/(1+%.8g*%s*%s)%s”
};

/***************************************************************************/
/* laser1()    (Based on S. Javro code, 1994)                              */
/* PURPOSE  : generate subcircuit for large-signal 2-rate-eqn. model       */
/* CALLED BY: main(argc,argv)                                              */
/***************************************************************************/
void laser1()
{
 int i;
 double Cph,Islas,tdiff;
 double X1,X2,X3,X4,X5,X6,X7,X8;
 double K1,K2,K3,K4,K5,K6,K7,K8,K9,K10;
 double K11,K12,K13,K14,K15,K16,K17,K18,K19,K20,K21;
 char str1[5],str2[5],str3[5];
 char R1expr[180],S1expr[180],R2expr[180],S2expr[180];

 for (i=0; i<No_of_vars; i++)
```

```
if (strcmp(var_name[i],”level”) == 0) level = (int) rint(var_val[i]);
    else
if (strcmp(var_name[i],”ne”) == 0) Ne = var_val[i];
    else
if (strcmp(var_name[i],”n”) == 0) n = var_val[i];
    else
if (strcmp(var_name[i],”ne2”) == 0) Ne2 = var_val[i];
    else
if (strcmp(var_name[i],”nw2”) == 0) nw2 = var_val[i];
    else
if (strcmp(var_name[i],”etai”) == 0) etai = var_val[i];
    else
if (strcmp(var_name[i],”lambda”) == 0) Lambda = var_val[i];
    else
if (strcmp(var_name[i],”nw”) == 0) Nw = var_val[i];
    else
if (strcmp(var_name[i],”vact”) == 0) Vact = var_val[i];
    else
if (strcmp(var_name[i],”gamma”) == 0) Gamma = var_val[i];
    else
if (strcmp(var_name[i],”vgr”) == 0) vgr = var_val[i];
    else
if (strcmp(var_name[i],”tp”) == 0) tp = var_val[i];
    else
if (strcmp(var_name[i],”etac”) == 0) etac = var_val[i];
    else
if (strcmp(var_name[i],”no”) == 0) No = var_val[i];
    else
if (strcmp(var_name[i],”nth”) == 0) Nth = var_val[i];
    else
if (strcmp(var_name[i],”go”) == 0) Go = var_val[i];
    else
if (strcmp(var_name[i],”gl”) == 0) gl = var_val[i];
    else
if (strcmp(var_name[i],”eps”) == 0) eps = var_val[i];
    else
if (strcmp(var_name[i],”tn”) == 0) tn = var_val[i];
    else
if (strcmp(var_name[i],”a”) == 0) A = var_val[i];
    else
if (strcmp(var_name[i],”b”) == 0) B = var_val[i];
    else
if (strcmp(var_name[i],”c”) == 0) C = var_val[i];
    else
if (strcmp(var_name[i],”ab”) == 0) Ab = var_val[i];
    else
if (strcmp(var_name[i],”bb”) == 0) Bb = var_val[i];
    else
if (strcmp(var_name[i],”cb”) == 0) Cb = var_val[i];
    else
if (strcmp(var_name[i],”betaa”) == 0) betaA = var_val[i];
    else
if (strcmp(var_name[i],”betab”) == 0) betaB = var_val[i];
    else
if (strcmp(var_name[i],”betac”) == 0) betaC = var_val[i];
    else
if (strcmp(var_name[i],”vbarr”) == 0) Vbarr = var_val[i];
```

```
        else
    if (strcmp(var_name[i],”tcapt”) == 0) tcapt = var_val[i];
        else
    if (strcmp(var_name[i],”tem”) == 0) tem = var_val[i];
        else
    if (strcmp(var_name[i],”cjo”) == 0) cjo = var_val[i];
        else
    if (strcmp(var_name[i],”mpow”) == 0) mpow = var_val[i];
        else
    if (strcmp(var_name[i],”vj”) == 0) vj = var_val[i];
        else
    if (strcmp(var_name[i],”fc”) == 0) fc = var_val[i];
        else
    if (strcmp(var_name[i],”delta”) == 0) delta = var_val[i];
        else
    if (strcmp(var_name[i],”del”) == 0) { del = var_val[i]; del_flag = 1; }
        else
    if (strcmp(var_name[i],”rs”) == 0) Rs = var_val[i];
        else
    if (strcmp(var_name[i],”is1”) == 0) Is1 = var_val[i];
        else
    if (strcmp(var_name[i],”n1”) == 0) n1 = var_val[i];
        else
    if (strcmp(var_name[i],”is2”) == 0) Is2 = var_val[i];
        else
    if (strcmp(var_name[i],”n2”) == 0) n2 = var_val[i];
        else
    if (strcmp(var_name[i],”cssc”) == 0) Cssc = var_val[i];
        else
    if (strcmp(var_name[i],”shtype”) == 0) shtype = (int) var_val[i];
        else
    if (strcmp(var_name[i],”r1”) == 0) R1 = var_val[i];
        else
    if (strcmp(var_name[i],”c1”) == 0) C1 = var_val[i];
        else
    if (strcmp(var_name[i],”lp1”) == 0) Lp1 = var_val[i];
        else
    if (strcmp(var_name[i],”lp2”) == 0) Lp2 = var_val[i];
        else
    if (strcmp(var_name[i],”tf”) == 0) Tf = var_val[i];
        else
               print_err(9);/* unknown model parameter */

/* check whether to use “m” or “m+del” */
 if (del_flag) {
    sprintf(delstr,”(v(m)+%.8g)”,del);
    sprintf(delsubstr,”-%.8g”,del);
 }

/* set tn to a nonzero value if not set by user and set A2 accordingly */
 if (!tn) {
     if (A != 0) { tn=1/A; A2=0; }
        else     { tn=1/(2*B*No); A2=-1/tn; }
 }
 else A2 = A - (1/tn);

/* set node-names according to parasitic circuit values */
```

```
 if (!Rs) strcpy(str1,”p”);
 else {
    if ((!Is1) && (!Is2)) strcpy(str1,”pi”);
    else                  strcpy(str1,”p1”);
 }
 if (!Is2) strcpy(str2,”pi”);
 else {
    if ((!Rs) && (!Is1)) strcpy(str2,”p”);
    else if (Rs && Is1)  strcpy(str2,”p2”);
    else            strcpy(str2,”p1”);
 }
 if ((!Rs) && (!Is1) && (!Is2)) strcpy(str3,”pi”);
 else                           strcpy(str3,”p”);

/* calculate gl if NOT set by user */
 if (!gl)
    switch (level) {
        case 2 :
        case 3 :gl = (A*No+2*B*No*No+3*C*No*No*No)/(A*No+B*No*No+C*No*No*No);
                break;
        case 4 :gl = (A*Nth+2*B*Nth*Nth+3*C*Nth*Nth*Nth)/
                     (A*Nth+B*Nth*Nth+C*Nth*Nth*Nth);
                break;
    }

/* adjust n to account for Tf */
 n  *= Tf;
 n1 *= Tf;
 n2 *= Tf;

/* calculate all additional variables */
 Cph = 2*tp;
 Islas = q*Nw*Vact*Ne/(2*etai*tn);
 tdiff = 2*tn;
 X1  = q*Nw*Vact/etai;
 X2  = 2*etai*tn/(q*Nw*Vact);
 X3  = Lambda*tp*q*Nw*Gamma*vgr/(etai*etac*h*c);
 X4  = Lambda*tp/(etac*Vact*h*c);
 X5  = A*No+B*No*No+C*No*No*No;
 X6  = A*Nth+B*Nth*Nth+C*Nth*Nth*Nth;
 X7  = Nw*etac*Vact*h*c/Lambda;
 X8  = tp*Nw*Gamma*vgr;
 K1  = A2*X1*X2;
 K2  = B*X1*X2*X2;
 K3  = C*X1*X2*X2*X2;
 K4  = X3*Go;
 K5  = A*X2/X5;
 K6  = B*X2*X2/X5;
 K7  = C*X2*X2*X2/X5;
 K8  = eps*Gamma*X4;
 K9  = X3*gl*Go;
 K10 = X2/No;
 K11 = gl*Go*X2*X3/No;
 K12 = gl*Go*X2*X3/Nth;
 K13 = X3*gl*Go-X3*Go*log(X6/X5);
 K14 = betaA*A*X2*X7;
 K15 = betaB*B*X2*X2*X7;
```

```
 K16 = betaC*C*X2*X2*X2*X7;
 K17 = X8*Go;
 K18 = X8*gl*Go;
 K19 = gl*Go*X2*X8/No;
 K20 = gl*Go*X2*X8/Nth;
 K21 = X8*gl*Go-X8*Go*log(X6/X5);

/* generate nonlinear source expressions */
 sprintf(R1expr,l1expr[0],K1,K2,K3);
 switch (level) {
    case 1: sprintf(S1expr,l1expr[1],K4,delstr,delstr,lnstr[outtype],
                              delta,K5,K6,K7,K8,delstr,delstr); break;
    case 2: sprintf(S1expr,l1expr[2],K9,delstr,delstr,lnstr[outtype],
                              delta,K10,K8,delstr,delstr); break;
    case 3: sprintf(S1expr,l1expr[3],delstr,delstr,K11,K9,K8,delstr,delstr);
            break;
    case 4: sprintf(S1expr,l1expr[3],delstr,delstr,K12,K13,K8,delstr,delstr);
            break;
 }
 sprintf(R2expr,l1expr[4],K14,K15,K16,delstr);
 switch (level) {
    case 1: sprintf(S2expr,l1expr[5],K17,delstr,lnstr[outtype],delta,
                              K5,K6,K7,K8,delstr,delstr,delsubstr);
            break;
    case 2: sprintf(S2expr,l1expr[6],K18,delstr,lnstr[outtype],delta,
                              K10,K8,delstr,delstr,delsubstr); break;
    case 3: sprintf(S2expr,l1expr[7],delstr,K19,K18,K8,delstr,delstr,delsubstr);
            break;
    case 4: sprintf(S2expr,l1expr[7],delstr,K20,K21,K8,delstr,delstr,delsubstr);
            break;
 }

/* generate subcircuit */
/**********************/

/* border subcircuit */
 fprintf(output_ptr,las_mod1[0]);

/* subcircuit declaration */
 fprintf(output_ptr,las_mod1[1],name,str3);

/* series parasitics and shunting space-charge capacitance */
 if (Rs) fprintf(output_ptr,las_mod1[2],str1,Rs);
 if (Is1) fprintf(output_ptr,las_mod1[3],str1,str2,name);
 if (Is2) fprintf(output_ptr,las_mod1[4],str2,name);
 if (Cssc) fprintf(output_ptr,las_mod1[5],Cssc);

/* additional parasitic shunting circuit */
 switch (shtype) {
    case 1: fprintf(output_ptr,las_mod1[6],str3,R1); break;
    case 2: fprintf(output_ptr,las_mod1[7],str3,C1); break;
    case 3: fprintf(output_ptr,las_mod1[8],str3,R1);
            fprintf(output_ptr,las_mod1[9],C1); break;
    case 4: fprintf(output_ptr,las_mod1[8],str3,R1);
            fprintf(output_ptr,las_mod1[10],C1);
            fprintf(output_ptr,las_mod1[11]);
            fprintf(output_ptr,las_mod1[12],VSstr[outtype],vstr[outtype],
```

```
                                            tlstr[outtype]);
            fprintf(output_ptr,las_mod1[13]);
            fprintf(output_ptr,las_mod1[14],Lp1);
            fprintf(output_ptr,las_mod1[15]);
            fprintf(output_ptr,las_mod1[16],Lp2); break;
 }

/* cavity diodes */
 fprintf(output_ptr,las_mod1[17],name);
 fprintf(output_ptr,las_mod1[32],Islas);
 fprintf(output_ptr,las_mod1[18]);
 fprintf(output_ptr,las_mod1[19],name);
 fprintf(output_ptr,las_mod1[33],Islas);

/* carrier equation recombination/stimulated emission current sources */
 fprintf(output_ptr,las_mod1[20],CSstr[outtype],istr[outtype],R1expr,
                                 tlstr[outtype]);
 fprintf(output_ptr,las_mod1[21],CSstr[outtype],istr[outtype],S1expr,
                                 tlstr[outtype]);

/* photon recombination terms */
 fprintf(output_ptr,las_mod1[22]);
 fprintf(output_ptr,las_mod1[23],Cph);

/*  photon equation recomb./stim. em. current sources */
 fprintf(output_ptr,las_mod1[24],CSstr[outtype],istr[outtype],R2expr,
                                 tlstr[outtype]);
 fprintf(output_ptr,las_mod1[25],CSstr[outtype],istr[outtype],S2expr,
                                 tlstr[outtype]);

/* output power voltage source */
 fprintf(output_ptr,las_mod1[26],VSstr[outtype],vstr[outtype],delstr,
                                 delstr,tlstr[outtype]);

/* subcircuit conclusion and diode model declarations */
 fprintf(output_ptr,las_mod1[27],name);
 fprintf(output_ptr,las_mod1[28],name,Islas,n);
 fprintf(output_ptr,las_mod1[29],name,Islas,n,tdiff,cjo,mpow,vj,fc);
 if (Is1) fprintf(output_ptr,las_mod1[30],name,Is1,n1);
 if (Is2) fprintf(output_ptr,las_mod1[31],name,Is2,n2);

/* finish border */
 fprintf(output_ptr,las_mod1[0]);

}

/***************************************************************************************/
/* Large-signal 3-rate equation model subcircuit text. (Based on S. Javro code, 1994)  */
/***************************************************************************************/
char *las_mod2[] = {
“*********************************************************************\n”,
“.subckt %s %s n pf\n”,
“Rs p %s %.8g\n”,
“Ds1 %s %s ds1mod_%s\n”,
“Ds2 %s pi ds2mod_%s\n”,
“Cssc pi n %.8g\n”,
“R1 %s n %.8g\n”,
```

```
“C1 %s n %.8g\n”,
“R1 %s sh1 %.8g\n”,
“C1 sh1 n %.8g\n”,
“C1 sh1 sh2 %.8g\n”,
“Vsh0 sh2 sh3 0\n”,
“%svsh sh3 n %sv(nl2)-v(nl1)%s\n”,
“Fl1 0 nl1 Vsh0 1\n”,
“Lp1 nl1 0 %.8g\n”,
“Gl2 0 nl2 nl1 0 1\n”,
“Lp2 nl2 0 %.8g\n”,
“D1 pi nt1 d1mod_%s\n”,
“Vt1 nt1 n 0\n”,
“D2 pi n d2mod_%s\n”,
“%srb pi n %s%s%s\n”,
“”,
“”,
“”,
“”,
“”,
“”,
“Rph m 0 1\n”,
“Cph m 0 %.8g\n”,
“%sr2 0 m %s%s%s\n”,
“%ss2 0 m %s%s%s\n”,
“%spf pf 0 %s%s*%s%s\n”,
“.ends %s\n”,
“.model d1mod_%s D Is=%.8g n=%.8g\n”,
“.model d2mod_%s D Is=%.8g n=%.8g tt=%.8g cjo=%.8g m=%.8g vj=%.8g fc=%.8g\n”,
“.model ds1mod_%s D Is=%.8g n=%.8g\n”,
“.model ds2mod_%s D Is=%.8g n=%.8g\n”,
“F1 n pi Vtw1 1\n”,
“Dw1  w ntw1 dw1mod_%s\n”,
“Icw1 w ntw1 %.8g\n”,
“Vtw1 ntw1 0 0\n”,
“Dw2  w 0 dw2mod_%s\n”,
“Icw2 w 0 %.8g\n”,
“%sr1 w 0 %s%s%s\n”,
“%ss1 w 0 %s%s%s\n”,
“F2 0 w Vt1 4\n”,
“.model dw1mod_%s D Is=%.8g n=%.8g\n”,
“.model dw2mod_%s D Is=%.8g n=%.8g tt=%.8g\n”,
“Ic1 pi nt1 %.8g\n”,
“Ic2 pi n %.8g\n”
};

char *l2expr[] = {
“%.8g*i(Vt1)+%.8g*i(Vt1)*i(Vt1)+%.8g*i(Vt1)*i(Vt1)*i(Vt1)”,
“%.8g*i(Vtw1)+%.8g*i(Vtw1)*i(Vtw1)+%.8g*i(Vtw1)*i(Vtw1)*i(Vtw1)”,
“%.8g*%s*%s*%s(%.8g+%.8g*i(Vtw1)+%.8g*i(Vtw1)*i(Vtw1)+%.8g*i(Vtw1)*i(Vtw1)*i(Vtw1))/
(1+%.8g*%s*%s)”,
“%.8g*%s*%s*%s(%.8g+%.8g*i(Vtw1))/(1+%.8g*%s*%s)”,
“%s*%s*(%.8g*i(Vtw1)-%.8g)/(1+%.8g*%s*%s)”,
“(%.8g*i(Vtw1)+%.8g*i(Vtw1)*i(Vtw1)+%.8g*i(Vtw1)*i(Vtw1)*i(Vtw1))/%s”,
“%.8g*%s*%s(%.8g+%.8g*i(Vtw1)+%.8g*i(Vtw1)*i(Vtw1)+%.8g*i(Vtw1)*i(Vtw1)*i(Vtw1))/
(1+%.8g*%s*%s)%s”,
“%.8g*%s*%s(%.8g+%.8g*i(Vtw1))/(1+%.8g*%s*%s)%s”,
“%s*(%.8g*i(Vtw1)-%.8g)/(1+%.8g*%s*%s)%s”
```

```
};

/****************************************************************************/
/* laser2() (Based on S. Javro code, 1994)                                  */
/* PURPOSE  : generate subcircuit for large-signal 3-rate-eqn. model        */
/* CALLED BY: main(argc,argv)                                               */
/****************************************************************************/
void laser2()
{
 int i;
 double Cph,Islas,Isw,tdiff,twd;
 double X1,X2,X3,X4,X5,X6,X7,X8,X9,X10;
 double K1,K2,K3,K4,K5,K6,K7,K8,K9,K10;
 double K11,K12,K13,K14,K15,K16,K17,K18,K19,K20,K21,K22,K23,K24;
 char str1[5],str2[5],str3[5];
 char RBexpr[180],R1expr[180],S1expr[180],R2expr[180],S2expr[180];

 for (i=0; i<No_of_vars; i++)
    if (strcmp(var_name[i],”level”) == 0) level = (int) rint(var_val[i]);
        else
    if (strcmp(var_name[i],”ne”) == 0) Ne = var_val[i];
        else
    if (strcmp(var_name[i],”n”) == 0) n = var_val[i];
        else
    if (strcmp(var_name[i],”ne2”) == 0) Ne2 = var_val[i];
        else
    if (strcmp(var_name[i],”nw2”) == 0) nw2 = var_val[i];
        else
    if (strcmp(var_name[i],”etai”) == 0) etai = var_val[i];
        else
    if (strcmp(var_name[i],”lambda”) == 0) Lambda = var_val[i];
        else
    if (strcmp(var_name[i],”nw”) == 0) Nw = var_val[i];
        else
    if (strcmp(var_name[i],”vact”) == 0) Vact = var_val[i];
        else
    if (strcmp(var_name[i],”gamma”) == 0) Gamma = var_val[i];
        else
    if (strcmp(var_name[i],”vgr”) == 0) vgr = var_val[i];
        else
    if (strcmp(var_name[i],”tp”) == 0) tp = var_val[i];
        else
    if (strcmp(var_name[i],”etac”) == 0) etac = var_val[i];
        else
    if (strcmp(var_name[i],”no”) == 0) No = var_val[i];
        else
    if (strcmp(var_name[i],”nth”) == 0) Nth = var_val[i];
        else
    if (strcmp(var_name[i],”go”) == 0) Go = var_val[i];
        else
    if (strcmp(var_name[i],”gl”) == 0) gl = var_val[i];
        else
    if (strcmp(var_name[i],”eps”) == 0) eps = var_val[i];
        else
    if (strcmp(var_name[i],”tn”) == 0) tn = var_val[i];
        else
    if (strcmp(var_name[i],”a”) == 0) A = var_val[i];
```

```
    else
if (strcmp(var_name[i],”b”) == 0) B = var_val[i];
    else
if (strcmp(var_name[i],”c”) == 0) C = var_val[i];
    else
if (strcmp(var_name[i],”ab”) == 0) Ab = var_val[i];
    else
if (strcmp(var_name[i],”bb”) == 0) Bb = var_val[i];
    else
if (strcmp(var_name[i],”cb”) == 0) Cb = var_val[i];
    else
if (strcmp(var_name[i],”betaa”) == 0) betaA = var_val[i];
    else
if (strcmp(var_name[i],”betab”) == 0) betaB = var_val[i];
    else
if (strcmp(var_name[i],”betac”) == 0) betaC = var_val[i];
    else
if (strcmp(var_name[i],”vbarr”) == 0) Vbarr = var_val[i];
    else
if (strcmp(var_name[i],”tcapt”) == 0) tcapt = var_val[i];
    else
if (strcmp(var_name[i],”tem”) == 0) tem = var_val[i];
    else
if (strcmp(var_name[i],”cjo”) == 0) cjo = var_val[i];
    else
if (strcmp(var_name[i],”mpow”) == 0) mpow = var_val[i];
    else
if (strcmp(var_name[i],”vj”) == 0) vj = var_val[i];
    else
if (strcmp(var_name[i],”fc”) == 0) fc = var_val[i];
    else
if (strcmp(var_name[i],”delta”) == 0) delta = var_val[i];
    else
if (strcmp(var_name[i],”del”) == 0) { del = var_val[i]; del_flag = 1; }
    else
if (strcmp(var_name[i],”rs”) == 0) Rs = var_val[i];
    else
if (strcmp(var_name[i],”is1”) == 0) Is1 = var_val[i];
    else
if (strcmp(var_name[i],”n1”) == 0) n1 = var_val[i];
    else
if (strcmp(var_name[i],”is2”) == 0) Is2 = var_val[i];
    else
if (strcmp(var_name[i],”n2”) == 0) n2 = var_val[i];
    else
if (strcmp(var_name[i],”cssc”) == 0) Cssc = var_val[i];
    else
if (strcmp(var_name[i],”shtype”) == 0) shtype = (int) var_val[i];
    else
if (strcmp(var_name[i],”r1”) == 0) R1 = var_val[i];
    else
if (strcmp(var_name[i],”c1”) == 0) C1 = var_val[i];
    else
if (strcmp(var_name[i],”lp1”) == 0) Lp1 = var_val[i];
    else
if (strcmp(var_name[i],”lp2”) == 0) Lp2 = var_val[i];
    else
```

```
    if (strcmp(var_name[i],”tf”) == 0) Tf = var_val[i];
        else
            print_err(9);       /* unknown model parameter */

/* check whether to use “m” or “m+del” */
 if (del_flag) {
    sprintf(delstr,”(v(m)+%.8g)”,del);
    sprintf(delsubstr,”-%.8g”,del);
 }

/* set tn to a nonzero value if not set by user and set A2 accordingly */
 if (!tn) {
    if (A != 0) { tn=1/A; A2=0; }
        else     { tn=1/(2*B*No); A2=-1/tn; }
 }
 else A2 = A - (1/tn);

/* set node-names according to parasitic circuit values */
 if (!Rs) strcpy(str1,”p”);
 else {
    if ((!Is1) && (!Is2)) strcpy(str1,”pi”);
    else                  strcpy(str1,”p1”);
 }
 if (!Is2) strcpy(str2,”pi”);
 else {
    if ((!Rs) && (!Is1)) strcpy(str2,”p”);
    else if (Rs && Is1)  strcpy(str2,”p2”);
         else            strcpy(str2,”p1”);
 }
 if ((!Rs) && (!Is1) && (!Is2)) strcpy(str3,”pi”);
 else                           strcpy(str3,”p”);

/* calculate gl if NOT set by user */
 if (!gl)
    switch (level) {
        case 2 :
        case 3 :    gl = (A*No+2*B*No*No+3*C*No*No*No)/(A*No+B*No*No+C*No*No*No);
                    break;
        case 4 :    gl = (A*Nth+2*B*Nth*Nth+3*C*Nth*Nth*Nth)/
                        (A*Nth+B*Nth*Nth+C*Nth*Nth*Nth);
                    break;
    }

/* adjust n to account for Tf */
 n   *= Tf;
 n1  *= Tf;
 n2  *= Tf;
 nw2 *= Tf;

/* calculate all additional variables */
 Cph = 2*tp;
 Islas = q*Vbarr*Ne/(2*etai*tcapt);
 tdiff = 2*tcapt;
 Isw = q*Nw*Vact*Ne2/(etai*tem);
 twd = 2*tem;
 X1  = 2*q*Nw*Vact/etai;
 X2  = etai*tem/(q*Nw*Vact);
```

```
 X3  = 2*Lambda*tp*q*Nw*Gamma*vgr/(etai*etac*h*c);
 X4  = Lambda*tp/(etac*Vact*h*c);
 X5  = A*No+B*No*No+C*No*No*No;
 X6  = A*Nth+B*Nth*Nth+C*Nth*Nth*Nth;
 X7  = Nw*etac*Vact*h*c/Lambda;
 X8  = tp*Nw*Gamma*vgr;
 X9  = q*Vbarr/etai;
 X10 = 2*etai*tcapt/(q*Vbarr);
 K1  = A*X1*X2;
 K2  = B*X1*X2*X2;
 K3  = C*X1*X2*X2*X2;
 K4  = X3*Go;
 K5  = A*X2/X5;
 K6  = B*X2*X2/X5;
 K7  = C*X2*X2*X2/X5;
 K8  = eps*Gamma*X4;
 K9  = X3*gl*Go;
 K10 = X2/No;
 K11 = gl*Go*X2*X3/No;
 K12 = gl*Go*X2*X3/Nth;
 K13 = X3*gl*Go-X3*Go*log(X6/X5);
 K14 = betaA*A*X2*X7;
 K15 = betaB*B*X2*X2*X7;
 K16 = betaC*C*X2*X2*X2*X7;
 K17 = X8*Go;
 K18 = X8*gl*Go;
 K19 = gl*Go*X2*X8/No;
 K20 = gl*Go*X2*X8/Nth;
 K21 = X8*gl*Go-X8*Go*log(X6/X5);
 K22 = Ab*X9*X10;
 K23 = Bb*X9*X10*X10;
 K24 = Cb*X9*X10*X10*X10;

/* generate nonlinear source expressions */
 sprintf(RBexpr,l2expr[0],K22,K23,K24);
 sprintf(R1expr,l2expr[1],K1,K2,K3);
 switch (level) {
    case 1: sprintf(S1expr,l2expr[2],K4,delstr,delstr,lnstr[outtype],
                                     delta,K5,K6,K7,K8,delstr,delstr); break;
    case 2: sprintf(S1expr,l2expr[3],K9,delstr,delstr,lnstr[outtype],
                                     delta,K10,K8,delstr,delstr); break;
    case 3: sprintf(S1expr,l2expr[4],delstr,delstr,K11,K9,K8,delstr,delstr);
            break;
    case 4: sprintf(S1expr,l2expr[4],delstr,delstr,K12,K13,K8,delstr,delstr);
            break;
 }
 sprintf(R2expr,l2expr[5],K14,K15,K16,delstr);
 switch (level) {
    case 1: sprintf(S2expr,l2expr[6],K17,delstr,lnstr[outtype],delta,
                                     K5,K6,K7,K8,delstr,delstr,delsubstr);
            break;
    case 2: sprintf(S2expr,l2expr[7],K18,delstr,lnstr[outtype],delta,
                                     K10,K8,delstr,delstr,delsubstr); break;
    case 3: sprintf(S2expr,l2expr[8],delstr,K19,K18,K8,delstr,delstr,delsubstr);
            break;
    case 4: sprintf(S2expr,l2expr[8],delstr,K20,K21,K8,delstr,delstr,delsubstr);
            break;
```

```
 }

/* generate subcircuit */
/***********************/

/* border subcircuit */
 fprintf(output_ptr,las_mod2[0]);

/* subcircuit declaration */
 fprintf(output_ptr,las_mod2[1],name,str3);

/* series parasitics and shunting space-charge capacitance */
 if (Rs) fprintf(output_ptr,las_mod2[2],str1,Rs);
 if (Is1) fprintf(output_ptr,las_mod2[3],str1,str2,name);
 if (Is2) fprintf(output_ptr,las_mod2[4],str2,name);
 if (Cssc) fprintf(output_ptr,las_mod2[5],Cssc);

/* additional parasitic shunting circuit */
 switch (shtype) {
case 1: fprintf(output_ptr,las_mod2[6],str3,R1); break;
case 2: fprintf(output_ptr,las_mod2[7],str3,C1); break;
case 3: fprintf(output_ptr,las_mod2[8],str3,R1);
        fprintf(output_ptr,las_mod2[9],C1); break;
case 4: fprintf(output_ptr,las_mod2[8],str3,R1);
        fprintf(output_ptr,las_mod2[10],C1);
        fprintf(output_ptr,las_mod2[11]);
        fprintf(output_ptr,las_mod2[12],VSstr[outtype],vstr[outtype],
                                        tlstr[outtype]);
        fprintf(output_ptr,las_mod2[13]);
        fprintf(output_ptr,las_mod2[14],Lp1);
        fprintf(output_ptr,las_mod2[15]);
        fprintf(output_ptr,las_mod2[16],Lp2); break;
 }

/* cavity diodes */
 fprintf(output_ptr,las_mod2[17],name);
 fprintf(output_ptr,las_mod2[48],Islas);
 fprintf(output_ptr,las_mod2[18]);
 fprintf(output_ptr,las_mod2[19],name);
 fprintf(output_ptr,las_mod2[49],Islas);

/* barrier layer recombination current source */
 if ( Ab || Bb || Cb)
 fprintf(output_ptr,las_mod2[20],CSstr[outtype],istr[outtype],RBexpr,
                                 tlstr[outtype]);

/* barrier layer well-coupling term */
 fprintf(output_ptr,las_mod2[37]);

/* well-barrier interaction elements */
 fprintf(output_ptr,las_mod2[38],name);
 fprintf(output_ptr,las_mod2[39],Isw);
 fprintf(output_ptr,las_mod2[40]);
 fprintf(output_ptr,las_mod2[41],name);
 fprintf(output_ptr,las_mod2[42],Isw);

/* carrier equation recombination/stimulated emission current sources */
```

```
 fprintf(output_ptr,las_mod2[43],CSstr[outtype],istr[outtype],R1expr,
                                 tlstr[outtype]);
 fprintf(output_ptr,las_mod2[44],CSstr[outtype],istr[outtype],S1expr,
                                 tlstr[outtype]);

/* well layer barrier-coupling term */
 fprintf(output_ptr,las_mod2[45]);

/* photon recombination terms */
 fprintf(output_ptr,las_mod2[27]);
 fprintf(output_ptr,las_mod2[28],Cph);

/* photon equation recomb./stim. em. current sources */
 fprintf(output_ptr,las_mod2[29],CSstr[outtype],istr[outtype],R2expr,
                                 tlstr[outtype]);
 fprintf(output_ptr,las_mod2[30],CSstr[outtype],istr[outtype],S2expr,
                                 tlstr[outtype]);

/* output power voltage source */
 fprintf(output_ptr,las_mod2[31],VSstr[outtype],vstr[outtype],delstr,
                                 delstr,tlstr[outtype]);

/* subcircuit conclusion and diode model declarations */
 fprintf(output_ptr,las_mod2[32],name);
 fprintf(output_ptr,las_mod2[33],name,Islas,n);
 fprintf(output_ptr,las_mod2[34],name,Islas,n,tdiff,cjo,mpow,vj,fc);
 fprintf(output_ptr,las_mod2[46],name,Isw,nw2);
 fprintf(output_ptr,las_mod2[47],name,Isw,nw2,twd);
 if (Is1) fprintf(output_ptr,las_mod2[35],name,Is1,n1);
 if (Is2) fprintf(output_ptr,las_mod2[36],name,Is2,n2);

/* finish border */
 fprintf(output_ptr,las_mod2[0]);

}

/************************************************************************/
main(int argc, char *argv[])
{ /* originally written by S. Javro, 1994 */
 if (argc != 4)
   {
    printf(“SYNOPSIS :  %s [infile] [outfile] [0-SPICE3, 1- HSPICE]\n\n”,argv[0]);
    printf(“NOTES    :  -infile must be different from outfile.\n”);
    printf(“            -The infile should be in spice format.\n”);
    printf(“            -The device names in the .Xmodel definitions should\n”);
    printf(“             be less than 28 characters long.\n”);
    exit(1);
   }

 outtype = atoi(argv[3]);

 if ((outtype != 0) && (outtype != 1)) print_err(10);
 if (strcmp(argv[1],argv[2]) == 0)   print_err(5);
 if ((input_ptr = fopen(argv[1],”r”)) == NULL) print_err(6);
 if ((output_ptr = fopen(argv[2],”w”)) == NULL) print_err(7);

 readln();                     /* read in current line */
```

```
 if (feof(input_ptr)) print_err(8);

 for (;(!feof(input_ptr));)
      {
       command[0] = ‘\0’;                    /* blank previous command */
       sscanf(in_buff,”%s”,command);         /* get new command        */
       if (strcmp(command,”.xmodel”) != 0)
         {
          fprintf(output_ptr,”%s\n”,in_buff);
          readln();                     /* read in next line */
         }
        else
         {
          parse_system();               /* reads the model parameters and  */
                                        /* loads in the next line for the  */
                                        /* next iteration of the loop.     */
          init_params();
          if      (strcmp(model,”laser1”) == 0) laser1();
          else if (strcmp(model,”laser2”) == 0) laser2();
          else print_err(9);
         }
      }

 fclose(input_ptr);
 fclose(output_ptr);
}
```

A.4 References

[A.1] B. Johnson, T. Quarles, A. R. Newton, D. O. Pederson, and A. Sangiovanni-Vincentelli, *SPICE3 Version 3e User’s Manual*, University of California, Berkeley, 1991.

[A.2] *HSPICE User’s Manual*, Meta-Software, Inc., 1996.

[A.3] *ISSPICE4 User’s Guide*, Intusoft, 1996.

[A.4] S. A. Javro and S. M. Kang, “Transforming Tucker’s linearized laser rate equations to a form that has a single solution regime,” *Journal of Lightwave Technology*, vol. 13, no. 9, pp. 1899-1904, 1995.

APPENDIX B

DERIVATION OF S_{21}-T_F RELATIONSHIP

In collaboration with M. Bruensteiner, we were able to derive the relationship between a laser's microwave modulation response S_{21} and its transfer function T_f. Consider the test setup of Fig. B.1. In this arrangement, the device under test (DUT) is a laser driven by a current source i_{src} with a source impedance R_s; the corresponding laser input current and voltage are i_1 and v_1, respectively. The laser's output is modeled by a voltage v_2 across a load R_L, where we have assumed that the detector response has been calibrated out of the measurement. The corresponding output current is i_2. We can define the laser transfer function as

$$T_f = \frac{v_2}{i_1} \tag{B.1}$$

while the input impedance is

$$Z_{in} = \frac{v_1}{i_1} \tag{B.2}$$

Below, we derive expressions for T_f and Z_{in} as functions of the S-parameters.

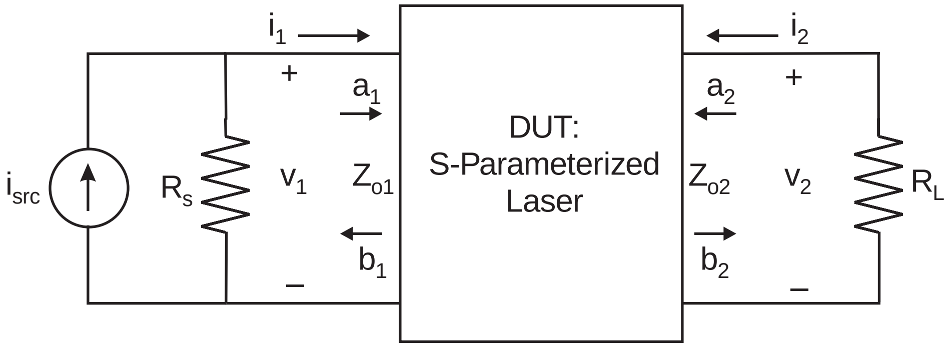

Figure B.1 Generic setup for the S-parameter characterization of a laser.

Let us assume that the DUT has been characterized via its S-parameters, with input and output reference impedances Z_{o1} and Z_{o2} [B.1]. In this case, the relevant variables are a_1 and b_1, the incident and reflected traveling waves at the input port, respectively, as well as a_2 and b_2, the corresponding traveling waves at the output port. These four variables can be related via the well-known S-parameter equations [B.1]:

$$b_1 = S_{11}a_1 + S_{12}a_2 \tag{B.3}$$

$$b_2 = S_{21}a_1 + S_{22}a_2 \tag{B.4}$$

where S_{11} and S_{22} account for reflection at each port, and S_{12} and S_{21} account for transmission from one port to the other. In general, these are not equivalent to the reflection and transmission coefficients unless the port impedances are matched by the source and load [B.1].

We can relate the traveling wave variables to the currents and voltages at the DUT's ports using the following expressions [B.1]:

$$v_1 = (a_1 + b_1)\sqrt{Z_{o1}} \tag{B.5}$$

$$i_1 = (a_1 - b_1)/\sqrt{Z_{o1}} \tag{B.6}$$

$$v_2 = (a_2 + b_2)\sqrt{Z_{o2}} \tag{B.7}$$

$$i_2 = (a_2 - b_2)/\sqrt{Z_{o2}} \tag{B.8}$$

Furthermore, we can define the reflection coefficient at the load impedance R_L as [B.2]

$$\Gamma_L = \frac{a_2}{b_2} = \frac{R_L - Z_{02}}{R_L + Z_{o2}}, \tag{B.9}$$

We can then use (B.3), (B.4), and (B.9) to obtain definitions of the traveling waves a_2, b_1, and b_2 in terms of a_1:

$$a_2 = \frac{\Gamma_L S_{21}}{1 - S_{22}\Gamma_L} \cdot a_1 \tag{B.10}$$

$$b_1 = \frac{S_{11} - (S_{11}S_{22} - S_{12}S_{21})\Gamma_L}{1 - S_{22}\Gamma_L} \cdot a_1 \tag{B.11}$$

$$b_2 = \frac{S_{21}}{1 - S_{22}\Gamma_L} \cdot a_1 \tag{B.12}$$

If we substitute (B.5)-(B.8) and (B.10)-(B.12) into (B.1) and (B.2), we obtain the following expressions for T_f and Z_{in}:

$$T_f = \sqrt{Z_{o1}Z_{o2}} \cdot \frac{S_{21}(1 + \Gamma_L)}{1 - S_{11} - (S_{22} - S_{11}S_{22} + S_{12}S_{21})\Gamma_L} \tag{B.13}$$

$$Z_{in} = Z_{o1} \cdot \frac{1 + S_{11} - (S_{22} + S_{11}S_{22} - S_{12}S_{21})\Gamma_L}{1 - S_{11} - (S_{22} - S_{11}S_{22} + S_{12}S_{21})\Gamma_L} \tag{B.14}$$

In the typical test setup, the input and output reference impedances are 50 Ω, as are the source and load impedances. In this case, $\Gamma_L = 0$ and (B.13) and (B.14) reduce to

$$T_f = 50 \cdot \frac{S_{21}}{1 - S_{11}} \tag{B.15}$$

$$Z_{in} = Z_o \cdot \frac{1 + S_{11}}{1 - S_{11}} \tag{B.16}$$

Thus, we have obtained expressions for the transfer function and input impedance as functions of the measured S-parameters. If we then solve (B.16) for S_{11} and substitute the resulting expression into (B.15), we can solve for S_{21} to obtain (2.70)

$$S_{21} = \frac{2T_f}{Z_{in} + 50} \tag{B.17}$$

B.1 References

[B.1] S. Y. Liao, *Microwave Circuit Analysis and Amplifier Design*. Englewood Cliffs, NJ: Prentice-Hall, Inc., 1987.

[B.2] N. N. Rao, *Elements of Engineering Electromagnetics*, 3rd. ed. Englewood Cliffs, NJ: Prentice Hall, 1991.

APPENDIX C

IMPLEMENTATION OF THE SIMPLE THERMAL VCSEL MODEL

Below, we summarize the HSPICE [C.1] and SABER [C.2] implementations of the simple thermal VCSEL model of Chapter 3. In addition to summarizing the model equations, we provide an HSPICE subcircuit, a MAST template, and an overview of the model parameters.

C.1 Summary of Model Equations

The model equations presented in Chapter 3 are

$$\frac{dN}{dt} = \frac{\eta_i(I - I_{off}(T))}{q} - \frac{N}{\tau_n} - \frac{G_o(N - N_o)S}{1 + \varepsilon S} \tag{C.1}$$

$$\frac{dS}{dt} = -\frac{S}{\tau_p} + \frac{\beta N}{\tau_n} + \frac{G_o(N - N_o)S}{1 + \varepsilon S} \tag{C.2}$$

$$P_o = kS = (v_m + \delta)^2 \tag{C.3}$$

$$I_{off}(T) = a_0 + a_1 T + a_2 T^2 + a_3 T^3 + a_4 T^4 \tag{C.4}$$

$$N = z_n v_n \tag{C.5}$$

$$T = T_o + (IV - P_o)R_{th} - \tau_{th}\frac{dT}{dt} \tag{C.6}$$

$$V = f(I, T) \tag{C.7}$$

where (C.1) is the rate equation for the carrier number N, (C.2) is the rate equation for the photon number S, (C.3) describes the optical output power P_o, (C.4) is the thermal offset current, (C.5) implements a scaled version of the carrier number, (C.6) is the rate equation for the temperature T, and (C.7) describes the dc voltage characteristics of the model. In addition to the above equations, a capacitor is included in parallel with the voltage source of (C.7) to account for parasitic shunting capacitance. Table C.1 summarizes the complete set of model parameters. Note that for convergence purposes, z_n should typically be set to a value on the order of 10^8.

Table C.1 Model parameters for the HSPICE and SABER implementations of the simple thermal VCSEL model.

Parameter	Simulator Name	Description, units	Default
η_i	ETAI	current-injection efficiency	1
β	BETA	spontaneous emission coupling coefficient	8.98×10^{-4}
τ_n	TN	carrier lifetime, s	5×10^{-9}
k	K	output-power coupling coefficient, W	1.165×10^{-8}
G_o	GO	gain coefficient, s^{-1}	10^4
N_o	NO	carrier transparency number	10^7
τ_p	TP	photon lifetime, s	10^{-12}
ε	EPS	gain-saturation factor	0
C_l	CLASER	shunting capacitance, F	10^{-12}
R_{th}	RTH	thermal impedance, ºC/W	2000
τ_{th}	TTH	thermal time constant, s	10^{-6}
a_0	A0	thermal-offset coefficient, A	0
a_1	A1	thermal-offset coefficient, $A \cdot K^{-1}$	0
a_2	A2	thermal-offset coefficient, $A \cdot K^{-2}$	0
a_3	A3	thermal-offset coefficient, $A \cdot K^{-3}$	0
a_4	A4	thermal-offset coefficient, $A \cdot K^{-4}$	0
z_n	ZN	carrier scaling factor	10^8
δ	DELTA	output-power correction factor	5×10^{-10}

C.2 HSPICE Implementation

As discussed in Section 3.2.3, we implemented our HSPICE subcircuit using the equivalent circuit of Fig. 3.3 and the netlist of Fig. 3.4. For convenience, we repeat the netlist in Fig. C.1, where we have modeled the voltage using the polynomial function of current and temperature from (3.15).

```
.SUBCKT las_statictherm  pd nd po td  etai=1 beta=8.98e-4 tn=5e-9
+                                     k=1.165e-8 go=1e4 no=1e7 tp=1e-12
+                                     rth=2000 a0=0 a1=0 a2=0 a3=0 a4=0
+                                  zn=1e8 delta=5e-10 eps=0 tth=1e-6 claser=1e-12
+                                     q=1.60219e-19 kb=1.38062e-23

* electrical representation of laser (V as a fn. of I and T)
ed   pd nd VOL=’(2.298+366.2*i(ed)- 6.097e4*i(ed)*i(ed)+           \\
                 6.76e6*i(ed)*i(ed)*i(ed))*                        \\
                (0.829-1.007e-3*v(td)+6.594e-6*v(td)*v(td)-        \\
                 2.18e-8*v(td)*v(td)*v(td))’
cl   pd nc claser
vcr  nc nd 0

* temperature circuit: v(td) = junction temperature
rth td 0 ’rth’
cth td 0 ’tth/rth’
gth 0 td CUR=’temper/rth + ((i(ed)+i(vcr))*v(pd,nd)-(v(m)+delta)*(v(m)+delta))’

* carrier number circuit (N=zn*v(n)), incl. thermal offset current (goff)
gn   0 n CUR=’i(ed)’
cn   n 0  ’q*zn/etai’
rn   n 0  ’etai*tn/(q*zn)’
gstn n 0  CUR=’(q*go/(etai*k))*(zn*v(n)-no)*(v(m)+delta)*(v(m)+delta)/   \\
                (1+eps*(v(m)+delta)*(v(m)+delta)/k)’
goff n 0  CUR=’a0 + a1*v(td) + a2*v(td)*v(td) +                      \\
                a3*v(td)*v(td)*v(td) + a4*v(td)*v(td)*v(td)*v(td)’

* photon circuit...
cph  m 0 ’2*tp’
rph  m 0 1
gsp  0 m CUR=’tp*beta*k*zn*v(n)/(tn*(v(m)+delta))’
gstm 0 m CUR=’go*tp*(zn*v(n)-no)*(v(m)+delta)/(1+eps*(v(m)+delta)*    \\
              (v(m)+delta)/k)-delta’

* optical output
epo po 0 VOL=’(v(m)+delta)*(v(m)+delta)’

.ENDS las_statictherm
```

Figure C.1 HSPICE-subcircuit implementation of the simple thermal VCSEL model.

Note that we have taken advantage of HSPICE's subcircuit parameter-passing capabilities.

The VCSEL model can be invoked within an HSPICE netlist by including this subcircuit (with an alternative voltage expression as needed) and the following line for each VCSEL:

```
xdevicename <pd> <nd> <po> <td> las_statictherm <model_parameters>
```

where `<pd>` and `<nd>` are the VCSEL electrical terminals, `<po>` is the output terminal whose node voltage models the optical output power P_o, `<td>` is an output node whose node voltage equals the junction temperature, and `<model_parameters>` are the parameter values for this invocation. Model parameters whose values are not set by the user retain their default values. A summary of the parameter names used in the netlist and their correspondence with the actual equation variables is given in Table C.1. Following is an example of a VCSEL invocation in HSPICE:

```
xlaser 1 0 2 3 las_statictherm  etai=1 beta=1e-6 tn=5e-9
+                                k=2.6e-8 go=1.6e4 no=1.6535203e7
+                                tp=2.0643602e-12 rth=9800
+                                a0=-0.2733576e-3 a1=-2.1246036e-5
+                               a2=1.8374405e-7 a3=3.1828248e-10 a4=0
+                                eps=0 tth=1e-6 claser=1e-17
+                                zn=1e8 delta=5e-10
```

C.3 SABER Implementation

We also implemented our model as a MAST template for use in Analogy's SABER. (Details on template authoring can be found in [C.3]). We repeat in Fig. C.2 the actual model template. As we can see, the voltage expression in this case, (3.15), is implemented through the template variable `vpn`, and can be changed as necessary by the user, while the variables `ipnc` and `vpnc` implement the capacitor C_l. The thermal rate equation (C.6) is implemented directly via the expression for `tjct` (T). Also, the rate equations, implemented in terms of v_m and v_n, are directly coded into the template via

```
element template las_statictherm  pd nd po = etai, beta, tn, k, go, no, tp, rth,
                                             a0, a1, a2, a3, a4, zn, delta,
                                             eps, tth, claser
electrical pd, nd, po             # pins (electrical- pd,nd; optical- po)
number etai = 1,                  # argument defaults
       beta = 8.98e-4,
       tn = 5e-9,
       k = 1.165e-8,
       go = 1e4,
       no = 1e7,
       tp = 1e-12,
       rth = 2000,
       a0 = 0, a1 = 0, a2 = 0, a3 = 0, a4 = 0,
       zn = 1e8, delta = 5e-10,
       eps = 0,
       tth = 1e-6,
       claser = 1e-12
external number temp            # simulation temperature

{
branch ipn = i(pd->nd), vpn = v(pd,nd)    # cavity branch vars.
branch ipnc = i(pd->nd), vpnc = v(pd,nd)  # capacitor branch vars.
var tc tjct             # junction temperature
var i iinj              # net injection current
val i ioff              # thermal offset current
var v vn                # internal voltage related to carriers
var v vm                # internal voltage related to photons
var i ipo               # current from output node po

# local variables and constants
number kb = 1.38062e-23,
       q  = 1.60219e-19

# define ioff as a function of junction temperature...
ioff  = a0 + a1*tjct + a2*tjct*tjct + a3*tjct*tjct*tjct + a4*tjct*tjct*tjct*tjct

# electrical representation of laser diode (V as a fn. of I and T)
vpn = (2.298 + 366.2*ipn - 6.097e4*ipn**2 + 6.76e6*ipn**3)*           \
      (0.829 - 1.007e-3*tjct + 6.594e-6*tjct**2 - 2.18e-8*tjct**3)
ipnc = d_by_dt(claser*vpnc)

# transformed rate equations (simple n-vn relat’n, quadratic photon transform)
# as well as relations for net injection current and junction temperature
tjct: tjct  = ((ipn+ipnc)*vpn - v(po))*rth + temp - d_by_dt(tth*tjct)
iinj: iinj = ipn - ioff
vn: vn = etai*tn*iinj/(q*zn) - d_by_dt(tn*vn) -                       \
         tn*go*(vn-no/zn)*(vm+delta)*(vm+delta)/k/(1+eps*v(po)/k)
vm: vm = -delta - d_by_dt(2*tp*vm) + tp*k*beta*zn*vn/(tn*(vm+delta)) +    \
         tp*go*(zn*vn-no)*(vm+delta)/(1+eps*v(po)/k)

# optical output
i(po) += ipo
ipo: v(po) = (vm+delta)*(vm+delta)
}
```

Figure C.2 MAST-template implementation of the simple thermal VCSEL model.

differential equations for `vm` and `vn`.

The model can be invoked in SABER via a symbolic representation during schematic entry, or a netlist invocation. In the latter case, the VCSEL model can be invoked using

```
las_statictherm.<element_name> <pd> <nd> <po> = <model_parameters>
```

where `<pd>` and `<nd>` are the VCSEL electrical terminals, `<po>` is the output terminal whose node voltage models the optical output power P_o, and `<model_parameters>` passes the model parameter values into the template. The parameters are the same as those used in the HSPICE subcircuit and can be found in Table C.1. Following is an example of the netlist invocation of the MAST template:

```
las_statictherm.las_statictherm1 1 0 2 = tn=5e-9, etai=1,        \
   go=1.6e4, no=1.6535203e7, eps=0, beta=1e-6, claser=1e-12,     \
   k=2.6e-8, tp=2.0643602e-12, a0=-0.2733576e-3,                 \
   a1=-2.1246036e-5, a2=1.8374405e-7, a3=3.1828248e-10, a4=0,    \
   rth=9800, tth=1e-6, zn=1e8, delta=5e-10
```

C.4 References

[C.1] *HSPICE User’s Manual*, Meta-Software, Inc., 1996.

[C.2] *SaberGuide Simulator Reference*, Analogy, Inc., 1996.

[C.3] *Guide to Writing Templates*, Analogy, Inc., 1996.

APPENDIX D

DERIVATION OF SIMPLIFIED GAIN EQUATION

In this Appendix, we derive the gain expression (4.5) that we presented in Chapter 4. Recall that we initially defined the gain as a function of optical energy using

$$g(\hbar\omega) = \frac{\pi q^2 \hbar}{n_g c \varepsilon_o m_o^2} \cdot \frac{1}{\hbar\omega} \cdot \int_{E_{c1v1}}^{\infty} |M_T|^2 \rho_r(E_{21})(f_2 - f_1)\mathcal{L}(\hbar\omega - E_{21})dE_{21} \qquad \text{(D.1)}$$

where $\hbar\omega$ is the optical energy, q is the electron charge, n_g is the index of refraction, c is the speed of light, ε_o is the free-space permittivity, $E_{c1v1} = E_{c1} - E_{v1}$ is the difference between the first electron and heavy-hole subband energies, $E_{21} = E_2 - E_1$ is the transition energy between a conduction-band electron state at energy E_2 and a heavy-hole state at energy E_1, $|M_T|^2$ is the transition matrix element, $\rho_r(E_{21})$ is the reduced density of states (DOS) for this particular subband transition, f_2 is the electron occupation probability at E_2, f_1 is the electron occupation probability at E_1, and $\mathcal{L}(\hbar\omega - E_{21})$ is the Lorentzian lineshape function. In order to generate (4.5), we need expressions for the various terms in (D.1).

If we assume a single TE-heavy-hole (TE-hh) subband transition, then we can define the transition matrix element $|M_T|^2$ for a quantum well as [D.1]

$$|M_T|^2 = \frac{1}{2}|M|^2 \cdot \frac{1 + \dfrac{\delta E_{c1}}{E_2 - E_{gB}}}{2} \qquad \text{(D.2)}$$

where $|M|^2$ is the bulk momentum matrix element of the quantum-well material, δE_{c1} is the first electron subband energy relative to the conduction band, and E_{gB} is the bulk bandgap of the quantum well.

Next, we define the reduced DOS $\rho_r(E_{21})$ for a quantum well as [D.2]:

$$\rho_r(E_{21}) = \frac{m_r}{\pi\hbar^2 L_z} \cdot H(E_{21} - E_{c1v1}) \qquad \text{(D.3)}$$

where m_r is the reduced DOS effective mass $(1/m_c + 1/m_{hh})^{-1}$, m_c is the electron effective mass, m_{hh} is the heavy-hole effective mass, L_z is the width of the quantum well, and $H(x)$ is the Heaviside step function.

The electron occupation probabilities, meanwhile, can be defined as Fermi functions [D.3]:

$$f_2 = \frac{1}{1 + \exp\left(\dfrac{E_2 - E_{fc}}{k_B T}\right)} \qquad \text{(D.4)}$$

$$f_1 = \frac{1}{1 + \exp\left(\dfrac{E_1 - E_{fv}}{k_B T}\right)} \qquad \text{(D.5)}$$

where E_{fc} is the electron quasi-Fermi-level, E_{fv} is the hole quasi-Fermi level, and k_B is Boltzmann's constant. Assuming charge neutrality ($n = p$), we can define f_2 and f_1 in terms of the electron density n using (4.3) and (4.4):

$$f_2 = \frac{1}{1 + \exp\left[\dfrac{(E_{21} - E_{c1v1})m_r}{k_b T m_c}\right]\left[\exp\left(\dfrac{\pi\hbar^2 L_z n}{m_c k_B T}\right) - 1\right]^{-1}} \qquad \text{(D.6)}$$

$$f_1 = \frac{1}{1 + \exp\left[\dfrac{-(E_{21} - E_{c1v1})m_r}{k_b T m_{hh}}\right]\left[\exp\left(\dfrac{\pi\hbar^2 L_z n}{m_{hh} k_B T}\right) - 1\right]} \qquad \text{(D.7)}$$

Finally, we can define the Lorentzian lineshape function $\mathcal{L}(\hbar\omega - E_{21})$ as [D.2]

$$\mathcal{L}(\hbar\omega - E_{21}) = \frac{1}{\pi} \cdot \frac{(\hbar/\tau_{in})}{(\hbar/\tau_{in})^2 + (\hbar\omega - E_{21})^2} \qquad \text{(D.8)}$$

where τ_{in} is the intraband relaxation time, typically on the order of 0.1 ps [D.2].

With these expressions in hand, we can now derive (4.5). Let us define the transition energy E_t as [D.3]

$$E_t = E_{21} - E_{c1v1} \tag{D.9}$$

Furthermore, we can define the individual energies E_2 and E_1 in terms of E_t using [D.3]

$$E_2 = E_{c1} + E_t \cdot \frac{m_r}{m_c} \tag{D.10}$$

$$E_1 = E_{v1} - E_t \cdot \frac{m_r}{m_{hh}} \tag{D.11}$$

Substituting (D.2)-(D.3) and (D.6)-(D.11) into (D.1) and noting that $E_{gB} = E_{c1} - \delta E_{c1}$, we finally obtain (4.5)

$$g(\hbar\omega) = \frac{q^2 m_r |M|^2 \lambda}{4\pi\tau_{in} L_z n_g c^2 \varepsilon_o m_o^2 h} \cdot \int_0^{\infty} \left(1 + \frac{\delta E_{c1}}{\delta E_{c1} + E_t \dfrac{m_r}{m_c}} \right) \cdot \frac{1}{\left(\dfrac{\hbar}{\tau_{in}}\right)^2 + (\hbar\omega - E_{c1v1} - E_t)^2} \tag{D.12}$$

$$\cdot \left(\frac{1}{1 + \exp\left(\dfrac{E_t m_r}{k_b T m_c}\right)\left[\exp\left(\dfrac{\pi\hbar^2 L_z n}{m_c k_B T}\right) - 1\right]^{-1}} - \frac{1}{1 + \exp\left(\dfrac{-E_t m_r}{k_b T m_{hh}}\right)\left[\exp\left(\dfrac{\pi\hbar^2 L_z n}{m_{hh} k_B T}\right) - 1\right]} \right) \cdot dE_t$$

D.1 References

[D.1] R. H. Yan, S. W. Corzine, L. A. Coldren, and I. Suemune, “Corrections to the expression for gain in GaAs,” *IEEE Journal of Quantum Electronics*, vol. 26, no. 2, pp. 213-216, 1990.

[D.2] L. A. Coldren and S. W. Corzine, *Diode Lasers and Photonic Integrated Circuits*. New York: John Wiley & Sons, Inc., 1995.

[D.3] S. L. Chuang, *Physics of Optoelectronic Devices*. New York: John Wiley & Sons, Inc., 1995.

APPENDIX E

IMPLEMENTATION OF THE SIMPLE VCSEL MODEL BASED ON SPATIALLY INDEPENDENT RATE EQUATIONS

Below, we summarize the HSPICE [E.1] and SABER [E.2] implementations of the simple VCSEL model of Section 4.4. In addition to summarizing the model equations, we provide an HSPICE subcircuit, a MAST template, and an overview of the model parameters.

E.1 Summary of Model Equations

The model equations presented in Section 2.4 are

$$\frac{dN_0}{dt} = \frac{\eta_i I}{q} - \frac{N_0}{\tau_n} - \frac{G_o(\gamma_0 N_0 - \gamma_1 N_1 - \gamma_0 N_t)S_o}{1 + \varepsilon S_o} \tag{E.1}$$

$$\frac{dN_1}{dt} = -\frac{N_1}{\tau_n}(1 + h_1) + \frac{G_o(\phi_0 N_0 - \phi_1 N_1 - \phi_0 N_t)S_o}{1 + \varepsilon S_o} \tag{E.2}$$

$$\frac{dS_o}{dt} = -\frac{S_o}{\tau_p} + \frac{\beta N_0}{\tau_n} + \frac{G_o(\gamma_0 N_0 - \gamma_1 N_1 - \gamma_0 N_t)S_o}{1 + \varepsilon S_o} \tag{E.3}$$

where (E.1) and (E.2) are the rate equations for the carrier numbers N_0 and N_1, respectively, and (E.3) is the rate equation for the photon number S_o. The output power P_o is modeled through $P_o = k_{fo}S_o$, where k_{fo} is the output-power coupling coefficient. While γ_0, γ_1, ϕ_0, and ϕ_1 in the above equations could be calculated through (4.23)-(4.26), the models presented here leave them as arbitrary parameters. The user is then free to choose alternate mode profiles to calculate their values.

As we did in the simple thermal VCSEL model of Chapter 3, we translated N_0, N_1, and P_o into variables v_{n0}, v_{n1}, and v_m, respectively, using

$$N_0 = z_n v_{n0} \tag{E.4}$$

$$N_1 = z_n v_{n1} \tag{E.5}$$

$$P_o = k_{fo} S_o = (v_m + \delta)^2 \tag{E.6}$$

where δ and z_n are arbitrary constants. Typically, z_n should be set to a value on the order of 10^8. Also, we modeled the VCSEL's electrical terminal characteristics through a series combination of resistance R_{laser} and a diode with saturation current I_o and ideality factor *nn*. We also included a shunting capacitance C_{laser} [E.3]. Note that the cavity injection current *I* is the current through the diode.

Table E.1 summarizes the complete set of model parameters.

E.2 HSPICE Implementation

We implemented the above model as an HSPICE netlist using the same techniques discussed in Chapters 2 and 3. After applying appropriate transformations to the various model equations, we obtained the complete equivalent circuit shown in Fig. E.1, where *p* and *n* are the electrical terminals and *po* is the output terminal whose node voltage models the optical power P_o. In addition to the electrical components mentioned above (where E_d models the diode), the various circuit elements are as

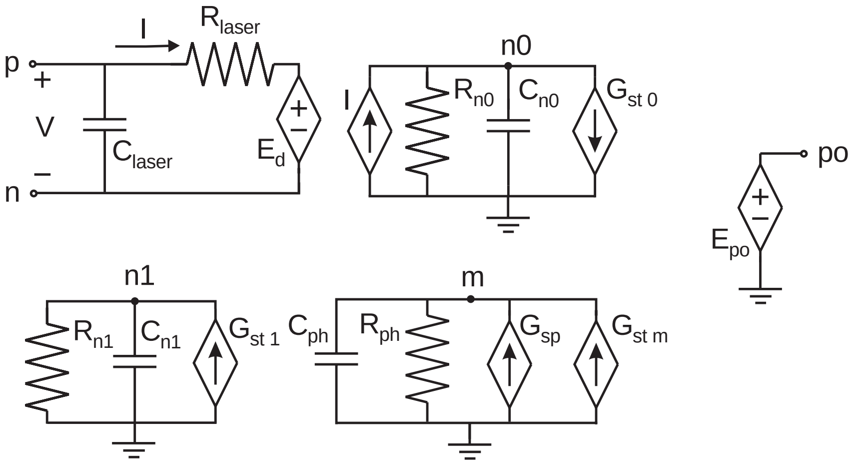

Figure E.1 Equivalent circuit of the simple VCSEL model.

Table E.1 Model parameters for the HSPICE and SABER implementations of the simple VCSEL model.

Parameter	Simulator Name	Description, units	Default
η_i	ETAI	current-injection efficiency	1
β	BE	spontaneous emission coupling coefficient	10^{-3}
τ_n	TN	carrier lifetime, s	5×10^{-9}
k_{fo}	KFO	output-power coupling coefficient, W	10^{-8}
G_o	GO	gain coefficient, s^{-1}	10^{4}
N_t	NT	carrier transparency number	10^{8}
τ_p	TP	photon lifetime, s	10^{-12}
ε	EPS	gain-saturation factor	0
γ_0	GAM0	N_0, S_o overlap integral value	1
γ_1	GAM1	N_0, S_o overlap integral value	1
ϕ_0	PHI0	N_1 overlap integral value	1
ϕ_1	PHI1	N_1 overlap integral value	1
h_1	H1	diffusion factor	1
R_{laser}	RLASER	series resistance, Ω	50
C_{laser}	CLASER	shunting capacitance, F	10^{-12}
I_o	IO	diode saturation current, A	10^{-14}
nn	NN	diode ideality factor	1
δ	DM	output power correction factor	5×10^{-10}
z_n	ZN	carrier scaling factor, V^{-1}	10^{8}

follows. Equation (E.1) is modeled via the current I, the capacitor $C_{n0} = qz_n/\eta_i$, the resistor $R_{n0} = \eta_i\tau_n/(qz_n)$, and the nonlinear dependent current source G_{st0}, where

$$G_{st0} = \frac{qG_o}{\eta_i k_{fo}} \cdot \frac{(\gamma_0 z_n v_{n0} - \gamma_1 z_n v_{n1} - \gamma_0 N_t)(v_m + \delta)^2}{1 + \varepsilon(v_m + \delta)^2 / k_{fo}} \tag{E.7}$$

Equation (E.2) is modeled via the capacitor $C_{n1} = qz_n/\eta_i$, the resistor $R_{n1} = \eta_i\tau_n/[qz_n(1+h_1)]$, and the nonlinear dependent current source G_{st1}, where

$$G_{st1} = \frac{qG_o}{\eta_i k_{fo}} \cdot \frac{(\phi_0 z_n v_{n0} - \phi_1 z_n v_{n1} - \phi_0 N_t)(v_m + \delta)^2}{1 + \varepsilon(v_m + \delta)^2 / k_{fo}} \tag{E.8}$$

Meanwhile, (E.3) is modeled by the capacitor $C_{ph} = 2\tau_p$, $R_{ph} = 1$, and nonlinear sources G_{sp} and G_{stm}, where

$$G_{sp} = \frac{\tau_p \beta k_{fo} z_n v_{n0}}{\tau_n (v_m + \delta)} \tag{E.9}$$

$$G_{stm} = \frac{G_o \tau_p (\gamma_0 z_n v_{n0} - \gamma_1 z_n v_{n1} - \gamma_0 N_t)(v_m + \delta)}{1 + \varepsilon(v_m + \delta)^2 / k_{fo}} - \delta \tag{E.10}$$

Finally, (E.6) is implemented via the nonlinear dependent voltage source E_{po}.

We implemented the equivalent circuit of Fig. E.1 using the HSPICE subcircuit of Fig. E.2. The model can be invoked within an HSPICE netlist by including this subcircuit and the following line for the VCSEL:

```
xlaser <p> <n> <po> las_diff <model_parameters>
```

where `<p>` and `<n>` are the VCSEL electrical terminals, `<po>` is the output terminal whose node voltage models the optical output power P_o, and `<model_parameters>` are the model parameter values. Parameters whose values are not set by the user retain their default values. A summary of the

```
.SUBCKT las_diff p n po   etai=1 tn=5e-9 go=1e4 nt=1e8 be=1e-3
+                         kfo=1e-8 tp=1e-12 eps=0
+                         gam0=1 gam1=1 phi0=1 phi1=1
+                         h1=1 dm=5e-10 zn=1e8
+                         rlaser=50 claser=1e-12 io=1e-14 nn=1
+                         q=1.60219e-19 kb=1.38062e-23

* electrical representation of laser diode
clas p n claser
rlas p x rlaser
ed   x n VOL=’(nn*kb*(temper+273.15)/q)*log(1+i(ed)/io)’

* carrier number circuits...

* N0 = zn*v(n0)
gn0  0  n0 CUR=’i(ed)’
cn0  n0 0  ‘q*zn/etai’
rn0  n0 0  ‘etai*tn/(q*zn)’
gst0 n0 0  CUR=’(q*go/(etai*kfo))*(gam0*zn*v(n0)-gam1*zn*v(n1)-gam0*nt)* \\
                (v(m)+dm)*(v(m)+dm)/(1+eps*(v(m)+dm)*(v(m)+dm)/kfo)’

* N1 = zn*v(n1)
cn1  n1 0  ‘q*zn/etai’
rn1  n1 0  ‘etai*tn/(q*zn*(1+h1))’
gst1 0  n1 CUR=’(q*go/(etai*kfo))*                                    \\
                (phi0*zn*v(n0)-phi1*zn*v(n1)-phi0*nt)*                \\
                (v(m)+dm)*(v(m)+dm)/(1+eps*(v(m)+dm)*(v(m)+dm)/kfo)’

* photon circuit...
cph  m 0 ‘2*tp’
rph  m 0 1
gsp  0 m CUR=’tp*be*kfo*zn*v(n0)/(tn*(v(m)+dm))’
gstm 0 m CUR=’go*tp*(gam0*zn*v(n0)-gam1*zn*v(n1)-gam0*nt)*(v(m)+dm)/    \\
              (1+eps*(v(m)+dm)*(v(m)+dm)/kfo) - dm’

* optical output
epo po 0 VOL=’(v(m)+dm)*(v(m)+dm)’

.ENDS las_diff
```

Figure E.2 HSPICE-subcircuit implementation of the simple VCSEL model.

parameter names used in the netlist and their correspondence with the actual variables can be found in Table E.1. Following is an example of a VCSEL invocation in HSPICE:

```
xlaser  1 0 2 las_diff  etai=1 tn=5e-9 go=4.4e4 nt=7.5e6 be=2e-7
+                       kfo=1.3e-8 tp=3e-12 eps=1e-6
+                       gam0=1 gam1=0.5 phi0=1 phi1=1
+                       h1=15 dm=5e-10 zn=1e8
+                       rlaser=50 claser=0.00001e-12 io=1e-21 nn=1
```

E.3 SABER Implementation

We also implemented our model as a MAST template for use in Analogy's SABER. Fig. E.3 illustrates the MAST template. As with the simple thermal model, the MAST template implements the core equations with little modification. The model can be invoked in SABER via a symbolic representation during schematic entry, or a netlist invocation. In the latter case, one should use

```
las_diff.<element_name> <p> <n> <po> = <model_parameters>
```

where `<p>` and `<n>` are the VCSEL electrical terminals, `<po>` is the output terminal whose node voltage models the optical output power P_o, and `<model_parameters>` passes the model parameter values into the template. The model parameters are the same as those used in the HSPICE subcircuit and can be found in Table E.1. Following is an example of the netlist invocation of the MAST template:

```
las_diff.las_diff1 p n po = etai=1, kfo=0.75e-8, tn=3e-9, be=2e-7, \
                            go=8e4, nt=15e6, eps=1e-6, tp=5e-12,   \
                            gam0=1, gam1=0.5, phi0=1, phi1=1,      \
                            h1=5, io=1e-21, nn=1, rlaser=50,       \
                            claser=1e-15, zn=1e8, dn=5e-10, dm=5e-10
```

```
element template las_diff p n po = etai, tn, go, nt, be, kfo, tp, eps,
                                   gam0, gam1, phi0, phi1,
                                   h1, dm, zn, rlaser, claser, io, nn
electrical p, n, po      # pins (electrical- p,n; optical- po)
number etai = 1, tn = 5e-9, go = 1e4, nt = 1e8,         # argument defaults
       be = 1e-3, kfo = 1e-8, tp = 1e-12, eps = 0,
       gam0 = 1, gam1 = 1, phi0 = 1, phi1 = 1,
       h1 = 1, dm = 5e-10, zn = 1e8,
       rlaser = 50, claser = 1e-12, io = 1e-14, nn = 1

external number temp      # simulation temperature

{
electrical x              # internal electrical node
branch ixn = i(x->n), vxn = v(x,n)       # cavity branch defns.
val v vpo                 # output power
val v n0,n1               # carrier number terms 0 and 1
var v vn0,vn1             # voltages related to carrier numbers
var v vm                  # voltage related to optical output power
var v gm                  # modal gain value
var i ipo                 # current from output node po

# local variables and constants
number kb = 1.38062e-23, q  = 1.60219e-19

# assign transforms for vpo, n0, and n1
vpo = (vm + dm)**2
n0  = zn*vn0
n1  = zn*vn1

# electrical representation of laser diode
cap.clas p n = claser
res.rlas  p x = rlaser
ixn = io*(limexp(q*vxn/(nn*kb*(temp+273.15)))-1)

# rate equations
vm: d_by_dt(vpo) = -vpo/tp + be*kfo*n0/tn +            \
         go*(gam0*n0 - gam1*n1 - gam0*nt)*vpo/(1+eps*vpo/kfo)
#
vn0: d_by_dt(n0) = etai*ixn/q - n0/tn               \
       - go*(gam0*n0 - gam1*n1 - gam0*nt)*vpo/kfo/(1+eps*vpo/kfo)
vn1: d_by_dt(n1) = -n1*(1+h1)/tn                    \
       + go*(phi0*n0 - phi1*n1 - phi0*nt)*vpo/kfo/(1+eps*vpo/kfo)
# modal gain definition (neglecting gain saturation)
gm: gm = go*(gam0*n0 - gam1*n1 - gam0*nt)

# optical output
i(po) += ipo
ipo: v(po) = vpo

}
```

Figure E.3 MAST-template implementation of the simple VCSEL model.

E.4 References

[E.1] *HSPICE User’s Manual*, Meta-Software, Inc., 1996.

[E.2] *SaberGuide Simulator Reference*, Analogy, Inc., 1996.

[E.3] J. J. Morikuni (private communication).

APPENDIX F

IMPLEMENTATION OF THE COMPREHENSIVE VCSEL MODEL

Below, we summarize the SABER [F.1] implementation of the comprehensive VCSEL models presented in Chapter 4. After summarizing the main model equations, we provide the MAST template for each model and an overview of the model parameters.

F.1 Summary of Model Equations

Following is the complete set of equations for our comprehensive VCSEL models:

$$\frac{dN_0}{dt} = \frac{\eta_i I_o}{q} - \frac{N_0}{\tau_n} - \sum_k \frac{G(T)\left[\gamma_{k0}N_0 - \sum_{i=1}^{\infty}\gamma_{ki}N_i - \gamma_{k0}N_t(T)\right]S_k}{1 + \sum_m \varepsilon_{mk}S_m} - \frac{I_l}{q} \tag{F.1}$$

$$\frac{dN_j}{dt} = \frac{-\eta_i I_o}{q}\cdot\zeta_j - \frac{N_j}{\tau_n}(1+h_j) + \sum_k \frac{G(T)\left[\phi_{jk0}N_0 - \sum_{i=1}^{\infty}\phi_{jki}N_i - \phi_{jk0}N_t(T)\right]S_k}{1 + \sum_m \varepsilon_{mk}S_m} \tag{F.2}$$

$$\frac{dS_k}{dt} = -\frac{S_k}{\tau_{pk}} + \frac{\beta_k}{\tau_n}\left[b_0N_0 - \sum_{i=1}^{\infty} b_iN_i\right] + \frac{G(T)\left[\lambda_{k0}N_0 - \sum_{i=1}^{\infty}\lambda_{ki}N_i - \lambda_{k0}N_t(T)\right]S_k}{1 + \sum_m \varepsilon_{mk}S_m} \tag{F.3}$$

$$G(T) = G_o\cdot\frac{a_{g0} + a_{g1}T + a_{g2}T^2}{b_{g0} + b_{g1}T + b_{g2}T^2} \tag{F.4}$$

$$N_t(T) = N_{to}(c_{n0} + c_{n1}T + c_{n2}T^2) \tag{F.5}$$

$$I_l = I_{lo}\exp\left(\frac{-a_0 + a_1 N_0 + a_2 N_0 T - \frac{a_3}{N_0}}{T}\right) \tag{F.6}$$

$$P_k = k_{fk} S_k \tag{F.7}$$

$$T = T_o + \left(I_{tot} V - \sum_k P_k\right) R_{th} - \tau_{th}\frac{dT}{dt} \tag{F.8}$$

$$V = f(I_o, T) \tag{F.9}$$

Equation (F.1) is the rate equation for the carrier number N_0, (F.2) is the general rate equation for the carrier number N_j ($j > 0$), and (F.3) is the general rate equation for the photon number S_k in the k^{th} mode. Equations (F.4)-(F.6) describe the temperature-dependent gain-constant, transparency number, and leakage current, respectively. Equation (F.7) relates the output power P_k in the k^{th} mode to the photon number S_k, while (F.8) is the rate equation for the device temperature T. Finally, (F.9) is the general expression for the device voltage V as a function of temperature and cavity injection current I_o. A capacitor C_{laser} is included in parallel with this voltage to model parasitic shunting capacitance.

As explained in Section 4.5.5, we transformed P_k, N_0, and N_j into the new variables v_{mk}, v_{n0}, and v_{nj} in order to improve the convergence properties of the model. These transformations are

$$P_k = (v_{mk} + \delta_m)^2 \tag{F.10}$$

$$N_0 = z_n(v_{n0} + \delta_n)^2 \tag{F.11}$$

$$N_j = z_n v_{nj} \tag{F.12}$$

Below, we review two different implementations of this model. The first uses a two-term expansion of the carrier profile (i.e., N_0 and N_1) and a single mode ($k = 0$), while the second uses a three-term expansion (N_0, N_1, and N_2) and two modes ($k = 0,1$).

F.2 Single-Mode Model Template

The MAST template for the single-mode model with a two-term carrier expansion implements (F.1)-(F.12) with $j = 1$ and $k = 0$. To facilitate switching between this model and the two-mode model of the next section, the template includes all of the parameters necessary for both. Extraneous parameters not needed by the single-mode equations (e.g. h_2) are simply ignored. The complete template is illustrated in Fig. F.1, while Table F.1 summarizes the complete set of model parameters used in the model. Note that the parameters h_j, b_i, ζ_j, γ_{ki}, ϕ_{jki}, and λ_{ki} are implemented as 1-D arrays, where the indices are incremented from lowest to highest order. For example, in the array for ϕ_{jki}, index i increments first, then k, and finally j. For the particular template of Fig. F.1, we modeled the device voltage using (4.72) with $R_1 = 12928.6$, $T_1 = 198.74$, $n_f = 1.468$, $I_1 = 3.907 \times 10^{-6}$. By changing the expression for `vpn` in the template, the user can implement alternative expressions.

The model can be invoked in SABER via a symbolic representation during schematic entry, or a netlist invocation. In the latter case, one should use the statement

```
vcsel12.<element_name> <p> <n> <pf0> <pf1> = <model_parameters>
```

where `<p>` and `<n>` are the VCSEL electrical terminals, `<pf0>` is the output terminal whose node voltage models the optical output power P_0, `<pf1>` is an extraneous node whose voltage is set to zero (and which is included for consistency with the two-mode model of the next section), and `<model_parameters>` passes the model parameter values into the template. Following is an example of the netlist invocation of the single-mode MAST template:

```
vcsel12.vcsel12_1 p n pf0 pf1 = kf0=1.5e-8, b=[1,0,0],             \
       tn=2.5e-9, eps10=0, eps11=5e-7,                              \
       lam=[1,0.37978,-0.0018753,1,0.12344,-0.1653],                \
```

```
element template vcsel12 p n pf0 pf1 = etai, tn, go, nto,
                                       tp0, tp1, kf0, kf1, be0, be1,
                                       b, eps00, eps01, eps10, eps11,
                                       lam, gam, phi, zet, h, tth,
                                       rth, ag0, ag1, ag2, bg0, bg1, bg2,
                                       cn0, cn1, cn2, ilo, a0, a1, a2, a3,
                                       claser, zn, dn, dm
electrical p, n, pf0, pf1          # pins (electrical- p,n; optical- pf0,pf1)
number etai = 1, tn = 5e-9, go = 1e4, nto = 1e8,      # argument defaults
       tp0 = 1e-12, tp1 = 1e-12, kf0 = 1e-8, kf1 = 1e-8, be0 = 1e-3, be1 = 1e-3,
       b[0:2] = [1,0,0], eps00 = 0, eps01 = 0, eps10 = 0, eps11 = 0,
       lam[0:1,0:2] = [1,0,0, 1,0,0], gam[0:1,0:2] = [1,0,0, 1,0,0],
       phi[1:2,0:1,0:2] = [1,0,0, 1,0,0, 1,0,0, 1,0,0],
       zet[1:2] = [0,0], h[1:2] = [1,1], tth = 0,
       rth = 1000, ag0 = 1, ag1 = 0, ag2 = 0, bg0=1, bg1 = 0, bg2 = 0,
       cn0 = 1, cn1 = 0, cn2 = 0, ilo = 0, a0 = 0, a1 = 0, a2 = 0, a3 = 0,
       claser = 1e-12, zn = 1e8, dn = 5e-10, dm = 5e-10
external number temp      # simulation temperature

{
branch ipn = i(p->n), vpn = v(p,n)     # cavity branch defns.
branch ipnc = i(p->n), vpnc = v(p,n)   # capacitor branch defns.
val v gth, ntth           # gain/transparency as fns. of temp.
var i fleak               # temp.-dependent leakage-current factor
val v p0                  # output power in modes 0,1,...
val v n0,n1               # carrier number term 0,1,...
var v vn0,vn1             # voltages related to carrier numbers
var v vm0                 # voltage related to modes 0,1,...
var v gm0                 # modal gain values for modes 0,1,...
var i ipf0,ipf1           # current from output node pf0,pf1,...
var tc tjct               # junction temperature

# local variables and constants
number kb = 1.38062e-23, q  = 1.60219e-19

# thermal-gain temperature defines...
gth   = go*(ag0+ag1*(tjct+273.15)+ag2*(tjct+273.15)**2)/                      \
           (bg0+bg1*(tjct+273.15)+bg2*(tjct+273.15)**2)
ntth  = nto*(cn0+cn1*(tjct+273.15)+cn2*(tjct+273.15)**2)
# leakage-current-factor definition
fleak = (ilo/q)*limexp((-a0+a1*zn*(vn0+dn)**2+a2*(tjct+273.15)*zn*(vn0+dn)**2 -   \
                     a3/(zn*(vn0+dn)**2))/(tjct+273.15))

# assign transforms for pk and nj
p0 = (vm0 + dm)**2
n0 = zn*(vn0+dn)**2
n1 = zn*vn1

# electrical representation of laser diode
vpn = 12928.567*ipn/(tjct+273.15-198.73691) +        \
      1.4679311*ln(1+255966.659082*ipn/(tjct+273.15-198.73691))
ipnc = d_by_dt(vpnc*claser)
```

Figure F.1 MAST-template implementation of the comprehensive VCSEL model for a single mode and a two-term expansion of the carrier profile (*continued on next page*).

```
# determine junction temperature
tjct: tjct = ((ipn+ipnc)*vpn - p0)*rth + temp - d_by_dt(tth*tjct)

# vcsel rate equations for photons
vm0: d_by_dt(p0) = -p0/tp0 + (be0*kf0/tn)*(b[0]*n0 - b[1]*n1)                   \
     + gth*(lam[0,0]*n0 - lam[0,1]*n1 - lam[0,0]*ntth)*p0/(1+eps00*p0/kf0)

# vcsel rate equation for carrier term n0
vn0: d_by_dt(n0) = etai*ipn/q - n0/tn                                           \
     - gth*(gam[0,0]*n0 - gam[0,1]*n1 - gam[0,0]*ntth)*p0/kf0/(1+eps00*p0/kf0)  \
     - fleak

# vcsel rate equation for carrier term n1
vn1: d_by_dt(n1) = -etai*ipn*zet[1]/q - n1*(1+h[1])/tn                          \
     + gth*(phi[1,0,0]*n0 - phi[1,0,1]*n1 -phi[1,0,0]*ntth)*p0/kf0/             \
           (1+eps00*p0/kf0)

# modal gain calculations (neglecting gain compression)
gm0: gm0 = gth*(lam[0,0]*n0 - lam[0,1]*n1 - lam[0,0]*ntth)

# optical output
i(pf0) += ipf0
i(pf1) += ipf1
ipf0: v(pf0) = p0
ipf1: v(pf1) = 0

}
```

Figure F.1 (*Continued.*)

```
go=3e4, phi=[2.3412,1.8193,0.62489,                         \
             0.76099,0.77999,-0.085866,                     \
             -0.020821,1.1254,1.7041,                       \
             -1.8352,-0.15465,0.94864],                     \
bg2=1.8e-5, zn=1e8, dn=5e-10, nto=1e7, bg1=-0.00974,        \
cn2=6e-6, claser=1e-15, dm=5e-10, tp1=1.8e-12, eps00=5e-7,  \
gam=[1,0.37978,-0.0018753,1,0.12344,-0.1653],               \
h=[15,16.7616], cn1=8e-3, bg0=1.3608, tp0=2.5e-12,          \
eps01=0, cn0=-1.0, a3=9.0147e9, be1=1e-3,                   \
zet=[0,0], ilo=0, a2=0.8e-7, be0=1e-3, ag2=7.65e-7,         \
a1=2.1176e-5, rth=900, ag1=0.00147, a0=4588.2353, etai=1.0, \
kf1=1.5e-8, ag0=-0.4, tth=1e-6
```

Table F.1 Model parameters for the SABER implementations of the comprehensive VCSEL model.

Parameter	Simulator Name	Description, units	Default
η_i	ETAI	current-injection efficiency	1
β_0, β_1	BE0, BE1	spontaneous emission coupling coefficients	10^{-3}, 10^{-3}
τ_n	TN	carrier lifetime, s	5×10^{-9}
k_{f0}, k_{f1}	KF0, KF1	output-power coupling coefficients, W	10^{-8}, 10^{-8}
G_o	GO	gain coefficient, s^{-1}	10^4
a_{g0}, a_{g1},a_{g2}, b_{g0}, b_{g1}, b_{g2}	AG0, AG1, AG2, BG0, BG1, BG2	thermal gain parameters	1, 0, 0, 1, 0, 0
N_{to}	NTO	carrier transparency number	10^8
c_{n0}, c_{n1}, c_{n2}	CN0, CN1, CN2	thermal transparency parameters	1, 0, 0
τ_{p0}, τ_{p1}	TP0, TP1	photon lifetimes, s	10^{-12}, 10^{-12}
ε_{00}, ε_{01}, ε_{10}, ε_{11}	EPS00, EPS01, EPS10, EPS11	gain-saturation factors	0, 0, 0, 0
b_i	B	integrated spontaneous emission factors	[1, 0, 0]
λ_{ki}	LAM	photon overlap integral values	[1, 0, 0, 1, 0, 0]
γ_{ki}	GAM	N_0 overlap integral values	[1, 0, 0, 1, 0, 0]
ϕ_{jki}	PHI	N_j overlap integral values	[1, 0, 0, 1, 0, 0 1, 0, 0, 1, 0, 0]
ζ_j	ZET	input-current integral values	[0, 0]
h_j	H	diffusion parameters	[1, 1]
R_{th}	RTH	thermal impedance, ºC/W	1000
τ_{th}	TTH	thermal time constant, s	0
I_{lo}, a_0, a_1, a_2, a_3	ILO, A0, A1, A2, A3	thermal leakage parameters	0, 0, 0, 0, 0
C_{laser}	CLASER	parasitic shunting capacitance, F	10^{-12}
z_n	ZN	carrier number scaling parameter	10^8
δ_n	DN	N_0-transform correction parameter	5×10^{-10}
δ_m	DM	photon-transform correction parameter	5×10^{-10}

F.3 Two-Mode Model Template

The MAST template for the two-mode model with a three-term carrier expansion implements (F.1)-(F.12) with $j = 1,2$ and $k = 0,1$. The complete template is illustrated in Fig. F.2. This model, unlike the single-mode version, incorporates all of the model parameters of Table F.1. As was the case with the single-mode version, the user can again implement arbitrary expressions for the device voltage by changing the expression for `vpn` in the template.

The two-mode model can be invoked in SABER via a symbolic representation during schematic entry, or a netlist invocation. The netlist invocation is

```
vcsel12.<element_name> <p> <n> <pf0> <pf1> = <model_parameters>
```

where `<p>` and `<n>` are the VCSEL electrical terminals, `<pf0>` and <`pf1`> are the output terminals whose node voltages model the optical output powers P_0 and P_1, respectively, and `<model_parameters>` passes the model parameter values into the template. Following is an example of the netlist invocation of the MAST template:

```
vcsel23.vcsel12_1 p n pf0 pf1 = kf0=1.5e-8, b=[1,0,0],             \
        tn=2.5e-9, eps10=0, eps11=5e-7,                            \
        lam=[1,0.37978,-0.0018753,1,0.12344,-0.1653], go=3e4,      \
        phi=[2.3412,1.8193,0.62489,0.76099,0.77999,-0.085866,      \
             -0.020821,1.1254,1.7041,-1.8352,-0.15465,0.94864],    \
        bg2=1.8e-5, zn=1e8, dn=5e-10, nto=1e7, bg1=-0.00974,       \
        cn2=6e-6, claser=1e-15, dm=5e-10, tp1=1.8e-12, eps00=5e-7, \
        gam=[1,0.37978,-0.0018753,1,0.12344,-0.1653],              \
        h=[5,16.7616], cn1=8e-3, bg0=1.3608, tp0=2.5e-12, eps01=0, \
        cn0=-1.0, a3=9.0147e9, be1=1e-3, zet=[0,0], ilo=9.61,      \
        a2=0.8e-7, be0=1e-3, ag2=7.65e-7, a1=2.1176e-5,            \
        rth=900, ag1=0.00147, a0=4588.2353, etai=1.0, kf1=1.5e-8,  \
        ag0=-0.4, tth=1e-6
```

```
element template vcsel23 p n pf0 pf1 = etai, tn, go, nto,
                                       tp0, tp1, kf0, kf1, be0, be1,
                                       b, eps00, eps01, eps10, eps11,
                                       lam, gam, phi, zet, h, tth,
                                       rth, ag0, ag1, ag2, bg0, bg1, bg2,
                                       cn0, cn1, cn2, ilo, a0, a1, a2, a3,
                                       claser, zn, dn, dm
electrical p, n, pf0, pf1          # pins (electrical- p,n; optical- pf0,pf1)
number etai = 1, tn = 5e-9, go = 1e4, nto = 1e8,      # argument defaults
       tp0 = 1e-12, tp1 = 1e-12, kf0 = 1e-8, kf1 = 1e-8, be0 = 1e-3, be1 = 1e-3,
       b[0:2] = [1,0,0], eps00 = 0, eps01 = 0, eps10 = 0, eps11 = 0,
       lam[0:1,0:2] = [1,0,0, 1,0,0], gam[0:1,0:2] = [1,0,0, 1,0,0],
       phi[1:2,0:1,0:2] = [1,0,0, 1,0,0, 1,0,0, 1,0,0],
       zet[1:2] = [0,0], h[1:2] = [1,1], tth = 0,
       rth = 1000, ag0 = 1, ag1 = 0, ag2 = 0, bg0=1, bg1 = 0, bg2 = 0,
       cn0 = 1, cn1 = 0, cn2 = 0, ilo = 0, a0 = 0, a1 = 0, a2 = 0, a3 = 0,
       claser = 1e-12, zn = 1e8, dn = 5e-10, dm = 5e-10
external number temp      # simulation temperature

{
branch ipn = i(p->n), vpn = v(p,n)    # cavity branch defns.
branch ipnc = i(p->n), vpnc = v(p,n)  # capacitor branch defns.
val v gth, ntth           # gain/transparency as fns. of temp.
var i fleak               # temp.-dependent leakage-current factor
val v p0,p1               # output power in modes 0,1,...
val v n0,n1,n2            # carrier number term 0,1,...
var v vn0,vn1,vn2         # voltages related to carrier numbers
var v vm0,vm1             # voltage related to modes 0,1,...
var v gm0,gm1             # modal gain values for modes 0,1,...
var i ipf0,ipf1           # current from output node pf0,pf1,...
var tc tjct               # junction temperature

# local variables and constants
number kb = 1.38062e-23, q  = 1.60219e-19

# thermal-gain temperature defines...
gth   = go*(ag0+ag1*(tjct+273.15)+ag2*(tjct+273.15)**2)/                      \
           (bg0+bg1*(tjct+273.15)+bg2*(tjct+273.15)**2)
ntth  = nto*(cn0+cn1*(tjct+273.15)+cn2*(tjct+273.15)**2)
# leakage-current-factor definition
fleak = (ilo/q)*limexp((-a0+a1*zn*(vn0+dn)**2+a2*(tjct+273.15)*zn*(vn0+dn)**2 -   \
                     a3/(zn*(vn0+dn)**2))/(tjct+273.15))

# assign transforms for pk and nj
p0 = (vm0 + dm)**2
p1 = (vm1 + dm)**2
n0 = zn*(vn0+dn)**2
n1 = zn*vn1
n2 = zn*vn2
```

Figure F.2 MAST-template implementation of the comprehensive VCSEL model for two modes and a three-term expansion of the carrier profile (*continued on next page*).

```
# electrical representation of laser diode
vpn = 12928.567*ipn/(tjct+273.15-198.73691) +        \
      1.4679311*ln(1+255966.659082*ipn/(tjct+273.15-198.73691))
ipnc = d_by_dt(vpnc*claser)

# determine junction temperature
tjct: tjct = ((ipn+ipnc)*vpn - p0 - p1)*rth + temp - d_by_dt(tth*tjct)

# vcsel rate equations for photons
vm0: d_by_dt(p0) = -p0/tp0 + (be0*kf0/tn)*(b[0]*n0 - b[1]*n1 - b[2]*n2)       \
     + gth*(lam[0,0]*n0 - lam[0,1]*n1 - lam[0,2]*n2 - lam[0,0]*ntth)*p0/      \
           (1+eps00*p0/kf0+eps10*p1/kf1)
vm1: d_by_dt(p1) = -p1/tp1 + (be1*kf1/tn)*(b[0]*n0 - b[1]*n1 - b[2]*n2)       \
     + gth*(lam[1,0]*n0 - lam[1,1]*n1 - lam[1,2]*n2 - lam[1,0]*ntth)*p1/      \
           (1+eps01*p0/kf0+eps11*p1/kf1)
#
# vcsel rate equation for carrier term n0
vn0: d_by_dt(n0) = etai*ipn/q - n0/tn                                         \
     - gth*(gam[0,0]*n0 - gam[0,1]*n1 - gam[0,2]*n2 - gam[0,0]*ntth)*p0/kf0/  \
           (1+eps00*p0/kf0+eps10*p1/kf1)                                      \
     - gth*(gam[1,0]*n0 - gam[1,1]*n1 - gam[1,2]*n2 - gam[1,0]*ntth)*p1/kf1/  \
           (1+eps01*p0/kf0+eps11*p1/kf1)                                      \
     - fleak
#
# vcsel rate equation for carrier term n1
vn1: d_by_dt(n1) = -etai*ipn*zet[1]/q - n1*(1+h[1])/tn                      \
     + gth*(phi[1,0,0]*n0 - phi[1,0,1]*n1 -                                 \
            phi[1,0,2]*n2 - phi[1,0,0]*ntth)*p0/kf0/                        \
           (1+eps00*p0/kf0+eps10*p1/kf1)                                    \
     + gth*(phi[1,1,0]*n0 - phi[1,1,1]*n1 -                                 \
            phi[1,1,2]*n2 - phi[1,1,0]*ntth)*p1/kf1/                        \
           (1+eps01*p0/kf0+eps11*p1/kf1)
#
# vcsel rate equation for carrier term n2
vn2: d_by_dt(n2) = -etai*ipn*zet[2]/q - n2*(1+h[2])/tn                      \
     + gth*(phi[2,0,0]*n0 - phi[2,0,1]*n1 -                                 \
            phi[2,0,2]*n2 - phi[2,0,0]*ntth)*p0/kf0/                        \
           (1+eps00*p0/kf0+eps10*p1/kf1)                                    \
     + gth*(phi[2,1,0]*n0 - phi[2,1,1]*n1 -                                 \
            phi[2,1,2]*n2 - phi[2,1,0]*ntth)*p1/kf1/                        \
           (1+eps01*p0/kf0+eps11*p1/kf1)
#
# modal gain calculations (neglecting gain compression)
gm0: gm0 = gth*(lam[0,0]*n0 - lam[0,1]*n1 - lam[0,2]*n2 - lam[0,0]*ntth)
gm1: gm1 = gth*(lam[1,0]*n0 - lam[1,1]*n1 - lam[1,2]*n2 - lam[1,0]*ntth)

# optical output
i(pf0) += ipf0
i(pf1) += ipf1
ipf0: v(pf0) = p0
ipf1: v(pf1) = p1

}
```

Figure F.2 (*Continued*.)

F.4 References

[F.1] *SaberGuide Simulator Reference*, Analogy, Inc., 1996.

VITA

Pablo Valente Mena was born in Evergreen Park, IL, on June 1, 1973. After graduating from Carl Sandburg High School in June 1990, he attended the University of Illinois at Urbana-Champaign (UIUC), where he received his B.S. in electrical engineering in January 1994. He graduated with highest honors. During his undergraduate years, he received a number of awards, including the E. C. Jordan Award (1993) and the William L. Everitt Award (1993). In addition, Mr. Mena enjoyed summer internships at Andrew Corporation (1992), where he helped develop software for controlling a satellite-dish test range, and at Intel (1993), where he worked on improving the reliability of a LAN adapter card's test interface. He also spent one semester as a grader for the undergraduate course "Introduction to Electromagnetic Fields."

In January 1994, Mr. Mena began his graduate study at UIUC, where he received his M.S. degree in electrical engineering in May 1995. He will earn his Ph.D. in October 1998. His M.S. thesis involved the design and simulation of a proof-of-principle CMOS integrated circuit with hybridly integrated optical interconnects, while his Ph.D. research has focused on the development of circuit-level semiconductor laser models for SPICE-like simulators. His Ph.D. study has included a one-year internship at Motorola's Applied Simulation and Modeling Research group in Schaumburg, IL, where he helped develop circuit-level optoelectronic device models.

Mr. Mena has had six publications, with three pending. In addition, he is a member of various honors societies, including Tau Beta Pi, Eta Kappa Nu, and Phi Kappa Phi. He is also a member of the IEEE and OSA.